Single Microbubble Imaging

Hendrik Jacob Vos

Financial support for the printing of this thesis is kindly provided by:

· Bracco Research S.A.
· Oldelft Ultrasound B.V.
· Olympus Nederland B.V.
· VisualSonics

Cover design by Margreet Bettenhaussen-Leclercq
Reproduced by Optima grafische communicatie BV, Rotterdam
ISBN 978 90 8559 916 6

For a printed version please contact:
Secretary Biomedical Engineering (January 2010: room Ee2302)
Erasmus Medical Center
PO BOX 2040, NL-3000 CA
Rotterdam, the Netherlands

Single Microbubble Imaging

Microbelbeeldvorming

Proefschrift

ter verkrijging van
de graad van doctor aan de
Erasmus Universiteit Rotterdam
op gezag van de
Rector Magnificus

Prof.dr. H.G. Schmidt,

en volgens besluit van het College voor Promoties.

De openbare verdediging zal plaatsvinden op
woensdag 20 januari 2010 om 15.30 uur door

Hendrik Jacob Vos
geboren te Zwartsluis

Promotiecommissie

Promotoren:	Prof.dr.ir. A. F. W. van der Steen Prof.dr.ir. N. de Jong
Overige Leden:	Prof.dr.ir. M. de Jong Dr. M. Versluis Prof.dr. P. Tortoli

This study was performed at Biomedical Engineering, Thorax Center, Erasmus MC Rotterdam, the Netherlands. A strong and lively cooperation with the Physics of Fluids group, University of Twente, Enschede, the Netherlands, and the Electronic Systems Engineering research group, Department of Electronics and Telecommunications, University of Florence, Italy, is acknowledged.

Preface

Preliminary work leading to this thesis started in a warm and sunny Florence, Italy, in the summer of 2004. After one year in Italy the work was continued in Rotterdam, contained within a PhD graduate trajectory. After some years of research this thesis will be defended in January 2010. Research was not new to me; ever since I was young I have been wondering about everything around me, observing it, studying it. My nerve cells got used to new impressions, and even more, they keep on asking for more; probably that is the fundamental drive behind curiosity, and ultimately, behind this thesis.

The thesis is about gas bubbles that are smaller than the eye can see, used as contrast agents in medical imaging with ultrasound. Current detection is suboptimal, and new methods are needed to image and characterize the behavior of single microbubbles.

Retrospectively, the studies presented in this thesis were motivated by a strong scientific interest. Ideas and concepts looked very simple initially but were found to be more complex. Subsequently the complex phenomena were studied and exploited. For instance, radiation force on microbubbles by ultrasound can produce a bias in the estimation of blood flow in larger vessels; this force is now used to characterize contrast agents (Chapter 2). A capillary wall in optical microbubble studies is gratefully used to study nonspherical oscillations of bubbles in close contact with stiff objects (Chapters 6 and 7). As a final example, nonlinear ultrasound propagation in water and tissue initially resisted the concept of the pulse-repetition excitation method that was filed in a patent during the graduate years. However, as can be read in Chapters 10 and 11, nonlinear propagation itself is now proposed as a useful bubble excitation mechanism.

A slightly different approach is used in the realization of Chapter 12. Based on the results of the other chapters a method is distilled that would greatly suppress tissue signals, and enhance contrast detection signals. Although this method has yet to be proven the preliminary numerical results seem promising.

I hope the work described in this thesis contributes to the development of better detection schemes, ultimately leading to higher diagnostic value of contrast-enhanced medical imaging with ultrasound.

Rik Vos
December 9, 2009, Rotterdam

Contents

Chapter 1

Introduction

Abstract - **The imaging of smaller vessels and organ perfusion has high clinical value for diagnosis of cardiovascular diseases and cancer. Ultrasound imaging is widely used in the clinic, but the diagnostic value for small vessel imaging is reduced since blood has lower scattering strength than tissue, and the imaging modality suffers from speckle production. Ultrasound contrast agents (UCAs) can potentially increase the scattering from blood. The agents consist of coated gas bubbles of sizes of some micrometer, and are injected intravenously. In the past it was found that the fundamental-frequency scattering of bubbles does not provide sufficient contrast. They can however also produce nonlinear acoustic responses, which are beneficial for the detection. In recent years many acoustic detection schemes have been proposed to enhance the contrast signals and suppress tissue signals. Yet, the proposed schemes have great difficulty to detect very low concentration or even single microbubbles if surrounded by tissue. Next to this standard application of contrast agents, upcoming diagnostic and therapeutic applications with the agents are threefold: a targeting modality, drug and gene delivery, and transient cell-membrane opening.**

Given this background the thesis investigates single contrast agent microbubbles with optical, acoustic, and numerical techniques to study the influence of the microbubble structure and size on the linear and nonlinear responses. Emphasis is given to phospholipids-coated microbubbles since only these are currently approved for clinical use in the Netherlands and in most other countries in the world. In the various studies the microbubbles are excited with clinically relevant pressure waves. The background of the thesis, and an introduction to the experimental methods, are provided in this Chapter.

1.1 Medical diagnostic ultrasound

Medical diagnostic ultrasound is widely used for paediatric screening, for assessing the condition of organs and the cardiovascular system, and for cancer diagnostics; to a lesser extent ultrasound is also used in e.g. ocular and auditory diagnostics and bladder size measurements.

Ultrasound scanners have a probe that transmits a pulsed wave into tissue. Tissue never is homogeneous and small variations in the density and compressibility will scatter the wave, producing echoes that are recorded by the same probe. Tissue echoes thus consist of the sum of all small contributions, producing constructive and destructive interference at the surface of the probe. The interferential pattern and scattering level are specific for the tissue type. Furthermore, the time-of-flight of the echo is converted to depth assuming a constant speed of sound (generally $\sim$ 1540 m/s). Also, the probe adds directionality to the waves, thus irradiating a volume of tissue like a sweeping light torch. The result is a 2-dimensional (2D) or 3D image from which the tissue anatomy can be recognized as grey-scale regions having different brightness and speckle pattern. The 2D image is produced at framing rates generally up to 50 frames per second, allowing a real-time feedback of the position of the probe which provides easy use for the operating clinician.

The final resolution of an image depends on the time length of the pulse (axial resolution), and the narrowness of the ultrasound beam (lateral resolution). Both generally show an inverse relation with frequency: a higher ultrasound frequency can give smaller time length and enables producing narrower beams. Given regular medical imaging frequencies of 1 – 10 MHz the volume resolution (voxel size) is in the range of 0.01 – 10 mm^3.

Imaging of blood supply through arteries, veins, arterioles, venules and the capillary bed has high diagnostic value. For instance, blood supply through the coronary arteries determines the heart's condition. Also, presence or absence of blood discriminates between a carcinoma and an abscess. On a smaller scale the structure of the arterioles in suspected cancer carcinoma and the microvascularity in atherosclerotic plaque can predict their development [Feinstein, 2004, 2006]. Therefore many ultrasound imaging modalities aim to depict vessels and their blood carrying properties.

Since the scattering strength of blood is lower than that of the surrounding tissue at regular medical imaging frequencies (at 4 MHz the scattering of blood is estimated 2% of that of heart muscle and 2% – 30% of liver tissue [Duck, 1990]), larger vessels and the heart cavities will show up as dark regions in brighter surroundings. An example of an ultrasound image of the left ventricular chamber of the heart is shown in Fig. 1.1(left). However, arterioles, venules and the vascular bed are more difficult to detect as they are masked by the speckle pattern of the surrounding tissue and/or are smaller than the voxel size. The fine structure of these

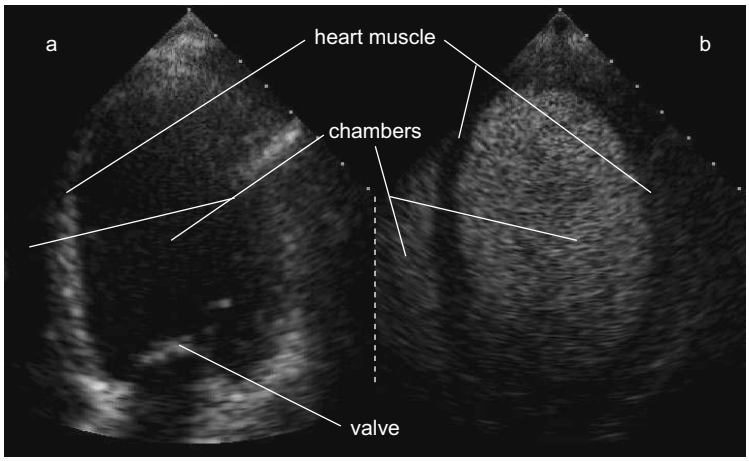

Figure 1.1: Ultrasound image of the left ventricular (LV) chamber of the heart with and without contrast agent. (a) Image without contrast mode. The LV cavity is darker than the heart muscle (myocardium); (b) Image with contrast mode. The cavity is brighter than the heart muscle. Images by courtesy of Dr. F. J. ten Cate, Thorax Center, Erasmus MC, Rotterdam, the Netherlands.

vessels in the heart muscle are thus indistinguishable.

A solution for imaging smaller vessels is bringing the probe closer to the region of interest. Ultrasound waves are attenuated while propagating, and in tissue the attenuation generally increases exponentially with frequency and distance. This poses a trade-off between imaging depth and resolution; the closer the image window to the probe, the higher the imaging frequency can be selected, and the higher the resolution can become. An example is intravascular ultrasound that employs an intravascular catheter-based ultrasound probe and imaging frequencies of 20–45 MHz. The resolution in the images of a vessel wall is increased compared to that obtained with a noninvasive probe. Other examples are a transrectal probe for imaging the prostate, a trans-esophageal probe for imaging the heart, and carotid artery scanning for assessing the overall chance of having severe atherosclerosis throughout the body [Feinstein, 2006].

A second solution to discriminate between blood and tissue is the use of Doppler-based techniques in which fast changes of the echo, induced by blood flow, are detected using a correlation technique [Evans and McDicken, 2000]. Tissue is not moving (except for slow movements induced by e.g. breathing and the heart beat) which allows for cancellation of tissue signals. This method works well for larger vessels, where blood flow is high, but has been shown inappropriate for smallest vascular structures where flow is low [Tortoli et al., 2000; Goertz et al., 2000, 2005].

A third solution for imaging smaller vessels is the use of ultrasound contrast

Figure 1.2: Collection of vials containing several types of contrast agents. In the background a SonoVue-package (Bracco Int.) is shown.

agents, as described in the next section.

1.2 Ultrasound contrast agent microbubbles

Ultrasound contrast agents (UCAs) are injected into the blood circulation to enhance echo signals from vessels and the heart chambers, thus imaging the vascular structure and organ perfusion, and clarifying the myocardial border by left ventricular opacification [Quaia, 2007; Dolan et al., 2009]. An example of a contrast-enhanced image is shown in the right panel of Fig. 1.1. The entire chamber is brighter than the heart muscle. The borders of the chamber are clearer than in the left image, which could assist in determination of the functioning of the heart. Depending on the time after bolus injection at which this frame was recorded, a darker heart muscle in the contrast-enhanced image (such as on the left side of the right panel) could indicate a poor blood perfusion in that part of the heart muscle.

In general, ultrasound contrast agents consist of small gas bubbles (0.5–10 μm diameter, see Fig. 1.3 for a microscopic image) typically stabilized by an albumin, phospholipids or polymer coating to reduce dissolution and prevent coalescence. Because of the size range they are generally referred to as microbubbles. In very general terms, gas has higher compressibility than surrounding liquid and tissue, thus acting as a high-scattering particle of the ultrasound wave; details on the scattering characteristics can be found in this thesis. At present SonoVue is the only agent clinically available in the entire EU, while Optison and Definity are available in North America; see Table 1.1 for an overview.

Administration of the UCA is done by intravenous injection, providing a first

Table 1.1: Overview of recent and current commercial contrast agents

Region	name	marketing authorization holder	comment	coating	gas
EU	SonoVue	Bracco International		phospholipids	SF_6
	Optison	GE Healthcare	EU marketing suspended since June 2008	human albumin	C_3F_8
	Luminity	(Lantheus Med. Imaging)	not marketed	Phospholipids	C_3F_8
	Levovist	Bayer Schering Pharma	partly marketed*	galactose, palmatic acid	air
USA,CA	Definity	Lantheus Med. Imaging		Phospholipids	C_3F_8
	Optison	GE Healthcare		human albumin	C_3F_8
	Imagify	Acusphere	in application process	polymer/ phospholipids	C_4F_10
Japan	Sonazoid	Daiichi Pharmaceutical		lipids	C_4F_{10}
World	Targestar	Targeson	Animal studies	phospholipids	C_4F_{10}
	MicroMarker	VisualSonics (manuf. Bracco)	Animal studies	phospholipids / fatty acids	N_2/ C_4F_{10}

Sources: European Medicines Agency, US Food and Drug Administration, Japanese Dep. of Health and Welfare, Bayer Schering Pharma, Targeson, Bracco, VisualSonics.
* According to the manufacture, Levovist is approved and available in Germany, Spain, Japan, and others, but in the Netherlands it is not available and the marketing authorization has been withdrawn.

passage through the pulmonary circulation before going through the systemic circulation. The size range allows passing the lung capillaries, but removal of bubbles larger than 5 μm is to be expected [Bouakaz and de Jong, 2007; Lindner et al., 2002]. This is advantageous from a safety standpoint, as the largest bubbles could increase the risk of blocking smaller vessels, preventing blood to flow to down-stream tissue. While circulating through the body, coated bubbles are deteriorating when passing the lungs and capillary bed, and/or are taken up by macrophages [Yanagisawa et al., 2007], or just deflate. Gases are generally selected to be inert and of low solubility, leading to circulation times of several minutes (see e.g. the Definity package insert, available on the Internet). Only Levovist, frequently used in the past, contains air which generally results in a lower circulation time than the other type of agents [Forsberg et al., 1999; Basude et al., 2000; Bouakaz and de Jong, 2007]. Ultimately the gas is exhaled (note that a vial of Definity contains 0.4 mℓ gas - and a single regular breath contains $\sim$ 500 mℓ). The agents have been shown to be safe compared to other non-ultrasound diagnostic contrast agents [Blomley, 2007] [1], and the merits are high [Cosgrove, 2006; Kaul, 2008; Feinstein, 2006; Dolan et al., 2009].

Owing to their size, microbubbles have similar kinetics in the vascular system as red blood cells [Levine et al., 1984; Tortoli et al., 2001; Lindner et al., 2002] and it is assumed that injected microbubbles will spread all over the cardiovascular system just like red blood cells. In fact, this can be translated into a fundamental assump-

[1] A special issue of Ultrasound in Medicine & Biology is devoted to safety of UCAs: Ultras Med Biol 33(2)pp.171-234, 2007

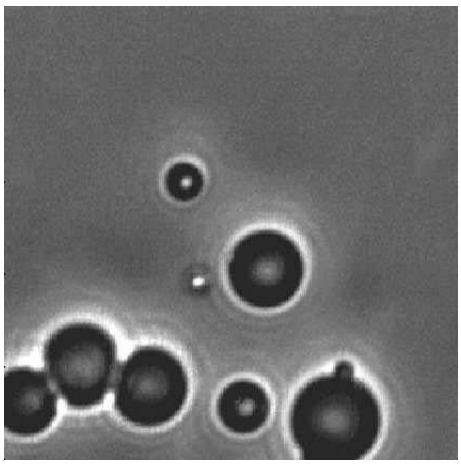

Figure 1.3: Photographic picture of BR14 microbubbles observed through a microscope. Picture size is 50 $\times$ 50 μm.

tion of contrast-enhanced ultrasound: if agent is detected somewhere in the body then that region contains a blood-carrying vessel; if no agent is detected then there is either no vessel or an occluded vessel. It is assumed that sufficient agent is administered to fill the entire vascular system. Given that e.g. a Definity vial contains up to $3 \cdot 10^{10}$ microbubbles in 2.5 mℓ of liquid [Package insert Definity], and given an average blood volume of 7 ℓ, the expected concentration can be calculated in the heart and vessels, see Table 1.2. With a 'bolus injection' the entire content of the vial is injected at once, as opposed to an 'infusion injection' with which the content is injected at constant rate during the examination. Statistically, capillaries smaller than 20 μm will contain less then one bubble per voxel, but on the other hand multiple capillaries are present within one voxel. Such concentration was also optically observed by e.g. Lindner et al. [2002]. Snapshot images using contrast-enhanced ultrasound will therefore not show the exact microvasculature but only an impression of the density and structure.

Microbubbles will regularly approximate a vessel wall and/or red blood cells, expectedly giving a dynamical interaction [Prentice et al., 2005; Zhao et al., 2005; Caskey et al., 2006, 2007; Garbin et al., 2007; Overvelde et al., 2007]. Furthermore they are contained in the plasma, which has higher viscosity than water, and which is at body temperature. Yet microbubble characterization experiments are regularly employed in water at room temperature, which might not give representative results for the *in vivo* situation.

Table 1.2: Estimate of bubble densities after bolus injection. Microbubble destruction is neglected.

	Vessel diameter [mm]	3D Concentration [bubbles / mm^3]	1D concentration [bubbles / mm vessel]
In vial	-	$1.2 \cdot 10^7$	-
Right atrium	-	$4 \cdot 10^3$	-
Artery	1	-	$3 \cdot 10^3$
Arteriole	$2 \cdot 10^{-2}$	-	1
Capillary	$5 \cdot 10^{-3}$	-	$1 \cdot 10^{-1}$

1.3 Advanced use of contrast agents

1.3.1 Sonoporation

Oscillating microbubbles nearby cells can enhance drug uptake which is called sonoporation [Mukherjee et al., 2000; van Wamel et al., 2006; Forbes et al., 2008]. Normal and shear stresses produce reversible openings of the membrane through which large drug or gene molecules can enter the cell. More violent collapses of microbubbles have been shown to produce microjets and high shear rates, generally destroying and removing cells grown on a substrate [Prentice et al., 2005; Ohl et al., 2006]. The oscillation amplitude therefore determines the strength of the effects, and cell cure and survival might be a delicate balance between too high and too low radial oscillations of the microbubbles [Forbes et al., 2008]. However the oscillation of microbubbles is influenced by many factors, including the exact bubble size and composition, the surroundings (fluid, mechanical, and geometrical properties), and excitation pressure and frequency. Microbubbles (but not specifically contrast agent microbubbles) have also been shown to play a large role in kidney stone fragmentation by high-intensity ultrasound, so-called shock wave lithotripsy. Microbubbles might also be used for blood cloth hammering.

1.3.2 Drug transport

An emerging application is drug transport and delivery by encapsulated microspheres [Bekeredjian et al., 2005; Kooiman et al., 2009]. In such an application microspheres contain gas, providing echogenicity, and a drug. With ultrasound the position and density of the microspheres at the site of interest can be monitored, and presumably the spheres are destroyed by high-intensity ultrasound delivered at the same position. Such application would lower the concentration of drugs at other parts of the body, thus lowering unwanted side-effects and potentially increasing the local concentration of drugs. In combination with the sonoporation effect by the oscillating gas bubble the drug uptake might even be enhanced. Drug carrying agents are relatively new and the efficacy has yet to be proven.

1.3.3 Targeting

In recent years microbubble coatings have been developed that contain 'adhesive' molecules (ligands) that adhere to cells that express disease-specific markers (e.g., aminoacids) on the membrane [Lindner, 2001; Christiansen and Lindner, 2005]. Thus microbubbles can target to a diseased region of the vessel. Targeted contrast agents are also applied in other clinical imaging modalities such as contrast-enhanced MRI and CT, and the methods and ligands from those modalities may also be used for ultrasound contrast agents. Currently a drawback of the method is that the ratio between targeted and freely circulating bubbles is low and echoes of targeted bubbles are shadowed by those of freely circulating microbubbles, reducing sensitivity. Some studies hypothesize that the echo characteristics of adhered bubbles will be different for targeted vs. freely circulating microbubbles [Zhao et al., 2007; Doikinov et al., 2009]. Moreover, it has been shown that targeted microbubbles have longer life time ($>$15 min) than freely circulating microbubbles ($\sim$ 4 min) which suggests a simple discrimination technique based on time. Such technique would still require a sensitive microbubble detection scheme.

1.4 Basics of microbubble detection methods

The previous sections have shown the great need for detection and imaging of low numbers of contrast agent microbubbles *in vivo*. A successful detection strategy discriminates between bubble signals and tissue signals, usually by enhancing signals from bubbles and suppressing the signals from tissue. This section provides a brief overview of the acoustic behavior of microbubbles and currently-linked detection methods.

1.4.1 Bubble behavior

The combination of gas, coating and surrounding liquid constitute a damped oscillator having a resonance frequency that strongly depends on the bubble radius [Minnaert, 1933; de Jong et al., 2002]. Resonant excitation yields higher scattering than that produced by only gas compressibility [de Jong et al., 1992]. Viscosity of the coating material and surrounding liquid has a damping effect [Gorce et al., 2000; van der Meer et al., 2007; Sijl et al., 2008]. Furthermore, scattering of bubbles has to compete with scattering of surrounding tissue, and simple detection of the fundamental-frequency response usually does not provide a high contrast-to-tissue signal ratio (CTR). Therefore most detection strategies are based on either the nonlinear microbubble responses to the imaging pulse or transient effects of the microbubble oscillation.

Phospholipids-coated microbubbles have been shown to generate higher harmonics of the excitation frequency [de Jong et al., 2002], subharmonics [Eller and

Flynn, 1969; Chomas et al., 2002; Shi et al., 2002; Goertz et al., 2007b; Needles et al., 2008], ultra low harmonics [Wu et al., 2005], and are shown to respond nonlinearly to the insonation pressure level [Emmer et al., 2007]. Also, they are able to act as nonlinear mixers in dual-frequency insonation fields producing cross-products [Deng et al., 2000; Shi and Forsberg, 2000; Chen et al., 2006; Yeh et al., 2008]. Transient effects have been extensively addressed by Morgan et al. [2000]; Borsboom [2004]; Shi et al. [2006]; Mleczko et al. [2007]. It has also been shown that ultrasound can destroy microbubbles.

1.4.2 Detection methods

Straightforward nonlinear detection signals can be obtained by selecting the frequency band that contains the second harmonic, super harmonic (e.g. 3^{rd} – 5^{th} harmonics, [Bouakaz et al., 2002]) or one-half subharmonic [Shi et al., 2002; Goertz et al., 2007b] of the excitation frequency. Since nonlinear responses generally have a squared relation with the pressure amplitude, it has been found useful to recombine the echoes of two or more detection pulses having different amplitude and/or phase [Quaia, 2007]. Furthermore, a dual-frequency technique has been suggested in which a low-frequency wave modulates the response of microbubbles to a high-frequency imaging pulse, called SURF imaging or radial modulation, see e.g. Bouakaz et al. [2007]; Måsøy et al. [2008]; Chérin et al. [2008]. Methods based on destruction have also been shown to be able to detect contrast agent.

Two major drawbacks of most of these detection methods have become progressively clear. First is that nonlinear tissue response, present in regular diagnostic ultrasound [Duck, 2002], degrades the efficacy of detection schemes based on frequency cross products such as second harmonics, radial modulation, and ultra low harmonics. Schemes based on subharmonic response and threshold behavior [Emmer et al., 2009] do not have this drawback since these effects are not present in nonlinear tissue propagation at diagnostic amplitudes. Second is that the signals originating from nonlinear responses have lower amplitude than the fundamental bubble response. Detection signals have therefore limited signal-to-noise ratio, reducing the penetration depth.

The *in vivo* size distribution of a population is currently not known, and neither is it exactly known what range of microbubble sizes generate highest detection signal for a given method [Gorce et al., 2000; Bouakaz and de Jong, 2007]. This precludes refining the method by e.g. pre-conditioning of the contrast agent size-distribution, or by adapting the insonation frequency.

1.5 Acoustic characterization techniques

Linear and nonlinear responses of microbubbles are widely studied with acoustic techniques. Two main experimental directions can be distinguished: A top-down and a bottom-up approach.

1.5.1 Population approach

In the top-down approach a population or subpopulation of microbubbles is insonified, and the response is acoustically recorded. Properties of single bubbles are then estimated from this response or from the specific attenuation characteristics [de Jong et al., 1992; Hoff et al., 2000; Goertz et al., 2007a; Kimmel et al., 2007; Tang and Eckersley, 2007; Emmer et al., 2009].

A first disadvantage of this approach is that responses of a subpopulation can be masked by responses of another subpopulation. An example is found in Emmer et al. [2009] where it is shown that threshold effects of single smaller bubbles have low contribution in the total acoustic scattering of a population, since small amount of larger bubbles, behaving linearly, dominate the fundamental frequency response in an experimental setting.

A second disadvantage is that, when extracting parameter values, a certain model has to be assumed. Effects not predicted by the model will lead to erroneous characterization. For example, the compression-only effect, in which the bubble oscillation shows significantly higher compression than expansion due to nonlinear shell behavior [de Jong et al., 2007], can be observed in population scattering by high-order harmonics of the insonation frequency. However, high-order harmonics can also be described by models having a simple viscous-elastic shell, and hence the compression-only effect is not recognized. Furthermore, models generally assume homogeneity and equality of the coating. Optical recordings have revealed the opposite for a phospholipids coating [Borden et al., 2004; van der Meer et al., 2007].

1.5.2 Single bubble approach

The bottom-up approach consists of recording the acoustic response of single isolated bubbles [Morgan et al., 2000; Vos et al., 2005; Sijl et al., 2006; Thomas et al., 2009]. Isolation is obtained by using capillary tubes, focused flow, high dilution, or radiation force using a hole in a sheet. The size of the responding microbubble is obtained by optical techniques or by a model-based estimate from the acoustic response.

Acoustic experiments with single bubbles produce reliable results. However, predicting the behavior of a population implies that many bubbles with a different radius have to be investigated, which poses an experimental challenge. This is

specifically the case for studying very small bubbles, that compose the majority of a population but have low acoustic response, and for studying very big bubbles that are not many in a population, but have a high acoustic response. Generally only part of the size range in a population is studied, introducing the risk of missing important features expressed by microbubbles that have a size out of the studied size range.

A minor problem is that the time between microbubble retraction from the product vial and the measurement is generally much longer than the time in clinical application between administration and measurement - time can introduce gas and lipid-material exchange between bubble and surrounding liquid.

1.6 Optical characterization techniques

In the last decade optical methods have been introduced that are able to resolve the microbubble oscillation. Imaging contrast microbubble oscillations demands framing rates from roughly 0.5 million frames per second (Mfps) up to 100 Mfps. Various methods have been developed to optically measure the radial dynamics. A 1D approach is presented by Guan and Matula [2004] in which a laser beam is illuminating single freely-floating microbubbles in a population. The optical scattering strength of the microbubble is sampled at high rate by a photo-sensitive device, and converted to a radius-time curve. A 2D approach is more commonly used, in which microbubbles are inserted in an optically transparent tube or chamber, and imaged by a fast-framing camera connected to a microscope. High framing rates are achieved by either a rotating mirror concept (like the Brandaris-128 camera, see below) or fast electronics [Dayton et al., 1997]. A third option is stroboscopic illumination in combination with a kfps-framing camera [Caskey et al., 2007]. An intermittent modality is provided by the Imacon digital system, that can record 8 2D frames and a streak image of the bubble, the latter providing a diameter-time curve of the oscillation at 100 million samples per second.

The optical high-speed recordings described in this thesis are acquired with the Brandaris-128 camera system [Chin et al., 2003], which is custom built by the Biomedical Engineering department of the Erasmus MC (Rotterdam, the Netherlands) and the Physics of Fluids group of the University of Twente (Enschede, the Netherlands). See Fig. 1.4. This camera system is based on a fast rotating mirror that sweeps the microscope image over 128 separate optical channels, each channel consisting of a set of lenses and a sensitive CCD camera. Thus, each camera is illuminated for very short time, roughly the reciprocal of the framing rate, and the CCD cameras are illuminated consecutively. The images are put one after another to assemble a movie of the oscillating bubble. The framing rate is dictated by the rotation speed of the mirror. The mirror is mounted on helium-driven turbine enabling rotation speeds up to 20,000 revolutions per second (i.e., 1.2 million revolutions per

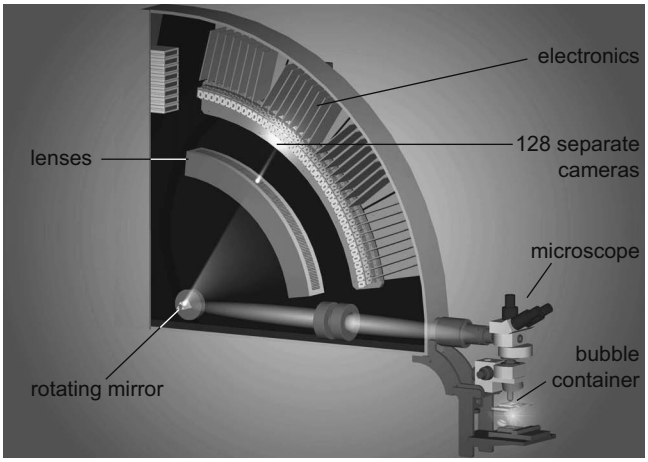

Figure 1.4: Drawing of the Brandaris-128 high-speed camera system. The microscope (right bottom) and relay lenses project the image of the microbubble on a fast rotating mirror (left bottom). The image is reflected at an angle by the mirror and sweeps along 128 sets of lenses and CCD cameras. A helium-driven turbine rotates the mirror, leading to frame rates up to 25 million frames per second.

minute), producing framing rates up to 25 Mfps. The combination with a microscope provides a resolution of roughly 0.1 – 0.2 μm per pixel, which is sufficient to resolve the shape and oscillation of microbubbles. Since the exposure time of each CCD is short, and the magnification is high, a strong flash lamp is used to illuminate the microbubbles.

A fundamental disadvantage of optical methods is that the echo response, which is the final quantity of interest, should be derived from the optically-measured radial response. The derivation could introduce errors.

1.7 This thesis

The general motivation for this thesis is the optimization of contrast agent detection schemes. The approach is to study the dynamics of single isolated microbubbles of various sizes, different composition, at different temperature, and with or without the presence of surrounding objects. Studies are performed in well-defined laboratorial environments in which microbubble oscillations are induced by ultrasound with varying amplitude and frequency.

Chapter 2 describes a characterization technique based on the primary radiation force on microbubbles. The chapter introduces a Rayleigh-Plesset based model describing the radial oscillations of a microbubble due to an acoustic wave. It further

introduces the displacement induced by the hydrodynamic coupling of the radial oscillations with the acoustic wave. The model is used to predict microbubble behavior for different frequencies and pressures and thus spans the basic concepts of microbubbles. It also exemplifies the influence of coating material. In Chapter 3 microbubbles are acoustically studied while their size is optically recorded. This chapter shows that larger bubbles have much higher scattering strength than smaller bubbles. Microbubbles can be characterized as a resonant system since the phase of the response changes around a resonant size. It also shows the phenomenon of ultrasound-induced deflation, a process that could deteriorate the fundamental-frequency echo signal of contrast agents when insonified for a longer period of time.

The relation between radial excursion and scattered echo of a microbubble is investigated in Chapter 4. A predictive equation to link the radial excursion to the scattered acoustic wave is confirmed using ultrafast framing optical and acoustic recordings. The chapter also shows that high-frequency spectral contents in radial oscillations are enhanced in the acoustic response. A possible application of the equation is a method that noninvasively monitors the oscillations of microbubbles *in vivo*, which is beneficial for evaluating excitation parameters in sonoporation applications. The predictive equation is applied in some subsequent chapters of the thesis. The methods described in Chapters 3 and 4 are combined in Chapter 5 to further study the relation between nonlinear oscillations and microbubble size.

The oscillation of a microbubble in contact with a vessel-mimicking wall is studied in Chapters 6 and 7. The results show that shape deformations occur at clinically relevant pressures and frequencies, which could in turn influence detection and sonoporation efficacy. The influence of liquid temperature is addressed in Chapter 8, showing that temperature has a mild effect on the microbubble oscillations.

Subsequent chapters deal more specifically with contrast detection schemes. Chapter 9 studies the dual-frequency radial modulation technique in which a low-frequency wave modulates the response of microbubbles to a high-frequency imaging pulse. It is concluded that advanced modeling of the viscous-elastic coating is needed to describe the observed high radial modulation. Chapters 10 and 11 describe the effect of nonlinear propagation in a bi-frequency transmission technique, and show its application for microbubble excitation. Chapter 12 introduces a novel method in which tissue signals are suppressed and bubble nonlinear responses are enhanced. This method is based on the knowledge gathered in the previous chapters. The results from this thesis are further discussed and summarized in the Discussion chapter.

Bibliography

Basude, R., J. Duckworth, and M. Wheatley, "Influence of environmental conditions on a new surfactant-based contrast agent: ST68," *Ultrasound Med Biol*, 26(4): pp. 621–628, 2000.

Bekeredjian, R., P. A. Grayburn, and R. V. Shohet, "Use of ultrasound contrast agents for gene or drug delivery in cardiovascular medicine," *J Am Coll Cardiol*, 45(3): pp. 329–335, 2005.

Blomley, "WFUMB safety symposium on ultrasound contrast agents: clinical applications and safety concerns," *Ultrasound Med Biol*, 33(2): pp. 180–186, 2007.

Borden, M. A., G. Pu, G. J. Runner, and M. L. Longo, "Surface phase behavior and microstructure of lipid/PEG-emulsifier monolayer-coated microbubbles," *Colloids Surfaces B-Biointerfaces*, 35: pp. 209–223, 2004.

Borsboom, J. M. G., Advanced detection strategies for ultrasound contrast detection, Ph.D. thesis, Erasmus University Rotterdam, 2004.

Bouakaz, A. and N. de Jong, "WFUMB safety symposium on echo-contrast agents: nature and types of ultrasound contrast agents," *Ultrasound Med Biol*, 33(2): pp. 187–196, 2007.

Bouakaz, A., S. Frigstad, F. J. ten Cate, and N. de Jong, "Super harmonic imaging: a new imaging technique for improved contrast detection," *Ultrasound Med Biol*, 28(1): pp. 59–68, 2002.

Bouakaz, A., M. Versluis, J. M. G. Borsboom, and N. de Jong, "Radial modulation of microbubbles for ultrasound contrast imaging," *IEEE Trans Ultrason Ferroelectr Freq Control*, 54(11): pp. 2283–2290, 2007.

Caskey, C. F., D. E. Kruse, P. A. Dayton, T. K. Kitano, and K. W. Ferrara, "Microbubble oscillation in tubes with diameters of 12, 25, and 195 microns," *Appl Phys Lett*, 88: p. 033902, 2006.

Caskey, C. F., S. M. Stieger, S. Qin, P. A. Dayton, and K. W. Ferrara, "Direct observations of ultrasound microbubble contrast agent interaction with the microvessel wall," *J Acoust Soc Am*, 122(2): pp. 1191–1200, 2007.

Chen, S., R. Kinnick, J. F. Greenleaf, and M. Fatemi, "Difference frequency and its harmonic emitted by microbubbles under dual frequency excitation," *Ultrasonics*, 44: pp. e123–e126, 2006.

Chérin, E., J. Brown, S.-E. Måsøy, H. H. Shariff, R. Karshafian, R. Williams, P. N. Burns, and F. S. Foster, "Radial modulation imaging of microbubble contrast agents at high frequency," *Ultrasound Med Biol*, 34(6): pp. 949–962, 2008.

Chin, C. T., C. T. Lancée, J. M. G. Borsboom, F. Mastik, M. E. Frijlink, N. de Jong, M. Versluis, and D. Lohse, "Brandaris 128: A 25 million frames per second digital camera with 128 highly sensitive frames," *Rev Sci Instr*, 74(12): pp. 5026–5034, 2003.

Chomas, J. E., P. A. Dayton, D. J. May, and K. Ferrara, "Nondestructive subharmonic imaging," *IEEE Trans Ultrason Ferroelectr Freq Control*, 49(7): pp. 883–892, 2002.

Christiansen, J. P. and J. R. Lindner, "Molecular and cellular imaging with targeted contrast ultrasound," *Proc IEEE*, 93(4): pp. 809–818, 2005.

Cosgrove, D., "Ultrasound contrast agents: An overview," *Eur J Radiol*, 60(3): pp. 324–330, 2006.

Dayton, P. A., K. E. Morgan, A. L. Klibanov, G. Brandenburger, K. R. Nightingale, and K. W. Ferrara, "A preliminary evaluation of the effects of primary and secondary radiation forces on acoustic contrast agents," *IEEE Trans Ultrason Ferroelectr Freq Control*, 44(6): pp. 1264–1277, 1997.

de Jong, N., A. Bouakaz, and P. Frinking, "Basic acoustic properties of microbubbles," *Echocardiography*, 19(3): pp. 229–240, 2002.

de Jong, N., M. Emmer, C. T. Chin, A. Bouakaz, F. Mastik, D. Lohse, and M. Versluis, “"compression-only" behavior of phospholipid-coated contrast bubbles,” *Ultrasound Med Biol*, 33(4): pp. 653–656, 2007.

de Jong, N., L. Hoff, T. Skotland, and N. Bom, “Absorption and scatter of encapsulated gas filled microspheres: theoretical considerations and some measurements,” *Ultrasonics*, 30(2): pp. 95–103, 1992.

Deng, C. X., F. L. Lizzi, A. Kalisz, A. Rosado, R. H. Silverman, and D. J. Coleman, “Study of ultrasonic contrast agents using a dual-frequency band technique,” *Ultrasound Med Biol*, 26(5): pp. 819–831, 2000.

Doikinov, A. A., S. Zhao, and P. A. Dayton, “Modeling of the acoustic response from contrast agent microbubbles near a rigid wall,” *Ultrasonics*, 49: pp. 195–201, 2009.

Dolan, M. S., S. S. Gala, S. Dodla, S. S. Abdelmoneim, F. Xie, D. Cloutier, M. Bierig, S. L. Mulvagh, T. R. Porter, and A. J. Labovitz, “Safety and efficacy of commercially available ultrasound contrast agents for rest and stress echocardiography,” *J Am Coll Cardiol*, 53(1): pp. 32–38, 2009.

Duck, F. A., Physical properties of tissue, Academic press Ltd., 1990.

Duck, F. A., “Nonlinear acoustics in diagnostic ultrasound,” *Ultrasound Med Biol*, 28(1): pp. 1–18, 2002.

Eller, A. and H. G. Flynn, “Generation of subharmonics of order one-half by bubbles in a sound field,” *J Acoust Soc Am*, 46(3 (part2)): pp. 772–727, 1969.

Emmer, M., A. van Wamel, D. E. Goertz, and N. de Jong, “The onset of microbubble vibration,” *Ultrasound Med Biol*, 33(6): pp. 941–949, 2007.

Emmer, M., H. J. Vos, D. E. Goertz, A. van Wamel, M. Versluis, and N. de Jong, “Pressure-dependent attenuation and scattering of phospholipid-coated microbubbles at low acoustic pressures,” *Ultrasound Med Biol*, 35(1): pp. 102–111, 2009.

Evans, D. H. and W. N. McDicken, Doppler ultrasound: Physics, Instrumentation, and Clinical Applications, John Wiley & Sons, Chichester, UK, second edn., 2000.

Feinstein, S. B., “The powerful microbubble: from bench to bedside, from intravascular indicator to therapeutic delivery system, and beyond,” *Am J Physiol Heart Circ Physiol*, 287(2): pp. H450–457, 2004.

Feinstein, S. B., “Contrast ultrasound imaging of the carotid artery vasa vasorum and atherosclerotic plaque neovascularization,” *J Am Coll Cardiol*, 48(2): pp. 236–243, 2006.

Forbes, M. M., R. L. Steinberg, and W. D. O’Brien Jr., “Examination of inertial cavitation of Optison in producing sonoporation of Chinese hamster ovary cells,” *Ultrasound Med Biol*, 34(12): pp. 2009–2018, 2008.

Forsberg, F., R. Basude, J.-B. Liu, J. Allessandro, W. T. Shi, N. M. Rawool, B. B. Goldberg, and M. A. Wheatley, “Effect of filling gases on the backscatter from contrast microbubbles: theory and *in vivo* measurements,” *Ultrasound Med Biol*, 25(8): pp. 1203–1211, 1999.

Garbin, V., D. Cojoc, E. Ferrari, E. Di Fabrizio, M. L. J. Overvelde, S. M. van der Meer, N. de Jong, D. Lohse, and M. Versluis, “Changes in microbubble dynamics near a boundary revealed by combined optical micromanipulation and high-speed imaging,” *Appl Phys Lett*, 90: p. ref. 114103, 2007.

Goertz, D. E., D. Christopher, J. L. Yu, R. Kerbel, P. N. Burns, and F. S. Foster, “High-frequency color flow imaging of the microcirculation,” *Ultrasound Med Biol*, 26(1): pp. 63–71, 2000.

Goertz, D. E., N. de Jong, and A. F. W. van der Steen, "Attenuation and size distribution measurements of Definity and manipulated Definity populations," *Ultrasound Med Biol*, 33(9): pp. 1376–1388, 2007a.

Goertz, D. E., M. E. Frijlink, D. Tempel, V. Bhagwandas, A. Gisolf, R. Krams, N. de Jong, and A. F. W. van der Steen, "Subharmonic contrast intravascular ultrasound for vasa vasorum imaging," *Ultrasound Med Biol*, 33(12): pp. 1859–1872, 2007b.

Goertz, D. E., A. Needles, P. N. Burns, and F. S. Foster, "High-frequency, nonlinear flow imaging of microbubble contrast agents," *IEEE Trans Ultrason Ferroelectr Freq Control*, 52(3): pp. 495–502, 2005.

Gorce, J.-M., M. Arditi, and M. Schneider, "Influence of bubble size distribution on the echogenicity of ultrasound contrast agents - a study of SonoVue," *Invest Radiol*, 35(11): pp. 661–671, 2000.

Guan, J. and T. J. Matula, "Using light scattering to measure the response of individual ultrasound contrast microbubbles subjected to pulsed ultrasound *in vitro*," *J Acoust Soc Am*, 116(5): pp. 2832–2842, 2004.

Hoff, L., P. C. Sontum, and J. M. Hovem, "Oscillations of polymeric microbubbles: Effect of the encapsulating shell," *J Acoust Soc Am*, 107(4): pp. 2272–2280, 2000.

Kaul, S., "Myocardial contrast echocardiography: A 25-year retrospective," *Circulation*, 118: pp. 291–308, 2008.

Kimmel, E., B. Krasovitski, A. Hoogi, D. Razansky, and D. Adam, "Subharmonic response of encapsulated microbubbles: Conditions for existence and amplification," *Ultrasound Med Biol*, 33(11): pp. 1767–1776, 2007.

Kooiman, K., M. R. Böhmer, M. Emmer, H. J. Vos, C. Chlon, W. T. Shi, C. S. Hall, S. H. P. M. de Winter, K. Schroën, M.Versluis, N. de Jong, and A. van Wamel, "Oil-filled polymer microcapsules for ultrasound-mediated delivery of lipophilic drugs," *J Control Release*, 133: pp. 109–118, 2009.

Levine, R., L. Teichholz, M. Goldman, M. Steinmetz, M. Baker, and R. Meltzer, "Microbubbles have intracardiac velocities similar to those of red blood cells," *J Am Coll Cardiol*, 3(1): pp. 28–33, 1984.

Lindner, J. R., "Targeted ultrasound contrast agents: Diagnostic and therapeutic potential (inv.)," in proc. IEEE Ultras Symp, vol. 1, pp. 1695–1703, 2001.

Lindner, J. R., J. Song, A. Jayaweera, J. Sklenar, and S. Kaul, "Microvascular rheology of Definity microbubbles after intra-arterial and intravenous administration," *J Am Soc Echocard*, 15(5): pp. 396–403, 2002.

Måsøy, S.-E., O. Standal, P. Näsholm, T. F. Johansen, B. Angelsen, and R. Hansen, "SURF imaging: *In vivo* demonstration of an ultrasound contrast agent detection technique," *IEEE Trans Ultrason Ferroelectr Freq Control*, 55(5): pp. 1112–1121, 2008.

Minnaert, M., "On musical air-bubbles and the sounds of running water," *Philosoph Mag*, 16: pp. 235–248, 1933.

Mleczko, M., W. Wilkening, and G. Schmitz, "Optimal pulse sequences for the suppression of memoryless tissue harmonics," in proc. IEEE Ultras Symp, pp. 542–545, New York, NY, USA, 2007.

Morgan, K. E., J. S. Allen, P. A. Dayton, J. E. Chomas, A. L. Klibanov, and K. W. Ferrara, "Experimental and theoretical evaluation of microbubble behavior: Effect of transmitted

phase and bubble size," *IEEE Trans Ultrason Ferroelectr Freq Control*, 47(6): pp. 1494–1509, 2000.

Mukherjee, D., J. Wong, B. Griffin, S. G. Ellis, T. R. Porter, S. Sen, and J. D. Thomas, "Ten-fold augmentation of endothelial uptake of vascular endothelial growth factor with ultrasound after systemic administration," *J Am Coll Cardiol*, 35(6): pp. 1678–1686, 2000.

Needles, A., D. E. Goertz, R. Karshafian, E. Chérin, A. Brown, P. N. Burns, and F. S. Foster, "High-frequency subharmonic pulsed-wave Doppler and color flow imaging of microbubble contrast agents," *Ultrasound Med Biol*, 34(7): pp. 1139–1151, 2008.

Ohl, C.-D., M. Arora, R. Ikink, N. de Jong, M. Versluis, M. Delius, and D. Lohse, "Sonoporation from jetting cavitation bubbles," *Biophys J*, 91(11): pp. 4285–4295, 2006.

Overvelde, M. L. J., V. Garbin, B. Dollet, D. Cojoc, E. Ferrari, N. de Jong, E. Di Fabrizio, D. Lohse, and M. Versluis, "3D optical micromanipulation of ultrasound contrast agents: bubble-wall and bubble-bubble interactions," in proc. Int Congr Acoust, Madrid, Spain, 2007.

Prentice, P., A. Cuschieri, K. Dholakia, M. Prausnitz, and P. Campbell, "Membrane disruption by optically controlled microbubble cavitation," *Nat Phys*, 1(2): pp. 107–110, 2005.

Quaia, E., "Microbubble ultrasound contrast agents: an update," *Eur Radiol*, 17: pp. 1995–2008, 2007.

Shi, W. T. and F. Forsberg, "Ultrasonic characterization of the nonlinear properties of contrast microbubbles," *Ultrasound Med Biol*, 26(1): pp. 93–104, 2000.

Shi, W. T., C. S. Hall, and P. Rafter, "Contrast resonance imaging with embedded ultrasound imaging pulses," in proc. IEEE Ultras Symp, pp. 212–215, Vancouver, 2006.

Shi, W. T., L. Hoff, and F. Forsberg, "Subharmonic performance of contrast microbubbles: an experimental and numerical investigation," in proc. IEEE Ultras Symp, pp. 1957–1960, Munich, Germany, 2002.

Sijl, J., M. Arditi, P. J. Frinking, N. de Jong, D. Lohse, and M. Versluis, "Acoustical study of the properties of individual phospholipid-based ultrasound contrast agent microbubbles," in proc. 11th Eur Symp Ultras Contrast Imaging, pp. 13–14, Rotterdam, the Netherlands, 2006.

Sijl, J., E. Gaud, P. J. Frinking, M. Arditi, N. de Jong, D. Lohse, and M. Versluis, "Acoustic characterization of single ultrasound contrast agent microbubbles," *J Acoust Soc Am*, 124(6): pp. 4091–4097, 2008.

Tang, M.-X. and R. J. Eckersley, "Frequency and pressure dependent attenuation and scattering by microbubbles," *Ultrasound Med Biol*, 33(1): pp. 164–168, 2007.

Thomas, D. H., M. B. Butler, T. Anderson, R. Steel, S. D. Pye, M. Poland, T. Brock-Fisher, W. N. McDicken, and V. Sboros, "Single microbubble response using pulse sequences: Initial results," *Ultrasound Med Biol*, 35(1): pp. 112–119, 2009.

Tortoli, P., V. Michelassi, M. Corsi, D. Righi, and Y. Takeuchi, "On the interaction between ultrasound and contrast agents during Doppler investigations," *Ultrasound Med Biol*, 27(9): pp. 1265–1273, 2001.

Tortoli, P., M. Pratesi, and V. Michelassi, "Doppler spectra from contrast agents crossing an ultrasound field," *IEEE Trans Ultrason Ferroelectr Freq Control*, 47(3): pp. 716–726, 2000.

van der Meer, S. M., B. Dollet, M. M. Voormolen, C. T. Chin, A. Bouakaz, N. de Jong, M. Versluis, and D. Lohse, "Microbubble spectroscopy of ultrasound contrast agents," *J Acoust Soc*

Am, 121(1): pp. 648–656, 2007.

van Wamel, A., K. Kooiman, M. Harteveld, M. Emmer, F. J. ten Cate, M. Versluis, and N. de Jong, "Vibrating microbubbles poking individual cells: Drug transfer into cells via sonoporation," *J Control Release*, 112(1): pp. 149–155, 2006.

Vos, H. J., F. Guidi, E. Boni, and P. Tortoli, "Acoustical investigation of freely moving single microbubbles," in proc. IEEE Ultras Symp, pp. 755–758, Rotterdam, the Netherlands, 2005.

Wu, C.-Y., J. Tsao, and Y.-H. Chou, "An ultrasonic microbubble semi-intermodulated imaging technique," *Ultrasound Med Biol*, 31(9): pp. 1199–1210, 2005.

Yanagisawa, K., F. Moriyasu, T. Miyahara, M. Yuki, and H. Iijima, "Phagocytosis of ultrasound contrast agent microbubbles by Kupffer cells," *Ultrasound Med Biol*, 33(2): pp. 318–325, 2007.

Yeh, C.-K., S.-Y. Su, C.-C. Shen, and M.-L. Li, "Dual high-frequency difference excitation for contrast detection," *IEEE Trans Ultrason Ferroelectr Freq Control*, 55(10): pp. 2164–2176, 2008.

Zhao, S., K. W. Ferrara, and P. A. Dayton, "Asymmetric oscillation of adherent targeted ultrasound contrast agents," *Appl Phys Lett*, 87: p. ref. 134103, 2005.

Zhao, S., D. E. Kruse, K. W. Ferrara, and P. A. Dayton, "Selective imaging of adherent targeted ultrasound contrast agents," *Phys Med Biol*, 52(8): pp. 2055–2072, 2007.

Chapter 2

Method for microbubble characterization using primary radiation force

Abstract - **Medical Ultrasound Contrast Agents (UCAs) have evolved from straight image enhancers to patho-physiological markers and drug delivery vehicles. However, the exact dynamic behavior of the encapsulated bubbles composing UCAs is still not entirely known. In this paper, we propose to characterize full populations of UCAs, by looking at the translational effects of ultrasound radiation force on each bubble in a diluted population. The setup involves a sensitive, fully programmable transmitter/receiver and two unconventional real-time display modes. Such display modes are used to measure the displacements produced by irradiation at frequencies in the range 2 – 8 MHz and pressures between 150 kPa and 1.5 MPa. The behavior of individual bubbles freely moving in a water tank is clearly observed, and it is shown that it depends on the bubble physical dimensions as well as on the viscoelastic properties of the encapsulation. A new method is also distilled that estimates the viscoelastic properties of bubble encapsulation by fitting the experimental bubble velocities to values simulated by a numerical model based on the modified Rayleigh-Plesset equation and the Bjerknes force. The fit results are a shear modulus of 18 MPa and a viscosity of 0.23 Pa·s for a thermoplastic PVC-AN shell (F04E, Matsumoto Yusi-Seiyaku, Osaka, Japan). Phospholipids shell elasticity and friction parameter of the experimental contrast agent BR14 (Bracco Research, Geneva, Switzerland) are estimated as 0.8 N/m and $1{\cdot}10^{-7}$ kg/s, respectively (shear modulus of 32 MPa and viscosity of 0.19 Pa·s, assuming 4 nm shell thickness).**

Appeared in the *IEEE Transactions of Ultrasonics, Ferroelectrics, and Frequency Control*, by H. J. Vos, F. Guidi, E. Boni and P. Tortoli, Vol. 54, Issue 7, pp. 1333-1345, July 2007. This work was supported by the European Union with grant QLG1-CT-2002-01518 (UMEDS Project) and by MIUR (COFIN-PRIN 2005). The authors acknowledge the valuable remarks on the manuscript by Dr. M. Arditi, Bracco Research, Geneva.

2.1 Introduction

Starting in 1980, ultrasound contrast agents (UCAs), i.e., gaseous microbubbles encapsulated by lipids or albumin-like materials, have been used in medical ultrasound (US) for enhanced imaging of the cardiovascular system [Ophir and Parker, 1989]. However, the exact underlying dynamics of the bubble vibration are still not well understood, as the encapsulation might involve complex phenomena like compression-only [Marmottant et al., 2005], buckling [Borden et al., 2005] and threshold effects [Emmer et al., 2005]. Thorough knowledge of the bubble behavior during US irradiation might help engineering bubbles for specific tasks like targeting [Lindner, 2001; Zhao et al., 2004; Borden et al., 2006] and drug delivery [Shortencarier et al., 2004; van Wamel et al., 2004].

The behavior of individual bubbles during irradiation has been optically observed with high-speed cameras [Dayton et al., 2002; Bouakaz et al., 2005; Sun et al., 2005]. Such an approach requires that the observation area is limited to a small region (typically 1 order of magnitude larger than the microbubble diameter). Hence, the microbubbles must be fixed in a gel, immobilized on Petri dishes [Klibanov et al., 2002] or, when suspended in a fluid, they can move only along short paths, typically within transparent tubes [Dayton et al., 2002; Bouakaz et al., 2005]. In another optical approach, the light scattering of a laser beam by microbubbles is collected to estimate the instantaneous diameter while irradiated with ultrasound [Guan and Matula, 2004]. Such setup allows investigation of individual bubbles without any constraint on the bubble vibration and motion. However, the combined optical and acoustic setup might be difficult and expensive to build. Acoustic methods to investigate the behavior of single bubbles have also been reported. In a first approach, freely floating bubbles were excited at frequencies around their resonance and imaged using higher frequencies [Deng et al., 2000; Shi et al., 2000]. More recently, single bubbles in an acoustically and optically transparent tube have been observed. Such setup has been preliminarily described by Sijl et al. [2006], who have used a microscope to estimate the initial and final radius of the bubble.

An interesting phenomenon revealed by both acoustic [Tortoli et al., 2000, 2005] and optical [Rensen et al., 2001; Dayton et al., 2002; Palanchon et al., 2005; Rychack et al., 2005; Sun et al., 2005] observations, is yielded by the primary US radiation force, also known as the Bjerknes force [Bjerknes, 1906]. The radiation force originates from the phase difference between the driving pressure and the volume oscillation of a bubble. The passing US wave induces a pressure gradient acting upon the bubble surface, resulting in an instant force proportional to the product of the pressure gradient by the bubble volume [Bjerknes, 1906]. Averaged over a full cycle, the resulting net force has a non-zero value in the direction of the sound propagation and the bubble is correspondingly accelerated in the same direction.

The bubble displacement due to radiation force has been so far simulated us-

ing Rayleigh-Plesset based equations to describe the radial motion, and the Bjerknes force model for the displacement. In early literature, approaches of this method are described in which the equations were linearized under the assumption of small radial motion (acoustic limit) [Dayton et al., 1997; Leighton, 1994; Tortoli et al., 2000; Rensen et al., 2001]. The time-domain evaluation of the differential equations [Dayton et al., 2002; Reddy and Szeri, 2002; Matula, 2003] has later allowed for a better accounting of transient effects [Morgan et al., 2000], as well as for the influence of the so-called added mass force, that considers the fluid motion surrounding the cavity [Dayton et al., 2002; Reddy and Szeri, 2002; Matula, 2003].

Both simulations and experiments have shown that the bubble displacement depends not only on the characteristics of the impinging US burst and on the fluid viscosity/density, but also on the bubble diameter as well as on the shell viscoelastic properties. All these parameters determine the reaction of the bubble volume to the pressure burst, and the drag on the bubble once it is moved by ultrasound.

This paper introduces a novel approach for investigation of microbubble behavior in acoustic fields. The proposed approach is based on the evaluation of the effects of radiation force impressed by a single element transducer on individual bubbles of a full population freely floating in a water tank. The displacement and velocities obtained at different transmission conditions are both evaluated through a simulation model and measured through an experimental setup based on a programmable US unit. An original multigate Doppler display mode is introduced which, together with a classic M-mode display, is shown capable of accurately tracking the movements of "individual" microbubbles over paths several millimeters long. This is confirmed by the good agreement between experimental observations and simulations for single bubbles of two different UCAs.

The paper is organized as follows. In Section 2.2, the simulation model that predicts the displacement of microbubbles encapsulated with a viscoelastic shell is reported. Section 2.3 describes the experimental setup, which includes a special bubble behavior testing (BBT) US system capable of irradiating according to different strategies two types of UCAs diluted in a water tank. Experimental and simulation results are presented in Section 2.4, which also illustrates a new method to estimate the viscoelastic shell properties of UCAs. The results are discussed in the final Section, which also reports on the major benefits and limitations of the proposed acoustic approach.

2.2 Simulation model

2.2.1 Bubble radial motion

The bubbles are modeled as encapsulated gaseous spheres in a viscoelastic fluid. The shell is assumed to show viscoelastic behavior. The shell mass is conserved

during vibration, and the thickness d_s is much smaller than the radius R. The radial movement is described by the Rayleigh-Plesset [1] equation [Vokurka, 1986; Leighton, 1994; Dayton et al., 2002] extended with terms describing the influence of the shell viscoelastic behavior [Church, 1995; Hoff et al., 2000],

$$\rho_l \left(R\ddot{R} + \frac{3}{2}\dot{R}^2 \right) = p_0 \left(\left(\frac{R_0}{R} \right)^{3\kappa} - 1 \right) - P(t) - 4\mu_l \frac{\dot{R}}{R} - 12\mu_s \frac{d_{s,0} R_0^2}{R^3} \frac{\dot{R}}{R} - 12G_s \frac{d_{s,0} R_0^2}{R^3} \left(1 - \frac{R_0}{R} \right) \quad (2.1)$$

The left hand side describes the inertial effects of the bubble surrounding liquid. R is the outer radius of the sphere and ρ the density in the surrounding medium (998 kg/m^3). In literature [Church, 1995; Hoff et al., 2000; Allen et al., 2002] the effect of the thickness of the shell is accounted for with extra terms on the left hand side. However, in additional simulations, it was seen that a finite shell thickness of 2.7% of the radius gives a difference in displacement of 4% compared to neglecting this thickness, which was assumed to be negligible.

On the right hand side, the first term contains the initial radius R_0 of the bubble, c the speed of sound in the medium (1500 m/s) and the surface tension σ. In the case of thick-shell encapsulation the surface tension might be neglected; additional simulations showed that this neglect gives a maximal error of 1% in the currently predicted displacement which is thought to be insignificant. The surface tension of a phospholipid shell in water is taken 0.052 N/m [Dayton et al., 2002]. The internal pressure of the gas is assumed to follow the polytropic relation $p_\mathrm{i} V^\gamma = \text{constant}$ with p_i the internal pressure, V the gas volume and γ the polytropic exponent. The value of the polytropic exponent is calculated as shown by Hoff et al. [2000] and Medwin [1977], with a specific heat ratio of 1.11 (polyatomic gasses). The second term in the equation accounts for the Laplace pressure increase due to surface tension; the third is the viscous damping of the fluid, with μ the medium viscosity ($0.9 \cdot 10^{-3}$ Pa·s at 25°C [CRC, 2001]). The fourth term contains the shell shear modulus G_s [Hoff et al., 2000], where the mass of the shell is conserved during vibration. The fifth term describes the shell friction due to viscosity, incorporating the shell viscosity parameter μ_sh [Hoff et al., 2000]. The sixth term takes the thermal damping δ_{th} of the bubble into account [Hoff et al., 2000], with ω the driving angular frequency. The final term on the right hand side contains the ambient and driving pressure, p_0 (101 kPa) and $p_\mathrm{driv}(t)$, respectively. Note that for thin shells, i.e. $d_\mathrm{s} \ll R$, the shell elasticity and viscosity are both a product of the shell thickness and the respective material properties G_s and μ_s. Using this model for shell parameter estimation, the shell thickness has to be given *a priori*.

[1] The original manuscript states that the equation is based on Herring's equation; However, the current equation for the radial dynamics assumes an incompressible medium, which is given by Rayleigh's equation, not Herring's, according to Vokurka [1986]

2.2.2 Bubble translation

Equating all translational forces that act on the bubble returns the acceleration along the US propagation direction. The driving US radiation force due to a pressure wave acting on a volume, reads [Leighton, 1994; Rensen et al., 2001]

$$\vec{F}_{US} = -V(t)\,\vec{\nabla} p(z,t) \tag{2.2}$$

with $V(t)$ the instantaneous volume of the bubble and $p(z,t)$ the external pressure working on the bubble. The bubbles are assumed to freely move and vibrate, secondary radiation forces being neglected [Dayton et al., 2002]. As the bubble is much smaller than the wavelength, and in the acoustic limit of the propagating wave, the Euler equation shows that the divergence of the pressure is a function of the pressure and velocity only,

$$\vec{\nabla} p_z = -\frac{1}{c}\frac{\partial p}{\partial t}\vec{e} \tag{2.3}$$

with $\vec{e}$ the unit vector along the US propagation direction. This force interacts with four other forces [Rensen et al., 2001]. The first is the buoyancy force. The bubble velocity due to buoyancy was estimated at 50 μm/s for a bubble with a diameter of 10 μm and density of 200 kg/m^3 [Takeuchi, 1997] in water. This velocity is two orders of magnitude lower than the US-induced velocities, so buoyancy forces are neglected in the bubble velocity simulation.

The second is the viscous drag on resonant bubbles, assuming quasi-steady drag [White, 1991, p.182]

$$\vec{F}_D = -\frac{1}{4}\pi C_D \,\mathrm{Re}\, R\, \mu\, \vec{u}_r \tag{2.4}$$

with C_D the drag coefficient, $\vec{u}_r$ the velocity vector of the bubble relative to the unperturbed fluid and the Reynolds number $\mathrm{Re} = 2R\rho\left|\vec{u}_r\right|/\mu$. Many implementations of the drag can be found in literature [Crum, 1975; Sherman, 1990; Rensen et al., 2001; Dayton et al., 2002; Reddy and Szeri, 2002]. By comparing those, it can be seen that in the Reynolds range under consideration (1 - 50) the calculated drag does not vary much. In particular, we have investigated the implementation of the history force as described by Magnaudet and Legendre [1998], which was discussed further by Reddy and Szeri [2002]. The history force vanishes as both the translational Reynolds number $\mathrm{Re} = 2R\rho\left|\vec{u}_r\right|/\mu \gg 1$ and the vibration Reynolds number $\left|\dot{R}/u_r\right|\mathrm{Re} \gg 1$ in our application for resonant bubbles. Hence, we can neglect the history term, and take a quasi-steady solution in which the drag is a function of the instant radius and speed only. We have chosen to implement the drag coefficient as given by White [1991, p.182]:

$$C_D = \frac{24}{\mathrm{Re}} + \frac{6}{1+\sqrt{\mathrm{Re}}} + 0.4 \tag{2.5}$$

This equation appeared from a parametric fit by White to experimental data from different sources, is validated for $\mathrm{Re} < 2 \cdot 10^5$, and shows at most 10% difference with observed values for rigid-shelled smooth spheres. Other implementations [Crum, 1975; Dayton et al., 2002; Matula, 2003] showed at most 5% higher drag than the coefficient shown here for Reynolds numbers below 50.

The third force originates from the inertia of the bubble itself, given by the product of its density ρ_b, initial volume V_0 and acceleration $\dot{\vec{u}}_\mathrm{r}$. The fourth force is the added mass force, originating from the inertia of the fluid surrounding the cavity [Magnaudet and Legendre, 1998; Matula, 2003; Leighton, 1994, p.116]. Following Magnaudet and Legendre [1998], the added mass is

$$\vec{F}_\mathrm{AM} = -\frac{1}{2}\rho\left(V\frac{\partial\vec{u}_\mathrm{r}}{\partial t} + \vec{u}_\mathrm{r}\frac{dV}{dt}\right). \tag{2.6}$$

All forces together give the acceleration,

$$\dot{\vec{u}}_\mathrm{r} = \frac{1}{V_\mathrm{o}\rho_\mathrm{b}}\left(\vec{F}_\mathrm{US} + \vec{F}_\mathrm{D} + \vec{F}_\mathrm{AM}\right) \tag{2.7}$$

Eqs. 2.1 and 2.7 are recursively solved for the radial vibration and bubble translation with a 5^{th} order Runga-Kutta method in MATLAB (The Mathworks, Natick, MA, USA). The Doppler velocity is determined as the product of Pulse Repetition Frequency (PRF) by the bubble displacement within one pulse repetition interval.

2.3 Experimental methods

Both the simulations and experiments described in this paper make reference to the same setup, including a tank of demineralized water ($T = 25$°C), in which a transducer transmits the US and receives the echo-signals backscattered from the immersed bubble population (Fig. 2.1). Bubbles were diluted in 1.9 ℓ of demineralized water at a maximum level of about 10^4 particles per mℓ. This concentration was thought to minimize bubble-bubble interactions and damping while still maintaining resonant particles in the focal region of the transducer. The bubbles are free to move, and will indeed slowly float around due to convectional fluid motion, acoustic streaming effects [Nowicki et al., 1998] and buoyancy. These effects tend to mix the solution, bringing various sized bubbles into the axial region of the transducer, where they experience the radiation force.

2.3.1 Microbubbles

In the experiments we used two different bubble populations. The first consisted of UCA mimicking microbubbles (Microsphere F-04E, Matsumoto Yusi Seiyaku Co., Osaka, Japan) having a PVC-AN copolymer shell. The bubbles initially contained a mixture of the hydrocarbon gases C_3H_8 and C_4H_{10} [Takeuchi, 1997].

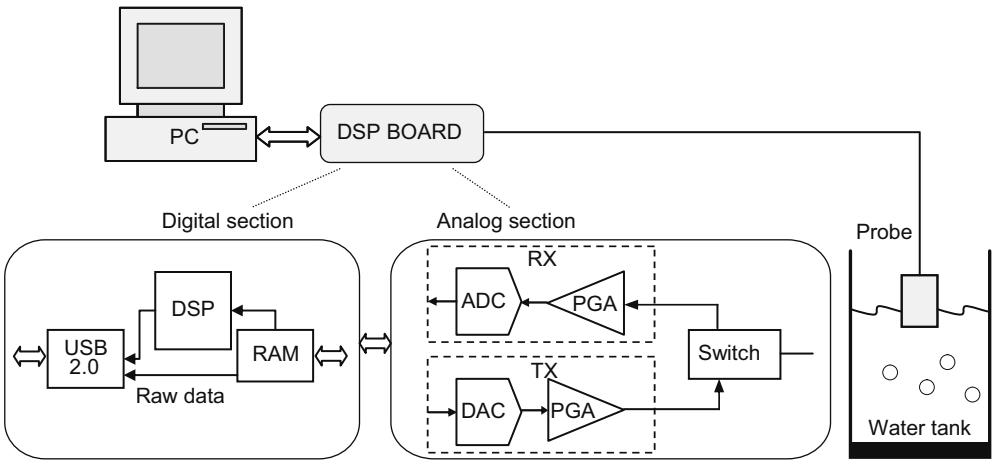

Figure 2.1: Experimental setup. The bubble behavior testing (BBT) system includes a PC and dedicated board containing all electronics needed to transmit programmable bursts, and process the received echoes (DSP = Digital Signal Processing, PGA = Programmable Gain Amplifier, USB = Universal Serial Bus).

However, in the years the bubbles have been stored in our lab, those gases should have been replaced by air due to gas exchange through the polymer shell (diffusivity of C_4H_{10} through PVC is $3 \cdot 10^{-18}$ m^2/s [Berens and Hopfenberg, 1982]). The bubbles were stored as dry product, and fresh air was available in the container as it was opened and closed several times. Once added to water, the polymer shell is strong and thick enough to cancel any surface tension, and the bubbles are stable for at least some days. The volume weighted mean diameter was 4.5 μm (diameters [2] range from 1 μm to 20 μm), and the initial shell thickness d_s was considered 2.7% of the radius, as the gas volume is estimated 90% of the bubble volume for all diameters [Takeuchi, 1997].

The viscoelastic properties of the shell are not known, although an initial estimate can be done. PVC encapsulated bubbles were investigated by Hoff et al. [2000], who estimate an average shear modulus of 12 MPa and a viscosity of 0.45 Pa·s, both considered as initial values in the optimization loop of our simulations. In later sections, we deduce parameter values that are more suitable to describe the observed F04E bubble behavior. The microbubbles have acoustic properties similar to albumin-shelled contrast agents [Tortoli et al., 2001], but are chemically very stable and pressure resistant, which makes them ideal for bubble model validation. For optimal mixing, one drop of surfactant (Symperonic N, BDH Laboratory, UK) was added, after which the emulsion was gently stirred with a magnetic stirrer for at

[2] obtained from personal communication with dr. Yasuhito Takeuchi, GE-Yokogawa Medical systems, Hino 191, Japan

least 30 minutes. Before the experiments, the emulsion was left for several minutes to obtain still water.

The second type is the experimental contrast agent BR14 (Bracco Research S.A., Geneva, Switzerland), which consists of decafluorobutane (C_4F_{10}) gas contained in a phospholipid shell with a thickness of about 4 nm. This thickness has to be considered as a rough estimate [Borden et al., 2005]; the influence of this estimate will be addressed in the discussion section. Gorce et al. [2000] have estimated the shell elasticity parameter, using population backscatter and attenuation experiments, of $S_p = 1.1$ N/m. This links to the shell shear modulus through $\chi = 6G_s d_s$ [de Jong, 1993], and $\chi = S_p/2$ (by comparing definitions) giving a shear modulus of 23 MPa with 4 nm shell thickness [3]. The shell friction parameter is estimated by $S_f = 0.15 \cdot 10^{-6}$ kg/s, which is converted by $S_f = 48\pi d_s \mu_s$ [de Jong, 1993] to a shell viscosity of 0.25 Pa·s. These values are initially used in simulations. The bubbles were reconstituted from a freeze-dried product using 5 mℓ of 0.9% NaCl solution, and shaken for 30 s, before being diluted in demineralized water. The experiments were performed within 30 minutes, in order to reduce decanting effects [Gorce et al., 2000; Leighton, 1994, Sec.4.4.1].

2.3.2 Bubble behavior testing (BBT) US system

A sensitive US system capable of recording the signals backscattered from single microbubbles, and equipped with coherent, programmable Transmit-Receive (TX-RX) sections to facilitate Doppler operation [Evans and McDicken, 2000; Szabo, 2004, Ch.11], has been developed [Ricci et al., 2006], and will be here referred to as Bubble Behavior Testing (BBT) system. The BBT system includes a PC connected through a USB port to a programmable electronic board that outputs arbitrary waveforms into a piezoelectric transducer (see Fig. 2.1). For each transmitted US burst, the radio-frequency (RF) echo-signals backscattered from UCAs are converted to 2048 digital samples with 14-bit resolution at 64 MHz rate. For each pulse repetition interval, 2048 RF samples can be directly processed or digitally down converted to complex (I/Q) base band samples. The start and range of the Region of Interest (ROI) can be arbitrarily set. A software program controls the on-board operations through a high speed Digital Signal Processor (TMS320C6713 Texas Instruments, Dallas, TX) and a high density FPGA device (Stratix I, Altera, San José, CA).

The PC user-interface produces two different real-time displays. The first is a standard M-mode display showing the instantaneous position of each bubble over a long observation interval. The second is a multigate Doppler (MGD) display, in which the instantaneous velocities of all bubbles moving over the ROI are reported. Examples of these displays will be shown in the Results section.

The BBT system is used with one of two focused single-element transducers:

[3] The original manuscript states that χ and S_p are equal, which is rectified in the current text.

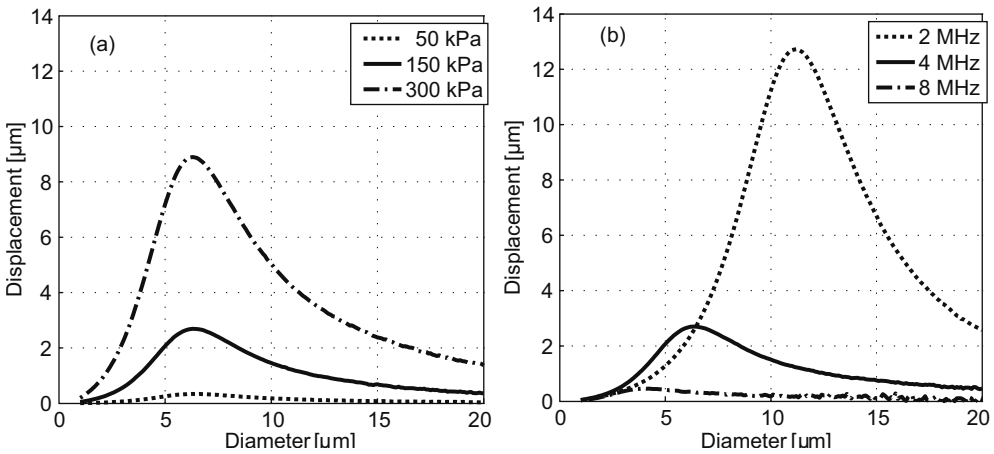

Figure 2.2: Simulated displacement of thermoplastic F04E microbubbles with varying diameter, frequency and driving pressures. The irradiation tone burst contained 50 cycles of: a) 4 MHz TX frequency at 50 kPa, 150 kPa and 300 kPa PRP; b) 2 MHz, 4 MHz and 8 MHz TX frequency at 150 kPa PRP.

a 3 MHz 70% Fractional Bandwidth (FBW) transducer manufactured by Vermon (M3, Tours, France) with a focal distance of about 75 mm, and a 6 MHz 70% FBW transducer by Imasonic (Besançon, France) with a focal distance of about 20 mm. The -6 dB beam width at the focal distance is 1 mm for both transducers. The pressure amplitudes radiated by the transducers were measured in water by using a calibrated capsule "golden lipstick" hydrophone (Onda Corp, Sunnyvale, CA). Pressure measurements had a manufacture-specified uncertainty of 15%. During the experiments, the bubbly medium sometimes showed shielding effects, that is, frequency-dependent attenuation and nonlinear propagation due to the bubbles that are in the acoustic path [Commander and Prosperetti, 1989; Eckersley and Tang, 2005]. Capturing the focal pressure with the hydrophone and using the digitized and scaled time signal as driving pressure in the simulations accounted for this effect.

2.4 Results

2.4.1 Simulation results

The dependency of the displacement on the bubble diameter was first investigated using the simulation model. Fig. 2.2a illustrates the displacement of a rigid-shelled bubble ($G_s = 12$ MPa, $\mu_s = 0.45$ Pa, 2.7% shell thickness) after irradiation with a 50-cycle, 4 MHz tone burst with peak rarefaction pressures (PRP) of 50 kPa, 150 kPa and 300 kPa, respectively. The figure confirms that the displacement de-

pends strongly on the initial bubble diameter and that the radiation force is highest at resonance. Obviously, the displacement increases with irradiating pressure, while the resonance frequency does not change significantly. The maximum displacement for the subsequent pressures, 50 kPa, 150 kPa and 300 kPa, increases by factors 1:8:26.

Figure 2.2b shows the displacements at 150 kPa PRP produced by a single 50-cycle burst at 3 different centre frequencies (2, 4 and 8 MHz). As expected, the resonant diameter of the bubbles decreases with increasing frequency. The maximum displacements at the various irradiation frequencies are 12.7 μm, 2.7 μm and 0.45 μm for the respective irradiation frequencies. They follow a very rough (1:6:28) proportionality to f^{-2}, with f the frequency of the tone burst. Figure 2.2b also shows that small bubbles (i.e., with a diameter smaller than 2.5 μm) are displaced by the same amount, independently from the driving frequency, when this frequency lies between 2 and 8 MHz.

When the same TX bursts used in Fig. 2.2 are applied to single phospholipid-encapsulated bubbles (G_s = 46 MPa, μ_{sh} = 0.25 Pa·s, ϵ = 4 nm), the displacements shown in Fig. 2.3 are obtained. With respect to the previous case, Fig. 2.3a suggests the following observations. First, as the pressure increases from 50 kPa to 150 kPa and 300 kPa, the maximum displacement increases by factors 1:7:16. Second, the diameter of maximum displacement tends to decrease from 3.0 μm to 2.7 μm and 2.4 μm, respectively. Finally, at increasing pressures, the symmetrical behavior around the resonance frequency vanishes.

Figure 2.3b shows the effect of irradiation with 50-cycle tone bursts at 2 MHz, 4 MHz and 8 MHz and 150 kPa PRP. Maximum displacements are found for diameters of 4.5 μm, 3 μm and 2 μm, respectively. At 2 MHz and 4 MHz irradiation, the saw tooth shape of the graph is more pronounced than at 8 MHz irradiation. When a bubble of 3.2 μm diameter is irradiated at 2 MHz, a local maximum in displacement can be observed. In this case, it seems excited at about half its fundamental resonance frequency, as can be seen from the 4 MHz line. At 4 MHz and 8 MHz transmission frequencies, such subharmonic resonance is not noticeable.

2.4.2 Experimental results

The first experimental test was performed to show that the proposed acoustic setup could actually track the movements impressed by radiation force to each microbubble. Fig. 2.4a shows the M-mode display obtained when the UCA concentration was so low that the US beam intercepted a few F04E microbubbles. In this graph the instantaneous backscatter level is coded to grey levels, so that the subsequent echoes from a scatterer moving away from the transducer (which is located at depth $z = 0$) produces a corresponding trace. In this experiment the irradiation tone burst contained 4 cycles at 4 MHz (400 kPa PRP, 4 kHz PRF). The inclination of

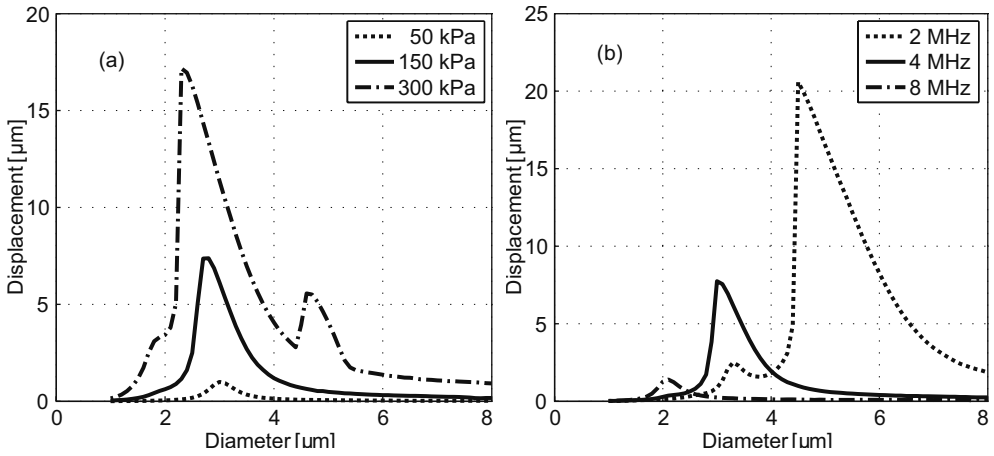

Figure 2.3: Simulated displacement of phospholipid encapsulated bubbles with varying diameters, at different frequencies and driving pressures. The irradiation tone burst contained 50 cycles of a) 4 MHz TX frequency at 50 kPa, 150 kPa and 300 kPa PRP and b) 2 MHz, 4 MHz and 8 MHz TX frequency, at 150 kPa PRP.

the trace at time $t = 11$ s is about 2.2 mm/s. This means that the average scatterer displacement for each transmitted pulse is about 0.55 µm. Bearing in mind that in Fig. 2.2a the irradiation time was 12.5 times longer than in this experiment (50 cycles compared to 4 cycles), the found displacement looks consistent with that reported in Fig. 2.2 for a single rigid-shelled microbubble.

An alternative (MGD) display mode suitable to reveal the effects of radiation force on microbubbles is reported in Fig. 2.4b. This display shows the Doppler spectra produced by bubbles intercepted by the US beam over the ROI. The spectral power estimated at each depth modulates the intensity of the corresponding horizontal line. Since each bubble slowly moves away from the transducer, its Doppler spectrum corresponds to a spotlight moving from top to bottom. The spotlight horizontal position corresponds to the bubble average velocity. Both velocity and intensity achieve maximal values when the bubble is in the focal region, as better visible in the accompanying movie[4]. The movement of the microbubble is also demonstrated in Fig. 2.4c, reporting the sequence of overlaying spotlights generated by the single bubble during its itinerary away from the transducer. Note that the peak Doppler frequency, $f_D = 12$ Hz, corresponds to a velocity of 2.2 mm/s according to the pulse-echo Doppler equation $u_D = cf_D/2f_c$, with c the speed of sound and f_c the TX frequency. This has to be considered the average bubble velocity within one pulse repetition interval, because the instantaneous velocity is non-zero only during

[4]online through DOI 10.1109/TUFFC.2007.393

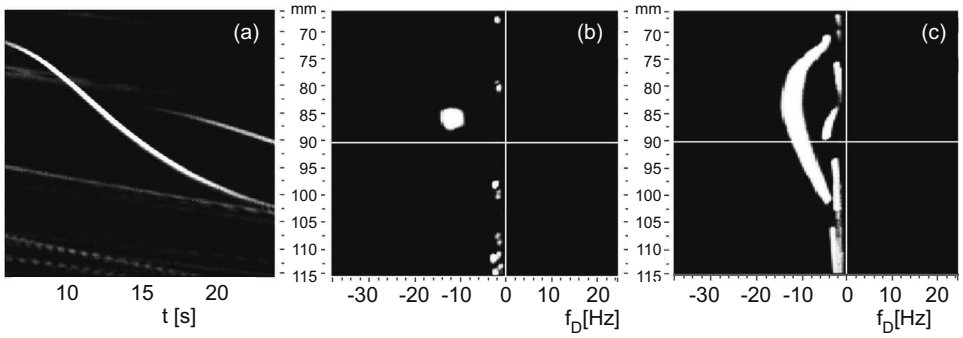

Figure 2.4: Display modes produced after irradiation of F04E bubbles with a 4-cycle tone burst at 4 MHz (PRF = 4kHz, PRP = 400 kPa) and evaluated at depths between 66 and 115 mm. a) M-mode display. b) MGD display produced around time t = 11 s. c) Recording of subsequent MGD images, showing the history of the bubble Doppler signal in the time interval 6 – 22 s.

the passage of the US burst over the bubble; the time between the pulses the velocity is zero (duty cycle $\sim$ 0.4%).

Fig. 2.5 shows an M-mode image obtained by transmitting multiple 8-cycle 8 MHz bursts at PRF = 5 kHz and 1.5 MPa PRP over a suspension of F04E bubbles. This high pressure was chosen to obtain considerable bubble displacements even out of the focal region. The graph reveals the different bubble reactions to irradiation. The trace inclination corresponds again to the extent at which the US radiation force pushes away the target. Each trace brightness and shape are variable, because they depend on the bubble scattering cross-section as well as on the depth at which the bubble is located. A higher brightness is always found in steeper traces, and at the level of the focal region (30 mm at 8 MHz). Finally, all bubbles experience lower pressures when they are beyond the focal region, where they are accordingly displaced less. This results in the S-shapes observable in many traces. At the intersection points of two or more traces, the echoes interfere on the transducer surface. This gives rapid amplitude oscillations in the observed echo level, like that visible at $t = 5.8$ s and $z = 32$ mm in Fig. 2.5.

Figure 2.6 shows the distribution of bubble velocities at different depths, estimated after averaging all recordings covering a long time interval. Due to the history function, individual traces have vanished and the maximum velocity achieved at each depth by resonating bubbles moving along the beam axis can be read. Non-resonating bubbles, and all bubbles out of the beam-axis achieve lower velocities, which are distributed between zero and a certain maximum limit for each depth. As

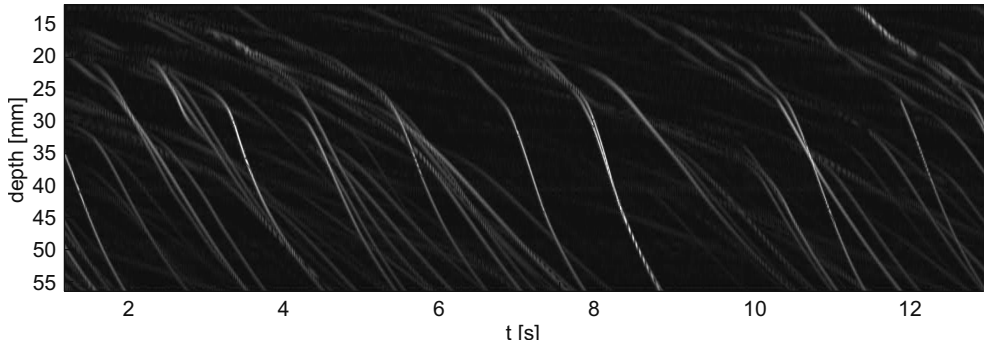

Figure 2.5: M-mode display of thermoplastic-shelled microbubbles. The irradiation tone burst contained 8 cycles at 8 MHz (PRF = 5 kHz, PRP = 1.5 MPa).

the population was irradiated for 8s, it is believed that such a long interval included the contribution of resonant bubbles capable of achieving the highest velocity (here about 12 mm/s).

2.4.3 Analysis

For a quantitative comparison between the simulation model and experimental results, the peak velocity profile simulated by assuming the viscoelastic parameters reported in Sec. 2.2, is superimposed in Fig. 2.6 (dotted line). In the model, the local pressure level along the beam axis was estimated using Field II software [Jensen and Svendsen, 1992]. The simulation returns the maximum average velocity obtained for a resonant bubble by the product of displacement per burst and the PRF. As can be seen, the maximum velocity predicted by the simulation model (4.5 mm/s) is significantly lower than the measured values (12 mm/s). Similar measurements have been repeated at different transmission frequencies (2, 2.5, 3, 3.5, 4, 5, 6, 7 and 8 MHz). The US bursts consisted of 50 cycles of a sine wave; this high number of cycles was chosen to limit transient effects in the transmitted burst and bubble response. Due to the frequency dependent efficiency of the transducers, the TX voltage was varied to obtain an equal focal PRP (about 430 kPa and 280 kPa in two different acquisition sessions) for all frequencies. The burst was repeated at 500 Hz PRF. The total acquisition time for each frequency was 33 seconds. In each acquisition, the maximum bubble velocity was manually scored off-line. The results are displayed in Fig. 2.7. This graph shows that the maximum velocity achieved by a bubble decreases with frequency, following the rough estimate of f^{-2}. The maximum observed velocity

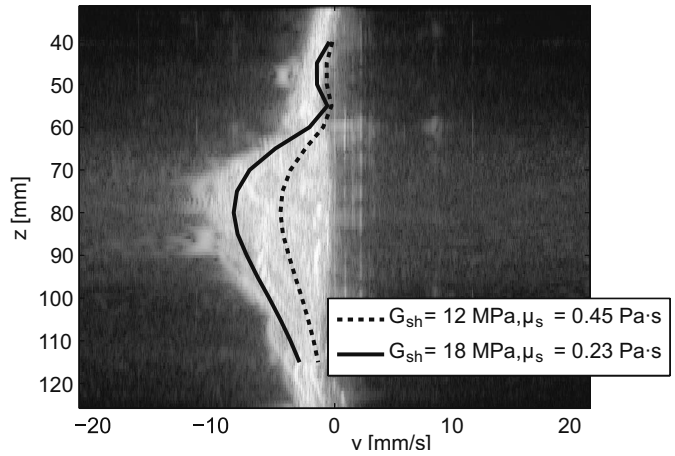

Figure 2.6: History graph of the MGD display showing the velocity profile for an F04E population. Black lines show the simulated maximum velocity for resonant bubbles evaluated by assuming two different sets of values for G_s, μ_s parameters. In these two conditions, the simulated resonant diameters are 8 μm and 10.5 μm, respectively. The US TX burst contained 10 cycles at 2.5 MHz (300 kPa PRP, 1 kHz PRF). The transducer was focused at 80 mm. The bubble density was approximately 10^4 particles/mℓ.

was 48 mm/s, at 2 MHz, and 4 mm/s at 8 MHz irradiation, for 430 kPa PRP in the acoustic focus of the transducer.

In order to tune the simulation parameters, the experimental maximum displacements depicted in Fig. 2.7 were used as input for a parametric fit with the simulation. The optimal fit was obtained by the Nealder-Mead multivariate iteration method, with the shell shear modulus and viscosity as varying parameters. The cost function was defined by the sum of squared errors between the simulated and measured velocities multiplied by the squared TX frequency. The initial parameter values were $G_s = 12$ MPa and $\mu_s = 0.45$ Pa·s [Hoff et al., 2000]. Within 80 iterations, the solution stabilized to a shear modulus of 18 MPa and a viscosity of 0.23 Pa·s. The resulting predicted velocities are superimposed on the experimental values in Fig. 2.7. As can be seen, the fit of the F04E population agrees almost over the full range of velocities, with a maximum deviation factor of 1.5 at 2 MHz and 290 kPa.

By looking back at Fig. 2.6, it can be observed that if such new values are inserted in the model, the velocities of resonant bubbles (solid line) show a better agreement with the experimental maximum velocities, compared to the results obtained with the original viscoelastic parameters (dotted line). The simulated resonant diameter has increased from 8 μm to 10.5 μm. In this comparison, it is assumed that the population in the acoustic focus includes some resonant bubbles, so that the curve defines a prediction of the upper limit of the velocity that any bubble in the

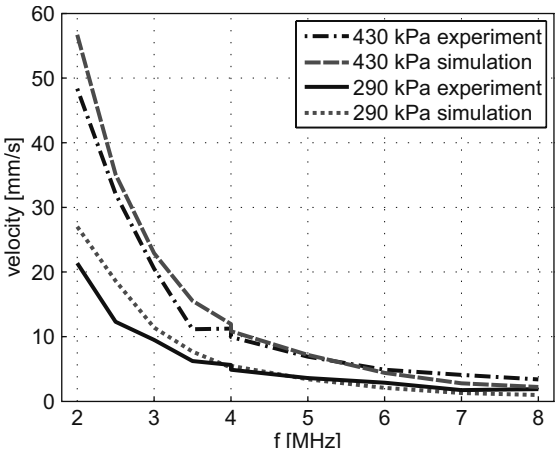

Figure 2.7: Measured and simulated maximum bubble velocities in the F04E population, obtained with irradiation at different frequencies and PRPs. The tone burst contained 50 cycles, and was repeated at 500 Hz. At 4 MHz, the experimental values were obtained with both the available (2 – 4 MHz and 4 – 8 MHz) transducers.

population could obtain.

To allow a qualitative but significant comparison of simulated and experimental displacements, the same conditions used in the experiments leading to Fig. 2.5 for the polymer shelled bubbles have been simulated for 4 bubbles of different diameters, free of moving along the transducer axis. As the pressure along the US beam axis varies with distance, the instant displacement at a certain depth was evaluated using the axial pressure computed at that distance by the Field II software and scaled to the values measured with the hydrophone. The results are shown in Fig. 2.8 and can be positively compared to the experimental results in Fig. 2.5. The dotted line depicts the trace of a simulated bubble moving at a distance of 1 mm from the beam axis. It shows a slightly different shape compared to the bubbles moving on the beam axis.

The concepts and findings applied to the thermoplastic-shelled microbubbles have also been adapted to the experimental contrast agent BR14. Figure 2.9 shows an M-mode display of BR14 irradiated at 320 kPa PRP by a 4-cycle tone burst with 4 MHz frequency. The PRF was 5 kHz. Again, single traces are thought to correspond to single bubbles, although some of them here show abrupt brightness changes (e.g. at $t = 2.2$ s and $z = 24$ mm in Fig. 2.9). From these traces, the displacement due to a single irradiation burst can be roughly estimated. For example the short trace at t = 2.2 s and z = 20 mm presents a slope of about 8.8 mm/s. With 5 kHz of PRF this results in a displacement of 1.8 μm per burst. After taking into account the difference in irradiation time, the value is comparable to those reported in Fig. 2.3.

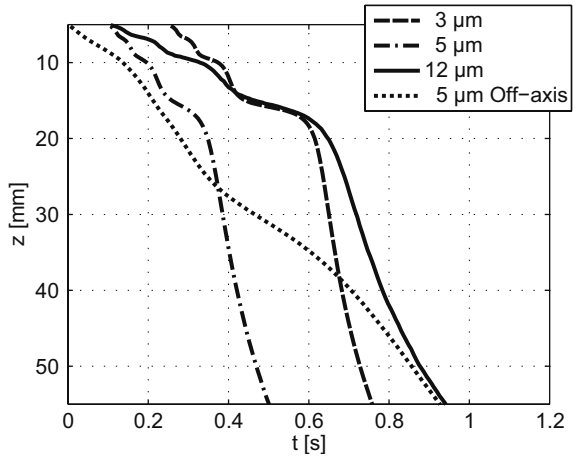

Figure 2.8: Simulated M-mode traces of F04E bubbles with diameters of 3 µm, 5 µm and 12 µm, moving at the beam axis, and for a 5 µm bubble moving along a line parallel to the beam axis (offset: 1 mm). The irradiation tone burst contained 8-cycles at 8 MHz (1.5 MPa PRP, 5 kHz PRF).

The population experiments for tuning the model parameters were also applied for BR14 shell parameter estimation. The echoes after irradiation with 50-cycle tone bursts were recorded for 17 s. The PRF was 1 kHz, while PRP were 290 and 150 kPa. These values were chosen lower than with the F04E population in order to limit the bubble rupture phenomenon [Borden et al., 2005]. The manually scored maximum velocities are plotted in Fig. 2.10. Again, the experimental velocities were used to tune the shell values in the simulation model using the parametric fit algorithm. As initial shell values, the shear modulus was taken as 46 MPa and 0.25 Pa·s, as reported in Sec. 2.2. The final phospholipid shell values in BR14 were estimated 32 MPa and 0.19 Pa·s at 4 nm constant thickness, and the predicted maximum velocities are also reported in Fig. 2.10. The BR14 experiments show larger deviation from the simulation for the higher pressure (290 kPa) and lowest frequencies (2 and 2.5 MHz), with a maximum overestimation of a factor of 2 (52 mm/s compared to 25 mm/s) at 2 MHz TX frequency.

2.5 Discussion

The simulation results in Figs. 2.2 and 2.3 confirm that the displacement is strongly related to the initial bubble radius. This is consistent with the fact that the radiation force depends on both the phase between the driving pressure and the radial excursion, and the amplitude of the radial excursion and pressure. At resonance, the phase difference is a quarter of a wave, and the radial excursion is highest, giving both ingredients for highest radiation force [Dayton et al., 2002]. The

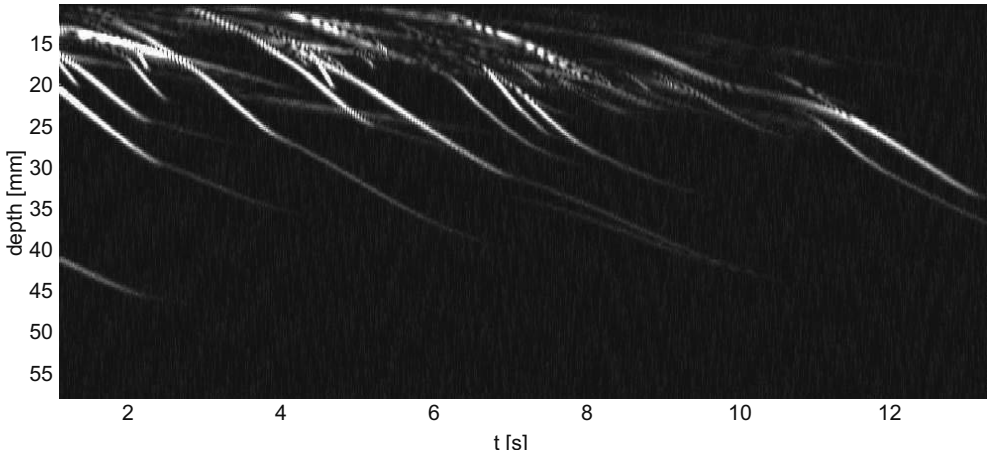

Figure 2.9: Experimental M-mode traces produced by BR14 microbubbles. The irradiation tone bursts contained 4 cycles at 4 MHz (320 kPa PRP, 5 kHz PRF).

instantaneous velocity that a bubble reaches can be very high. For example, Fig. 2.2a reports a simulated displacement of 9 μm after irradiation with a 300 kPa tone burst of duration of 12.5 μs. Hence, the instantaneous velocity must reach values on the order of 1 m/s for short instances [Dayton et al., 2002]. Pulsing of the US results in an average velocity equal to the displacement per burst times the PRF, which leads to the lower average velocities reported in this work (1–50 mm/s).

Nonlinear phenomena introduce vibrations at other frequencies than the irradiating one, which interact with the driving pulse. In a small-signal (linear) approach, one can assume that drag is in the Stokes regime (drag force proportional to velocity) and the radiation force is quadratic with pressure [Leighton, 1994]. Passing the pressure from 50 kPa to 150 kPa and 300 kPa, a ratio of 1:9:36 is expected. In Fig. 2.2, the maximum displacement for the subsequent pressures increases by a ratio 1:8:26, giving a maximum deviation of 28%. Figure 2.3a reports an even stronger effect for the phospholipid-shelled bubbles, where the maximum displacement gives a ratio of 1:7:16. The difference in encapsulation and, therefore, the viscous damping, which mainly results in a difference in radial excursion, could explain this difference between the BR14 and F04E bubbles. In additional simulations, we irradiated a resonant bubble with a 4 MHz, 150 kPa tone burst. The thermoplastic-shelled bubble showed 9% peak-to-peak radial excursion, while a phospholipid shelled bubble had a diameter excursion of 68%. This latter results in stronger nonlinear effects, which have already been investigated for radial motion only [Prosperetti, 1974; Sun et al., 2005] and for the translation [Reddy and Szeri, 2002], and is not predicted by a linearized model [Leighton, 1994; Tortoli et al., 2000]. Figure 2.2b also suggests that

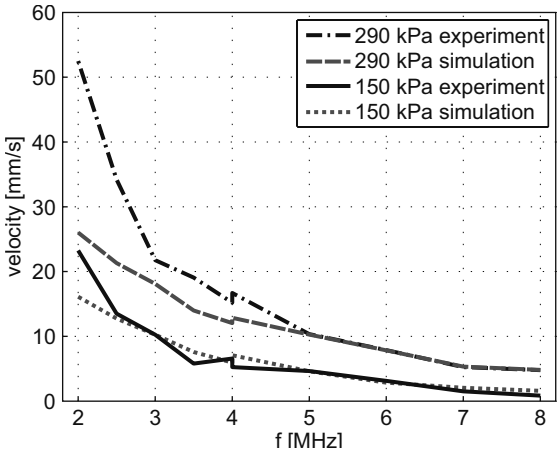

Figure 2.10: Measured and simulated maximum bubble velocities in the BR14 population for different frequencies and PRPs. The tone bursts contained 50 cycles, and were repeated at 1 kHz. At 4 MHz, the experimental values were obtained with both the available transducers.

bubbles with diameter < 2.5 μm have a maximum displacement which is independent of the TX frequency, at least in the range 2 – 8 MHz. This seems to originate from over-damped bubble systems, as discussed in detail by e.g. Khismatullin and Nadim [2002].

Another interesting feature is seen in Fig. 2.3b. Looking at the 150 kPa irradiation pressure and 50 cycles at 2 MHz, the model predicts two local maxima in the displacement, one at a diameter of 4.5 μm, and one at 3.1 μm. This latter diameter corresponds to a resonance frequency of 4 MHz. In other words, a bubble with resonant diameter to 4 MHz can be excited at its first subharmonic frequency ($1/2\, f_r$), 2 MHz [Eller and Flynn, 1969; Sun et al., 2005]. This volumetric vibration next interacts with the driving pressure. At 4 MHz and 8 MHz TX frequency, such subresonance is hardly noticeable due to increased damping at these frequencies.

The traces shown in the M-mode display of Figs. 2.4 and 2.5 have been associated to individual bubbles of a full population. From the acquisitions only, no exclusive proof can be supplied to the hypothesis that each corresponds to a single bubble. However, looking at the large similarities between the simulation and experiments we have strong circumferential proof that those are indeed produced by single bubbles. Some thermoplastic-shelled bubbles showed sudden change of velocity and backscatter intensity at 2 MHz TX frequency and higher pressures. An example is shown in Fig. 2.11, where F04E bubbles are irradiated with a 4-cycle tone burst of 4 MHz at 620 kPa. A trace suddenly stops at $t = 30$ s and $z = 79$ mm. The disappearance of the bubble involves a strong decorrelation in subsequent echoes, and a

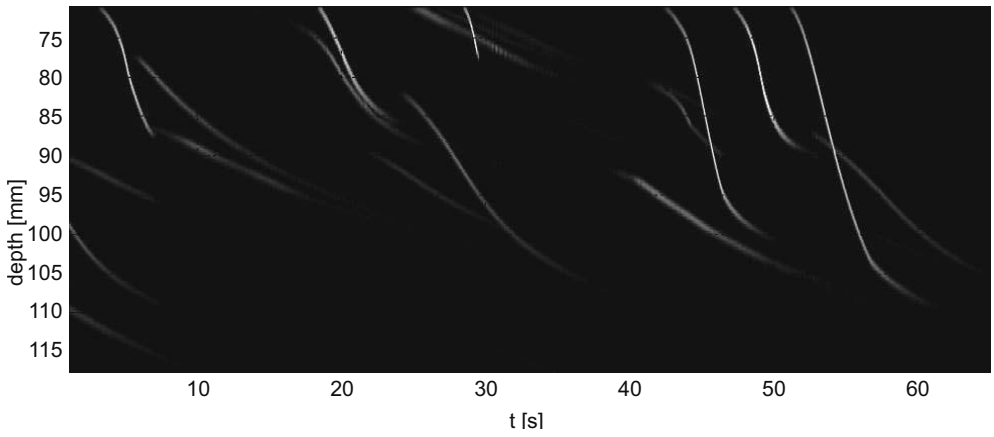

Figure 2.11: M-mode display obtained by irradiating F04E bubbles with 4-MHz 4-cycle bursts (PRP = 620 kPa, PRF = 1 kHz). At t = 28 s, the trace suddenly stops, showing rupture of the bubble.

corresponding wideband noise [Evans and McDicken, 2000; Tortoli et al., 2005] can be seen in the accompanying MGD movie[5]. It is believed that these bubbles are ruptured, or at least have suddenly changed their intrinsic properties. This effect was not seen for frequencies higher than 2.5 MHz or at pressures lower than 500 kPa. In the maximum velocity detection, bubbles showing noncontinuous behavior were left out. The process of acoustic dissolution might have deflated the BR14 bubbles after such long, high pressure bursts, repeated more than thousand times [Borden et al., 2005; Sun et al., 2005]. Borden et al. [2005] showed that soft-shelled bubbles will deflate to a certain critical radius, after which the average radius will not change any more. This might damage our "full population" assumption, as the population could be conditioned. This deflation effect is also likely to cause the phenomenon seen in Fig. 2.9, around $t = 3.8$ s and $z = 25$ mm, where the bubble suddenly showed lower scattering and displacement.

As was seen in Figs. 2.7 and 2.10, the simulated maximum velocities and the measured values agree on major features. The errors are comparable to those reported by Dayton et al. [2002], where the displacements of phospholipid-shelled microbubbles with a decafluorobutane core were optically measured and compared to a simulation model in which the influence of the encapsulation is described through a thin-film approach. In our case, for the lowest irradiation frequencies (2 MHz and 2.5 MHz), the deviation between simulation results and experiments is larger than for other TX frequencies. Apart from the deflation and rupture hypothesis discussed

[5]online through DOI 10.1109/TUFFC.2007.393

before, the difference might be due to the fact that the radial excursion is inversely related to frequency, and the relation between strain and stress can be nonlinear [Borden et al., 2004; Marmottant et al., 2005]. Furthermore, for large radial excursion, the fluid dynamics around the bubble might be more complex than described by the drag term Eqs. 2.4 and 2.5 in the simulation model. Further experiments in the lower-frequency range should be applied to resolve these points.

The model, and hence the iteration method, is sensitive to the inserted model parameter values. We assumed a fixed shell thickness of 2.7% of the radius for the polymer-encapsulated bubbles and 4 nm for BR14. Unfortunately we were not able to validate these values independently. However, if we consider the predicting quality of the model only, we should always use these thickness values when predicting the behavior of these bubbles, and the error made in the shell thickness should cancel out. This drawback is equally present in established shell estimation methods [Hoff et al., 2000]. If, on the other hand, the wall would be very thin at certain spots on the bubble surface, much thinner than the mean thickness of the shell, it would appear as the material having a lower shear modulus when we assume a constant thickness. As a result, our method might underestimate the shear modulus of the material. This could explain why the found value of the thermoplastic shell (18 MPa) is so much lower than the shear modulus of PVC obtained in bulk at 1 MHz, about 1 GPa (Young's modulus 3 GPa) [Lagakos et al., 1986].

We have also investigated the shape of F04E thermoplastic shell and BR14 using an optical microscope (Fig. 2.12). The shape of the F04E encapsulation is frequently not spherical, but it looks rather like small rocks. Looking at the equations that describe our simulation model, most terms assume spherical symmetry. However, the effects that dominate the displacement are the gas and shell properties, the driving Bjerknes force and the drag force. Neither the gas law nor the Bjerknes force assumes spherical symmetry. If the shape is more or less spherical, the drag will be higher than predicted by Eq. 2.5, but the value will still be reasonable. The term describing the shell elasticity and damping will be affected by the exact structure, which could again explain a part of the discrepancy of the elasticity values found in our study compared to literature values. Further investigation of the exact vibration of these thermoplastic-shelled bubbles, for example with fast framing cameras, might reveal the influence of the nonspherical structure.

A special feature of the bubble-US system can be directly seen in Figs. 2.2 and 2.3. By looking at these figures, it might look as if the bubble radius could be derived only from the bubble velocity, giving an opportunity for a novel apparatus to measure bubble diameter distributions. However, two different bubble diameters, one having a sub-resonant and one having super-resonant radius can achieve the same displacement. This feature blocks the possibility of directly estimating the bubble diameter of single observed bubbles in a parametric fit approach. This radial

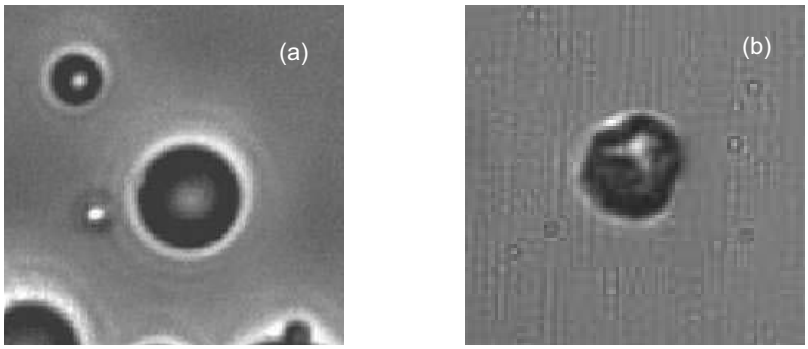

Figure 2.12: Typical microscopic images of a) BR14 bubble and b) thermoplastic shelled microbubble. The diameter of the largest bubbles shown here is approximately 8 μm.

ambiguity is absent only for bubbles irradiated at exactly their resonance frequency, which finding we have used in the shell characterization experiments addressed in previous sections.

2.6 Conclusion

In this paper, we have described an acoustic setup for UCAs characterization based on the observation of effects of US radiation force. The system flexibility, combined with the Doppler method, a sensitive coherent receive section and the use of focused transducers have allowed for minute in-vitro investigations of two different types of microbubbles.

While irradiating low UCA concentrations in water an accurate tracking of the movements of multiple scatterers by means of an original multigate Doppler display and a classic M-mode display was possible. By comparing these results with the predictions of a simulation model, it seems reasonable to assimilate each of these scatterers to an individual bubble in the population. It was also possible to observe phenomena that can be interpreted as bubble destruction and deflation.

Comparison between the experimental observations and simulation results has also allowed estimating viscoelastic values for both thermoplastic and phospholipid shelled microbubbles. The values estimated for the former, 18 MPa and 0.23 Pa·s seem to suggest that the PVC-AN shell behaves like a PVC shell. As the phospholipid shell of BR14 is presumably very thin (4 nm), bulk values of the shell material (32 MPa and 0.19 Pa·s) have little meaning. However, converting into the frequently used shell elasticity parameter and shell friction, values of $\chi = 0.8$ N/m

and $S_f = 1 \cdot 10^{-7}$ kg/s, respectively, are obtained. These are on the same order of magnitude of those reported in literature.

Bibliography

Allen, J. S., D. J. May, and K. W. Ferrara, "Dynamics of therapeutic ultrasound contrast agents," *Ultrasound Med Biol*, 28(6): pp. 805–816, 2002.

Berens, A. R. and H. B. Hopfenberg, "Diffusion of organic vapors at low concentrations in glassy pvc, polystyrene, and pmma," *J Membrane Sci*, 10: pp. 283–303, 1982.

Bjerknes, V., Fields of Force, Columbia University Press, New York, 1906.

Borden, M. A., D. E. Kruse, C. F. Caskey, S. Zhao, P. A. Dayton, and K. W. Ferrara, "Influence of lipid shell physicochemical properties on ultrasound-induced microbubble destruction," *IEEE Trans Ultrason Ferroelectr Freq Control*, 52(11): pp. 1992–2002, 2005.

Borden, M. A., G. Pu, G. J. Runner, and M. L. Longo, "Surface phase behavior and microstructure of lipid/peg-emulsifier monolayer-coated microbubbles," *Colloids Surfaces B-Biointerfaces*, 35: pp. 209–223, 2004.

Borden, M. A., M. R. Sarantos, S. M. Stieger, S. I. Simon, K. W. Ferrara, and P. A. Dayton, "Ultrasound radiation force modulates ligand availability on targeted contrast agents," *Molecular Imaging*, 5(3): pp. 139–147, 2006.

Bouakaz, A., M. Versluis, and N. de Jong, "High-speed optical observations of contrast agent destruction," *Ultrasound Med Biol*, 31(3): pp. 391–399, 2005.

Church, C. C., "The effects of an elastic solid surface layer on the radial pulsations of gas bubbles," *J Acoust Soc Am*, 97(3): pp. 1510–1521, 1995.

Commander, K. W. and A. Prosperetti, "Linear pressure waves in bubbly liquids: Comparison between theory and experiments," *J Acoust Soc Am*, 85(2): pp. 732–746, 1989.

CRC, Handbook of Chemistry and Physics (82th edition), CRC, Boca Raton, FL, 2001.

Crum, L. A., "Bjerknes forces on bubbles in a stationary sound field," *J Acoust Soc Am*, 57: pp. 1363–1370, 1975.

Dayton, P. A., J. S. Allen, and K. W. Ferrara, "The magnitude of radiation force on ultrasound contrast agents," *J Acoust Soc Am*, 112(5): pp. 2183–2192, 2002.

Dayton, P. A., K. E. Morgan, A. L. Klibanov, G. Brandenburger, K. R. Nightingale, and K. W. Ferrara, "A preliminary evaluation of the effects of primary and secondary radiation forces on acoustic contrast agents," *IEEE Trans Ultrason Ferroelectr Freq Control*, 44(6): pp. 1264–1277, 1997.

de Jong, N., Acoustic properties of ultrasound contrast agents, Ph.D. thesis, Erasmus University Rotterdam, 1993.

Deng, C. X., F. L. Lizzi, A. Kalisz, A. Rosado, R. H. Silverman, and D. J. Coleman, "Study of ultrasonic contrast agents using a dual-frequency band technique," *Ultrasound Med Biol*, 26(5): pp. 819–831, 2000.

Eckersley, R. J. and M.-X. Tang, "Nonlinear corruption of ultrasound transmission by microbubble contrast agents," in proc. IEEE Ultrasonics symposium, pp. 1691–1694, Montréal, 2005.

Eller, A. I. and H. G. Flynn, "Generation of subharmonics of order one-half by bubbles in a sound field," *J Acoust Soc Am*, 46(3 (part2)): pp. 772–727, 1969.

Emmer, M., J. Borsboom, A. van Wamel, M. Versluis, and N. de Jong, "Optical investigation

of ultrasound induced encapsulated microbubble oscillations: threshold and hysteresis effects," in proc. IEEE Ultras Symp, vol. 1, pp. 981–984, Rotterdam, The Netherlands, 2005.

Evans, D. H. and W. N. McDicken, Doppler ultrasound: Physics, Instrumentation, and Clinical Applications, John Wiley & Sons, Chichester, UK, second edn., 2000.

Gorce, J.-M., M. Arditi, and M. Schneider, "Influence of bubble size distribution on the echogenicity of ultrasound contrast agents - a study of SonoVue," *Invest Radiol*, 35(11): pp. 661–671, 2000.

Guan, J. and T. J. Matula, "Using light scattering to measure the response of individual ultrasound contrast microbubbles subjected to pulsed ultrasound *in vitro*," *J Acoust Soc Am*, 116(5): pp. 2832–2842, 2004.

Hoff, L., P. C. Sontum, and J. M. Hovem, "Oscillations of polymeric microbubbles: Effect of the encapsulating shell," *J Acoust Soc Am*, 107(4): pp. 2272–2280, 2000.

Jensen, J. A. and N. B. Svendsen, "Calculation of pressure fields from arbitrarily shaped, apodized, and excited ultrasound transducers," *IEEE Trans Ultrason Ferroelectr Freq Control*, 39(2): pp. 262–267, 1992.

Khismatullin, D. B. and A. Nadim, "Radial oscillations of encapsulated microbubbles in viscoelastic liquids," *Phys Fluids*, 14(10): pp. 3524–3557, 2002.

Klibanov, A. L., M. S. Hughes, J. K. Wojdyla, J. H. Wible, and G. H. Brandenburger, "Destruction of contrast agent microbubbles in the ultrasound field: The fate of the microbubble shell and the importance of the bubble gas content," *Acad Radiol*, 9(1 (Supp.)): pp. S41–S45, 2002.

Lagakos, N., J. Jarzynski, J. H. Cole, and J. A. Bucaro, "Frequency and temperature dependence of elastic moduli of polymers," *J Appl Phys*, 59(12): pp. 4017–4031, 1986.

Leighton, T. G., The Acoustic Bubble, Academic Press, London, UK, 1994.

Lindner, J. R., "Targeted ultrasound contrast agents: Diagnostic and therapeutic potential (inv.)," in proc. IEEE Ultras Symp, vol. 1, pp. 1695–1703, 2001.

Magnaudet, J. and D. Legendre, "The viscous drag force on a spherical bubble with a time-dependent radius," *Phys Fluids*, 10(3): pp. 550–554, 1998.

Marmottant, P., S. M. van der Meer, M. Emmer, M. Versluis, N. de Jong, S. Hilgenfeldt, and D. Lohse, "A model for large amplitude oscillations of coated bubbles accounting for buckling and rupture," *J Acoust Soc Am*, 118(6): pp. 3499–3505, 2005.

Matula, T. J., "Bubble levitation and translation under single-bubble sonoluminescence conditions," *J Acoust Soc Am*, 114(2): pp. 775–781, 2003.

Medwin, H., "Counting bubbles acoustically: a review," *Ultrasonics*, 15: pp. 7–13, 1977.

Morgan, K. E., J. S. Allen, P. A. Dayton, J. E. Chomas, A. L. Klibanov, and K. W. Ferrara, "Experimental and theoretical evaluation of microbubble behavior: Effect of transmitted phase and bubble size," *IEEE Trans Ultrason Ferroelectr Freq Control*, 47(6): pp. 1494–1509, 2000.

Nowicki, A., T. Kowalewski, W. Secomski, and J. Wójcik, "Estimation of acoustical streaming: theoretical model, Doppler measurements and optical visualisation," *Eur J Ultras*, 7: pp. 73–81, 1998.

Ophir, J. and K. J. Parker, "Contrast agents in diagnostic ultrasound," *Ultrasound Med Biol*, 15(4): pp. 319–333, 1989.

Palanchon, P., P. Tortoli, A. Bouakaz, and N. de Jong, "Optical observations of acoustical ra-

diation force effects on individual air bubbles," *IEEE Trans Ultrason Ferroelectr Freq Control*, 52(1): pp. 104–110, 2005.

Prosperetti, A., "Nonlinear oscillations of gas bubbles in liquids: steady-state solutions," *J Acoust Soc Am*, 56(3): pp. 878–885, 1974.

Reddy, A. J. and A. J. Szeri, "Coupled dynamics of translation and collapse of acoustically driven microbubbles," *J Acoust Soc Am*, 112(4): pp. 1346–1352, 2002.

Rensen, J., D. Bosman, J. Magnaudet, C.-D. Ohl, A. Prosperetti, R. Tögel, M. Versluis, and D. Lohse, "Spiraling bubbles: How acoustic and hydrodynamic forces compete," *Phys Rev Lett*, 86(21): pp. 4819–4822, 2001.

Ricci, S., E. Boni, F. Guidi, T. Morganti, and P. Tortoli, "A programmable real-time system for development and test of new ultrasound investigation methods," *IEEE Trans Ultrason Ferroelectr Freq Control*, 53(10): pp. 1813–1819, 2006.

Rychack, J. J., A. L. Klibanov, and J. A. Hossack, "Acoustic radiation force enhances targeted delivery of ultrasound contrast microbubbles: in vitro verification," *IEEE Trans Ultrason Ferroelectr Freq Control*, 52(3): pp. 421–433, 2005.

Sherman, F. S., Viscous flow, Mechanical Engineering Series, McGraw-Hill, int. edn., 1990.

Shi, W. T., F. Forsberg, R. Bautista, C. Vecchio, R. Bernardi, and B. B. Goldberg, "Active enhancement of ultrasound contrast imaging," in proc. IEEE Ultras Symp, 2000.

Shortencarier, M. J., P. A. Dayton, S. H. Bloch, P. A. Schumann, T. O. Matsunaga, and K. W. Ferrara, "A method for radiation-force localized drug delivery using gas-filled lipospheres," *IEEE Trans Ultrason Ferroelectr Freq Control*, 51(7): pp. 822–831, 2004.

Sijl, J., M. Arditi, P. J. A. Frinking, N. de Jong, D. Lohse, and M. Versluis, "Acoustical study of the properties of individual phospholipid-based ultrasound contrast agent microbubbles," in proc. 11th Eur Symp Ultras Contrast Imaging, pp. 13–14, Rotterdam, The Netherlands, 2006.

Sun, Y., D. E. Kruse, P. A. Dayton, and K. W. Ferrara, "High-frequency dynamics of ultrasound contrast agents," *IEEE Trans Ultrason Ferroelectr Freq Control*, 52(11): pp. 1981–1991, 2005.

Szabo, T., Diagnostic Ultrasound Imaging: Inside Out, Elsevier Science & Technology, Oxford UK, 2004.

Takeuchi, Y., "Industrial use thermoplastic microballoon to mimic the contrast agents and its in-vitro behavior including released gas dynamics," in proc. IEEE Ultras Symp, pp. 1579–1582, 1997.

Tortoli, P., E. Boni, M. Corsi, M. Arditi, and P. Frinking, "Different effects of microbubble destruction and translation in Doppler measurements," *IEEE Trans Ultrason Ferroelectr Freq Control*, 52(7): pp. 1183–1188, 2005.

Tortoli, P., V. Michelassi, M. Corsi, D. Righi, and Y. Takeuchi, "On the interaction between ultrasound and contrast agents during Doppler investigations," *Ultrasound Med Biol*, 27(9): pp. 1265–1273, 2001.

Tortoli, P., M. Pratesi, and V. Michelassi, "Doppler spectra from contrast agents crossing an ultrasound field," *IEEE Trans Ultrason Ferroelectr Freq Control*, 47(3): pp. 716–726, 2000.

van Wamel, A., A. Bouakaz, M. Versluis, and N. de Jong, "Micromanipulation of endothelial cells: ultrasound-microbubble-cell interaction," *Ultrasound Med Biol*, 30(9): pp. 1255–1258, 2004.

Vokurka, K., "Comparison of Rayleigh's, Herring's, and Gilmore's models of gas bubbles,"

Acustica, 59(3): pp. 214–219, 1986.

White, F. M., Viscous fluid flow, McGraw-Hill, New York, 1991.

Zhao, S., M. A. Borden, S. H. Bloch, D. E. Kruse, K. W. Ferrara, and P. A. Dayton, "Radiation-force assisted targeting facilitates ultrasonic molecular imaging," *Molecular Imaging*, 3(3): pp. 135–148, 2004.

Chapter 3

Microbubble characterization through acoustically-induced deflation

Abstract - **Ultrasound contrast agent (UCA) populations are typically polydisperse and contain microbubbles with radii over a given range. Although the behavior of microbubbles of certain sizes might be masked by the behavior of others, the acoustic characterization of UCA is typically made on full populations. In this paper, we have combined acoustic and optical methods to investigate the response of isolated lipid-shelled microbubbles to low-pressure (49 kPa and 62 kPa peak negative pressure) ultrasound tone bursts. These bursts induced slow deflation of the microbubbles. The experimental setup included a microscope connected to a fast camera acquiring one frame per pulse transmitted by a single-element transducer. The behavior of each bubble was measured at multiple frequencies, by cyclically changing the transmission frequency over the range 2 – 4 MHz during subsequent pulse repetition intervals. The bubble echoes were captured by a second transducer and coherently recorded.**

Over 50 individual microbubbles were observed. Microbubbles with radii larger than 3 μm did not experience any size reduction. Smaller bubbles slowly deflated, generally until the radius reached a value around 1.4 μm, independent of the initial microbubble size. The detected pressure amplitude backscattered at 2.5 cm distance was very low, decreasing from about 5 Pa down to 1 Pa at 2 MHz as the bubbles deflated.

The resonant radius was evaluated from the echo amplitude normalized with respect to the geometrical cross section. At 2 MHz excitation, deflating microbubbles showed highest normalized echo when the radius was 2.2 μm while, at higher excitation frequencies, the resonant radius was lower. The relative phase shift of the echo during the deflation process was also measured. It was found to exceed π/2 in all cases. A heuristic procedure based on the analysis of multiple bubbles of a same population was used to estimate the undamped natural frequency. It was found that a microbubble of 1.7 μm has an undamped natural frequency of 2 MHz. The difference between this size and the resonant radius is discussed as indicative of significant damping.

Accepted for publication in the *IEEE Transactions of Ultrasonics, Ferroelectrics, and Frequency Control*, by F. Guidi, H. J. Vos, R. Mori, N. de Jong, and P. Tortoli, 2009. The authors would like to acknowledge P. van Neer (Erasmus MC Rotterdam) and J. Sijl (University of Twente) for the calibration of the receiving transducer, and E. Boni (University of Florence) for his contribution in BBT system optimization. We also thank dr. T. Hay (University of Twente) for proof reading of the manuscript.

3.1 Introduction

The accurate characterization of coated microbubbles is important to optimize their use as ultrasound contrast agents (UCAs) in clinical applications. Microbubbles are efficient ultrasound (US) scatterers due to the high compressibility of the internal gas. It is generally assumed that their scattering cross section is significantly increased by resonance. The extent of such an increase, as well as the resonance frequency, are strongly related to the physical properties of the microbubbles and, in particular, of their shell [van der Meer et al., 2007]. Hence, efficient insonation of an UCA population can only be achieved once the UCA behavior in US fields is suitably characterized.

The most popular methods for UCA characterization are based on optical and/or acoustic observations. A typical model-based approach consists of measuring the acoustic attenuation and/or scattering spectra of a population to estimate the related visco-elastic parameters [de Jong et al., 1992; Gorce et al., 2000]. In turn, the model predicts the scattering cross section of the coated bubbles. Although the inherent linearity assumption is violated for phospholipids coated microbubbles [Emmer et al., 2007; Tang and Eckersley, 2007], the method is still widely used, probably because the possible nonlinear response of single bubbles in the population is masked by the linear response of others [Emmer et al., 2007]. More recent models also consider possible shell modifications due to nonlinear effects such as buckling or rupture [Marmottant et al., 2005; Doinikov and Dayton, 2007; Stride, 2008; Tsiglifis and Pelekasis, 2008]. It should be noted that such models propose a time-invariant system, not accounting for possible slow changes in the shell structure and/or gas dissolution, which could happen when microbubbles are repeatedly exposed to imaging pulses [Borden et al., 2005; Thomas et al., 2009].

To overcome the problems faced in population-based studies, optical methods are used to resolve the radial response of single bubbles to a limited number of excitation pulses [Morgan et al., 2000; Guan and Matula, 2004; Sun et al., 2005; van der Meer et al., 2007; Chetty et al., 2008]. In this case, the characterization of an entire population is assembled by repeating the basic measurements on bubbles of different radii. Only few experimental studies address the echo of single microbubbles (for example [Dayton et al., 1999; Guidi et al., 2003; Vos et al., 2007; Sijl et al., 2008, 2007; Thomas et al., 2009]). In Sijl et al. [2007, 2008], coated microbubbles were insonified with low-pressure pulses taking care to incorporate only bubbles that maintained their initial size. Bubble images were simultaneously recorded together with their echo-signals.

The objective of this work is to investigate the behavior of single lipid-shelled microbubbles exposed to a long series of low-pressure US pulses. First, optical recording of the bubble size during the acoustically-induced deflation allows tracking the dissolution behavior as a function of insonation parameters. Second, acous-

tic sampling of a same bubble while deflating presents a convenient way to contribute to UCA characterization. In contrast to previous studies in which a relatively small number of bubble radii were examined, this approach allows quasi-continuous recording of both the echo amplitude and phase corresponding to an interval of bubble sizes. Information on the resonance characteristics and damping are thus obtained.

3.2 Methods

3.2.1 Experimental setup

Definity™ (Lantheus Medical Imaging, North Billerica, MA, USA) microbubbles were used in the experiments. They comprise perfluoropropane gas coated with a flexible phospholipids shell and product literature claims a mean diameter between 1.1 μm and 3.3 μm in the population.

The microbubbles under test were contained in a capillary fibre immersed in a water tank at room temperature (T $\approx$ 22°C). The cellulose capillary fibre (Cuprophan, Akzo Nobel Faser AG, Germany) had inner diameter of 160 μm and was nearly transparent both acoustically and optically.

As shown in Fig. 3.1, the experimental setup combines an acoustical system with a microscope and a video-camera. The acoustical section consists of the US Bubble Behavior Testing (BBT) system. This is a custom integrated electronic board, developed at the Microelectronic Systems Design Laboratory (University of Florence, Italy), which includes two programmable transmitters and two low-noise receivers, a real-time processing section and USB 2.0 interface to a host PC [Ricci et al., 2006]. The transmitters and receivers operate coherently at 64 million samples per second. In this work, the BBT system was configured to use one single-element transducer (PA076 1 inch focus, Precision Acoustics, Dorchester, UK) as transmitter (TX) and another (C381-SU 1 inch focus, Panametrics-NDT, Waltham, MA, USA) as receiver (RX). The two transducers were co-focally positioned with relative 100° angle to intercept the same portion of the fibre, i.e., the region of interest (ROI). The RX circuitry was optimized to obtain an equivalent input noise of only 0.9 nV/$\sqrt{\text{Hz}}$, and thus to guarantee the high sensitivity requested to detect the weak echoes produced by single bubbles.

The optical equipment consists of a water-immersion 40× objective (LUMPLFL 40×/W N.A. 0.8, Olympus, Tokyo, Japan) having the focal plane in the ROI, which is illuminated by a continuous light source. The objective was mounted on the microscope (Olympus BX-FM, 4× extra zoom), which projected the images on a commercial digital camera (Redlake, MotionPro™, San Diego, CA, USA), configured to store 250 frames/s with a shutter time of 2 ms, and having 4 GB circular memory storage capability. The final resolution was up to 13.4 pixels/μm.

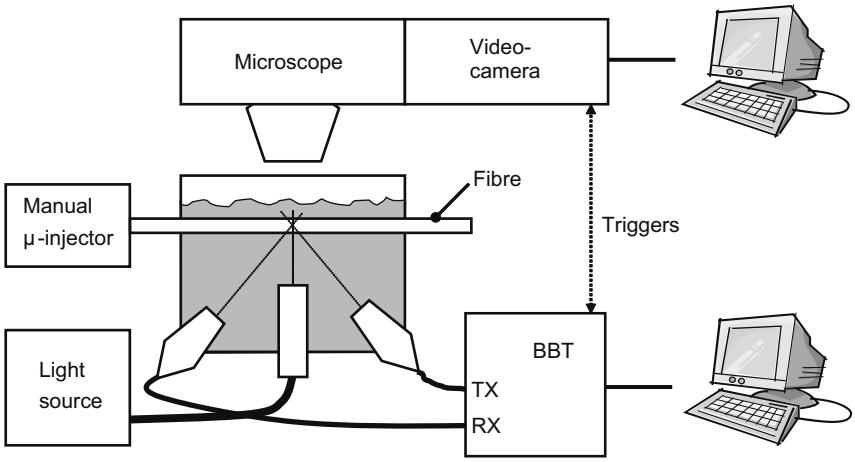

Figure 3.1: Experimental setup. Two US transducers and the microscope are co-focused on the fibre. The video-camera is synchronized to the Bubble Behavior Testing system (BBT) to acquire a single frame per transmitted acoustic pulse.

Frame acquisition was synchronized with operation of the BBT system in order to guarantee the correlation between acquired acoustical and optical data. Both video and US sub-systems were controlled by real-time software running on a host PC. For each transmitted pulse one frame and the corresponding radiofrequency (RF) bubble echo were stored. The amount of available memory was adequate to record acousto-optical data over 64 $\times$ 1024 insonation pulses (about 4 minutes at 250 Hz repetition frequency).

3.2.2 Experimental procedure

UCA vials were prepared according to the instructions of the manufacturer. A small amount of the agent was extracted, diluted in Isotone II (Beckman Coulter, Fullerton, CA, USA), shaken and slightly filtered by flotation to remove smaller bubbles. The suspension was injected in the capillary tube. The capillary was flushed using a manual micro-syringe until optical inspection revealed that a single bubble was present in the ROI, with no other bubbles around within +/- 1 mm. The procedure takes a time between few minutes and one hour to complete.

The TX transducer was excited by specific excitation sequences characterized by a Pulse Repetition Frequency (PRF) of 250 Hz. Each tone burst contained 15 cycles at a pressure level of either 49 or 62 kPa, as specified in Table 3.1. The TX frequency was cyclically changed in steps of 0.5 MHz between subsequent pulses. The frequency range covered 2 – 4 MHz.

Both the BBT system and the RX transducer have been characterized to convert

the RX voltage readout to a pressure value at the transducer surface [van Neer et al., 2007].

Special care was taken to remove the contribution of acoustic clutter echoes and fixed image patterns. In particular, each acquisition was followed by a second acquisition in which no bubble was present, to get "clutter reference" data to be subtracted from the raw data.

3.2.3 Data analysis

The available data were divided into different data-sets, i.e., collections of acquisitions obtained under the same firing conditions (see Table 3.1).

Video frames and corresponding backscattered echoes were analyzed using MATLAB © (Mathworks Inc., Natick, MA, USA). The *bubble radius*, R, was estimated from the video frames using an edge-tracking minimum cost algorithm [van der Meer et al., 2007]. The *echo amplitude* was evaluated as follows. First, a time gating window was applied around the RF echo signal. The trace was filtered around the first harmonic through a zero phase second order band-pass Butterworth filter (bandwidth 500 kHz). Finally the analytical signal was extracted, and the envelope peak was converted to Pascal to produce the *echo amplitude* value, P_s. The *normalized scattering cross-section* was computed by taking the ratio of the measured acoustical scattering cross-section SCS (i.e., the ratio between the scattered power and the incident intensity [Leighton, 1994]) and the geometrical cross-section,

$$SCS_{\text{norm}} = \frac{\frac{P_s^2}{P_a^2} 4\pi r^2}{4\pi R^2} \tag{3.1}$$

with P_a the amplitude of the excitation pressure (at the location of the microbubble), r the distance to the RX transducer (equal to 25 mm as obtained with a conventional time-of-flight measurement) and R the equilibrium radius during the pulse repetition interval (PRI). The normalized SCS can be interpreted as the scattering strength of the microbubble compared to a geometrical scatterer having equal size as the microbubble.

The *relative echo phase* was preliminarily evaluated as the instantaneous phase of

Table 3.1: Specification of 2 datasets used in the experiments.

Dataset	Acoustic pressure [kPa]	Number of acquisitions	TX Frequencies (min:max - step) [MHz]
P_1	49	6	2 : 4 - 0.5
P_2	62	43	

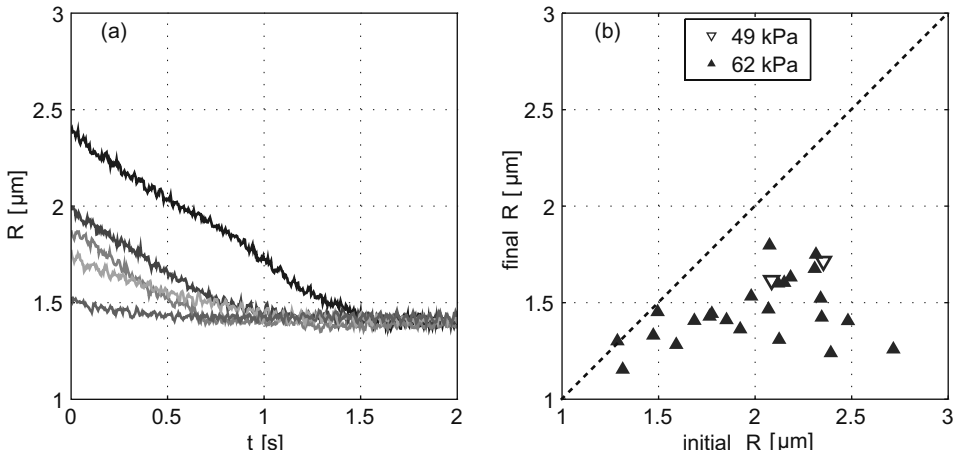

Figure 3.2: a) Radius as function of time for 5 different bubbles exposed to the P_2 pulse sequence; b) Final radius vs. initial radius of P_1 and P_2 datasets (see Table 3.1).

the complex demodulated samples selected in the central part of each echo signal. The *absolute echo phase* values can then be estimated by combining the information obtained through the analysis of multiple bubbles of a same population, as explained in detail in Sec. 3.3.3.

3.3 Experiments

3.3.1 Deflation analysis

About 50 microbubbles with arbitrary initial radii were studied. About 30% of the bubbles either moved out of the ROI before the end of the experiment, or maintained a stable equilibrium radius over subsequent PRIs. Bubbles in the latter group typically had radii larger than 3 µm.

The remaining bubbles exhibited similar behavior. Typically, a gradual bubble size reduction was observed: the bubbles initially showed slow deflation, which accelerated in the intermediate range. At the end of the deflation process, the deflation stopped and the bubbles assumed a "final" stable size which was maintained independent of further insonation.

Fig. 3.2a illustrates the final part of radius-time curves measured for different bubbles excited by the 62 kPa pulse sequence P_2. Fig. 3.2b reports the final stable radii vs. the initial radii measured for the two collected data-sets. Independent of the initial radius, the final radius was 1.44 ± 0.17 µm (0.4 correlation coefficient).

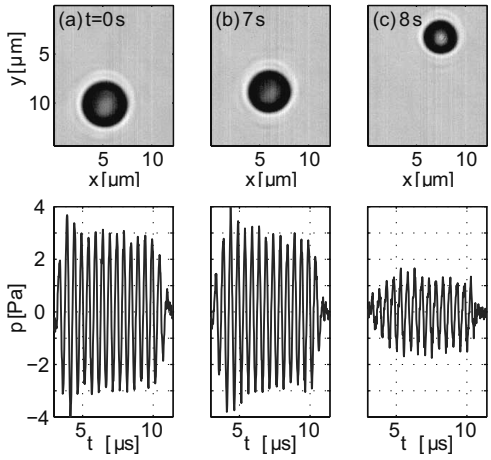

Figure 3.3: Images (top) and corresponding full echoes (bottom) of a deflating Definity bubble recorded at different times. The bubble was insonified at 250 Hz PRF for about 10 s by the sequence P_1. These results, in particular, show the bubble response to the 2 MHz TX frequency.

3.3.2 Single-frequency analysis

Although all the experiments were made using multiple-frequency excitation (Table 3.1), it is useful first showing the results obtained by selecting the data at a single-frequency (2 MHz). The analysis related to other frequencies is presented in Sec. 3.3.4.

The deflation of one bubble is exemplified in Fig. 3.3. Three video-frames and the corresponding acoustic echoes of the bubble excited by the 49 kPa sequence are shown. The echo is in response to the 2 MHz excitation pulse. At the start of the excitation ($t = 0$ s, Fig. 3.3a), the bubble has a spherical shape with radius around 2.4 μm. The corresponding echo envelope (Fig. 3.3a, bottom) shows stable amplitude after a transient 2-cycle oscillation.

After about 7 s of insonation (Fig. 3.3b), the bubble has deflated by about 0.2 μm, and the echo exhibits slightly longer rise time followed by a stable amplitude (close to that observed for the previous echo). When the bubble is deflated to about 1.8 μm (Fig. 3.3c), the shape is still spherical, and the backscattered echo is characterized by lower amplitude (about 1.5 Pa) and longer rise time (about 4 cycles). Fig. 3.3 also shows that the observed bubble was displaced due to radiation force. In all experiments the actual displacement was small (few micrometer as observed optically) in comparison with the insonation wavelengths ($> 375\,\mu$m). We may therefore neglect any effect due to the bubble translation.

As described in the previous section, suitable processing of images like those shown in Fig. 3.3 allowed extracting the equilibrium bubble radius, while the echo

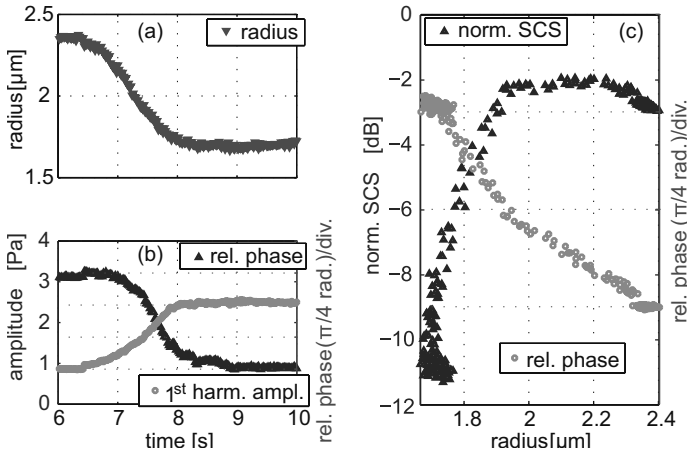

Figure 3.4: Results of the analysis of a Definity bubble insonified by the P_1 sequence, (a) bubble radius vs. time, (b) echo amplitude and relative echo phase vs. time, at 2 MHz insonation, (c) normalized scattering cross-section (SCS, left axis) and phase vs. radius (right axis) at a frequency of 2 MHz.

amplitude and phase were estimated from the full echo-signals (bottom) received in each pulse repetition interval. Fig. 3.4 reports the results of such measurements made between the 6^{th} and the 10^{th} second of the same acquisition interval. Fig. 3.4a shows that the bubble deflated from 2.4 μm down to the minimum radius of 1.7 μm, which was then maintained regardless of further insonation. The curve exhibits a typical sigmoid shape similar to earlier observations for lipid-shelled bubbles [Borden et al., 2005].

As shown in Fig. 3.4b, both the amplitude and phase gradually changed during 2.5 seconds of acquisition, which corresponded to about 600 pulse repetition intervals (PRIs). The echo-amplitude behavior had shape similar to that observed for the radius, with variation between 3 Pa down to about 1 Pa. The echo phase shows a shift of $\pi/2$ radians. These results were obtained from the raw data, with neither averaging nor smoothing.

For the smallest radius, 1.7 μm, the scattered pressure has a level of 1 Pa, which is 3 times lower than that obtained for radii between 2.2 and 2.4 μm. This shows the large size dependency of the scattered pressure. The combination of data shown in Fig. 3.4a and 3.4b allows presenting the experimental normalized SCS (as defined in Eq. 3.1) and phase versus the bubble radius (Fig. 3.4c). The normalized SCS shows a broad peak centered at a radius of about 2.2 μm, which corresponds to the 2 MHz resonant size (note that we use the definitions given in [Khismatullin and Nadim, 2002] for the undamped natural frequency, damped frequency, and resonance frequency of a microbubble). Furthermore, the maximum level is -2 dB. Since this value

can be interpreted as the scattering strength, the microbubble scatters the ultrasound with a relative power of 63% compared to a geometrically scattering particle of the same size. Microbubbles are commonly denoted to have a high scattering strength *due to* resonance effects, but these results suggest that the scattering strength of a microbubble is low, even at resonance. A general cause for low scattering would be a large damping of the oscillation, which could also cause the observed broadening of the resonance peak (see for a theoretical example [Leighton, 1994, its Fig. 4.4]). Note that Sijl et al. [2008] report similar scattering strength for another type of phospholipids coated microbubbles (BR14, Bracco Research S.A., Geneva), but they did not observe resonance behavior.

The observed phase shift ranges over 0.5 π radians in the size range 1.7 – 2.4 μm. This phase is the relative phase difference between the excitation wave and the radial oscillation, and the results shown here actually proof that the microbubble is a resonant system. The phase decreases with increasing microbubble size, consistent with theory [Leighton, 1994]. Moreover, in this size range the phase varies linearly with radius, which could also be explained by strong damping.

Fig. 3.5 combines the results obtained for 16 microbubbles excited with the 62 kPa sequence, evaluated at the TX frequency of 2 MHz. Twenty-seven out of the 43 experiments were discarded because of absence of deflation (17 bubbles), fast bubble movements capable of significantly affecting the acoustical response (3 bubbles) and because of residual limitations (7 bubbles), such as acoustic interferences, bubble sticking to the wall, and misalignment issues. The initial radius of remaining bubbles was between 1.3 and 2.7 μm, while the final radius was in a range compressed around 1.4 μm (*cf.* Fig. 3.2b).

All bubbles exhibited similar echo-amplitude behavior, despite their different initial radius and covered radius intervals. The normalized SCS clearly exhibits two regions with different trends: for radius larger than 2.2 μm it slowly decreases with increasing radius, while for radius smaller than 1.7 μm the normalized SCS shows more than 30 dB/μm slope. In the same graph, a regression curve with relative confidence bounds (calculated on linearly-scaled data and represented on logarithmic scale) were added. This curve has been computed by a local weighted linear least-square regression method, using a linear polynomial ("Lowess" smoothing in MATLAB ©) with a relative span of 0.5. The confidence interval was derived from the sum of squared errors using the same weight and sliding of the smoothing process. The resulting average deviations are 6.1 dB and 2.6 dB for the upper and the lower bounds, respectively.

3.3.3 Phase analysis

The phase relation between the radial oscillation and the US pressure wave indicates the regimes of bubble oscillation, it is therefore a useful parameter to detect

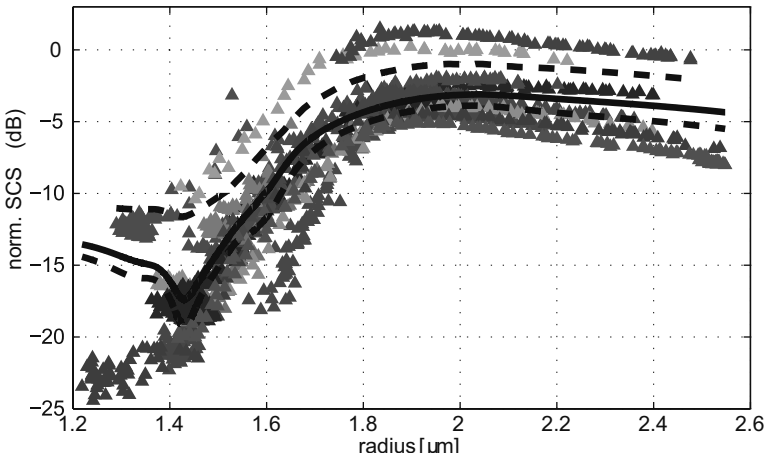

Figure 3.5: 2 MHz normalized SCS of 16 bubbles excited with the P_2 sequence. A regression curve is over-imposed (continuous line) with confidence bounds (dotted lines).

resonance effects (as also suggested by van der Meer et al. [2007, its Sec. II.C]). In particular, a phase lag of $\pi/2$ radians indicates an excitation at the undamped natural frequency. The radius where this occurs can be compared to the resonant radius (i.e., where the normalized SCS is maximum) to evaluate the magnitude of the damping. As will be shown, it is difficult to accurately estimate the sizes corresponding to the undamped natural frequency and resonance, but the results can still provide a qualitative estimate of the significance of damping.

The coherence of the BBT system TX and RX operations allows determining the changes in the echo phase. Although a direct estimation of the "absolute" phase between the driving pressure and the echo is not available (see Sec. 3.4.1), its indirect estimate was possible through the following procedure.

First, the offset of each phase curve was adjusted to minimize the squared differences in the overlapping regions. Second, a local regression curve was obtained using the same technique described above. Then the 'absolute' offset for this composite curve was estimated by one of the two following criteria:

1. If the slope of the phase curve at the largest radius is low, it suggests that such radius is much larger than resonant: the phase at that point is set to $-\pi$ radians.

2. If the slope at the largest radius is non negligible, the phase value corresponding to the maximum slope is set to $-\pi/2$, according to resonant system theory [Leighton, 1994].

3. Fig. 3.6 shows the absolute echo phase responses and the regression curve obtained with the same data-set used in Fig. 3.5. It is seen that the slope at

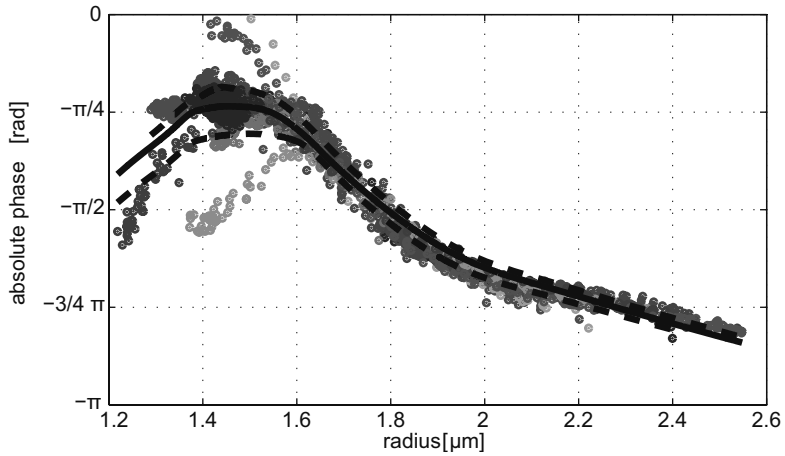

Figure 3.6: 2 MHz phase responses of the same bubbles considered in Fig. 3.5. A regression curve (continous line) and the confidence bounds (dotted lines) are over-imposed.

2.5 μm is not zero, preventing application of the first criterion described above. Hence, the second criterion was adopted, and the phase at radius of 1.7 μm, where the curve shows the steepest slope, was set to $-\pi/2$ radians.

3.3.4 Multiple-frequency analysis

Since we used an excitation sequence with five different TX frequenties, the normalized SCS and phase behavior were also extracted from the responses to the 2.5, 3, 3.5, and 4 MHz pulses. Fig. 3.7 shows the results obtained at all frequencies. For clarity of presentation, raw data is omitted and only the regression curves are shown.

The normalized SCSs (Fig. 3.7 left panels) reveal a peak at a radius which is larger than 2 μm at 2 MHz, and smaller than 1.8 μm at 4 MHz. The SCS overall excursion is in the range 10 – 20 dB, with typically larger values at lower frequencies. The confidence bounds are close to the regression curves especially when the SCS is high, except at 2.5 MHz where the confidence interval is over 6 dB also in the highest value range.

The phase regression curves (right panels in Fig. 3.7 reveal a clear trend: at all frequencies, the overall phase excursion is larger than $\pi/2$ radians, covering about $\frac{3}{4}\pi$ radians at 2.5 MHz. At 2.5, 3, 3.5 and 4 MHz frequency, the slope is low at the largest radii and, according to the criteria described earlier, the phase at largest radius was set to $-\pi$ radian (first criterion), while the 2 MHz curve was set to $-\pi/2$ rad (second criterion). The bubble radius corresponding to the undamped natural frequency [Khismatullin and Nadim, 2002], producing $\pi/2$ phase lag [van der Meer

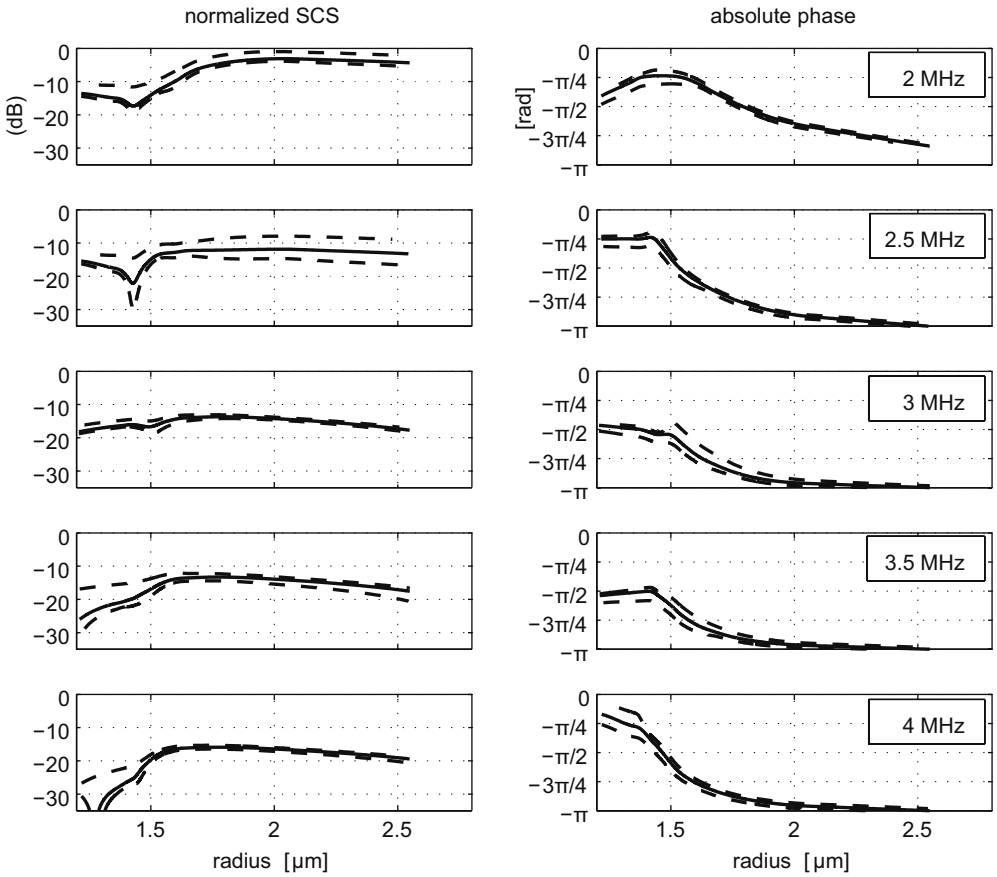

Figure 3.7: Normalized SCS (left) and phase (right) regression curves evaluated over 16 bubbles excited (from top to bottom) at 2, 2.5, 3, 3.5, 4 MHz, by the sequence P_2.

et al., 2007; Hilgenfeldt et al., 1998], decreases with increasing frequency, from about 1.8 μm at 2 MHz to 1.4 μm at 4 MHz.

3.4 Discussion

3.4.1 Experimental uncertainties

Insonifying phospholipids coated microbubbles with 2 – 4 MHz ultrasound pulses at 49 or 62 kPa pressure amplitude led to slow deflation of the microbubbles. At 250 Hz PRF, it typically covered an interval of several seconds, enabling dense sampling of the phenomenon. The current setup satisfied the requirement of large memory buffers to store the bubble echoes and images during the full deflation process.

The radius, echo amplitude and phase were directly extracted from the raw data without averaging between subsequent images / US pulses. This was possible thanks to an ultra low-noise receiver, designed for this application, combined with a sensitive transducer. In the echo-signals received from very small bubbles (1.2 μm radius) the S/N was estimated a value around 11 dB.

The accurate system calibration is demonstrated by the good agreement between estimated and experimental received pressure. As a reference, assuming linear scattering theory in inertial regime [Leighton, 1994], the pressure level scattered by a 2.3 μm radius microbubble excited by 49 kPa pulses, is 4.5 Pa at 25 mm distance: such value is close to that reported (3 Pa) in Fig. 3.3.

Compared to the approaches used in other bubble characterization studies in which differently sized bubbles are subsequently observed [Sijl et al., 2008], a same bubble with varying radius was considered in the current study. It is implicitly assumed that bubble acoustical or structural properties do not depend on the initial size. This might not always be true, though results like those shown in Figs. 3.5 – 3.7 seem not to suggest significant changes. The hypothesis is further corroborated by the observation that bubbles with different initial size subjected to the same type of US excitation show similar deflation profiles (see, e.g., Fig. 3.2b), and similar acoustical responses (Figs. 3.5 – 3.7)

This similarity is helpful for the absolute phase computation. The measured phase is intended as "relative" and not absolute, because the latter is affected by factors such as initial bubble position, transducer-fibre alignment, water bath temperature, etc. A phase offset adjustment was thus necessary to remove this phase bias when estimating the "absolute" phase curves from multiple experiments. Ideally the phase curve covers $[0, -\pi]$ radians if the bubbles have negligible damping, and when they are deflating from well above resonance to well below resonance [Leighton, 1994]. However, the measured phase curves showed less than π variation, expected to be caused by both damping and a finite deflation range. Therefore,

the availability of echo data from multiple bubbles behaving similarly helped in the enlargement of the covered range.

Due to buoyancy the bubbles float against the upper fiber wall, and stay in contact, as confirmed by the in-focus sequence of images (see Fig. 3.3). This capillary wall proximity was surely not ideal. since it could change the bubble behavior in terms of oscillation shape [Zhao et al., 2005; Vos et al., 2008], amplitude [Zhao et al., 2005; Caskey et al., 2006; Garbin et al., 2007], and resonance [Overvelde et al., 2007]. The influence of these effects could not be estimated in the current study.

Due to radiation force [Dayton et al., 2002; Vos et al., 2007] the microbubbles were slightly displaced parallel to the wall. However, some bubbles visibly remained still. Such sticking effect is not understood, although it has been frequently observed in similar optical studies with the cellulose capillary fibre, also for nondeflating bubbles (from experience in the past years in the labs).

Since the experimental procedure was such that the time between agent extraction from the vial and the actual recording could last from few minutes up to one hour, air could have been dissolved from the bulk into the microbubbles. Such diffusion would result in an initial growth of the microbubbles (since air diffusivity is much larger than that of perfluorocarbon). However the microbubbles are not monitored during the dilution after extraction from the vial and such possible growth could not be observed.

Finally, although a single bubble was visible in the inspected ROI, the possible presence of bubbles close to - but out of - the ROI could not be excluded. When such a presence was clearly revealed in the echo, the related acquisition was discarded but, in general, an undesired interference by proximal bubbles was always possible.

3.4.2 Results: deflation phenomenon

Most observed bubbles exhibited a similar deflation behavior, consisting of a gradual size reduction upon insonification which stopped when the bubble achieved a final steady-state condition. This happened for all bubbles with initial radius between 2.7 μm and 1.3 μm, while larger bubbles needed higher TX power to start deflating or did not react at all.

The TX frequency range was selected to include the resonance frequencies of bubbles with diameter within the mean range of the Definity population. Each TX pulse was long enough to allow neglecting transient effects. A low pulsing frequency was used to extinguish possible transient oscillations due to the previous TX pulse. The PRF was, however, high enough to avoid the influence of slow changes of bubble properties due to natural dissolution [Borden and Longo, 2002; Pu et al., 2006].

During deflation the coating of the bubble can experience significant changes, such as folding, disruption of monomolecularity, and shedding of material through

vesicles and micelles [Borden and Longo, 2002; Pu et al., 2006]. However, we often found that the bubbles deflated maintaining a spherical shape (see, e.g., Fig. 3.3). This behavior is consistent with observations reported in Borden and Longo [2002].

The sigmoid behavior visible in, e.g., Fig. 3.4a is in accordance with the results shown by Borden et al. [2005]. The range of radii of accelerated dissolution corresponds to the region around resonance, where radial oscillations are highest, and gas pressure fluctuation inside the microbubble is out of phase with the driving US pulse. In such conditions the partial gas pressures at opposite sides of the shell are highest, giving highest potential for gas diffusion. Large oscillations are also expected to increase the rate at which the bubble shell sheds material, increasing the effective surface tension [Lipp et al., 1998; Borden and Longo, 2002; Marmottant et al., 2005; Pu et al., 2005]. Moreover, during the expansion half-cycle of the oscillation, the lipid coating concentration might be too low to cover the full bubble surface [Marmottant et al., 2005; Pu et al., 2005], thus diminishing its resistance to dissolution. Comparison of the 2 datasets suggests that the size of the stable final radius was influenced by the excitation amplitude. This dependency is supported by the analysis of other datasets (not reported here) with excitation pressures in the range 49 – 170 kPa. In general, the higher the pressure, the smaller the final radius.

The fact that the stable final radius did not depend on the initial value (see Fig. 3.2) also suggests that lipid molecules are shed during the deflation. On the other hand, the existence of a stable radius might be hypothesized to originate from a dense packing of the phospholipids molecules at the surface, thus both increasing the resistance to diffusion and reducing the surface tension [Marmottant et al., 2005; Pu et al., 2005]. The lower radial excursion of small bubbles might not be able to force the shedding.

3.4.3 Results: acoustic response

The echo changes during deflation (see Fig. 3.3). At the larger initial size (left frame) the echo exhibits the highest amplitude and quasi sinusoidal oscillations while, when the bubble is deflated (right frame), the amplitude decreases and nonlinear contributions can be recognized. After a partial deflation (centre frame) the echo amplitude is similar to that obtained at larger bubble size. This demonstrates the nonlinear relation between geometrical and scattering cross-section, which is recognized in Fig. 3.4 comparing the echo amplitude and radius curves, emphasized in Fig. 3.4c through the normalization. Here the maximum normalized scattering is not obtained at the maximum bubble size, but at resonance. Comparison with the results reported by Sijl et al. [2008] shows that the longtime response of deflating bubble does not significantly differ from the response of single bubbles of different constant sizes.

The curves represented in Figs. 3.5 and 3.6 obtained from 16 different bubbles

highlight a similar behavior, as confirmed by the narrow confidence intervals. The small differences between the individual curves (up to 6 dB at 2.5 MHz) are consistent with previous studies showing that phospholipids coated microbubbles with equal size show different acoustic behavior [Dayton et al., 2002; de Jong et al., 2007; Sijl et al., 2008]. Heterogeneity of phospholipids packing in different bubbles of the same population [Borden et al., 2005; Pu et al., 2006] might have contributed to the observed differences. Moreover the phase regression curves are surely affected by the uncertainty coming from the re-combination of the different curves.

The results shown in Figs. 3.5 – 3.7 suggest that the chosen frequency range is sufficient to consider the resonant behavior of the bubbles. For each transmitted frequency, two different resonant radii can be identified, based on the analysis of the echo-amplitude and of the relative echo phase, respectively, as explained below.

The normalized SCS curves in Figs. 3.5 and 3.7 are nearly constant for large radii (where the bubble is mainly "mass-controlled": inertia dominates the motion [Leighton, 1994]), while it rapidly decays when the bubble shrinks towards the minimum size (the oscillation is mainly "stiffness-controlled": the elastic force dominate the motion [Leighton, 1994]). In between these states ("resistance-controlled" oscillation) the normalized SCS curves show a peak, here defined as the "first harmonic amplitude-resonant" radius.

In the echo phase curves, monotonic behavior within the 0 to $-\pi$ range was observed. The driving frequency is considered coincident with the undamped natural frequency [Khismatullin and Nadim, 2002] when the phase is equal to $-\pi/2$. The radius corresponding to this condition is here defined the *phase-resonant* radius.

Although the measurements may have limited accuracy (especially at smaller bubble radii where the S/N ratio is lower), or may be affected by the subjective criteria used in giving the reference phase value, they show a clear trend. In Fig. 3.7, the amplitude-resonant radii range from about 2 μm at 2 MHz to less than 1.8 μm at frequencies $\geq$ 3 MHz. The phase-resonant radii range from about 1.8 μm at 2 MHz to 1.5 μm at 2.5 MHz and about 1.4 μm at higher frequencies. The difference between these two resonant radii, being in the order of 0.3 μm at 2 MHz, is indicative of significant damping of the oscillation [Khismatullin and Nadim, 2002]. Such damping also explains the absence of visible echo-peaks around resonance, and the slow rate of change of both amplitude and phase curves versus radius [Leighton, 1994].

3.4.4 Clinical implication

The results suggest that if experimental conditions equivalent to those adopted in the current study were used in clinical applications, significant consequences would emerge. Bubbles close to resonance would rapidly shrink and, after prolonged excitation, only bubbles much smaller or much larger than the resonant size

would contribute to the agent detection signal. Accordingly, in fundamental imaging applications, the largest signal is expected to come from larger bubbles, as size seems more important than resonance. This is consistent with findings earlier reported in literature [Bouakaz et al., 1998; Gorce et al., 2000; Sijl et al., 2008].

3.5 Conclusion

Two goals have been simultaneously pursued in this paper. First, the phenomenon of acoustically-induced bubble deflation has been described in detail. A final stable radius was identified that was maintained independent of further insonation. The acoustic response of the deflating bubble was strongly correlated to the instantaneous radius, but not related to the initial radius. Second, it has been shown that a forced decrease of microbubble radius offers a means to contribute to UCA characterization in terms of resonance and damping effects. Significant damping was indirectly shown by the difference of amplitude-resonant and phase-resonant radii, and by the absence of large increase of fundamental-frequency scattering for bubbles around resonance.

Future work will be directed to understand the relative importance of microbubble size and other properties in UCA detection schemes. Furthermore, the setup will be integrated with specialized equipment such as an optical tweezer [Garbin et al., 2007], capable of eliminating residual interference by the nearby fiber wall, and with an ultrafast camera [Chin et al., 2003] to simultaneously resolve the radial oscillations of deflating microbubbles optically.

Bibliography

Borden, M. A., D. E. Kruse, C. F. Caskey, S. Zhao, P. A. Dayton, and K. W. Ferrara, "Influence of lipid shell physicochemical properties on ultrasound-induced microbubble destruction," *IEEE Trans Ultrason Ferroelectr Freq Control*, 52(11): pp. 1992–2002, 2005.

Borden, M. A. and M. L. Longo, "Dissolution behavior of lipid monolayer-coated, air-filled microbubbles: Effect of lipid hydrophobic chain length," *Langmuir*, 18(24): pp. 9225–9233, 2002.

Bouakaz, A., N. de Jong, C. Cachard, and K. Jouini, "On the effect of lung filtering and cardiac pressure on the standard properties of ultrasound contrast agent," *Ultrasonics*, 36(1-5): pp. 703–708, 1998.

Caskey, C. F., P. A. Kruse, Dustin E. Dayton, T. K. Kitano, and K. W. Ferrara, "Microbubble oscillation in tubes with diameters of 12, 25, and 195 microns," *Appl Phys Lett*, 88: p. 033902, 2006.

Chetty, K., E. Stride, C. A. Sennoga, J. V. Hajnal, and R. J. Eckersley, "High-speed optical observations and simulation results of SonoVue microbubbles at low-pressure insonation," *IEEE Trans Ultrason Ferroelectr Freq Control*, 55(6): pp. 1333–1342, 2008.

Chin, C. T., C. T. Lancée, J. M. G. Borsboom, F. Mastik, M. E. Frijlink, N. de Jong, M. Versluis, and D. Lohse, "Brandaris 128: A 25 million frames per second digital camera with 128

highly sensitive frames," *Rev Sci Instr*, 74(12): pp. 5026–5034, 2003.

Dayton, P. A., J. S. Allen, and K. W. Ferrara, "The magnitude of radiation force on ultrasound contrast agents," *J Acoust Soc Am*, 112(5): pp. 2183–2192, 2002.

Dayton, P. A., K. E. Morgan, A. L. Klibanov, G. H. Brandenburger, and K. W. Ferrara, "Optical and acoustical observations of the effects of ultrasound on contrast agents," *IEEE Trans Ultrason Ferroelectr Freq Control*, 46(1): pp. 220–232, 1999.

de Jong, N., M. Emmer, C. T. Chin, A. Bouakaz, F. Mastik, D. Lohse, and M. Versluis, ""compression-only" behavior of phospholipid-coated contrast bubbles," *Ultrasound Med Biol*, 33(4): pp. 653–656, 2007.

de Jong, N., L. Hoff, T. Skotland, and N. Bom, "Absorption and scatter of encapsulated gas filled microspheres: Theoretical considerations and some measurements," *Ultrasonics*, 30(2): pp. 95–103, 1992.

Doinikov, A. A. and P. A. Dayton, "Maxwell rheological model for lipid-shelled ultrasound microbubble contrast agents," *J Acoust Soc Am*, 121(6): pp. 3331–3340, 2007.

Emmer, M., A. van Wamel, D. E. Goertz, and N. de Jong, "The onset of microbubble vibration," *Ultrasound Med Biol*, 33(6): pp. 941–949, 2007.

Garbin, V., D. Cojoc, E. Ferrari, E. Di Fabrizio, M. L. J. Overvelde, S. M. van der Meer, N. de Jong, D. Lohse, and M. Versluis, "Changes in microbubble dynamics near a boundary revealed by combined optical micromanipulation and high-speed imaging," *Appl Phys Lett*, 90: p. ref. 114103, 2007.

Gorce, J.-M., M. Arditi, and M. Schneider, "Influence of bubble size distribution on the echogenicity of ultrasound contrast agents - A study of SonoVue," *Invest Radiol*, 35(11): pp. 661–671, 2000.

Guan, J. and T. J. Matula, "Using light scattering to measure the response of individual ultrasound contrast microbubbles subjected to pulsed ultrasound *in vitro*," *J Acoust Soc Am*, 116(5): pp. 2832–2842, 2004.

Guidi, F., E. Boni, P. Tortoli, M. Arditi, and P. Frinking, "Acoustic method for real-time visualization of microbubble movements and rupture," in proc. IEEE Ultras Symp, vol. 2, pp. 1183–1186, 2003.

Hilgenfeldt, S., D. Lohse, and M. Zomack, "Response of bubbles to diagnostic ultrasound: a unifying theoretical approach," *Eur Phys J B, Condensed Matter Phys*, 4(2): pp. 247–255, 1998.

Khismatullin, D. B. and A. Nadim, "Radial oscillations of encapsulated microbubbles in viscoelastic liquids," *Phys Fluids*, 14(10): pp. 3524–3557, 2002.

Leighton, T. G., The Acoustic Bubble, Academic Press, London, UK, 1994.

Lipp, M. M., K. Y. C. Lee, D. Y. Takamoto, J. A. Zasadzinski, and A. J. Waring, "Coexistence of buckled and flat monolayers," *Phys Rev Lett*, 81(8): pp. 1650–1653, 1998.

Marmottant, P., S. M. van der Meer, M. Emmer, M. Versluis, N. de Jong, S. Hilgenfeldt, and D. Lohse, "A model for large amplitude oscillations of coated bubbles accounting for buckling and rupture," *J Acoust Soc Am*, 118(6): pp. 3499–3505, 2005.

Morgan, K. E., J. S. Allen, P. A. Dayton, J. E. Chomas, A. L. Klibanov, and K. W. Ferrara, "Experimental and theoretical evaluation of microbubble behavior: Effect of transmitted phase and bubble size," *IEEE Trans Ultrason Ferroelectr Freq Control*, 47(6): pp. 1494–1509, 2000.

Overvelde, M. L. J., V. Garbin, B. Dollet, D. Cojoc, E. Ferrari, N. de Jong, E. Di Fabrizio,

D. Lohse, and M. Versluis, "3D optical micromanipulation of ultrasound contrast agents: bubble-wall and bubble-bubble interactions," in proc. Int Congr Acoust, Madrid, Spain, 2007.

Pu, G., M. A. Borden, and M. L. Longo, "Collapse and shedding transitions in binary lipid monolayers coating microbubbles," *Langmuir*, 22: pp. 2993–2999, 2006.

Pu, G., M. L. Longo, and M. A. Borden, "Effect of microstructure on molecular oxygen permeation through condensed phospholipid monolayers," *J Am Chem Soc*, 127(18): pp. 6524–6525, 2005.

Ricci, S., E. Boni, F. Guidi, T. Morganti, and P. Tortoli, "A programmable real-time system for development and test of new ultrasound investigation methods," *IEEE Trans Ultrason Ferroelectr Freq Control*, 53(10): pp. 1813–1819, 2006.

Sijl, J., E. Gaud, P. J. Frinking, M. Arditi, N. de Jong, D. Lohse, and M. Versluis, "Acoustic characterization of single ultrasound contrast agent microbubbles," *J Acoust Soc Am*, 124(6): pp. 4091–4097, 2008.

Sijl, J., H. J. Vos, N. de Jong, D. Lohse, and M. Versluis, "Combined optical and acoustical characterization of individual US contrast microbubbles," in proc. Int Congr Acoust, Madrid, Spain, 2007.

Stride, E., "The influence of surface adsorption on microbubble dynamics," *Phil Trans R Soc A*, 366(1873): pp. 2103–2115, 2008.

Sun, Y., D. E. Kruse, P. A. Dayton, and K. W. Ferrara, "High-frequency dynamics of ultrasound contrast agents," *IEEE Trans Ultrason Ferroelectr Freq Control*, 52(11): pp. 1981–1991, 2005.

Tang, M.-X. and R. J. Eckersley, "Frequency and pressure dependent attenuation and scattering by microbubbles," *Ultrasound Med Biol*, 33(1): pp. 164–168, 2007.

Thomas, D. H., M. B. Butler, T. Anderson, R. Steel, S. D. Pye, M. Poland, T. Brock-Fisher, W. N. McDicken, and V. Sboros, "Single microbubble response using pulse sequences: Initial results," *Ultrasound Med Biol*, 35(1): pp. 112–119, 2009.

Tsiglifis, K. and N. Pelekasis, "Nonlinear radial oscillations of encapsulated microbubbles subject to ultrasound: The effect of membrane constitutive law," *J Acoust Soc Am*, 123(6): pp. 4059–4070, 2008.

van der Meer, S. M., B. Dollet, M. M. Voormolen, C. T. Chin, A. Bouakaz, N. de Jong, M. Versluis, and D. Lohse, "Microbubble spectroscopy of ultrasound contrast agents," *J Acoust Soc Am*, 121(1): pp. 648–656, 2007.

van Neer, P. L. M. J., G. Matte, J. Sijl, J. M. G. Borsboom, and N. de Jong, "Transfer functions of US transducers for harmonic imaging and bubble responses," *Ultrasonics*, 46(4): pp. 336–340, 2007.

Vos, H. J., B. Dollet, J. G. Bosch, M. Versluis, and N. de Jong, "Nonspherical vibrations of microbubbles in contact with a wall - A pilot study at low mechanical index," *Ultrasound Med Biol*, 34(4): pp. 685–688, 2008.

Vos, H. J., F. Guidi, E. Boni, and P. Tortoli, "Method for microbubble characterization using primary radiation force," *IEEE Trans Ultrason Ferroelectr Freq Control*, 54(7): pp. 1333–1345, 2007.

Zhao, S., K. W. Ferrara, and P. A. Dayton, "Asymmetric oscillation of adherent targeted ultrasound contrast agents," *Appl Phys Lett*, 87: p. ref. 134103, 2005.

Chapter 4

Simultaneous optical and acoustic recording of the dynamics of a single ultrasound contrast microbubble

Abstract - **A full understanding of the contrast enhancing abilities of microbubbles in ultrasound imaging, targeted drug delivery with microbubbles, and enhanced drug uptake by using ultrasonically driven microbubbles starts with studying both optically and acoustically the response of a single microbubble subjected to ultrasound. In this chapter, single isolated ultrasonically-driven microbubbles are imaged with an ultra-high speed camera (recording up to $25 \cdot 10^6$ frames per second). The sound emission is recorded simultaneously with a calibrated single element transducer. We show that the sound emission can be predicted from the optically-recorded radial dynamics, and vice versa, that the radial dynamics can be determined from the remotely recorded acoustic response.**

In preparation for submission to the Journal of the Acoustical Society of America, 2009, by J. Sijl, H. J. Vos, T. Rozendal, N. de Jong, D. Lohse and M. Versluis, "Combined optical and acoustical characterization of single ultrasound contrast microbubbles". We thank Dr. B. Dollet, M. Overvelde, Dr. V. Garbin and Dr. S. van der Meer (University of Twente) for very fruitful discussions. Bracco Research S.A., Geneva, Switzerland, is acknowledged for kindly providing the experimental contrast agent BR-14.

4.1 Introduction

Microbubbles are used as contrast agents for medical ultrasound imaging [Lindner, 2004]. With a mean bubble radius between 1 and 5 μm the bubbles are resonant scatterers at typical medical ultrasound frequencies of 1 to 6 MHz. The bubbles scatter ultrasound more efficiently than a solid particle of the same size, at up to nine orders of magnitude, owing primarily to the compressibility of their gas. In addition, microbubbles scatter ultrasound nonlinearly at harmonic frequencies of the driving frequency. The nonlinear acoustic response of the bubbles allows for a discrimination from the quasi-linear tissue echo, thereby improving the contrast-to-tissue ratio and forming the basis for the development of harmonic imaging methods, including power modulation imaging [Mor-Avi et al., 2001], and pulse inversion imaging [Hope Simpson et al., 1999].

A driving pressure pulse forces microbubbles into a pulsation which in turn converts into an acoustic response in the far field, the echo. The final acoustic response thus depends strongly on the linear and nonlinear dynamics of the microbubbles. Small radial excursion leads to a radial response that depends linearly on the driving pressure, but larger excursion leads to a nonlinear relation [de Jong et al., 2002]. Common equations to describe the radial dynamics are based on the Rayleigh-Plesset equation, which is an ordinary nonlinear differential equation. In linearized form, i.e., for small radial excursions, it takes the analytical form of a harmonic oscillator [van der Meer et al., 2007].

Microbubbles have a limited lifetime as a result of the capillary pressure (related to surface tension and radius) which gives rise to a partial pressure difference inside and outside the microbubble. The capillary pressure which is of the order of the atmospheric pressure thus reduces the time of dissolution of the bubble to several milliseconds. In order to stabilize clinical microbubbles the interface is coated with a protein, lipid, or polymer layer. The coating resists gas diffusion an decreases surface tension. In addition, gas exchange to the surrounding liquid is reduced by the choice of a low-solubility gas, such as perfluorocarbon or sulfurhexafluoride.

The coating has a pronounced effect on the bubble dynamics. The dilatational viscous properties of the shell material result in an overall damping of the oscillation, while the elasticity of the shell material results in an increase of the resonance frequency [de Jong et al., 2002]. Moreover, the viscoelastic properties can be nonlinear which adds to the intrinsic nonlinear features of the bubble dynamics. The Rayleigh-Plesset equation can be modified to model the contributions of the shell. The viscoelastic properties are then captured in a set of shell parameters, which values can be determined experimentally. A possible experimental approach would be to optically record the radial dynamics of a microbubble subjected to ultrasound, from which the shell parameters are extracted by comparing the experimental curves with those of the theoretical predictions [van der Meer et al., 2007].

The acoustic emission of the bubble directly follows from the radial dynamics. The conversion from energy of the flow around the pulsating bubble into acoustic energy depends on the geometrical size of the bubble, and the velocity and the acceleration of the bubble wall. For larger radial excursions this conversion can enhance the nonlinear higher harmonic contributions to the acoustic response. The total nonlinear acoustic response of the bubble therefore originates from a combination of the intrinsic nonlinear contributions of the bubble dynamics, coupled to those of the nonlinear shell properties and the transformation of the radial dynamics into acoustic energy in the far field.

Since the efficacy of many contrast detection schemes depends on nonlinear signals, it is worthwhile to investigate the significance of each contribution. The influence of nonlinear shell properties has been extensively studied theoretically and experimentally by e.g. Marmottant et al. [2005]; Doinikov and Dayton [2007]; Emmer et al. [2007]; Sijl et al. [2008]; Stride [2008]; Emmer et al. [2009]. The conversion from radial excursion to the scattered sound wave has had far less attention. Although a theoretical derivation exists based on the equation of motion and energy-conservation laws [Leighton, 1994; Hilgenfeldt et al., 1998], microbubbles may not comply to the assumptions made in the derivation. Studying the significance of the conversion therefore needs recordings of both the radial response $R(t)$ and the resulting acoustic response $P(t)$ of a microbubble. The Rayleigh-Plesset equation for example assumes the bubble to be isolated in an infinite medium and the bubble to remain spherical at all times. From *in vitro*, *ex vivo* and *in vivo* studies it is know that bubbles are located in confined geometries which lead to interactions with adjacent walls [Lindner et al., 2002; Zhao et al., 2005; Vos et al., 2008; Caskey et al., 2007]. Neighboring bubbles are acoustically coupled. For molecular imaging applications microbubbles are targeted to diseased cells through ligands introducing complex biomolecular interactions. Many of these interactions lead to nonspherical bubble oscillations and *a priori* it is not known how these translate into the acoustic response. Vice versa it would be important to know if and how the radial dynamics could be inferred from the measured acoustic response. This reverse calculation is nontrivial and to our knowledge has never been done in the context of ultrasound contrast agents.

Here we present a detailed experimental investigation of the different contributions to the overall acoustic response of coated microbubbles. We employ the ultra-high speed camera Brandaris 128 to resolve the radial dynamics of a single microbubble and combine the results with a sensitive and calibrated acoustic setup to quantitatively assess its acoustic response. Through this combined setup we can monitor both the bubble dynamics and the emitted sound and we can verify to what degree these two types of signals correspond to each other. The data are also used to investigate if it is possible to predict the radial dynamics of the bubble explicitly

from its acoustic signature and resting radius.

4.2 Theory

The acoustic response of a coated microbubble to a driving pressure pulse is determined in two steps. Both steps are schematically shown in Fig. 4.1. The first step determines the bubble dynamics as a response to the driving pressure pulse. In the case of volumetric oscillations, the dynamics of the bubble is completely described by the radius time curve, $R(t)$. The radius-time curve can be recorded optically with ultra-high speed imaging [Chin et al., 2003]. For an uncoated bubble the relation between the driving pressure and the dynamics is well described by the Rayleigh-Plesset equation (see below). According to the Rayleigh-Plesset equation the dynamics of a bubble is determined by the initial radius of the bubble, R_0, the driving pressure amplitude and its frequency. The Rayleigh-Plesset equation is nonlinear, and it can introduce higher harmonics into the dynamic response of a microbubble. The shell of an ultrasound contrast agent microbubble introduces even more nonlinearities to the dynamic response. According to the model of Marmottant et al. [2005] these additional nonlinearities can be accounted for by three shell parameters: the shell viscosity, the shell elasticity, and the initial surface tension of the microbubble $\sigma(R_0)$.

The second step, which is of main importance for contrast-enhanced ultrasound imaging, describes how the radial dynamics of the bubble converts into an acoustic response at a certain distance, r, from the bubble. Conservation of mass and momentum in the liquid completely determine this step. Moreover, this step changes the nonlinear content of the final acoustic bubble response as will be shown below. Both steps are detailed in the following subsections.

4.2.1 Bubble dynamics

If a bubble experiences a time-varying pressure field (such as an incoming ultrasound wave) it will react with compression or expansion. The kinetic energy supplied to the surrounding liquid should balance the difference between the work performed by the fluid far from the bubble and that at the bubble wall. If we assume the bubble to remain spherical and the liquid to be incompressible the Rayleigh-Plesset equation is obtained [Brenner et al., 2002; Leighton, 1994]:

$$\underbrace{\rho\left(R\ddot{R}+\frac{3\dot{R}^2}{2}\right)}_{\textit{kinetic energy}} = \underbrace{(p_L - p_\infty)}_{\textit{pressure difference}} \tag{4.1}$$

In this equation R, $\dot{R}$, and $\ddot{R}$ describe the radius, the velocity and the acceleration of the bubble wall, respectively. The density of the water is described by $\rho = 10^3$ kg/m^3 and the pressure difference is determined by the pressure in the water at the bubble

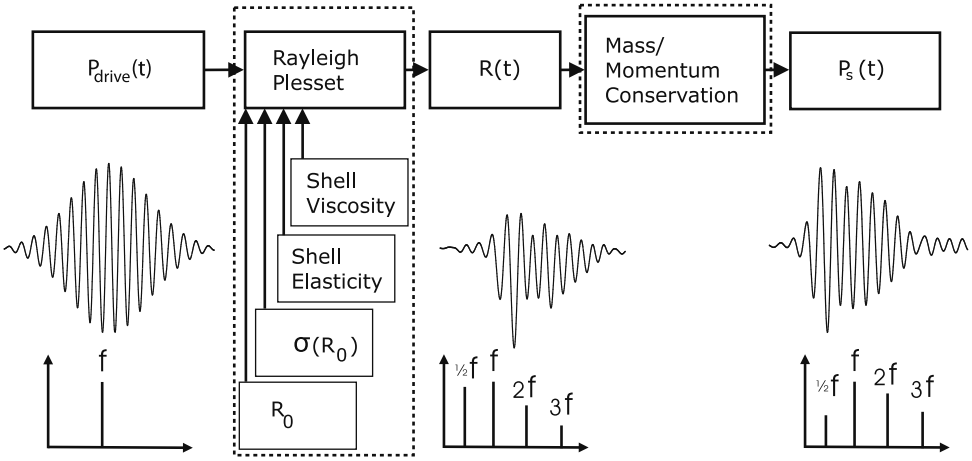

Figure 4.1: A schematic view on the origin and enhancement of the harmonic acoustic responses of an ultrasound contrast agent microbubble to a monotone driving pressure pulse.

wall, p_L , and the pressure far from the bubble wall, p_∞. This equation can be worked out and extended in various ways, for example to include the effect of a coating on the bubble dynamics. A recent version of the equation that accounts for nonlinear elasticity characteristics of a phospholipid coating is provided by Marmottant et al. [2005]:

$$\begin{aligned}
&\rho\left(R\ddot{R}+\frac{3}{2}\dot{R}^2\right)\\
&=\overbrace{\left(P_0+\frac{2\sigma(R_0)}{R_0}\right)\left(\frac{R_0}{R}\right)^{3\gamma}\left(1-\frac{3\gamma\dot{R}}{c}\right)-\frac{2\sigma(R)}{R}}^{p_L}\\
&\underbrace{-4\mu\frac{\dot{R}}{R}-4\kappa_s\frac{\dot{R}}{R^2}}_{p_L}\underbrace{-P_0-P_{\mathrm{A}}(t)}_{p_\infty},
\end{aligned}\tag{4.2}$$

In this equation $c = 1500$ m/s denotes the speed of sound in the water. The initial bubble radius is given by R_0 and the ambient pressure by P_0. The driving pressure pulse is described by $P_{\mathrm{A}}(t)$. The relation between the internal gas pressure (p_g), the gas temperature and bubble volume is described by the polytropic ideal gas law, $p_g \propto R^{-3\gamma}$ where γ is the polytropic exponent. For isothermal oscillations $\gamma = 1$ and for adiabatic oscillations γ is equal to the ratio of the specific heats of the gas inside the bubble, C_p/C_v, with C_p the specific heat at constant pressure and C_v the one at constant volume. In the experiments discussed in this paper we may approximate the oscillations as adiabatic [Marmottant et al., 2005; van der Meer et al., 2007].

For the used experimental agent BR-14 (Bracco Research S.A., Geneva, Switzerland) the gas core consists of perfluorocarbon-gas with $\gamma = C_p/C_v = 1.07$ [Marmottant et al., 2005; van der Meer et al., 2007]. The main damping of the bubble oscillations results from the liquid viscosity $\mu = 1 \cdot 10^{-3}$ Pa·s and the damping introduced by the phospholipid shell described by $\kappa_s = 3 \cdot 10^{-8}$ kg/s [van der Meer et al., 2007]. In the model proposed by Marmottant et al. [2005] the surface tension of the bubble is assumed to depend on the bubble radius, $\sigma(R)$.

The theoretical influence of the nonlinear strain-stress relation of the shell is studied in Ch. 9 (Radial modulation) of this dissertation and is therefore not further addressed in the current Chapter.

4.2.2 Sound emission

The sound emitted by an oscillating microbubble consists of two parts. The first is a passive contribution that results from the geometrical scattering of the microbubble (could also be a non-oscillating body) in the incident ultrasound field and the second is an active contribution that results from the volumetric oscillations of the bubble. In regular applications, ultrasound contrast microbubbles are much smaller than the incident wavelength and the passive contribution can be safely neglected, as shown previously by Hilgenfeldt et al. [1998]. The active contribution is determined by the radial dynamics of the microbubble, described by the radius-time curve $R(t)$. From the conservation of mass and momentum it follows that the emitted pressure wave $P_s(r,t)$, at a distance r, is determined from the second time derivative of the volume V of the bubble,

$$P_s(r, t - r/c) = \frac{1}{4\pi}\frac{\rho}{r}\ddot{V}(t) = \frac{1}{3}\frac{\rho}{r}\frac{\partial^2}{\partial t^2}[R(t)^3] \tag{4.3}$$

where ρ is the density of the surrounding liquid. The finite time for the pressure wave to travel a distance r from the bubble wall to the transducer surface is accounted for by the term r/c where c again is the speed of sound in the liquid medium. A regularly used form of Eq.4.3 is obtained by rewriting:

$$P_s(r, t - r/c) = \frac{\rho}{r}\left(R(t)^2\ddot{R}(t) + 2R(t)\dot{R}(t)^2\right). \tag{4.4}$$

In the equations it is assumed that the receiver is sufficiently far from the microbubble to neglect the Bernoulli pressure (also referred to as the kinetic wave), which decreases with $1/r^4$ [Vokurka, 1985; Leighton, 1994]. Furthermore, Eq. 4.3 accounts only for volumetric oscillations of the bubble; we will validate later that surface modes do not contribute significantly to the sound emission. Translation of the bubble as a result of the acoustic driving also results in additional sound scattering [Hilgenfeldt et al., 1998; Garbin et al., 2009]. However, this contribution is of the same order as that of the passive contribution and can therefore be safely neglected.

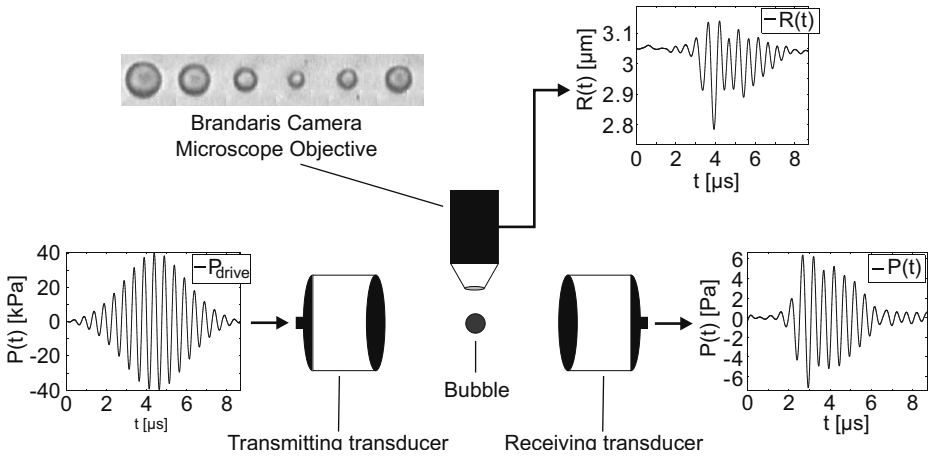

Figure 4.2: A schematic view of the setup. A Gaussian apodized driving pressure waveform was transmitted by a focused transducer. The echo response of the bubble was received by a second focused calibrated transducer. Simultaneously the radial dynamics of the microbubble was recorded through a 100× microscope objective connected to the Brandaris-128 ultra-high speed camera.

Finally, both equations assume an isolated single bubble; the sound emitted from neighboring pulsating bubbles is not taken into account.

4.3 Experimental setup

To investigate the theoretically-derived relations between the radial dynamics of the microbubble and its scattered sound we combine the Brandaris-128 ultra-high speed camera with an acoustic setup capable of quantitatively recording the sound transmitted by a single oscillating microbubble. The contrast agent studied was BR-14, an experimental contrast agent containing microbubbles with a phospholipid shell and a perfluorocarbon-gas core.

The combined setup is schematically shown in Fig. 4.2. It consists of a cylindrical Plexiglas container which was mounted below an upright microscope (BX-FM, Olympus, Tokyo, Japan). Within the container the microbubbles were confined in a 200 µm diameter cellulose capillary tube with an 8-µm wall thickness (Product no. 132294, Spectrum Europe, Breda, the Netherlands). The capillary tube was mounted horizontally in the center of the container.

4.3.1 Single bubble selection

It is not straightforward to ensure that the acoustic response received by the transducers results from a single microbubble. It requires the isolation of the mi-

crobubble with an initial bubble radius of around 2 μm in a volume as large as 2 mm^3 (i.e., dimensions comparable to the wavelength of the ultrasound). We have achieved this with the use of a micropipette. With reference to Fig. 4.3, a microbubble suspension was injected in a small reservoir. On one side the reservoir was connected to a 200 μm diameter cellulose capillary tube that led to the measurement section. This capillary tube entered the bubble reservoir 400 μm below the top surface of the reservoir; this prevented bubbles that are touching the top surface from flowing into the tube. The other side of the bubble reservoir was open to the atmospheric pressure. Capillary forces prevented the solution from flowing out. With a micropipette connected to a syringe we entered the bubble reservoir from the open side. With a 3D-translation stage connected to the pipette, we could move the pipette around inside the reservoir and select a bubble. The micropipette had a tip size of 0.5 μm which is smaller than the typical bubble size. By applying a negative pressure to the pipette we grabbed a single bubble, brought it down, and released it inside the capillary tube [Kim et al., 2003]. With a syringe pump connected to the other side of the capillary tube we moved the bubble through the capillary tube into the measurement section. Note that the bubble remains in the capillary tube during the experiments.

4.3.2 Setup

The radial dynamics of the bubble were recorded with the Brandaris-128 ultra-high speed camera [Chin et al., 2003] coupled to the microscope having a 100× microscope objective (LUMFPL 100×/W, Olympus) which was focused onto the capillary tube. The focal distance of the objective was 1.1 mm. In our measurements we recorded series of 6 movies of 128 frames each at a frame rate near 13 million frames per second (Mfps). The time interval between recordings was 2.5 s. The microbubble was illuminated from below with a high intensity xenon flashlight (MVS 7010 XE, Perkin Elmer, Waltham, MA). A continuous light source (ACE I, Schott, NY) in combination with a single CCD video camera (LCL-902K, Watec, Qwonn) was used to monitor the bubble in between experiments.

To simultaneously record the sound emitted by the oscillating microbubble, the microscope was confocally aligned with two focused transducers. One of the transducers, a 3-MHz center frequency transducer (PA168, PVDF-type, Precision Acoustics Ltd., Dorset, UK) was used to excite the bubble with an ultrasound pulse. The second calibrated transducer (C381-1 inch focus, 3.5 MHz, 100% –6 dB relative bandwidth, Panametrics, Olympus NDT, Waltham, MA) received the acoustic bubble response [Sijl et al., 2008]. The transducers were aligned in the same plane of the capillary tube under an angle of 50° to the capillary tube and at a 100° angle to each other in order to minimize specular reflection of the driving ultrasound on the capillary. Two calibrated 0.2 mm needle hydrophones (Precision Acoustic Ltd., Dorset,

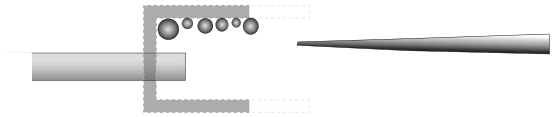

(a) Initial situation

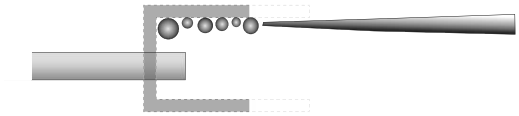

(b) Select a bubble with the micropipet

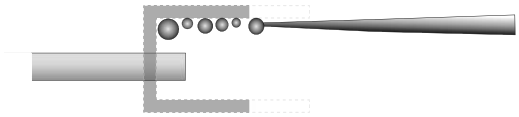

(c) Grab the bubble with the micropipet by applying a negative pressure

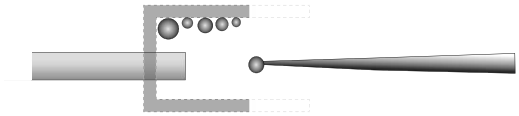

(d) Move the bubble down

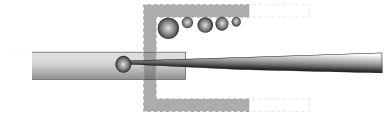

(e) Move the bubble inside the capillary fiber

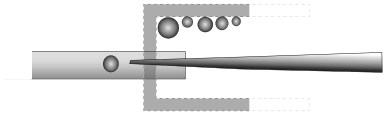

(f) Release the bubble

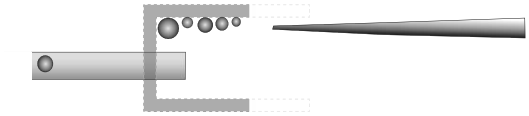

(e) Move micropipet back

Figure 4.3: Schematic view on the bubble selection and isolation method using a translating micropipette.

UK) were mounted in the Plexiglas container exactly opposite to the two transducers. The hydrophones could be moved in and out of the focus of the two transducers and were used to confocally align the two transducers with the microscope objective. The transmit transducer was excited with pulses generated by an arbitrary waveform generator (AWG 8026, Tabor Electronics Ltd., Tel Hanan, Israel) and amplified by a linear power amplifier (350L, ENI, Rochester, NY). The received bubble echoes were amplified 59.3 dB by a low-noise amplifier (AU-1519-10289, Miteq, Hauppauge, NY) and digitized by a digital oscilloscope (TDS 3012, Tektronix, Beaverton, OR). The digitized data were stored on a PC through a GPIB-link for off-line analysis.

4.3.3 Data generation and processing

Gaussian-apodized driving pressure pulses with frequencies ranging from 1 to 4 MHz were used to drive the bubbles. All pulses had a peak negative pressure amplitude of 40 kPa and had a length of 8.9 μs. The optical frames are analyzed to obtain the $R(t)$ curves through a semi-automatic minimum cost algorithm [van der Meer et al., 2007] in MATLAB (The Mathworks, Natick, MA). The acoustically-received voltage *vs.* time curves on the oscilloscope were converted into pressure-time curves using the receive transfer function of the transducer following the procedure described in Sijl et al. [2008]. The setup, including the capillary tube, produces a steady acoustic background signal. For each experiment this background signal was also recorded in the absence of a microbubble and subtracted from the signal recorded in the presence of a microbubble.

Fig. 4.4a shows a typical recording of the responses of an isolated bubble of 3.7 μm radius to pulses with an increasing frequency of 1.7 to 2.7 MHz. The optically-recorded radial response is shown in Fig. 4.4b. At the lowest driving frequency (left hand trace) the bubble follows the driving pressure pulse, although the period-averaged radius shows a decrease during the oscillation, resulting in "compression-only" behavior [de Jong et al., 2007]. At higher driving frequencies the "compression-only" behavior is still visible, but also a strong subharmonic component develops after few cycles of the driving pulse. The amplitude of the radial excursion decreases with increasing frequency, which is expected for bubbles that are driven with frequencies increasingly higher than the resonance frequency. The simultaneously recorded acoustic response (Fig. 4.4c) shows similar envelopes as the driving pulse, and also shows the subharmonic component, although at lesser extent than in the optical data; this effect will be extensively addressed later.

4.4 Results

A total of 16 different microbubbles were studied at different pressures and frequencies resulting in a set of 194 recordings. Depending on the initial bubble radius and the driving frequency a selection of bubbles were observed to oscillate

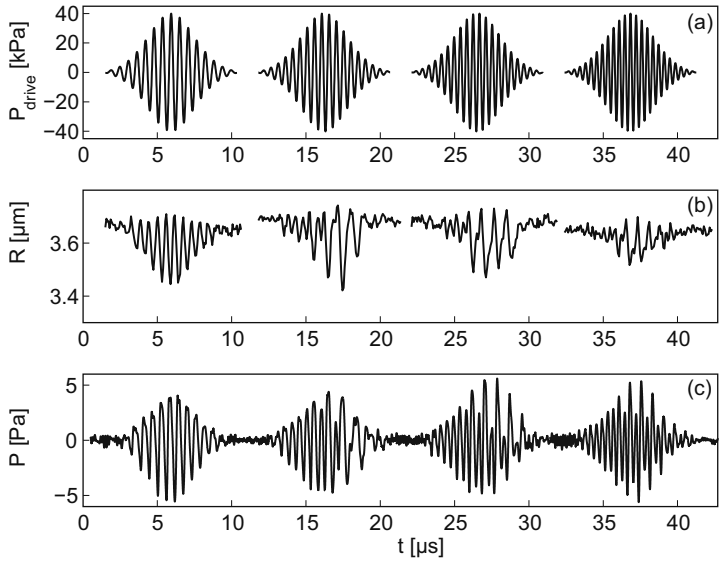

Figure 4.4: A typical example of the simultaneously recorded radial dynamics (b) and acoustic responses (c) of an isolated 3.7 μm bubble. Driving pressure pulses had a frequency of 1.7 MHz, 2 MHz, 2.3 MHz and 2.6 MHz, respectively (a).

linearly, while the other bubbles oscillated nonlinearly, i.e., a nonlinear harmonic or subharmonic component could be identified in the radius-time curve. In section 4.4.1 we will first focus on the linear bubble dynamics at the fundamental frequency. Nonlinear dynamics will be discussed in section 4.4.2.

4.4.1 Linear response

A typical example of the recorded oscillations of a 6.5 μm bubble subject to a 1 MHz, 40 kPa driving pulse is shown in Fig. 4.5a. The camera was recording at a framing rate of 12.5 Mfps. From the absence of harmonics in the spectra of the $R(t)$ curve, shown in Fig. 4.5b, we conclude that the oscillations are linear. As a result of the oscillations of the bubble wall, a spherical acoustic wave travels outward from the bubble. With Eq. 4.3 and the experimentally determined $R(t)$ curve we have calculated the resulting $P_s(t)$. The distance r in Eq. 4.3 is taken equal to 2.54 cm since this is the focal distance of the receiving transducer. The predicted $P_s(t)$ is shown together with the actually measured pressure time curve in Fig. 4.5c. The agreement between the two curves is very good. Interestingly, both the acoustic setup and the optical setup in combination with Eq. 4.3 are able to pick up and correctly predict pressure variations of the order of 1 Pa on an ambient pressure of 10^5 Pa.

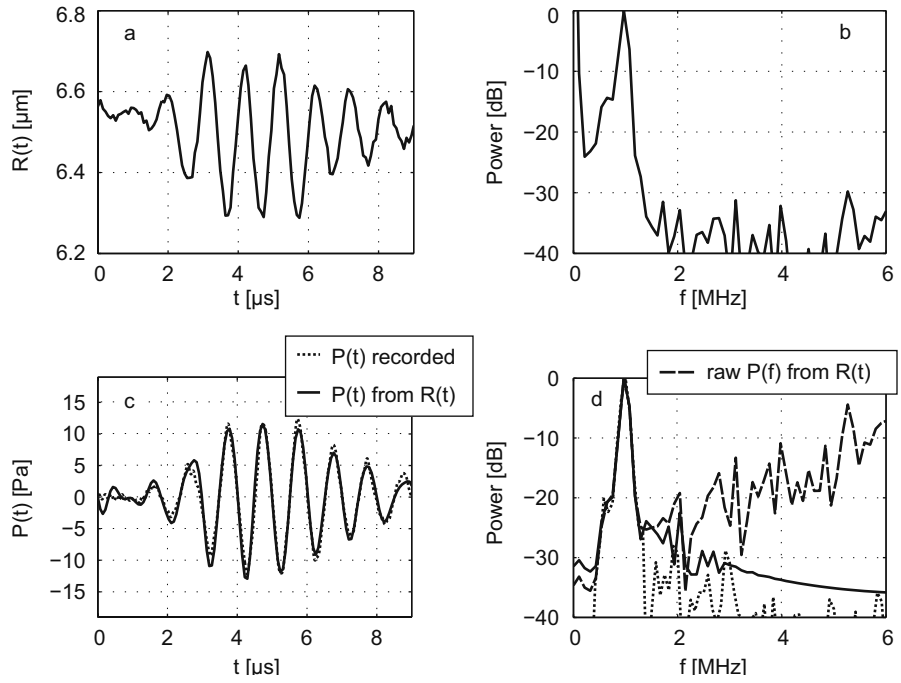

Figure 4.5: Comparison of predicted and measured acoustic responses of a bubble with an initial bubble radius of 6.5 µm, responding linearly to the driving pulse. The driving pressure pulse had a peak amplitude of 40 kPa and a frequency of 1 MHz. (a) The recorded radial response $R(t)$; (b) the frequency spectrum of the $R(t)$ curve showing no higher harmonics; (c) comparison of the acoustic response calculated from the $R(t)$ curve with Eq. 4.4 (solid line) and the acoustic response (dotted line) measured by the receive transducer; (d) the power spectra of the measured $P(t)$ curve (dotted), and of the filtered (solid line) and unfiltered (dashed line, 'raw P(f)') predicted curve. See text for filter characteristics.

As will be discussed in the next section, the higher frequency content in the $R(t)$ curve are enhanced in the calculated $P(t)$ curve. The typical noise content on the $R(t)$ curve determined from the high-speed movie is around 35 dB lower than the fundamental response, as clearly visible in Fig. 4.5b. Because of the frequency-dependent enhancement (see next section) the high-frequency noise level can become as high as the bubble response signal, as observed in Fig. 4.5c. To compare the results in time domain it was necessary to apply a low-pass filter to the raw predicted $P(t)$ curve. The used filter was a low-pass fourth order Butterworth filter with a cut-off frequency of 2 MHz. In Fig. 4.5d both the unfiltered and the filtered power spectrum of the calculated $P(t)$ curve are shown.

The data processing shown above for a single bubble was repeated for all recordings. From the recorded and predicted $P(t)$ curves the maximum amplitude

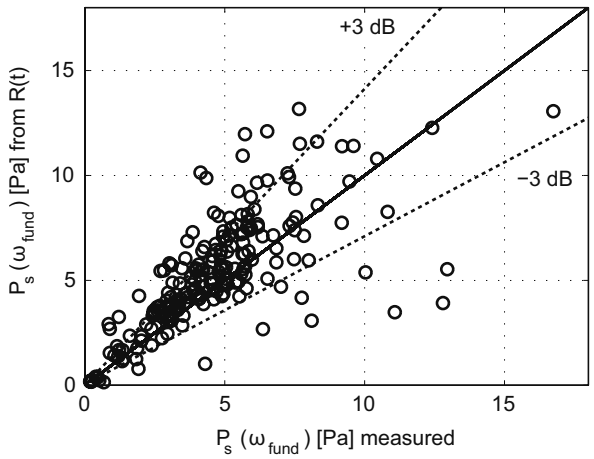

Figure 4.6: A comparison between the amplitude of the acoustic bubble response at the fundamental driving pressure frequency as measured by the receive transducer and the acoustic response as predicted from the measured $R(t)$ curve for 194 different experiments for 16 different bubbles. The driving pressure amplitude of 40 kPa is fixed for all experiments while the driving pressure frequency was varied. The dotted lines represent the +3 dB and –3 dB bounds of the data set.

of the acoustic response was determined. The amplitudes for all data are shown in the scatter plot in Fig. 4.6. The data shows worse agreement than presented in Fig. 4.5c, but generally the agreement is acceptable. The middle line in this figure denotes the expectation of equal pressure amplitudes from the recorded and the derived pressure traces. The dotted lines in Fig. 4.6 represent a difference of 3 dB between the two data sets. In 70% of the experiments the fundamental response predicted from the $R(t)$ curve is within 3 dB of the measured fundamental response. In 90% of the experiments the difference is within 6 dB. We observe that the measured fundamental acoustic response is typically 1 dB lower than the acoustic response predicted from the $R(t)$ curve. Several possible causes can be identified. First possible cause is the acoustic attenuation of the wall of the cellulose capillary tube. Second is an error in determination of the bubble radius, R. Preliminary studies have shown that small differences in optical focusing could result in a stochastic measurement error in the radius of 15%. Third is a possible error in the calibration value of the receiving transducer; the hydrophone used as a standard for the calibration has an calibration accuracy of 10%, or 0.8 dB, as stated by the manufacturer.

4.4.2 Nonlinear response

In order to understand the effect of Eq. 4.3 on the nonlinear bubble response it is insightfull to linearize Eq. 4.3. For this purpose we assume the radial dynamics to be

described by $R(t) = R_0 \{1 + \epsilon \cdot \sin(\omega t)\}$ where $\epsilon \ll 1$ and ω the angular frequency of the oscillation. Inserting this into Eq. 4.3 and ignoring terms of second and higher order we obtain

$$P_s(r, t - r/c) = \frac{\rho \omega^2 R_0^3 \epsilon \cdot sin(\omega t)}{r} \tag{4.5}$$

First of all, this relation shows that the scattered sound of the bubble increases cubically with the initial bubble radius. Therefore for a similar relative radial excursion ϵ, a larger bubble will scatter more sound than a smaller bubble. Similarly, the amplitude of the scattered sound of an oscillating bubble increases quadratically with the frequency of oscillation. As a result, the ratio of the second harmonic oscillations to that of the fundamental is enhanced by a factor of four for the acoustic response as compared to the radial response. This also explains the origin of the increase of the high frequency noise in the $P(t)$ curve calculated from the experimentally recorded $R(t)$ curve presented in Fig. 4.5.

In the example presented in Fig. 4.5 the bubble is oscillating linearly, and no signal is present at the higher frequencies. The latter implies that high frequency noise on the predicted $P(t)$ curve can be removed by a low-pass filter without signal loss. However, a nonlinearly oscillating bubble will show higher harmonic oscillations and the use of a low-pass filter could result in signal loss.

An example of a nonlinearly oscillating bubble is shown in Fig. 4.7a. The bubble has an initial bubble radius of 4.9 μm and it was excited with a driving pulse with a frequency of 1.8 MHz. Since this driving frequency was close to twice its resonance frequency [van der Meer et al., 2007], the bubble responds nonlinearly with subharmonic oscillations at 0.9 MHz. The radial subharmonic response is higher than the fundamental response at 1.8 MHz. The resulting acoustic response from these nonlinear oscillations is calculated with Eq. 4.3. Fig. 4.7b shows the power spectrum of the resulting acoustic response which is compared to the power spectrum of the simultaneously measured acoustic response. For the fundamental response and the subharmonic response the agreement is good. As explained by the ω^2-relation in Eq. 4.5 the subharmonic acoustic response has decreased significantly relative to the fundamental acoustic response. In the measured acoustic response we clearly observe higher harmonic contents at frequencies of 2.7 MHz and 3.6 MHz, which are not visible in the response predicted from the recorded radial dynamics. The noise in the radial response curve is visible at nearly 25 dB below the fundamental response, see Fig. 4.7a, while the acoustic recording shows its superior resolving power of the higher harmonic responses with a noise level of –40 dB.

4.4.3 The inverse problem

In the previous two sections we have shown that it is possible to correctly predict the acoustic response of an oscillating microbubble based on its experimentally

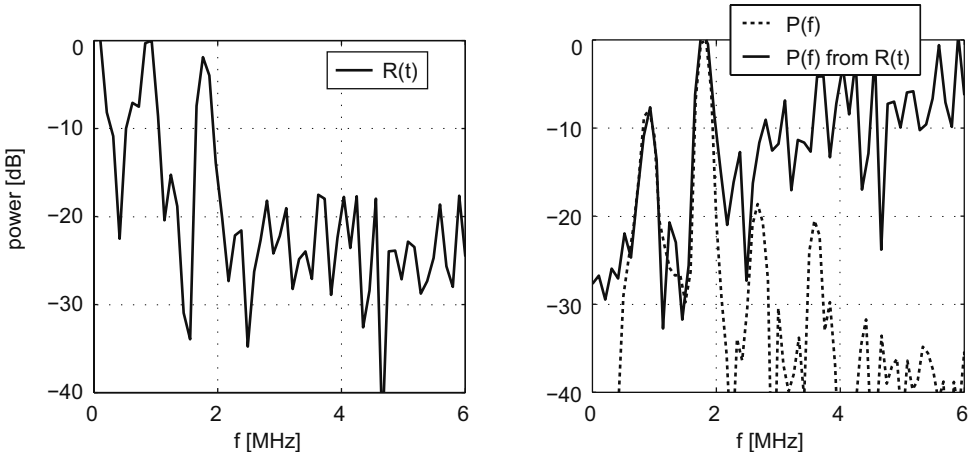

Figure 4.7: (left) Frequency power spectrum of the radial response of a bubble with an initial radius of 4.9 μm. A subharmonic response is visible at 0.9 MHz, which is half of the driving pressure frequency of 1.8 MHz. (right) The spectrum of the pressure calculated from the $R(t)$ curve (solid line) and the simultaneously measured one (dotted line).

recorded $R(t)$ curve. It is clear that especially the fundamental and subharmonic *acoustic* response are correctly predicted from the optically recorded radial dynamics of a microbubble. However as a result of the noise on the measured $R(t)$ curve and the limited resolving power of the optical system, higher harmonics are difficult to study optically. The high frequency enhancement in the acoustic response and the sensitivity of an acoustic recording makes the recording of the acoustic response of a microbubble therefore complementary to an optical recording.

We hypothesize that it is possible to reconstruct the radial dynamics from the measured $P(t)$ curve. The radial dynamics can be recovered from a double integration of Eq. 4.3:

$$R^3(t) = R^3(0) + \dot{R}^3(0) + \frac{3r}{\rho}\int_0^t dt' \int_0^{t'} P_s(r,s)ds. \tag{4.6}$$

For a known initial bubble radius and a known initial bubble wall velocity (in general $\dot{R} = 0$) together with a known distance r between the receiving transducer and the microbubble the acoustic response can be integrated numerically to give the bubble radius $R(t)$ as a function of time. The integration is numerically calculated with the trapezoidal rule in MATLAB.

In Fig. 4.8 the result from solving this inverse problem is shown for the acoustic response of the very same bubble as presented in Fig. 4.5. The bubble had a radius of 6.5 μm and it was subjected to a 1 MHz pulse. The acoustic response $P_s(t)$ was numerically integrated twice to give $R^3(t)$. The noise of the recorded acoustic

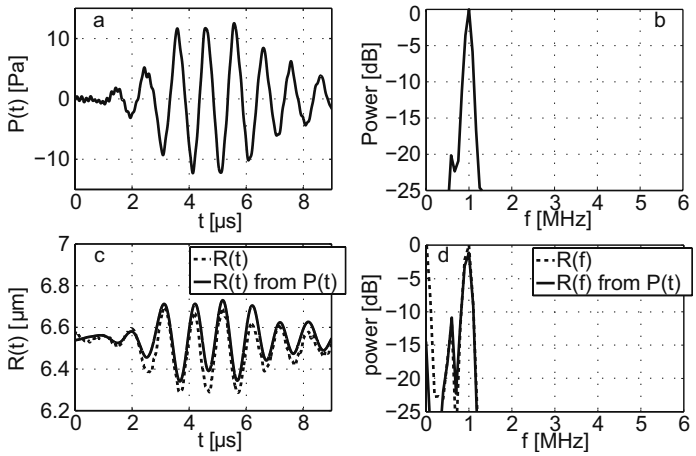

Figure 4.8: Example of results obtained with the inverse method. (a) The recorded acoustic response of a 6.6 μm radius microbubble; the distance between the focused transducer and microbubble was 2.54 cm (same as in Fig. 4.5a). (b) Power spectrum of signal in (a); (c) predicted dynamics compared to the optically recorded radial response; (d) Power spectrum of both signals.

response on average gives the $P(t)$ curve a small offset. The double integration is extremely sensitive to low frequencies and a small offset results in a drift and an unphysical growth of the bubble size in the final $R(t)$ curve. We corrected for this drift by applying a second order Butterworth 0.2 MHz high-pass filter on $\dot{R}^3(t)$ after the first integration step. For sufficiently small time steps ($\Delta t < 5 \cdot 10^{-8}$ s) the double integration was found to converge to the predicted $R(t)$ curve as shown in Fig. 4.8. The good agreement between the predicted and recorded radial dynamics is remarkable. Oscillations of the bubble wall smaller than 100 nm are correctly predicted from an acoustic response measured at a distance of 2.5 cm.

A small difference in the radial offset during the oscillation can be observed between the predicted and the measured $R(t)$ curves. As discussed before, "compression-only" behavior [Marmottant et al., 2005; de Jong et al., 2007] gives an offset to the mean radius during the oscillation. The offset can be looked upon as a low-frequency component. Since the receive transducer is not sensitive to such low frequency component it is not detected; conversion from the recorded $P(t)$ into an $R(t)$ will therefore not predict the low-frequency offset.

To investigate the accuracy of the inverse method for all bubble recordings, the amplitudes of the optically-recorded radial responses were compared to those of the predicted ones, at the fundamental frequency. The agreement between the two was of similar quality as the one resulting from the agreement seen with the forward method (see Fig. 4.6) and therefore not plotted. In 60% of the experiments

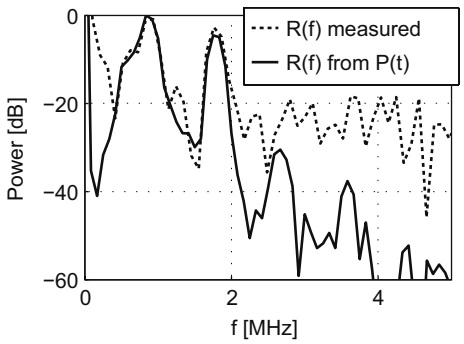

Figure 4.9: Example of acoustically-predicted higher-harmonic radial responses that are are not detected optically. The graph shows the power spectra of the $R(t)$ curves of a bubble with an initial bubble radius of 4.9 μm subjected to a 1.8 MHz pressure pulse (same response as in Fig. 4.7a). The noise in the optical data is higher than the levels of the expected higher harmonic oscillations.

the fundamental response of the radial dynamics predicted from the $P(t)$ curve is within 3 dB of the measured fundamental response. In 80% of the experiments the difference is within 6 dB. On average the acoustically-derived radial response had a slightly lower amplitude of oscillation than the optically-observed radial response.

In Fig. 4.9 the power spectrum of an optically recorded $R(t)$ curve is presented together with the spectrum of the radial dynamics as predicted from the measured $P(t)$ curve. The curves are normalized with the same factor, and we can identify a quantitative agreement between the two curves. Furthermore, Fig. 4.9 confirms the hypothesis that acoustic techniques can be used to study the higher harmonic radial dynamics of ultrasound contrast agent microbubbles, more sensitive than ultra-high speed imaging can. The higher harmonic oscillations of the bubble that are invisible in the optically recorded $R(t)$ curve are clearly visible in the dynamics determined from the recorded acoustic response.

4.4.4 Subharmonic responses

In some of the conducted experiments, nonspherical shape oscillations were observed. Since these oscillations are predominately of a period-doubling nature [Dollet et al., 2008] it can be hypothesized that these surface modes transmit subharmonic sound. If the surface modes would emit sound at the subharmonic frequency there should be a difference between the sound transmission calculated from the radius time curve, which is based only on the volumetric bubble oscillations through

Table 4.1: Overview of occurrence of subharmonic scattering and surface modes. Total number of recordings is 192.

	Acoustic subharmonic	No acoustic subharmonic
Surface modes	15	54
No surface modes	8	115

Eq. 4.3, and the scattered sound measured simultaneously with the transducer.

Of the set of 16 bubbles a total of 4 bubbles in 23 different experiments showed an acoustic subharmonic response. The threshold for the occurrence of a subharmonic response was set at –20 dB compared to the fundamental-frequency response. Examples of these subharmonic responses are shown in Figs. 4.4 and 4.7b. As in Fig. 4.7b the predicted and measured sound emission at the subharmonic frequency overlap within 2.5 dB for 20 of the 23 experiments, independent of the occurrence of surface modes; see Table 4.1. Furthermore in 54 other experiments surface modes were observed in the absence of any volumetric subharmonic oscillation or subharmonic acoustic emission. The occurrence of surface modes was scored manually from the optical data.

4.5 Discussion

4.5.1 Noise, sensitivity and bandwidth

The examples presented in Fig. 4.7b and Fig. 4.9 show an acoustic measurement that is superior in terms of sensitivity, owing to the good noise characteristics of the transducer and amplifier. Strictly speaking, the high sensitivity is only present in a limited frequency band. Current optimized single-element transducers have a bandwidth of typically 1–6 MHz. Low frequency features of the radial dynamics such as "compression-only" behavior might therefore not be captured by acoustic methods. In future experiments one could try to work around this by the addition of a dedicated low-frequency transducer. The Brandaris-128 ultra-high speed camera has an effective bandwidth of 0–12.5 MHz when operated at its maximum frame rate of 25 Mfps and can therefore inherently capture the low-frequency contents.

If smaller bubbles are studied than presented here, the acoustic signals are expected to decrease on average. For equal radial excursion and frequency the acoustic amplitude depends cubically on the radius (Eq. 4.5). Hence, if smaller bubbles are studied the acoustic signal to noise ratio (SNR) will also decrease. On the other hand, it can be shown that the SNR in the optical movies also depend on the radius because of the finite pixel size in the frames (with the $100\times$ objective the pixel size is ~ 0.11 μm). Therefore, even for smaller bubbles the acoustic method is expected to be more sensitive than the optical method to study higher harmonic responses.

The sensitivity of the optically recorded radial response could be improved. One could try to increase the optical zoom to decrease the influence of the finite pixel size. Another improvement would be to reduce motion blur of the oscillating bubble wall by decreasing the exposure times within the design of the Brandaris-128 camera. This also requires either more sensitive CCDs or an increased intensity of the illumination. A third option would be to use laser-induced fluorescence techniques and high-intensity illumination to increase the contrast of the bubble wall with respect to the background illumination. Finally, improved data processing of the ultra-high speed movies into $R(t)$ curves may eventually lead to noise reduction. An improvement of 20 to 30 dB, if we take Fig. 4.9 as a reference, will then be the ultimate challenge.

4.5.2 Remote acoustic detection of *in vivo* mechanical forcing

The inverse acoustic method provides a sensitive method to study the radial dynamics of ultrasound contrast agent microbubbles. An advantage of the method is that the recording can be performed remotely, at a distance of 10 cm or more from the bubble, while optical methods with a microscope inherently need an objective mounted close to the bubble, regularly at a distance on the order of 1 mm. Such objective might produce unwanted acoustic reflections that interfere with the bubble signals.

The inverse method could potentially provide a new tool to *in vivo* investigate the relation between local mechanical action and enhanced drug uptake by cells [Marmottant and Hilgenfeldt, 2003; Van Wamel et al., 2006; Ohl et al., 2006]. In literature it is suggested that strain caused by oscillating bubbles close to a cell membrane results in opening of the cell and enhanced drug uptake. Strain could be estimated from the oscillation amplitude of the bubble [Marmottant and Hilgenfeldt, 2003; Prentice et al., 2005; Ohl et al., 2006; Liu and Wu, 2009] – see also Ch. 7 of this thesis. Thus, in future a remote acoustic detection method may give direct feedback on the locally controlled mechanical forcing near cells. One requirement for such application is to know the initial bubble radius to enable the integration of Eq. 4.6. Acoustic techniques based on off-resonant bubble sizing [Medwin, 1977; Phelps and Leighton, 1996] could provide an estimate of the initial bubble radius. More elegantly, the size requirement could be fulfilled by the use of monodisperse ultrasound contrast agent microbubbles that can be produced through flow focusing in a lab-on-a-chip device [Hettiarachchi et al., 2007; Dollet et al., 2008].

4.5.3 Subharmonic responses

From the analysis of the absence or presence of subharmonic signals we may conclude that surface modes do not transmit sound at the subharmonic frequency in the far field. Surface modes may still play a role in the initiation of volumetric

subharmonic oscillations. Furthermore, the optical plane of the microscope is parallel to the wall, and any nonspherical modes with an orientation normal to the wall will not be visible in the optical images [Vos et al., 2008]. Therefore a more detailed investigation of the sound emission of surface modes requires a 'side view' microscope to visualize the nonspherical modes of the bubble normal to the wall, as in Vos et al. [2008].

4.6 Conclusions

In conclusion, we have experimentally shown that the radial dynamics of an isolated oscillating microbubble can predict the acoustic emission resulting from these dynamics. It is shown that the higher order harmonics in the radial dynamics of the microbubbles are enhanced in the acoustic emission, which is in agreement with the theoretical predictions. Vice versa, we show that the measured acoustic emission resulting from an isolated oscillating microbubble with known initial bubble radius can be converted to correctly describe the bubble dynamics. Ultra-high speed imaging and acoustic recordings are shown to complement each other in the characterization of both the dynamic and the acoustic behavior of ultrasound contrast agent microbubbles. Small amplitude and higher harmonic behavior is shown to be more sensitively characterized by acoustic techniques. Nonspherical oscillations and low frequency behavior such as "compression only" behavior, essential for modeling and predicting bubble behavior, are exclusively visible in optically recorded bubble dynamics.

Bibliography

Brenner, M. P., S. Hilgenfeldt, and D. Lohse, "Single-bubble sonoluminescence," *Rev Mod Phys*, 74(2): pp. 425–483, 2002.

Caskey, C. F., S. M. Stieger, S. Qin, P. A. Dayton, and K. W. Ferrara, "Direct observations of ultrasound microbubble contrast agent interaction with the microvessel wall," *J Acoust Soc Am*, 122(2): pp. 1191–1200, 2007.

Chin, C. T., C. Lancée, J. M. G. Borsboom, F. Mastik, M. E. Frijlink, N. de Jong, M. Versluis, and D. Lohse, "Brandaris 128: A digital 25 million frames per second camera with 128 highly sensitive frames," *Rev Sci Instr*, 74(12): pp. 5026–5034, 2003.

de Jong, N., A. Bouakaz, and P. J. A. Frinking, "Basic acoustic properties of microbubbles," *Echocardiography*, 19(3): pp. 229–240, 2002.

de Jong, N., M. Emmer, C. T. Chin, A. Bouakaz, F. Mastik, D. Lohse, and M. Versluis, ""compression-only" behavior of phospholipid-coated contrast bubbles," *Ultrasound Med Biol*, 33(4): pp. 653–656, 2007.

Doinikov, A. A. and P. A. Dayton, "Maxwell rheological model for lipid-shelled ultrasound microbubble contrast agents," *J Acoust Soc Am*, 121(6): pp. 3331–3340, 2007.

Dollet, B., W. van Hoeve, J. P. Raven, P. Marmottant, and M. Versluis, "Role of the channel geometry on the bubble pinch-off in flow-focusing devices," *Phys Rev Lett*, 100(3): p.

ref. 034504, 2008.

Emmer, M., A. van Wamel, D. E. Goertz, and N. de Jong, "The onset of microbubble vibration," *Ultrasound Med Biol*, 33(6): pp. 941–949, 2007.

Emmer, M., H. J. Vos, and N. de Jong, "Radial modulation of single microbubbles," *IEEE Trans Ultrason Ferroelectr Freq Control*, 56(11): pp. 2370–2379, 2009.

Garbin, V., B. Dollet, M. Overvelde, D. Cojoc, E. Di Fabrizio, L. van Wijngaarden, A. Prosperetti, N. de Jong, D. Lohse, and M. Versluis, "History force on coated microbubbles propelled by ultrasound," *Phys Fluids*, 21(9): pp. ref. 092003–7, 2009.

Hettiarachchi, K., E. Talu, M. L. Longo, P. A. Dayton, and A. P. Lee, "On-chip generation of microbubbles as a practical technology for manufacturing contrast agents for ultrasonic imaging," *Lab on a Chip*, 7: pp. 463–468, 2007.

Hilgenfeldt, S., D. Lohse, and M. Zomack, "Response of bubbles to diagnostic ultrasound: a unifying theoretical approach," *Eur Phys J B, Condensed Matter Phys*, 4(2): pp. 247–255, 1998.

Hope Simpson, D., C. T. Chin, and P. N. Burns, "Pulse inversion Doppler: a new method for detecting nonlinear echoes from microbubble contrast agents," *IEEE Trans Ultrason Ferroelectr Freq Control*, 46(2): pp. 372–382, 1999.

Kim, D. H., M. J. Costello, P. B. Duncan, and D. Needham, "Mechanical properties and microstructure of polycrystalline phospholipid monolayer shells: Novel solid microparticles," *Langmuir*, 19(20): pp. 8455–8466, 2003.

Leighton, T. G., The Acoustic Bubble, Academic Press, London, UK, 1994.

Lindner, J. R., "Microbubbles in medical imaging: Current applications and future directions," *Nat Rev Drug Discov*, 3(6): pp. 527–533, 2004.

Lindner, J. R., J. Song, A. R. Jayaweera, J. Sklenar, and S. Kaul, "Microvascular rheology of Definity microbubbles after intra-arterial and intravenous administration," *J Am Soc Echocard*, 15(5): pp. 396–403, 2002.

Liu, X. and J. Wu, "Acoustic microstreaming around an isolated encapsulated microbubble," *J Acoust Soc Am*, 125(3): pp. 1319–1330, 2009.

Marmottant, P. and S. Hilgenfeldt, "Controlled vesicle deformation and lysis by single oscillating bubbles," *Nature*, 423(6936): pp. 153–156, 2003.

Marmottant, P., S. M. van der Meer, M. Emmer, M. Versluis, N. de Jong, S. Hilgenfeldt, and D. Lohse, "A model for large amplitude oscillations of coated bubbles accounting for buckling and rupture," *J Acoust Soc Am*, 118(6): pp. 3499–3505, 2005.

Medwin, H., "Counting bubbles acoustically: a review," *Ultrasonics*, 15: pp. 7–13, 1977.

Mor-Avi, V., E. G. Caiani, K. A. Collins, C. E. Korcarz, J. E. Bednarz, and R. M. Lang, "Combined assessment of myocardial perfusion and regional left ventricular function by analysis of contrast-enhanced power modulation images," *Circulation*, 104(3): pp. 352–357, 2001.

Ohl, C. D., M. Arora, R. Ikink, N. de Jong, M. Versluis, M. Delius, and D. Lohse, "Sonoporation from jetting cavitation bubbles," *Biophys J*, 91(11): pp. 4285–4295, 2006.

Phelps, A. D. and T. G. Leighton, "High-resolution bubble sizing through detection of the subharmonic response with a two-frequency excitation technique," *J Acoust Soc Am*, 99(4): pp. 1985–1992, 1996.

Prentice, P., A. Cuschieri, K. Dholokia, M. Prausnitz, and P. Campbell, "Membrane disruption by optically controlled microbubble cavitation," *Nat Phys*, 148: pp. 1–4, 2005.

Sijl, J., E. Gaud, P. J. A. Frinking, M. Arditi, N. de Jong, D. Lohse, and M. Versluis, "Acoustic

characterization of single ultrasound contrast agent microbubbles," *J Acoust Soc Am*, 124(6): pp. 4091–4097, 2008.

Stride, E., "The influence of surface adsorption on microbubble dynamics," *Phil Trans R Soc A*, 366(1873): pp. 2103–2115, 2008.

van der Meer, S., B. Dollet, M. Voormolen, C. T. Chin, A. Bouakaz, N. de Jong, M. Versluis, and D. Lohse, "Microbubble spectroscopy of ultrasound contrast agents," *J Acoust Soc Am*, 121(1): pp. 648–656, 2007.

Van Wamel, A., K. Kooiman, M. Harteveld, M. Emmer, F. J. ten Cate, M. Versluis, and N. de Jong, "Vibrating microbubbles poking individual cells: Drug transfer into cells via sonoporation," *J Control Release*, 112(2): pp. 149–155, 2006.

Vokurka, K., "On rayleigh's model of a freely oscillating bubble. I. Basic relations," *Czechoslovak J Phys*, 35(1): pp. 28–40, 1985.

Vos, H. J., B. Dollet, J. G. Bosch, M. Versluis, and N. de Jong, "Nonspherical vibrations of microbubbles in contact with a wall - a pilot study at low mechanical index," *Ultrasound Med Biol*, 34(4): pp. 685–688, 2008.

Zhao, S., K. W. Ferrara, and P. A. Dayton, "Asymmetric oscillation of adherent targeted ultrasound contrast agents," *Appl Phys Lett*, 87: p. ref. 134103, 2005.

Chapter 5

Ultrafast framing optical and acoustic recording of nonlinearly oscillating microbubbles

Abstract - **Microbubble nonlinear behavior improves detection efficacy of ultrasound contrast agents (UCAs), but not all microbubble sizes present in the dispersed UCA population will contribute to the detection signal. This paper experimentally studies the relation between size and nonlinear response of isolated lipid-coated microbubbles, held in a transparent tube. The echo from microbubbles is acoustically recorded with a sensitive custom electronic system, and simultaneously the radial excursion is optically recorded with an ultrafast framing camera. Ultrasound-induced deflation is used to sample the bubble at multiple sizes. At sizes smaller than the resonant size the bubbles show compression-only behavior accompanied by strong second harmonic scattering. Subharmonics are observed for bubble sizes larger than resonant.**

Appeared as a proceedings paper for the IEEE International Ultrasonics Symposium, Rome, Italy, 2009, by H. J. Vos, R. Mori, J. Viti, J. Sijl, F. Guidi, P. Tortoli, and N. de Jong.

5.1 Introduction

Characterization of single ultrasound contrast agent (UCA) microbubbles is necessary to improve detection strategies, which generally favor nonlinear behavior of microbubbles. Previous studies have shown that nonlinear behavior can produce strong harmonic distortion [Marmottant et al., 2005], subharmonic emission [Kimmel et al., 2007], and thresholding effects, in which coated bubbles do not show an oscillation if the pressure amplitude is below a certain threshold value [Emmer et al., 2007]. These effects are strictly related to the bubble size, and to the insonation pressure and frequency. For characterization purposes, this implies that microbubbles of known size should be isolated and tested. Optical methods with fast cameras have the advantage that multiple bubbles can be recorded in one movie, and the size is inherently known. However, the optically observed radial excursions should be translated to an echo, which might introduce errors. Acoustic methods, on the other hand, should use very sensitive equipment since the echo amplitude of single microbubbles is low; furthermore, the size should be measured independently. The latter condition suggests the incorporation in the setup of a microscope and an optically and acoustically transparent tube. Furthermore, an extremely highly dilution of the agent is requested to yield the necessary acoustic isolation of single microbubbles [Dayton et al., 1999; Sijl et al., 2008; Guidi et al., 2009]. This dilution procedure is cumbersome and time consuming when many different radii are to be studied.

We have earlier proposed a combined acoustic-optical method in which single phosholipid-coated microbubbles are isolated by dilution, and are slowly deflating due to many ultrasound excitation pulses [Guidi et al., 2009] – see also Ch. 3. The echo from the microbubble is acoustically recorded, and the steady-state bubble size is measured with an optical microscope. The slow controlled deflation allows dense sampling of the response as a function of size. Three deflation stages could be identified when using pulses of 60 kPa amplitude, 15 cycles, 2 to 4 MHz at a repetition frequency of 250 Hz [Guidi et al., 2009]: (1) bubbles larger than ~ 3 μm do not deflate at all; (2) those between ~ 3 μm and ~ 1.8 μm deflate in roughly 2 s, while (3) bubbles smaller than ~ 1.8 μm deflate slower and eventually reach a stable final size of 1.44 μm $\pm$ 0.17 μm. The curious behavior of a stable final size was earlier observed by Borden et al. [2005] and is not fully understood.

This paper expands the acoustic deflation method described by Guidi et al. [2009] with a simultaneous optical recording of the radial behavior with the ultrafast Brandaris-128 camera. This allows further exploration of the observed phenomena of Chs. 3 and 4 of this thesis.

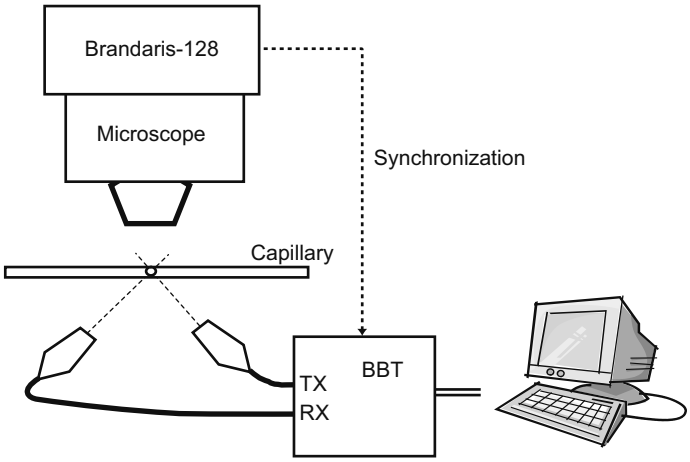

Figure 5.1: Schematic drawing of the setup. BBT = Bubble Behavior Testing system which is a custom electronic board developed by the MSDLab of the University of Florence, Italy. TX = analog channel configured for transmission, RX = analog channel configured for reception.

5.2 Experimental methods

5.2.1 Setup

With reference to Fig. 5.1, highly diluted Definity (Lantheus Medical Imaging, North Billerica, MA) contrast agent is injected in a transparent cellulose capillary; flow is manually controlled using a small syringe connected to a fine pitch micrometer screw. The tube is flushed until isolated microbubbles are positioned in the region of interest (ROI). One transducer (PA076 PVDF, Precision Acoustics, Dorchester, UK) transmits the wave and the other (Panametrics C381, Olympus NDT) records the echo (2.5 cm focus). Both are connected to the Bubble Behavior Testing (BBT) system, which is a custom coherent transmit/receive low-noise electronic system [Ricci et al., 2006; Guidi et al., 2009].

Optical images are simultaneously captured by the Brandaris-128 ultrafast framing camera operating at about 14.5 million frames per second [Chin et al., 2003], through a 60× water immersion microscope objective. Using additional 4× magnification in the microscope the final resolution in the images is 0.09 μm per pixel. This allows the full capture of the microbubble size, shape, and oscillation. The camera acquires one movie of 128 frames per ultrasound pulse, and has a recovery time of about 80 ms. After recording 25 movies the frames are downloaded to a PC, which takes some minutes to complete. This allows fresh bubbles to be placed in the region of interest. A trigger is generated by the camera to synchronize the acoustic system.

5.2.2 Pulsing sequences

Isolated microbubbles are insonified with two alternating pulse sequences (see Fig. 5.2). The first sequence contains 5 *probing* tone bursts, each of 10 cycles, $\sim$ 60 kPa peak negative pressure, and frequency changing from 2 to 4 MHz in steps of 0.5 MHz, so that the behavior of a same bubble at different frequencies is observed. The pulse repetition time (PRT) is 80 ms, equal to the recovery time of the camera system. The probing sequence is followed by the *deflation* sequence, containing 18 pulses of 2 MHz, 15 cycles, 60 kPa, 4 ms PRT (thus fitting within 1 recovery interval) aimed to induce a size reduction. The probing and deflation sequences are repeated 5 times per experiment, giving a total acquisition time of 2.0 s.

Fig. 5.2 reports the overall acquisition process. The top row shows the echoes from the microbubble at the different frequencies and stages as a function of 'slow' time (units of milliseconds). The middle row shows the simultaneously recorded radial excursion (for clarity only the resting radius is plotted for the 2^{nd}, 3^{rd} and 4^{th} sequence pair). The bottom row shows one example of post-processed data, here corresponding to the relative phase of the echo while deflating. The phase relation is derived from the 2-MHz echo using standard Doppler processing, which is possible thanks to the coherent transmit/receive front end [Guidi et al., 2009]. Note that a decrease of bubble size induces a decrease of its oscillatory inertia, and thus an increase in phase between the bubble oscillation and the driving pulse (Fig. 5.2 bottom).

5.2.3 Acoustic data processing

The digitized acoustic data are corrected for background signals and converted to absolute pressures after careful calibration of the transducer and system [van Neer et al., 2007]. Signal amplitudes of the fundamental and harmonic responses are computed by taking the maximum of the analytic signal amplitude after band-pass filtering (Butterworth, 2^{nd} order, 500 kHz bandwidth). No further averaging was applied.

5.2.4 Optical data processing

In order to quantitatively compare the optically-recorded radial excursion with the acoustically-recorded echo, it is useful to convert the radial excursion into a prediction of the scattered echo. This is done in two steps. First, optical frames are analyzed to extract the radius as a function of time ($R(t)$) using a minimum-cost algorithm [van der Meer et al., 2007]. Second, since the radius is small compared to the wavelength, the scattered wave from a microbubble is spherically diverging and the echo can be predicted at distance r (2.5 cm in the experiments) by [Leighton,

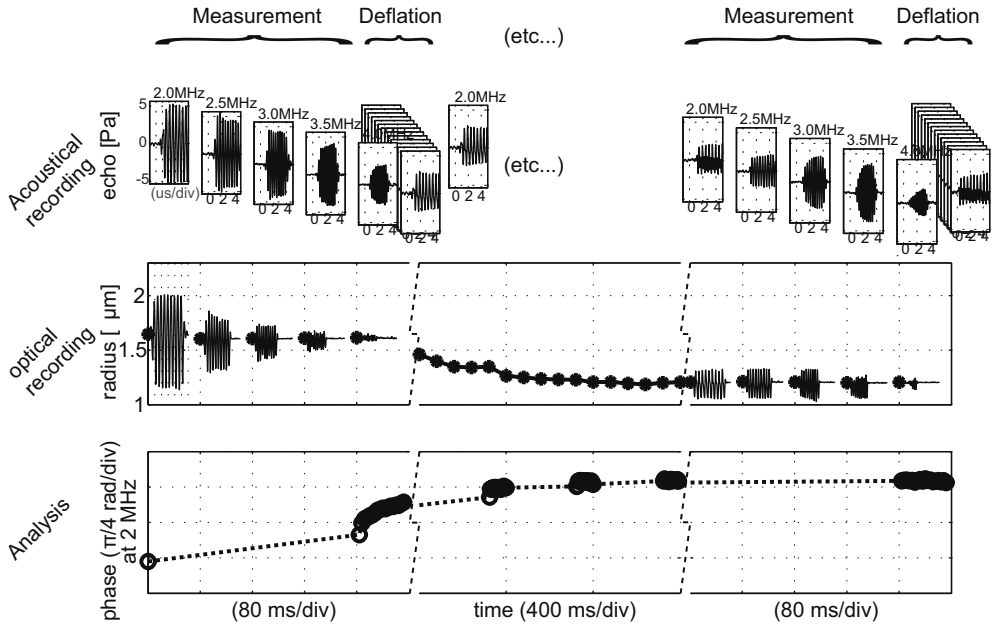

Figure 5.2: Schematic representation of the acquisition sequences. Frequency-modulated measurement pulses are alternated with 2 MHz deflation pulses. The deflation pulses induce a small size reduction, thus allowing for dense sampling of the size-dependent behavior of the microbubble within the same experiment.

1994; Sijl et al., 2007] – see also Ch. 4:

$$p(r, t - r/c) = \frac{1}{3}\frac{\rho}{r}\frac{\partial^2}{\partial t^2}R(t)^3 \tag{5.1}$$

where ρ is the density of water (1000 kg/m^3). The finite travel time of the echo is accounted for by the delay factor r/c, with c the sound velocity. The second time derivative of the cubed radius is obtained with a second order difference scheme,

$$\frac{\partial^2}{\partial t^2}R_n^3 \approx \frac{R_{n+1}^3 - 2R_n^3 + R_{n-1}^3}{\Delta t^2} \tag{5.2}$$

with n the frame number (1 – 128, R_0 is the initial radius) and Δt the interframe time of the camera.

For the interpretation of the experimental results it is insightful to linearize Eq. 5.1. Assuming a radial excursion $R(t) = R_0 + A\sin(\omega t)$, with A the excursion amplitude and ω the oscillation angular frequency, for $A \ll R_0$, it yields

$$p(r, t - r/c) \approx -\frac{\rho\omega^2 R_0^2 A\sin(\omega t)}{r}. \tag{5.3}$$

This relation shows that the amplitude of the radial oscillation (A) is amplified by a factor R_0^2, i.e. bigger bubbles produce higher echo amplitudes for a given radial excursion amplitude. Note that Eq. 4.5 in the previous chapter is similar to Eq. 5.3 but with a different, relative or absolute, notation of the amplitude: $\epsilon = A/R_0$. It also shows that the scattering level of a second harmonic radial motion is amplified by a factor 4 because of the gain factor ω^2 in Eq. 5.3.

5.3 Results and discussion

5.3.1 Size dependency

Fig. 5.3 shows the overall experimental results, obtained from 5 bubbles with different initial radii. Data are shown for the 2-MHz insonation pulses. In the bottom panel the amplitudes of the echo at the fundamental, second harmonic, and subharmonic frequency are drawn as a function of radius. In the top panel three optically-recorded radial excursion plots are shown, taken from the recording of a small, a middle-sized, and a large bubble, respectively.

The smallest bubble shows a radial excursion of 0.4 μm peak-peak and produces an echo amplitude of 2 Pa. The bubble with 1.8 μm radius (which, at 2 MHz, is close to resonance [Guidi et al., 2009]) produces an echo amplitude of 10 Pa with a radial excursion of about 1 μm peak-peak. The echo amplitude of the largest bubble, with radius of 3.35 μm, is also about 10 Pa, despite its smaller radial excursion of 0.4 μm peak-peak. This behavior is consistent with that predicted by Eq. 5.3, which states

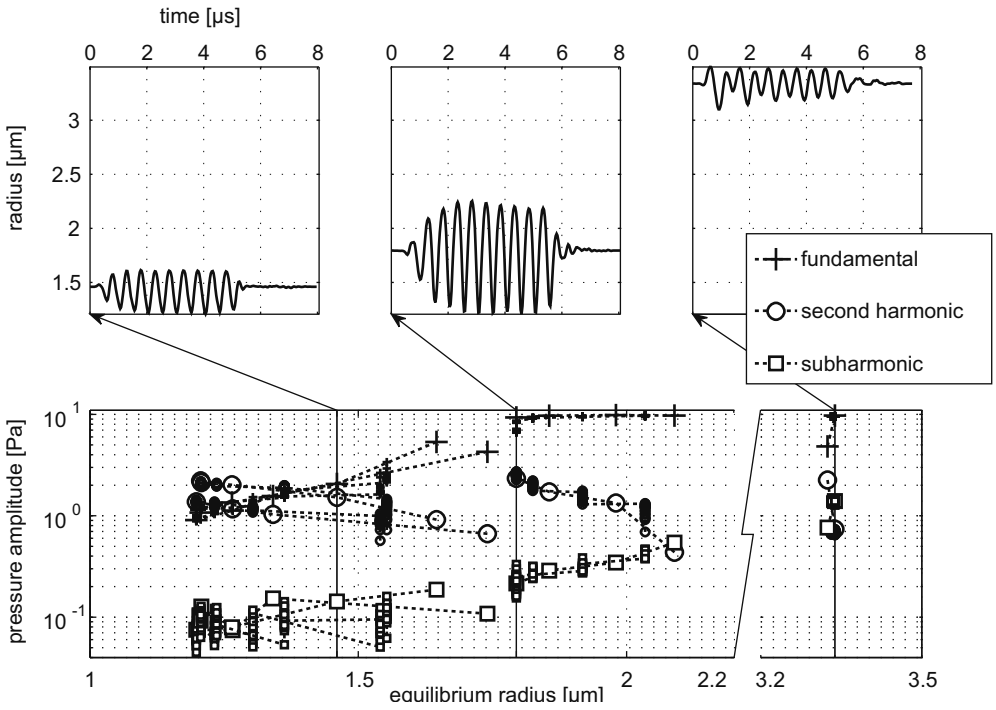

Figure 5.3: (Bottom) Amplitudes of the fundamental, second harmonic, and subharmonic frequency components in the echo as a function of microbubble size. (Top) examples of radial excursions of a small, middle, and large microbubble. Data are extracted from the 2 MHz recordings, and the middle bubble is excited around its resonance frequency.

that the echo amplitude depends squarely on the bubble size for a given excursion amplitude and frequency.

Two distinct size ranges can be identified where the second harmonic response (circles in Fig. 5.3) is relatively large. The first range is around the resonant radius of 1.8 μm. The second range is where the bubble radius is < 1.6 μm. Remarkably, in the second range, the second harmonic response can become higher than the fundamental frequency response. The smallest bubble size in the dataset (1.2 μm radius) produces fundamental-frequency echo amplitude of 1 Pa and a second harmonic amplitude of 2.3 Pa. The radial excursion (see top-left panel) in the small-radius region shows asymmetric oscillation having larger compression than expansion, which is the so-called compression-only phenomenon [de Jong et al., 2007]. Other examples of small-bubble behavior, including expansion-only, will be given below.

The subharmonic response (squares in Fig. 5.3) is large for the large bubble, as expected from the general theory that predicts that bubbles insonified at twice their

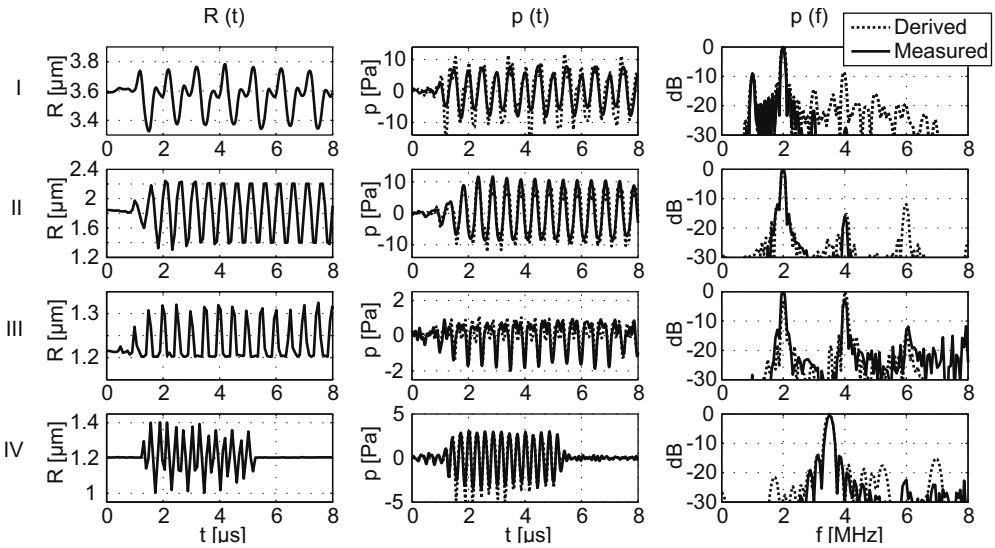

Figure 5.4: Examples of radial excursion (left), and the time and frequency representation of the optically-derived and acoustically-measured echo. The transmission frequency was 2 MHz in example I, II, and III, and 3.5 MHz in example IV. Solid lines are acoustically recorded, dashed lines are the echoes derived from the radial excursions.

resonance frequency have lowest threshold for subharmonic instabilities to grow [Prosperetti, 1975]. The radius is larger than 3 µm and is thus in the regime where coated microbubbles are found to be insensitive to the deflation pulses [Guidi et al., 2009].

5.3.2 Correlation between radial excursion and echo

Eq. 5.1 is used to assess the acoustic and optical recordings. Fig. 5.4 shows four examples of recordings. The left panels show the radial excursion of the different bubbles, insonified at 2 MHz (example I, II, and III) and 3.5 MHz (example IV). The different insonation frequencies in the experiments are useful for observing different bubble behavior. Example I and IV show subharmonic oscillation, example II a resonant response, and example III expansion-only behavior. The examples are ordered in decreasing microbubble size. In the middle and right panels the time traces and frequency spectra of the echoes are given, obtained with two different methods: direct acoustic *measurement*, and *derivation* from the optically-measured radial excursion by applying Eq. 5.1.

The time trace and frequency spectra show high correlation between the measured and derived echo signal at the fundamental frequency. However, there are differences in nonlinear responses. First, the second and third harmonic responses

are not always correlating well (example I at 4 MHz and 6 MHz, example II at 6 MHz, and example IV at 7 MHz). This decorrelation seems coincident with relatively low amplitude of the measured echo, and could partly be explained by noise in optical recording masking the low-amplitude higher-harmonic response (see also Ch. 4 of this thesis). Second, subharmonics in the echoes of a large bubble (example I) correlate very well, but those of a small bubble (example IV) do not. In the latter case nonspherical shapes were visible in the optical recordings. These nonspherical shapes might influence the optically-appearing radial excursion, while the volumetric oscillation, that dominates the echo, is not affected [Longuet-Higgins, 1989].

5.4 Conclusions

Size plays a large role in the behavior of microbubbles. The combined acoustic/optical setup allows a direct measurement of the dynamics of differently-sized microbubbles and deflation allows for a dense radial sampling. Even at low excitation levels (MI < 0.05) highly nonlinear oscillations, yielding compression-only and expansion-only behavior for smaller microbubbles and subharmonics for larger microbubbles, have been identified.

Echoes that are derived from the optically-measured radial excursion correlate well at the fundamental frequency with acoustically-measured echoes, but the amplitudes of the nonlinear responses sometimes differ significantly. Possible errors can be due to a wrong calibration of the system, which is likely to occur for frequencies higher than 4 MHz, and/or noise in the optically-recorded radial excursion.

Bibliography

Borden, M. A., D. E. Kruse, C. F. Caskey, S. Zhao, P. A. Dayton, and K. W. Ferrara, "Influence of lipid shell physicochemical properties on ultrasound-induced microbubble destruction," *IEEE Trans Ultrason Ferroelectr Freq Control*, 52(11): pp. 1992–2002, 2005.

Chin, C. T., C. T. Lancée, J. M. G. Borsboom, F. Mastik, M. E. Frijlink, N. de Jong, M. Versluis, and D. Lohse, "Brandaris 128: A 25 million frames per second digital camera with 128 highly sensitive frames," *Rev Sci Instr*, 74(12): pp. 5026–5034, 2003.

Dayton, P. A., K. E. Morgan, A. L. Klibanov, G. H. Brandenburger, and K. W. Ferrara, "Optical and acoustical observations of the effects of ultrasound on contrast agents," *IEEE Trans Ultrason Ferroelectr Freq Control*, 46(1): pp. 220–232, 1999.

de Jong, N., M. Emmer, C. T. Chin, A. Bouakaz, F. Mastik, D. Lohse, and M. Versluis, ""compression-only" behavior of phospholipid-coated contrast bubbles," *Ultrasound Med Biol*, 33(4): pp. 653–656, 2007.

Emmer, M., A. van Wamel, D. E. Goertz, and N. de Jong, "The onset of microbubble vibration," *Ultrasound Med Biol*, 33(6): pp. 941–949, 2007.

Guidi, F., H. J. Vos, R. Mori, N. de Jong, and P. Tortoli, "Microbubble characterization through acoustically-induced deflation," *Accepted in IEEE Trans Ultrason Ferroelectr Freq Control*, 2009.

Kimmel, E., B. Krasovitski, A. Hoogi, D. Razansky, and D. Adam, "Subharmonic response of

encapsulated microbubbles: Conditions for existence and amplification," *Ultrasound Med Biol*, 33(11): pp. 1767–1776, 2007.

Leighton, T. G., The Acoustic Bubble, Academic Press, London, UK, 1994.

Longuet-Higgins, M. S., "Monopole emission of sound by asymmetric bubble oscillations. Part 1. Normal modes," *J Fluid Mech*, 201: pp. 525–542, 1989.

Marmottant, P., S. M. van der Meer, M. Emmer, M. Versluis, N. de Jong, S. Hilgenfeldt, and D. Lohse, "A model for large amplitude oscillations of coated bubbles accounting for buckling and rupture," *J Acoust Soc Am*, 118(6): pp. 3499–3505, 2005.

Prosperetti, A., "Nonlinear oscillations of gas bubbles in liquids: transient solutions and the connection between subharmonic signal and cavitation," *J Acoust Soc Am*, 57(4): pp. 810–821, 1975.

Ricci, S., E. Boni, F. Guidi, T. Morganti, and P. Tortoli, "A programmable real-time system for development and test of new ultrasound investigation methods," *IEEE Trans Ultrason Ferroelectr Freq Control*, 53(10): pp. 1813–1819, 2006.

Sijl, J., E. Gaud, P. J. Frinking, M. Arditi, N. de Jong, D. Lohse, and M. Versluis, "Acoustic characterization of single ultrasound contrast agent microbubbles," *J Acoust Soc Am*, 124(6): pp. 4091–4097, 2008.

Sijl, J., H. J. Vos, N. de Jong, D. Lohse, and M. Versluis, "Combined optical and acoustical characterization of individual us contrast microbubbles," in proc. Int Congr Acoust, Madrid, Spain, 2007.

van der Meer, S. M., B. Dollet, M. M. Voormolen, C. T. Chin, A. Bouakaz, N. de Jong, M. Versluis, and D. Lohse, "Microbubble spectroscopy of ultrasound contrast agents," *J Acoust Soc Am*, 121(1): pp. 648–656, 2007.

van Neer, P. L. M. J., G. Matte, J. Sijl, J. M. G. Borsboom, and N. de Jong, "Transfer functions of US transducers for harmonic imaging and bubble responses," *Ultrasonics*, 46(4): pp. 336–340, 2007.

Chapter 6

Nonspherical vibrations of microbubbles in contact with a wall - a pilot study at low mechanical index

Abstract - **Radially oscillating microbubbles can deform when in contact with a wall. These nonspherical shapes have a preferential orientation perpendicular to the wall. Conventional microscope setups for microbubble studies have their optical axis perpendicular to the wall ('top view'), consequently they have a limited view of the deformation of the bubble. We developed a method to image the bubble in a side view by integrating a mirror in the microscope setup. The image was recorded at 14.5 million frames per second by the high-speed Brandaris 128 camera. When insonified by a 1 MHz, 140 kPa ultrasound pulse, a 9 μm diameter coated bubble appeared spherical in the top view, but strongly nonspherical in the side view. Its shape was alternatively oblate and prolate, with maximum second order spherical harmonic amplitude equal to the radius.**

Appeared in *Ultrasound in Medicine & Biology*, by H. J. Vos, B. Dollet, J. G. Bosch, M. Versluis, and N. de Jong; Vol 34, Issue 4, pp. 685-688, April 2008.

6.1 Introduction

Ultrasound contrast agents (UCAs) consist of micron sized gaseous bubbles, stabilized by a thin coating of e.g. phospholipids or denatured albumin. They enhance the echoes from the blood circulation system in the body, facilitating quantification of physiologic parameters such as the cardiac output, myocardial perfusion, and vasculature of liver carcinoma [Feinstein, 2004]. More recently, UCA bubbles have been adopted to perform more sophisticated tasks such as specific targeting of bubbles to pathological tissue, so called molecular imaging [Lindner, 2004], and enhancing drug uptake of cells [van Wamel et al., 2006]. The physical mechanisms underlying these emerging applications are now subject of many detailed studies of bubble-wall interactions.

Over the past 15 years, multiple studies have addressed the acoustic response of ultrasound contrast agents. In early years, agents were characterized by the acoustical scattering and attenuating properties of a population of bubbles [de Jong et al., 1992; Hoff et al., 2000]. From that moment, advances in experimental technology gradually provided more insight in individual bubble dynamics. Optical systems were developed that fully captured the bubble's behavior. One method exploited laser-light scattering [Guan and Matula, 2004], which gives a relative value of the instantaneous 1-dimensional (1D) size. In 1999, bubble dynamics were resolved in a 1D streak image using a microscope and camera setup [Morgan et al., 2000]. The camera (Imacon 468) could additionally store seven 2D frames at high frame rate, facilitating the interpretation of the streak images. Higher frame numbers were available in the Ultranac system (twenty-four 2D frames) [Kuribayashi et al., 1999], and in the Brandaris 128 camera system, which is able to record 128 frames at rates up to 25 million frames per second (Mfps) [Chin et al., 2003]. Following this historical line, a setup that is able to image the bubble in 3 dimensions is believed to provide even more insight in the dynamics of a vibrating bubble.

A typical microbubble setup with a microscope includes an optically and acoustically transparent wall, to which bubbles float up by buoyancy; this allows for precise focusing of the optical equipment. The bubbles are typically imaged by an upright microscope, in which case the optical axis is perpendicular to the wall (a 'top view'). At low Mechanical Index (M.I.[1]) insonation of < 0.04, bubbles were observed to remain spherical during their vibration [van der Meer et al., 2007]. At higher pressures and long bursts, parametric instabilities lead to nonspherical surface modes, a range of ultrasound conditions that we do not address in this paper. From literature it is known that vibrating bubbles close to or in contact with a wall can show nonspherical shapes oriented perpendicularly to the wall [Blake et al., 1986; Prentice et al., 2005; Zhao et al., 2005; Fong et al., 2006]. In numerical simulation studies

[1] M.I. is defined as the ratio of peak negative pressure of an ultrasound pulse, in MPa, and the square root of its frequency in MHz

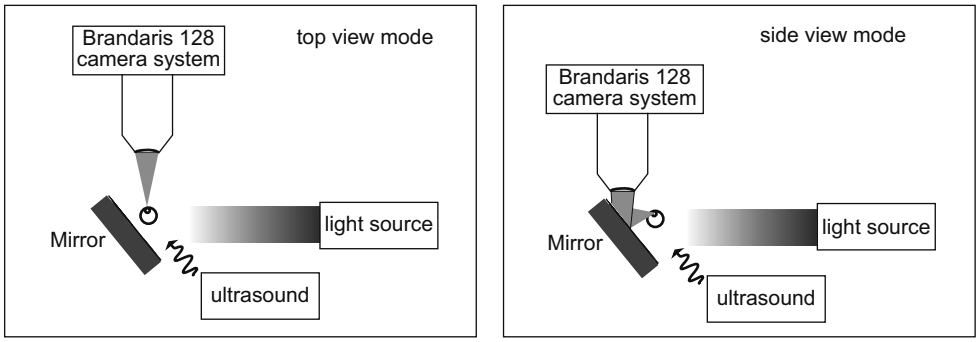

Figure 6.1: Experimental setup. The bubble is imaged inside the capillary tube, and the imaging mode ('top view' or 'side view') is selected only by the position of the microscope.

by Fong et al. [2006], this effect was already significant after excitation of a bubble with a one and half cycle, 80 kPa ultrasound pulse at its resonance frequency. Their model excluded any viscous and thermal damping and assumed a free gas-liquid surface of the bubble. In studies of UCA bubbles, the nonspherical oscillations were thought to be less significant as the coating of UCA microbubbles was expected to damp potential nonspherical oscillations. However, the commonly-used vertical microscope setups do not allow for imaging such nonspherical phenomena that are expected to occur parallel to the optical axis.

Thus, our aims here were two-fold. The first was to develop a method to quasi-simultaneously project the bubble vibration in two orthogonal planes, as an improvement to the 2D setups used in the past. The second was to estimate the amplitude of potential nonspherical oscillations of a UCA bubble in contact with a rigid wall. The method and first results are presented here.

6.2 Material and Methods

The experimental setup (see Fig. 6.1) consisted of a mirror, a microscope and the high-speed Brandaris-128 camera [Chin et al., 2003]. Highly diluted Definity agent (Bristol Myers Squibb MI - currently Lantheus Medical Imaging, North Billerica, MA, USA) was inserted in a cellulose tube (Cuprophan, Akzo Nobel Faser AG, Germany), which has an inner diameter of 160 μm and wall thickness of 20 μm, and which was submersed in a water tank.

Buoyancy forces the bubbles in the agent to float to the top. There they were imaged along two perpendicular optical axes, denoted 'top view' and 'side view',

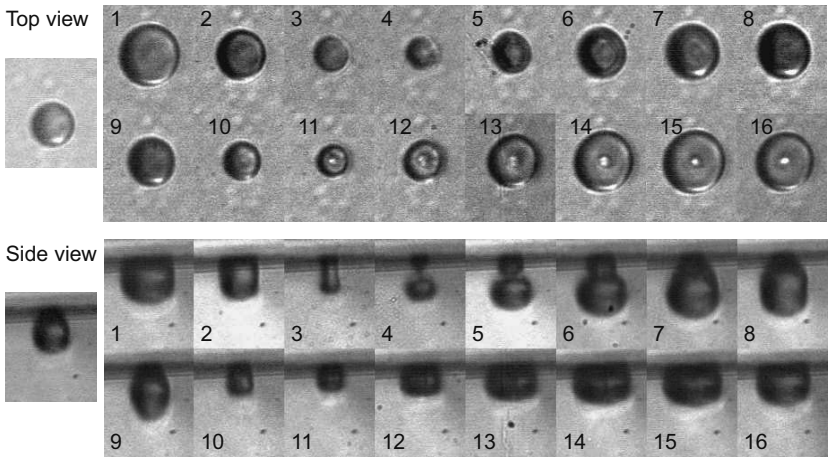

Figure 6.2: Optical images of the bubble during 2 cycles of the ultrasound pulse. Top panel shows top view images at an interframe time of 138 ns. The bottom panel shows the same segment of bubble oscillations in side view, recorded 2 minutes later. The bubble wall appears as a grey region on the top. Resting diameter of the bubble (left) was 9 μm.

respectively. In top view, a single bubble is imaged from above, which is the conventional optical detection mode. In the side view mode, the bubble is observed through a mirror positioned at an angle of 45° to the optical axis of the microscope. The viewing mode is selected by adjusting the position of the microscope with respect to the mirror. The distance between the bubble in the tube and the mirror surface was 0.50 mm.

Ultrasound pulses were generated by a 1-MHz broadband focused transducer (V302-SU 3", Panametrics-NDT, Waltham, MA, USA), which was driven by a high power RF linear amplifier (A-500, ENI, Rochester, United Kingdom). The ultrasound pulse contained 6 cycles at 1 MHz with a cosine-tapered window. The pressure in the focus of the transducer, 140 kPa in the experiment reported here, was measured with a calibrated hydrophone in a separate setup.

6.3 Results

A bubble with a diameter of 9 μm, which is close to the expected resonant size at 1 MHz for a similar type of microbubble [van der Meer et al., 2007], was studied in these experiments. The oscillation dynamics were recorded in top view mode. Next, the dynamics of the very same bubble was recorded in side view mode. Both recordings contain 128 frames at a rate of 14.5 Mfps, and sixteen frames of each recording are selected for Fig. 6.2. The sequence in Fig. 6.2 starts at maximum expansion of the bubble, and covers 2 cycles of ultrasound insonation.

In top view (top panel of Fig. 6.2), the bubble shows a circular shape throughout, without deformation. When viewed from the side (bottom panel) a strikingly different behavior is observed. In frame 3, the bubble shape is strongly prolate (defined by having two short axes and one long axis). In frames 4 – 6, the original bubble even seems to momentarily split. Between frames 9 and 10, the bubble wall velocity in the sequence is one order higher (10 μm/0.14 μs ∼ 70 m/s) than the typical wall velocity during oscillation. Starting in frame 12, the bubble shows a strongly oblate shape (i.e., two long orthogonal axes and one short), until the shape of frame 16 resembles the one in frame 1.

The circumferential edge of the bubble was tracked using a special implementation of a minimum cost algorithm in all frames [Bosch et al., 1995]. In this implementation, the contour in the previous frame was used as an estimate in the next frame and in two iterations the final shape was detected. The algorithm does not assume a spherical or convex shape. Decomposition of the circumferential edge into spherical harmonic amplitudes involved two steps. First, the contour was mapped onto polar coordinates (R, θ) having its origin in the center of gravity. Second, the amplitudes A_n for $n = 0$ and $n = 2$ were calculated from $R(\theta)$ using the Legendre polynomials,

$$A_n = (0.5 + n) \int_0^{\pi} R(\theta)\, P_n(\cos\theta) \sin\theta \, d\theta \tag{6.1}$$

where P_n represents the Legendre polynomial of order n. These steps were repeated for all frames. In the present configuration, a positive value of A_2 denotes a prolate shape.

Fig. 6.3 shows the amplitudes of the modes as observed in top view and side view as a function of time. The top panels show the radial mode excursion, while the bottom panels show the amplitudes of the second order shape mode. In the top view mode, the maximum radial excursion shows a 1.8 μm amplitude (40% of the initial radius), and second order surface modes shows negligible amplitude.

The side view analysis shows a radial oscillation having an initial increase of the amplitude (0 – 2.5 μs), a steady state oscillation (2.5 – 4.5 μs), and decaying amplitude (4.5 – 8.5 μs). The second order shape oscillation shows significant amplitude, up to 2 μm, which is equal to the instant radius at that instant of time. It also displays a clear subharmonic behavior. Note that the bubble size was reduced by 10% in the 2-minute interval between the two recordings.

6.4 Discussion

The side view setup has sufficient spatial and temporal resolution to resolve the oscillatory shapes of a microbubble in contact with a rigid wall, at low mechanical index (M.I. value of 0.14). The observed nonspherical shapes are not visible in the conventional imaging ('top view') mode, because the deformation has an orientation

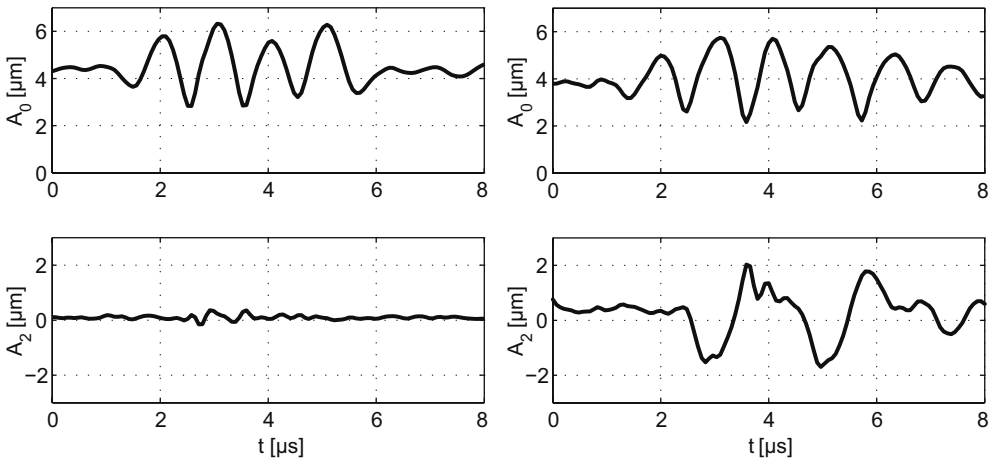

Figure 6.3: Amplitudes of the radial oscillation A_0 (top panel) and second order surface modes A_2 (bottom panel) as a function of time, when (left) imaged from the top and (right) imaged from the side.

perpendicular to the wall; a projection in top view of such a deformed bubble is circular. Moreover, the bubble volume cannot be quantified from the projected area observed in top view, as the oblate shape appears larger than the prolate shape, even though the volume of the bubble is conserved in the rarefaction phases of the ultrasound pulse. As a consequence, in top view, the alternating oblate and prolate shapes appear as an additional subharmonic oscillation, i.e., an oscillation with a frequency equal to half the excitation frequency. This could explain the results found by Chomas et al. [2002] regarding their observed subharmonic vibrations.

In this experiment, the amplitude of the second order nonspherical vibration reached values about equal to the instantaneous radius, correlating with a transient breakup of the bubble. Such finding is in line with the findings of Zhao et al. [2005] who also found strong prolate and oblate shapes for UCA bubbles excited at an M.I. of 0.2. Prentice et al. [2005] used an optical tweezer to position a microbubble close to a wall and insonified it at higher M.I., 0.7, than used here. They showed that jets can occur, which are deformations in an extreme sense. On the other hand, Garbin et al. [2007] have shown that for low M.I. insonation no significant deformations occur when bubbles interact with a wall or neighboring bubbles.

As mentioned in the Results section, the bubble had slightly reduced its size in the second sequence. Such deflation might have implications for the shell structure and overall bubble-dynamics and should be considered when accurately modeling the bubble behavior in 3 dimensions. Therefore the setup is currently being optimized to simultaneously image the bubble from both sides.

Further studies using the proposed side-view method could assist in establishing more quantitative understanding of the observed bubble-wall interaction, and might separate a range of conditions for which the nonspherical phenomena are significant from a range where they are not. The method can also be used to study the interactions between bubbles and biological tissue, providing detailed knowledge on mechanisms related to molecular imaging and drug delivery applications.

Bibliography

Blake, J. R., B. B. Taib, and G. Doherty, "Transient cavities near boundaries. Part 1. Rigid boundary," *J Fluid Mech*, 170: pp. 479–497, 1986.

Bosch, J. G., L. H. Savalle, G. van Burken, and J. H. C. Reiber, "Evaluation of a semiautomatic contour detection approach in sequences of short-axis two-dimensional echocardiographic images," *J Am Soc Echocard*, 8(6): pp. 810–821, 1995.

Chin, C. T., C. T. Lancée, J. M. G. Borsboom, F. Mastik, M. E. Frijlink, N. de Jong, M. Versluis, and D. Lohse, "Brandaris 128: A 25 million frames per second digital camera with 128 highly sensitive frames," *Rev Sci Instr*, 74(12): pp. 5026–5034, 2003.

Chomas, J., P. Dayton, D. May, and K. Ferrara, "Nondestructive subharmonic imaging," *IEEE Trans Ultrason Ferroelectr Freq Control*, 49(7): pp. 883–892, 2002.

de Jong, N., L. Hoff, T. Skotland, and N. Bom, "Absorption and scatter of encapsulated gas filled microspheres: Theoretical considerations and some measurements," *Ultrasonics*, 30(2): pp. 95–103, 1992.

Feinstein, S. B., "The powerful microbubble: from bench to bedside, from intravascular indicator to therapeutic delivery system, and beyond," *Am J Physiol Heart Circ Physiol*, 287(2): pp. H450–457, 2004.

Fong, S. W., E. Klaseboer, C. K. Turangan, B. C. Khoo, and K. C. Hung, "Numerical analysis of a gas bubble near bio-materials in an ultrasound field," *Ultrasound Med Biol*, 32(6): pp. 925–942, 2006.

Garbin, V., D. Cojoc, E. Ferrari, E. Di Fabrizio, M. L. J. Overvelde, S. M. van der Meer, N. de Jong, D. Lohse, and M. Versluis, "Changes in microbubble dynamics near a boundary revealed by combined optical micromanipulation and high-speed imaging," *Appl Phys Lett*, 90: p. ref. 114103, 2007.

Guan, J. and T. J. Matula, "Using light scattering to measure the response of individual ultrasound contrast microbubbles subjected to pulsed ultrasound *in vitro*," *J Acoust Soc Am*, 116(5): pp. 2832–2842, 2004.

Hoff, L., P. C. Sontum, and J. M. Hovem, "Oscillations of polymeric microbubbles: Effect of the encapsulating shell," *J Acoust Soc Am*, 107(4): pp. 2272–2280, 2000.

Kuribayashi, K., N. Kudo, M. Natori, and K. Yamamoto, "A high-magnification and high-speed system for the observation of microbubbles under ultrasound exposure," in proc. IEEE Ultras Symp, vol. 1, pp. 1755–1758, Lake Tahoe, Nevada, 1999.

Lindner, J. R., "Microbubbles in medical imaging: Current applications and future directions," *Nat Rev Drug Discov*, 3(6): pp. 527–532, 2004.

Morgan, K. E., J. S. Allen, P. A. Dayton, J. E. Chomas, A. L. Klibanov, and K. W. Ferrara, "Experimental and theoretical evaluation of microbubble behavior: Effect of transmitted

phase and bubble size," *IEEE Trans Ultrason Ferroelectr Freq Control*, 47(6): pp. 1494–1509, 2000.

Prentice, P., A. Cuschieri, K. Dholakia, M. Prausnitz, and P. Campbell, "Membrane disruption by optically controlled microbubble cavitation," *Nat Phys*, 1(2): pp. 107–110, 2005.

van der Meer, S. M., B. Dollet, M. M. Voormolen, C. T. Chin, A. Bouakaz, N. de Jong, M. Versluis, and D. Lohse, "Microbubble spectroscopy of ultrasound contrast agents," *J Acoust Soc Am*, 121(1): pp. 648–656, 2007.

van Wamel, A., K. Kooiman, M. Harteveld, M. Emmer, F. J. ten Cate, M. Versluis, and N. de Jong, "Vibrating microbubbles poking individual cells: Drug transfer into cells via sonoporation," *J Control Release*, 112(1): pp. 149–155, 2006.

Zhao, S., K. W. Ferrara, and P. A. Dayton, "Asymmetric oscillation of adherent targeted ultrasound contrast agents," *Appl Phys Lett*, 87: p. ref. 134103, 2005.

Chapter 7

Nonspherical shape oscillations of microbubbles in close contact with a wall

Abstract - **Ultrasound-driven oscillating microbubbles can induce cell membrane permeability (so-called sonoporation) which is favorable for enhanced drug uptake of the cell. The exact mechanism is not known, although it is generally believed that sonoporation is caused by normal and/or shear stresses, and/or by micro fluidic jets induced by the oscillating microbubbles. Quantification of these effects needs detailed observations of microbubbles. The shape of oscillating microbubbles in close contact with a wall can become nonspherical, and the center of gravity can translate towards and away from the wall in an oscillatory motion; both can also be of period-doubling nature. Both the exact shape and translation cannot be observed in the classical 'top view' used in microscope studies. In this study we expand the classical microscope with a second microscope objective placed orthogonally to the conventional objective; the images are recorded with an ultrafast framing camera. The nonspherical and translational behavior of many individual microbubbles of different sizes are thus systematically observed and categorized. A newly-developed theory based on potential flow and an acoustic boundary layer is used to estimate, from the recorded microbubble behavior, the normal and shear stresses on the wall.**

In preparation for submission; by H. J. Vos, B. Dollet, M. Versluis and N. de Jong. Parts of this chapter are published in the proceedings of the IEEE Ultrasonics Symposium 2007, New York, NY, USA. The authors whish to thank the technicians G. Springeling, W. van Alphen and C. Pakvis of the Erasmus MC, Rotterdam, the Netherlands, for their valuable effort in producing the setup.

7.1 Introduction

Ultrasound Contrast Agents (UCAs) consist of coated microbubbles and are injected into the blood circulation to image the cardiovascular system and blood perfusion. Owing to the high compressibility of gas compared to blood, microbubbles effectively scatter sound waves that are generated by the ultrasound equipment. In regular clinical ultrasound conditions, microbubbles can compress by over 50% of the initial radius, and they can expand by several factors of the initial radius [Caskey et al., 2005]. The expansion and compression are reduced when the microbubbles are located in confined spaces [Caskey et al., 2005, 2007; Thomas et al., 2009]. Despite the large amount of literature addressing the oscillation of microbubbles in confined spaces (see Qin et al. [2009] for an overview), fewer reports can be found on experimental reports of the interaction of contrast microbubbles with nearby surfaces. This is even more surprising since therapeutic use of coated microbubbles is widely investigated, in which this interaction plays a central role. It is know that ultrasound-driven microbubbles can open cell membranes to enhance drug and gene uptake, so called microbubble-enhanced sonoporation [Nyborg and Miller, 1982; van Wamel et al., 2004; Prentice et al., 2005; Bekeredjian et al., 2005; van Wamel et al., 2006; Ohl et al., 2006; Forbes et al., 2008; Wu and Nyborg, 2008]. The correlation between driving acoustic pressure amplitude and microbubble-enhanced drug uptake has been investigated by e.g. Forbes et al. [2008]; Kinoshita and Hynynen [2007], but no direct correlation between the radial oscillations of microbubbles and drug uptake has been quantified so far. The reason for this paucity is that special camera equipment is needed since the oscillation has a frequency in the order of several MHz, and the framing rate should be higher than the oscillation frequency. Furthermore, special methods (usually based on fluorescent techniques) are needed to observe both the uptake of drugs or genes, and cell survival.

Moreover, an aspect specifically addressed in this paper, a near surface can induce nonspherical shape deformations, micro fluidic jets, and translation of the microbubble towards and away from the wall during its oscillation. From literature it is known that nonspherical shape deformations relate to the radial oscillatory amplitude. See Fig. 7.1 for a schematic picture of possible nonspherical shapes of a microbubble during its oscillation. At very small amplitudes (excursion of some percent of the radius) the bubble predominantly keeps its spherical shape [Marmottant et al., 2006]. At larger amplitudes (10 – 50%) shape deformations become increasingly important, as shown both in experiments and in theory [Blake et al., 1986; Klaseboer and Khoo, 2004; Caskey et al., 2007; Qin et al., 2009]. These shape deformations generally have a period-doubling effect (i.e., at a one-half subharmonic) compared to the driving oscillation. When the oscillation amplitude further increases, towards a situation where the bubble radius is larger than about twice the initial radius, violent destructive effects will occur such as fragmentation [Chomas

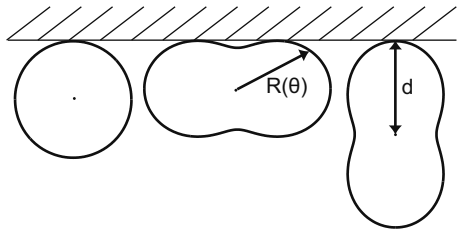

Figure 7.1: Schematic drawing of surface modes of a microbubble in contact with a wall. The distance between the center of gravity and the wall is denoted by d.

et al., 2001] and jets [Blake et al., 1986].

Several studies preliminary showed that ultrasound-driven coated microbubbles, in contact with a cellulose wall, also show nonspherical shape oscillations [Zhao et al., 2005; Vos et al., 2008; Dollet et al., 2008; Patil and Hossack, 2009]. Nonetheless, no study has yet been reported that systematically describes the shape oscillations perpendicular to the wall as a function of size and driving pressure amplitude. This paper performs such systematic description. Moreover, since translation and the nonspherical shape oscillations have a preferential direction normal to the wall, we have adapted the classical microscope setup to have simultaneous views on the bubble in two orthogonal planes. The observed microbubble behavior is numerically analysed using potential flow theory to estimate the resulting normal and shear stresses on the wall. It is anticipated that these data can be useful for clarifying the relation between microbubble oscillations and sonoporation effects.

7.2 Setup

7.2.1 Acoustic setup and insonation pulses

Tone bursts were generated by an arbitrary waveform generator (AWG 8026, Tabor Electronics, Tel Hanan, Israel) and power amplifier (A-500, ENI, Rochester, UK) that was connected to a PVDF-type focused ultrasound transducer (PA076, 2.5 cm focus, Precision Acoustics, Dorchester, UK). The transmission frequency was 2.25 MHz. Pulses contained 6 cycles, unless stated otherwise, and they were Gaussian-tapered. During an experiment microbubbles were insonified with 12 subsequent pulses, having increasing amplitudes of about 30 to 300 kPa peak rarefaction pressure. Acoustic pressures were measured in a separate setup with a calibrated hydrophone (0.2 mm PVDF, Precision Acoustics, Dorchester, UK).

7.2.2 Microbubbles and capillary

Experiments were performed with the small-animal ultrasound contrast agent Targestar P (Targeson, Charlottesville, VA), which consists of C_4F_{10}-filled microbubbles coated with phospholipids and an emulsifier. A diluted population (dilution higher than 1:1000 from the original vial) was inserted into a cellulose capillary tube (Cuprophan, Akzo Nobel Faser AG, Germany) with 20 μm wall thickness and 160 μm inner diameter. The microbubbles floated up to the inner top area of the tube. Flow in the tube was controlled with a syringe connected to a manual fine pith micrometer screw. Microbubbles with radius ranging from 1.3 to 3 μm were thus positioned in the focal area of the setup.

7.2.3 Optical setup

Both the nonspherical shape deformations and the translation of the center of gravity of microbubbles have a preferential direction perpendicular to the wall. Therefore both cannot be imaged in the classical 'top view' that is generally used in optical studies with a microscope. In this study we expand the classical microscope with a second microscope objective placed orthogonally to the conventional objective. See Fig. 7.2 for a schematic drawing of the setup. The orthogonal placement, and the focal distance of the microscope objectives, constrains the allowed physical size of the objective lenses. Fourty-times magnification water immersion lenses (LUMPLFL 40×/W, N.A. 0.8, Olympus, Tokyo, Japan) were selected that have a focal distance of 3.3 mm, and a lens diameter of about 6.5 mm. These dimensions allow simultaneous focusing of both objectives on the region of interest, although a protective cap had to be removed from both lenses to make it fit. To time-resolve microbubble oscillations having a frequency of several MHz, the camera system should have higher framing rates than several MHz. We therefore used the unique Brandaris-128 ultrafast framing camera that can record 2D frames at a rate up to 25 million frames per second (Mfps) [Chin et al., 2003]. The uniqueness of the camera implies that the images from both objectives have to be merged to allow simultaneous recording of the 'top view' and 'side view'. Therefore the collimated optical beams from the two objectives are mirrored towards a semi-transparent mirror at which they are combined (see Fig. 7.2). The objective lenses are mounted on separate manual precision stages.

In standard mode the Brandaris-128 camera records 6 movies of 128 frames. In this study the camera system was used in a segmented mode, thus dividing the frame sequence in 2 separate segments of 64 frames each, providing 12 movies per experiment [van der Meer et al., 2007]. The final resolution in the recorded frames was 0.17 μm per pixel, which was sufficient for accurately resolving the bubble shape.

Simultaneous to the ultrafast framing recordings, the side view was recorded

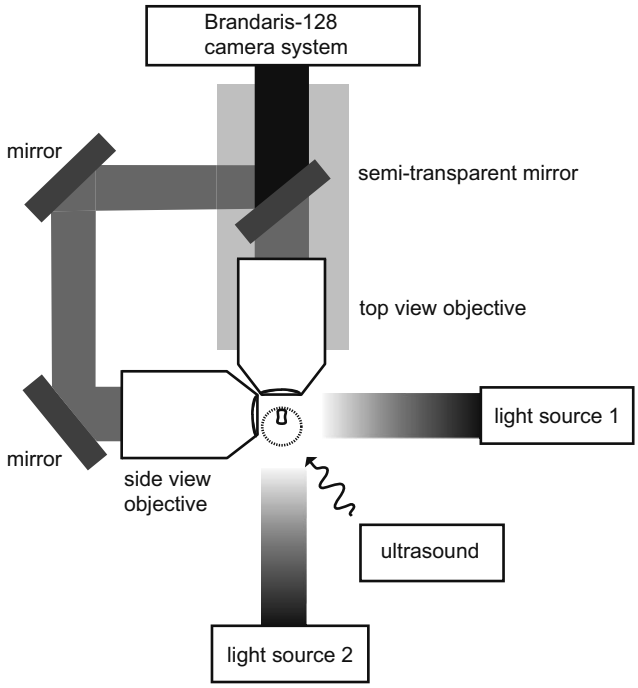

Figure 7.2: Schematic drawing of the setup showing the recombination of images of two objectives placed orthogonally.

with a regular video camera (Wat 902-H, Watec, Orangeburg, NY) operating at 30 fps, which frames were digitized and stored to a personal computer.

7.2.4 Image processing and data analysis

In order to quantify the nonspherical shape deformations, a spherical harmonic decomposition was applied as described in Vos et al. [2008]. Edge detection of the bubble in both side view and top view using a minimum cost algorithm as described in van der Meer et al. [2007] resulted in the bubble contour $R(\theta)$. The minimum cost algorithm was applied twice on the same microbubble image: In the first iteration the center of mass (c.o.m.) of the bubble is obtained; In the second iteration the final circumference is tracked around the correct c.o.m.. Decomposition of the circumferential shape into spherical harmonic amplitudes A_n, $n = 0$ and 2, was achieved using

$$A_n = (0.5 + n) \int_0^{\pi} R(\theta)\ P_n(\cos\theta)\ \sin\theta\, d\theta \tag{7.1}$$

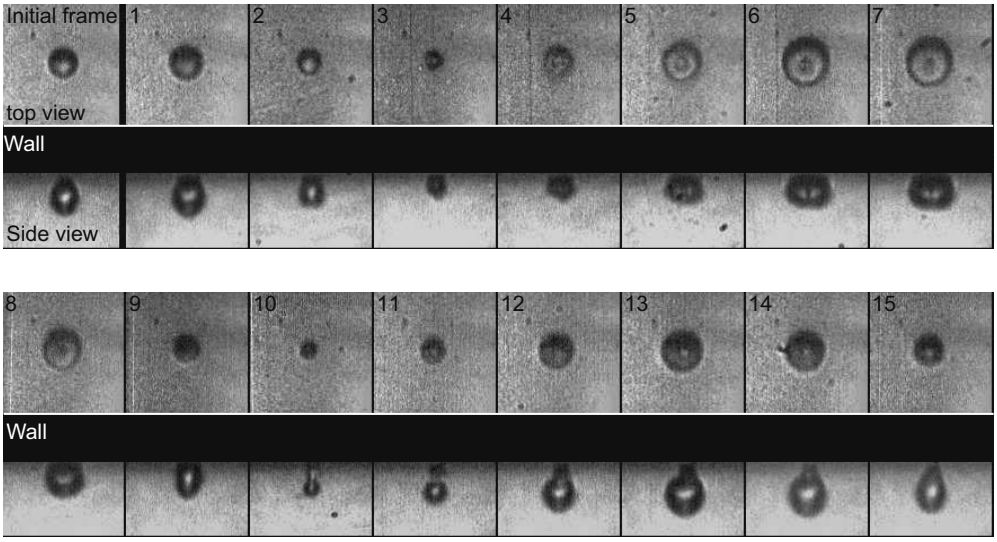

Figure 7.3: Selected frames from the recording of a bubble with a radius of 2.3 μm. Top rows show the top view of the bubble and lower rows show the same bubble in a side view, at the same moment. Ultrasound excitation pulse has 270 kPa amplitude, $f = 2.25$ MHz. Sampling time is 65 ns.

where P_n represents the Legendre polynomial of degree n and zero order. Note that a zero-order spherical harmonic shape assumes cylindrical symmetry around the axis perpendicular to the wall, which we will validate by the spherical symmetry of the bubble seen in top view. In the present configuration, a positive value of A_2 denotes an oblate (flattened) shape, and a negative value denotes a prolate (elongated) shape. The value of A_1, the translation mode, is always zero because the origin of $R(\theta)$ is equal to the center of mass (c.o.m.). The distance of the c.o.m. to the wall is denoted by d. From analysis of many recordings we estimate a root-mean-square noise level of 0.15 μm in $A_0(t)$, $d(t)$, and $A_2(t)$.

7.3 Results

7.3.1 Single bubble experiments

Fig. 7.3 shows selected frames from a recording of a 2.3 μm-radius bubble. The bubble was insonified with a pressure level of 270 kPa and a frequency of 2.25 MHz. The camera recorded at a frame rate of 15.3 Mfps corresponding to an interframe time of 65 ns. Full frames were cropped to two subframes of 108 × 108 pixels, showing both the top view and side view of the bubble.

The most-left frame in Fig. 7.3 shows the initial shape of the bubble and frames 1 – 15 depict the bubble oscillation. The shown frame sequence starts at the 3rd

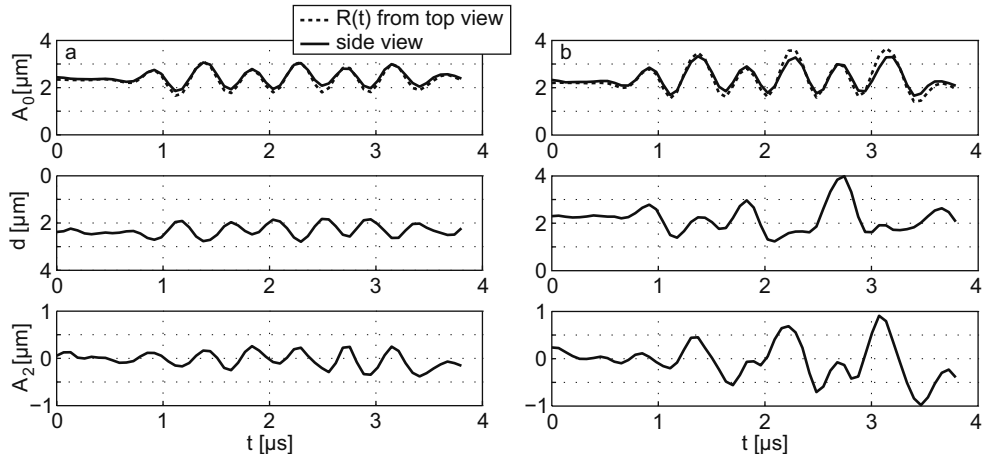

Figure 7.4: Shape analysis of bubble oscillation seen in top-view and seen in side-view. Ultrasound pulses had (a) 200 kPa and (b) 270 kPa pressure amplitude, a frequency of 2.25 MHz and contained 6 cycles.

expansion half-cycle of the bubble oscillation, and the sequence lasts for 2 cycles. The top view shows a spherical shape throughout, while the side view clearly shows nonspherical shapes of the vibrating bubble. A closer look at frames 5 – 7 reveals a torroidal shape of the bubble. Frames 9 – 12 show an elongated shape. Strikingly, in the top view images a torroidal shape (frame 7) appears larger than the elongated shape (frame 15) although the volume of the microbubble might not be different between frame 7 and frame 15. Furthermore, the side-view images show that the vibrating bubble stays in contact with the wall.

The bubble contour was decomposed into spherical harmonic amplitudes using Eq. 7.1. Fig. 7.4 shows the A_0, A_2, and d, the position of the c.o.m. relative to the wall, as a function of time. The microbubble was insonified at a pressure of 200 kPa (Fig. 7.4a) and 270 kPa (Fig. 7.4b) and with a frequency of 2.25 MHz. In Fig. 7.4a the A_0 oscillations shows a relative amplitude of 22% (calculated by ($1/2 \times$ peak-to-peak excursion) / R_0 = 0.5 µm / 2.3 µm). The relative amplitudes of d and A_2 are up to 25% and 17% in side view. By definition, a larger value of d corresponds to a bubble that has moved down, away from the tube wall. Detailed analysis using the Hilbert transform of the signal showed that no conclusive data on the oscillatory phase shift between $A_0(t)$ and $d(t)$, and between $A_0(t)$ and $A_2(t)$, can be given because of noise in the derived signals. This is a pity since the phase shifts determine the acoustic microstreaming around an oscillating microbubble [Marmottant et al., 2006].

Insonation at an amplitude of 270 kPa (Fig. 7.4b) leads to an excursion of A_0 of 52%. The $d(t)$ shows a more complex trajectory. In the first cycle, $d(t)$ roughly fol-

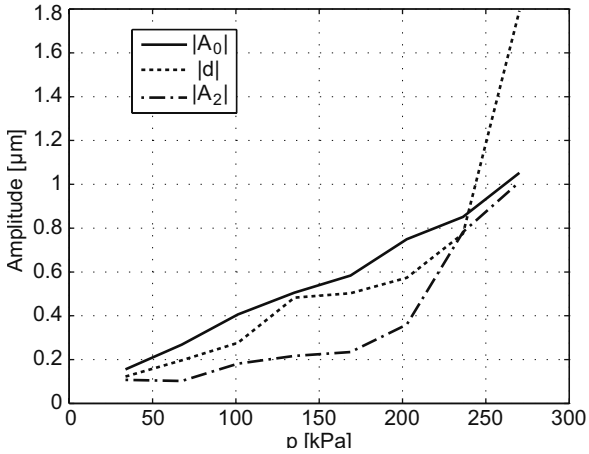

Figure 7.5: Pressure dependency of amplitude of radial mode oscillation ($|A_0|$), of distance $|d|$ and second order spherical harmonic ($|A_2|$). Frequency 2.25 MHz, microbubble initial radius of 2.3 µm.

lows the radial excursion (like in Fig. 7.4a). In subsequent cycles, a period-doubling response increasingly dominates the overall curve, while a small fundamental frequency component is still visible. The peak-to-peak excursion of d is almost 3 µm, which is large compared to the inital radius of 2.3 µm. At t = 2.7 µs, d is momentarily larger than A_0. Frame 11 in Fig. 7.3, corresponding to this time instance, shows that the microbubble is momentarily split up in two smaller bubbles: the largest bubble is far from the wall, and a smaller bubble is in contact with the wall. Some frames later the two bubbles have coalesced into a single bubble that is again in full contact with the wall.

The top view recordings show a spherical shape throughout the oscillations, from which we conclude that the axis of symmetry is indeed normal to the wall. As already addressed in Vos et al. [2008], an A_2 shape oscillation can produce an additional subharmonic component in top view in the radius-time curve, which could be erroneously interpreted as a volumetric subharmonic oscillation. The period-doubling response is also visible in the A_0-oscillation but it is not the dominant contribution. Additional analysis of the top view images showed that the radial oscillation observed in top view ($R(t)$) has about 25% higher subharmonic oscillation than the 'real' radial subharmonic oscillation of the bubble (A_0) as observed in side view.

In another experiment, the single bubble was excited with 12 pressure pulses with increasing pressure levels ranging from 30 to 300 kPa. Following the side-view analysis as depicted in Fig. 7.4, the amplitudes of oscillation of the 3 parameters (A_0, d, and A_2) are plotted as a function of the excitation pressure, see Fig. 7.5. The

amplitude of oscillation was obtained by taking the maximum of the envelope of the time traces. The envelope was calculated with the Hilbert transform. At a pressure larger than 270 kPa, the bubble resting size had decreased by more than 10% of the initial radius, and therefore results obtained at higher pressures were omitted in Fig. 7.5. The amplitudes of oscillation of the 3 parameters show an increase with increasing driving pressure level. Furthermore, the amplitude of d is smaller than, but on the same order of, the amplitude of the A_0 oscillation up to a driving pressure level of 230 kPa. This means that the oscillatory translation of the center of mass is significant, as also observed in Fig. 7.3. Also, the amplitude of oscillation of A_2 is roughly half of that of A_0, up to a driving pressure level of 200 kPa. This means that the nonspherical shape deformations are also significant. Remarkably, at 240 kPa and 270 kPa, when the bubble shows additional subharmonic response (Fig. 7.4b), the amplitude of oscillation of d becomes higher than that of A_0.

7.3.2 Multiple bubble results - fundamental-frequency response

Twenty differently-sized bubbles were subjected to similar analysis as described above, and generalized results are obtained. Since we are interested in both the fundamental-frequency response and the observed period-doubling effects, the time curves of A_0, d and A_2 are band-pass filtered to obtain a response at the fundamental frequency and at the subharmonic frequency. The amplitude of the filtered responses is then obtained by taking the maximum of the Hilbert transform of the filtered curves. Fig. 7.6 shows the amplitude of A_0 and d at the fundamental frequency as a function of radius and insonation pressure. The amplitude of oscillation *vs.* radius and pressure is coded into a gray color. White denotes the lowest amplitude and black the highest amplitude. The amplitudes are binned for better visualization. For some combinations of size and pressure no reliable data was available because of either fragmentation or fast deflation of the microbubbles within the duration of the excitation pulse. This area is filled with a course grid of lines, see for example the region around 1.6 μm radius and insonation pressure of 300 kPa in Fig. 7.6.

At an insonation pressure of 100 kPa, the maximum response of A_0 is seen for microbubbles with radius of 1.8 μm, which will therefore be referred to as the resonant size of these bubbles at 2.25 MHz. This value is within range of those found in literature for phospholipids coated microbubbles [Chomas et al., 2002; van der Meer et al., 2007; Vos et al., 2009].

A relative comparison between the oscillation amplitude of A_0 and d can be made based on the dataset. At any point in the experimental radius-pressure domain depicted in Fig. 7.6, the ratio between $|A_0|$ and $|d|$ is 0.6 on average, and always within the range 0.5 – 0.7. The ratio between $|A_2|$ at the fundamental frequency (not shown) and $|A_0|$ is at most 0.5.

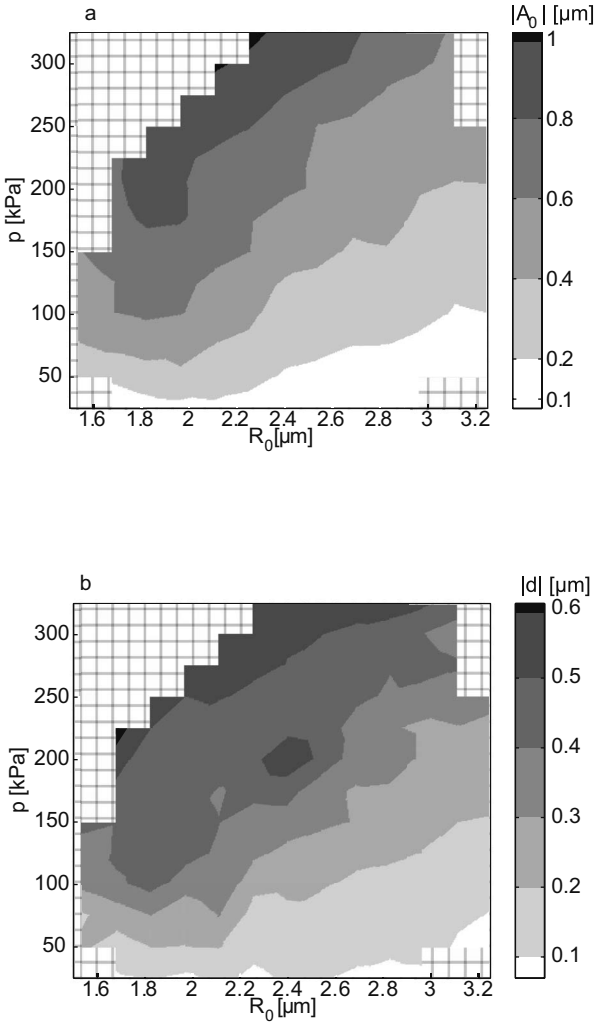

Figure 7.6: Generalized response obtained from 20 different bubbles (188 recordings). The grayscale denote the amplitudes of oscillation, at the fundamental frequency, of (a) A_0 and (b) d

7.3.3 Multiple bubble results - period-doubling response

The values of A_0, d and A_2 at the subharmonic frequency (i.e., 1.125 MHz) are shown in Fig. 7.7. Below an excitation level of 100 kPa, the values are at the noise level, but they show significant values above 100 kPa. Moreover, insonation pressure levels above 100 kPa lead to a fast increase of the amplitude of the subharmonic response. Therefore, 100 kPa is a threshold level for period-doubling nonspherical shape oscillations for the current setup, transmission frequency, and microbubbles. The threshold is lowest for a radius of 2.1 μm, which value is comparable to the minimum-threshold radius predicted by Chomas et al. [2002].

It is generally assumed that a subharmonic response is highest when the transmission frequency is roughly twice the resonance frequency [Prosperetti, 1975; Eller and Flynn, 1969; Sun et al., 2005]. According to van der Meer et al. [2007], a resonance frequency of 1.125 MHz would correspond to a radius of 4.3 μm, not 2.1 μm. The current observations are therefore in conflict with the general assumption of subharmonic response. However, a clear distinction should be made between a volumetric subharmonic response, and the period-doubling response of the nonspherical shape oscillations observed in this paper. A volumetric subharmonic response is generated because of a nonlinear relation between the driving pressure and the radial excursion. Period-doubling nonspherical shape oscillations are parametrically driven by the fundamental frequency oscillations [Longuet-Higgins, 1989]. Hence, it can be expected that nonspherical shape oscillations are highest when microbubbles are insonified close to their resonance frequency, as observed in this study. Unfortunately, bubbles with a radius of around 4.3 μm, that might show volumetric subharmonic oscillations, were out of range in the current experiments.

As already stated before, the occurrence of surface modes might bias the radial dynamics that are seen in a classical top view microscope setup. Based on the current dataset it can be shown that the subharmonic radial oscillation observed in top view has roughly 5% – 20% higher amplitude, except for where the occurrence of non-sphericity (A_2 modes and higher) is high: where the A_2-mode shows amplitude larger than 0.6 μm (corresponding to $R = 2.4\,\mu$m, p = 300 kPa), the subharmonic amplitude observed in top-view is overestimated by 80% compared to the subharmonic amplitude in side-view.

7.3.4 Destruction and fragmentation

When the oscillation amplitude becomes too high, microbubbles partially deflate within the duration of one pulse, or show fragmentation. Deflation and fragmentation prevents a good contour tracking and data analysis, and the recordings are excluded from the dataset represented in Figs. 7.6 and 7.7. The exclusion area is filled with the coarse gridlines in the figures. On the other hand, the information obtained from this exclusion is that especially smaller bubbles insonified with high

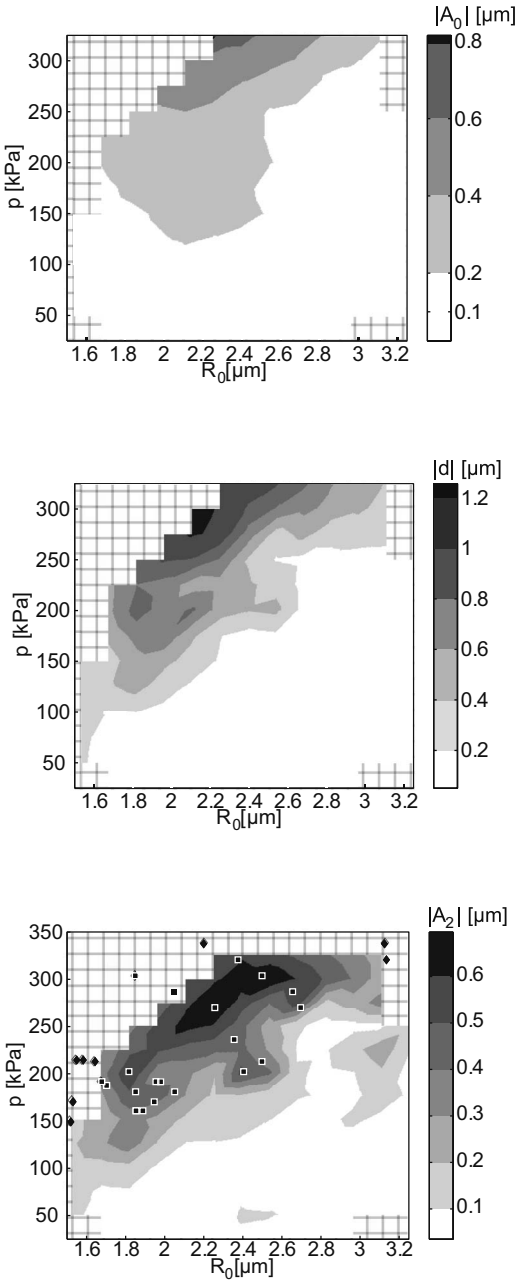

Figure 7.7: Generalized amplitudes of the subharmonic oscillation of (a) A_0; (b) d; and (c) A_2. The latter contains squares to denote the occurrence of jets, and diamonds to denote the occurrence of fragmentation.

pressure are destructed; this observation is concurring with the findings described earlier by Chomas and co-workers [Chomas et al., 1999, 2001, 2002]. The destruction threshold reported by Chomas et al. [2001] correlates well to the left-upper boundary between exclusion and analysis area in Figs. 7.6 and 7.7.

The frames in Fig. 7.3 shows an example of a transient fragmentation (frames 10 and 11), but regularly the high-amplitude nonspherical shape modes also lead to a persistent breakup of the bubble into 2 seperate bubbles. One bubble stays in contact with the wall while the other bubble is located at a distance of 5 to 10 μm from the wall. This effect was earlier observed by Zhao et al. [2005] without further analysis. We have manually scored the recordings and a diamond is drawn in Fig. 7.7c at the location where persistent bubble breakup occurs (N = 8). As expected the diamonds are located in the data-exclusion area. Highest chance of persistent bubble breakup is observed for a radius between 1.5 and 1.7 μm and an insonation pressure of 150 to 220 kPa.

During some recordings, the side-view image was also recorded with the 30 fps video camera. In these recordings the freely floating bubble that was formed after the bubble breakup, was seen to survive for at least 1 s while dragged away by residual flow in the capillary. The radius was about 0.5 μm. Uncoated bubbles, despite the relatively insoluble gas, would not survive for such long time, therefore the pinched-off bubbles are believed to have a phospholipids coating inherited from the original microbubble.

7.3.5 Jetting

Another observation in Fig. 7.3 is the spot in the center of the bubble in top view (frames 4 – 7). Careful observations of the side-view images reveal a thin dark line, with a width on the order of some pixels (i.e., roughly 0.5 μm). The line was visible despite a size close to the expected optical diffraction limit of the microscope and camera system. The combination of observation of the spot and the thin line leads us to believe that this is a microjet [Benjamin and Ellis, 1966; Zhao et al., 2005; Ohl et al., 2006]. The recordings were manually scored for the occurrence of such jet, and the results are plotted in Fig. 7.7c (N=22). A high correlation with the A_2 modes are seen, which is the reason why it is plotted in this graph. Moreover, it is observed that the occurrence of such jets do not signify instantaneous microbubble destruction.

7.3.6 Narcissus effect

As described by Marmottant et al. [2006], bubbles can be significantly attracted towards the wall by their image bubble. This attraction is a transient effect, i.e., after the insonation pulse the bubble restores its initial position. To investigate if such effect could also be observed with coated microbubbles, a 2.3 μm bubble was

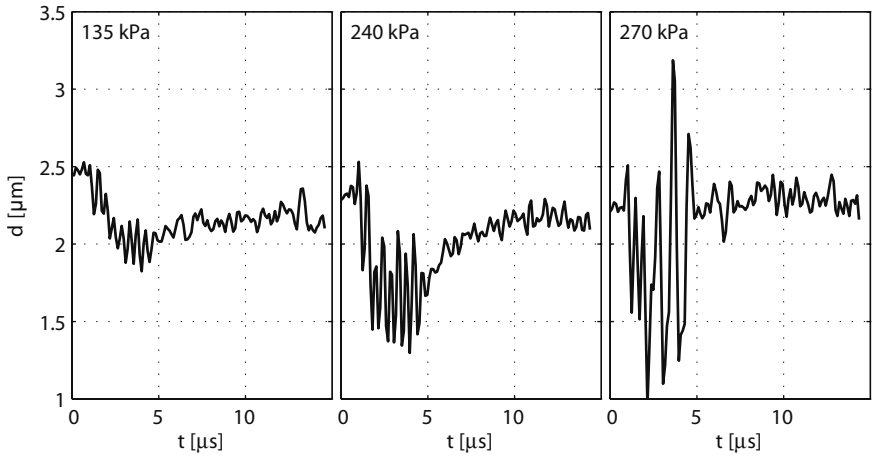

Figure 7.8: Narcissus effect and its cancellation by nonspherical oscillations. From left to right the excitation pressure was 135 kPa, 240 kPa, and 270 kPa.

insonified with 2.25 MHz tone bursts of 8 cycles. The camera was operated in its regular mode, providing 128 frames per movie, and at relatively low framing rate (∼8.5 Mfps) to have a long recording (14 µs) of possible attraction and recovery of the bubble's position. Fig. 7.8 shows the position of the center of mass as a function of time of the bubble when insonified with increasing pressure (135 kPa, 240 kPa, 270 kPa). In Fig. 7.8a the fundamental frequency oscillation of the bubble leads eventually to an average smaller distance between the bubble center and the wall. The bubble size (in terms of A_0) was not smaller after the insonation. In Fig. 7.8b, where the excitation pressure was 240 kPa, the attractive effect is stronger but similar in behavior as to the 135 kPa insonation. When the oscillation stops the initial distance slowly restores (time constant of about 3 µs). Fig. 7.8c, where the excitation pressure was only slightly higher, shows the effect of period-doubling nonspherical shape oscillations: after 2 initial cycles, the period-doubling oscillation starts to develop. Right after the end of the driving pulse ($t = 5\,\mu s$) the average distance to the wall is equal to the initial distance; nonspherical shape oscillations may cancel the Narcissus effect.

7.3.7 Effect of pulse length

The effect of the pulse length is investigated in Fig. 7.9. This graph shows the A_0 and A_2 oscillations of a 1.8 µm bubble insonified with two pulses, one containing 2 cycles and one containing 4 cycles at a frequency of 2.25 MHz and a pressure amplitude of 170 kPa. The oscillation starts at $t = 0.7\,\mu s$, and the bubble stays spherical up to about 1.4 µs, i.e., the value of A_2 is small during 1 full cycle of the driving

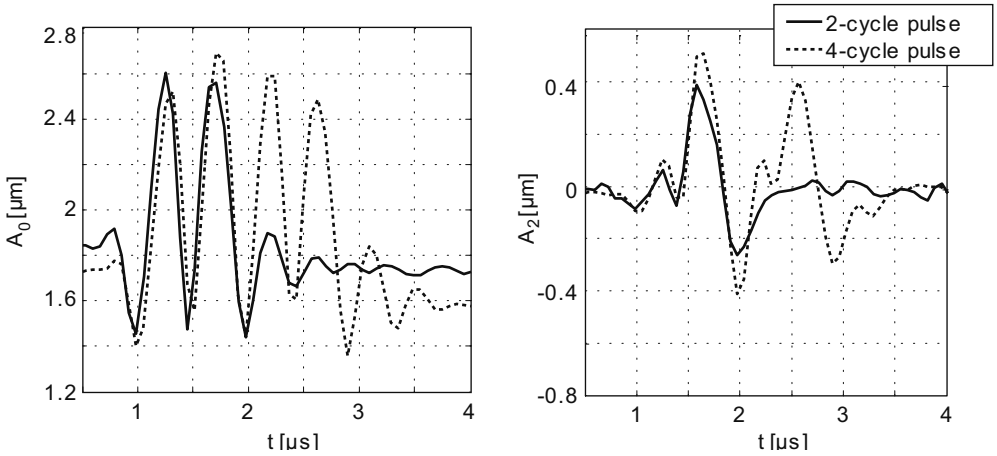

Figure 7.9: Influence of pulse length on the shape modes; (a) A_0 oscillation, (b) A_2 oscillation. Some ultrasound-induced deflation has reduced the initial size by 0.1 µm between the recording of the 2 cycle and the 4 cycle pulse (80 ms later)

pulse. At $t = 1.4$ µs the nonspherical shape oscillation starts, and the amplitude of the second cycle of the shape oscillation is almost equal to the amplitude of the first cycle. These graphs suggest that the nonspherical shape oscillation has developed after 3 cycles of the driving pulse, irrespective of any further cycles of the driving pulse. From this measurement it can be concluded that the results shown in Figs. 7.3 – 7.7 are not significantly affected by the choice of the pulse length, 6 cycles.

7.4 Discussion and analysis

7.4.1 General observations

The combination of the orthogonal microscope and an ultrafast framing camera provides a unique tool for studying the behavior of ultrasound contrast agent microbubbles in contact with a wall.

We observed nonspherical shape deformations and displacement of phospholipids coated microbubbles insonified at clinically relevant frequencies and pressures. This is consistent with findings reported in literature [Vos et al., 2008; Zhao et al., 2005]. The amplitude of the oscillation of the distance was about 0.6 times the radial excursion at the excitation frequency. Such translation might introduce additional viscous drag in the fluid, resulting in extra damping of the radial oscillation.

Period-doubling nonspherical shape oscillations were observed that lead also to a subharmonic frequency component in A_0 and d. The subharmonic behavior was earlier studied by Chomas et al. [2002] although that paper suggested that this oscillation occurred when the excitation frequency was twice the linear resonance

frequency. In our study, the resonant radius appeared to be very close to the radius where the nonspherical shape oscillations have lowest threshold. This leads us to believe that the subharmonic component is caused by a parametrically driven nonspherical shape oscillation that couples back to the volumetric oscillation [Longuet-Higgins, 1989].

7.4.2 Numerical estimate of normal and shear stresses

The goal of this subsection is to give an estimate of the shear stress and the pressure exerted on a wall by a neighboring bubble undergoing volumetric oscillations, translation, and nonspherical deformation. The model has not been validated yet with experimental results and therefore the results should be considered as preliminary.

We take several simplifying assumptions:

1. We assume that the wall is rigid, more precisely that its acoustic impedance is infinity. This is not the case, but to our knowledge, the general case of a nonrigid wall of arbitrary acoustic impedance has only been proposed in the case of an incident spherical wave [Ingard, 1951], hence does not apply when the bubble translates and deforms.

2. In agreement with our experimental results, we consider a translation only perpendicular to the wall, and we limit ourselves to the second axisymmetric mode of deformation. Moreover, we assume that the amplitudes of translation and deformation are small with respect to that of the volumetric oscillations.

3. We assume that the flow is potential everywhere, except in a thin boundary layer located close to the wall. To be rigorous, another boundary layer and a wake build up in the vicinity of the bubble when it starts oscillating, but we assume these regions not to interact with the boundary layer at the wall.

4. We assume that the wavelength is much bigger than all other relevant lengths; at a frequency $f = 2.25$ MHz and with a sound velocity $c = 1.5$ km/s, the wavelength equals $\lambda = c/f = 0.7$ mm, which is indeed two orders of magnitude higher than the bubble radius and the distance of the bubble center to the wall.

5. Gravity is neglected.

The viscous shear at the wall writes:

$$\tau_w(r,t) = \rho_L \nu \frac{\partial v_r}{\partial z}(r, z=0, t), \tag{7.2}$$

where $\rho_L = 10^3$ kg/m^3 is the liquid density, $\nu = 10^{-6}$ Pa s is the liquid kinematic viscosity, and v_r is the velocity component parallel to the wall. If the boundary layer

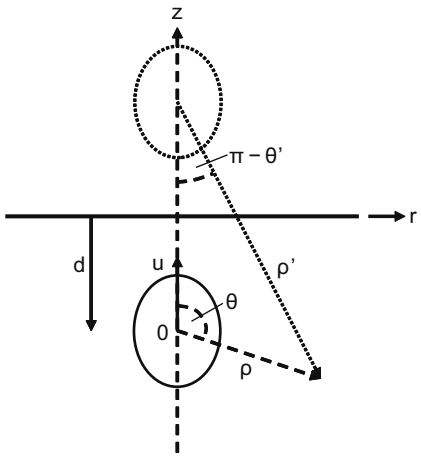

Figure 7.10: Notations for the analysis of the bubble-wall interaction.

is thin with respect to the typical scale d over which the velocity varies significantly, then v_r varies from zero at the wall (no slip boundary condition) to its potential value $V(r) = \partial\Phi/\partial r(r, z = 0)$, where Φ is the velocity potential. Using the classical results of the boundary layer theory Schlichting [1962],

$$v_r(r, z, t) = \int_{-\infty}^{t} \frac{\partial V}{\partial t'}(r, t')\mathrm{erf}\ \frac{z}{2\sqrt{\nu(t - t')}}\mathrm{d}t',$$

where erf is the error function; inserting this expression in Eq. 7.2 yields:

$$\tau_w(r, t) = \rho_L \sqrt{\frac{\nu}{\pi}} \int_{-\infty}^{t} \frac{\partial V}{\partial t'}(r, t') \frac{\mathrm{d}t'}{\sqrt{t - t'}}. \tag{7.3}$$

Similarly, the pressure at the wall writes Schlichting [1962]:

$$p(r, t) = -\rho_L \frac{\partial \Phi}{\partial t}(r, z = 0, t) - \frac{1}{2}\rho_L V(r, z = 0, t)^2, \tag{7.4}$$

where Φ is the velocity potential, from which these two expressions can be calculated.

Therefore, we have to determine the potential flow associated to a bubble undergoing volumetric oscillations, translation, and nonspherical deformation close to a wall. This problem has been addressed by Krasovitski and Kimmel [2004] with a boundary integral method, and by van der Geld and Kuerten [2009] with both an analytical and boundary integral methods. In our case, we seek explicit expressions of the shear stress and pressure exerted on the wall as functions of the coefficients A_0, A_2 and of the velocity u of the center of mass, hence we consider the analytical

method. Since the wall is a plane of symmetry, there is a general expression for the velocity potential satisfying Laplace equation $\Delta\Phi = 0$ and the boundary condition $\partial\Phi/\partial z = 0$ at the wall [Doinikov, 2001; van der Geld and Kuerten, 2009]:

$$\Phi(\rho,\theta) = \sum_{k=0}^{+\infty}\left[\alpha_k\left(\frac{R}{\rho}\right)^{k+1} + \left(\frac{\rho}{R}\right)^{k}\sum_{q=0}^{+\infty}\frac{(k+q)!}{k!q!}\left(\frac{R}{2d}\right)^{k+q+1}\alpha_q\right]P_k(\mu),$$

where P_k is Legendre polynomial of degree k, and $\mu = \cos\theta$. The coefficients are then determined from the boundary conditions to be satisfied at the bubble surface, at any order in $R/2d$. However, this expression is only valid for $R < 2d$ and diverges when $\rho \to +\infty$, hence cannot be used to predict the shear stress and pressure everywhere at the wall.

Therefore, we will use the simpler method of images, which is the simple superposition of the velocity potential of the real bubble in the absence of the wall with that of its image bubble (dashed shape in Fig. 7.10): the velocity potential is then regular at infinity, but the boundary conditions cannot be fulfilled exactly on the bubble surface, with errors appearing at second order in $R/2d$. We will therefore write:

$$\Phi(\vec{r}) = \Phi_{\text{real}}(\vec{r}) + \Phi_{\text{image}}(\vec{r}). \tag{7.5}$$

The velocity potential associated to an isolated bubble undergoing volumetric oscillations, translation, and nonspherical deformation in an unbounded fluid has been considered by various authors [Benjamin and Ellis, 1990; Feng and Leal, 1995; Doikinov, 2004]. We take the approach of Doikinov [2004]: if the bubble surface is described by the equation:

$$S(\rho,\theta,t) = \rho - R(t) - \sum_{n=2}^{+\infty} A_n(t)P_n(\mu) = 0,$$

and the velocity potential by:

$$\Phi(\rho,\theta,t) = -\frac{R^2\dot{R}}{\rho} + \sum_{n=0}^{+\infty} a_n(t)P_n(\mu) = 0,$$

where it is assumed that $|A_n| \ll R$, $|a_n| \ll R|\dot{R}|$ and $|u| \ll |\dot{R}|$, then at leading order $a_0 = 0$, $a_1 = -R^3u/2$ and $a_n = -(2A_n\dot{R} + \dot{A}_nR)R^{n+1}/(n+1)$. Therefore, we take the following velocity potentials:

$$\Phi_{\text{real}}(\vec{r}) = -\frac{R^2\dot{R}}{\rho} - \frac{1}{2}R^3u\frac{\mu}{\rho^2} - \frac{1}{3}R^3(2A_2\dot{R} + \dot{A}_2R)\frac{P_2(\mu)}{\rho^3}, \tag{7.6}$$

and by mirror symmetry with respect to the wall,

$$\Phi_{\text{image}}(\vec{r}) = -\frac{R^2\dot{R}}{\rho'} + \frac{1}{2}R^3u\frac{\mu'}{\rho'^2} - \frac{1}{3}R^3(2A_2\dot{R} + \dot{A}_2R)\frac{P_2(\mu')}{\rho'^3}. \tag{7.7}$$

Inserting Eqs. 7.6 and 7.7 in Eq. 7.5, and using the geometrical relations (see Fig. 7.10) $\rho^2 = r^2 + (d+z)^2$, $\rho'^2 = r^2 + (d-z)^2$, $\mu = (d+z)/\rho$ and $\mu' = (z-d)/\rho$ the velocity potential becomes:

$$\begin{aligned}\Phi(r,z) &= -R^2\dot{R}\left[\frac{1}{\sqrt{r^2+(d+z)^2}} + \frac{1}{\sqrt{r^2+(d-z)^2}}\right] \\ &\quad -\frac{1}{2}R^3 u\left\{\frac{d+z}{[r^2+(d+z)^2]^{3/2}} + \frac{d-z}{[r^2+(d-z)^2]^{3/2}}\right\} \\ &\quad -\frac{1}{3}R^3(2A_2\dot{R} + \dot{A}_2 R)\left\{\frac{2(d+z)^2 - r^2}{[r^2+(d+z)^2]^{5/2}} + \frac{2(d-z)^2 - r^2}{[r^2+(d-z)^2]^{5/2}}\right\}.\end{aligned}$$

The values of $\dot{\Phi}$, V and $\dot{V}$ can be computed from the experimental data. When time derivation is concerned, the relation $\dot{d} = -u$ should be used. Also, second order terms of the form u^2, $A_2 u$ and their time derivatives appear, which we discard since we have truncated the velocity potential at first order. After all calculations, the pressure Eq. 7.4 becomes:

$$\begin{aligned}p(r,t) &= -\rho\left\{-\frac{2(R^2\ddot{R} + 2R\dot{R}^2)}{\sqrt{r^2+d^2}} - \frac{(5R^2\dot{R}u + R^3\dot{u})d}{(r^2+d^2)^{3/2}}\right. \\ &\quad -R^2(2R\ddot{R}A_2 + 6\dot{R}^2A_2 + 6R\dot{R}\dot{A}_2 + R^2\ddot{A}_2)\frac{2d^2 - r^2}{3(r^2+d^2)^{5/2}} \\ &\quad \left.+2r^2\left[\frac{R^4\dot{R}^2}{(r^2+d^2)^3} + \frac{3R^5 du\dot{R}}{(r^2+d^2)^4} + R^5\dot{R}(2A_2\dot{R} + \dot{A}_2 R)\frac{4d^2 - r^2}{(r^2+d^2)^5}\right]\right\}.\end{aligned}$$

The time derivative of the velocity at the wall equals:

$$\begin{aligned}\dot{V}(r,t) &= r\left[\frac{2(R^2\ddot{R} + 2R\dot{R}^2)}{(r^2+d^2)^{3/2}} + \frac{3(5R^2\dot{R}u + R^3\dot{u})d}{(r^2+d^2)^{5/2}}\right. \\ &\quad \left.+R^2(2R\ddot{R}A_2 + 6\dot{R}^2A_2 + 6R\dot{R}\dot{A}_2 + R^2\ddot{A}_2)\frac{4d^2 - r^2}{3(r^2+d^2)^{7/2}}\right].\end{aligned}$$

The shear stress Eq. 7.3 can be calculated from the time derivative of the velocity potential at the wall $\dot{V}(r,t)$. However, the history kernel in Eq. 7.3 has a factor that goes to infinity if t' approaches t. This problem was solved using the solution given by Garbin et al. [2009]. The integral in Eq. 7.3 is divided into three intervals. The first, from $-\infty$ to 0, is set to zero since it is assumed that the bubble is in rest before the arrival of the insonation pulse. The second interval ranges from 0 to $t' - \Delta t$ ($\Delta t \ll 1/f$) and the integration is carried out by a regular numerical forward integration (trapezoidal method) in MATLAB. In the final interval, $t' - \Delta t$ to t', the time derivative $\dot{V}$ can be considered constant and the integral is approximated by $2\dot{V}\sqrt{\Delta t}$. Setting the value of $\Delta t \approx 1/(35f)$, f the insonation frequency, yielded a stable solution.

The double time derivations of A_0, d and A_2 enhance the high-frequency noise present in those signals. Therefore time traces were first band-pass filtered to keep the subharmonic and fundamental frequency response, before the time derivatives were calculated.

Fig. 7.11 shows an example of results obtained with the analysis. The microbubble had an initial radius of 2.1 μm and the insonation pressure was 180 kPa. The bubble was oscillating in the regime where a period-doubling A_2 surface mode and translation was present; see Fig. 7.11a for the time curves of A_0, d, and A_2.

The shear stress at the wall varies as a function of time and lateral distance r (see Fig. 7.10 for the definition of r). The shear stress is zero at $r = 0$ for reasons of symmetry of the problem, and also at $r \to \infty$ where the fluid perturbation by the bubble has vanished. For these specific bubble and oscillations a maximum peak value of the shear stress was found at $r = 0.65$ μm; Fig. 7.11b shows the time dependency of the shear stress at that distance. For convenience a trend line was added (dotted line) that was obtained by low-pass filtering of the original shear stress curve. Strikingly, a steady non-zero shear stress is seen after three cycles of the original frequency. The non-zero shear stress is caused by a fluid motion regularly denoted as microstreaming around an oscillating bubble [Marmottant et al., 2006]. Moreover, the development of microstreaming means that the shear stresses have higher peak-values after some initial cycles than during the initial cycles.

Fig. 7.11c shows the time trace of the normal stress on the wall at $R = 0$, and Fig. 7.11d shows the peak-positive and peak-negative values of the time traces of the normal stress as a function of r. The maximum normal stresses are found at $r = 0$, which is expected since the wall motion of the microbubble with respect to the wall is highest at $R = 0$. It is also observed that the peak-negative pressure is generally larger than the peak-positive pressure. The bubble is more 'pulling' than 'pushing' at the wall.

Similar analysis as shown above is repeated for all microbubble recordings. The results are summarized in Fig. 7.12, that shows, as a function of microbubble radius and insonation pressure: (a) the maximum observed peak-positive normal stress; (b) the maximum observed peak-negative normal stress; (c) the maximum observed shear stresses; (d) the observed steady shear stresses during the final cycles of the insonation pulse.

Some general results can be extracted from the data plotted in Fig. 7.12. First is that the pulling forces on the wall are larger than the pushing forces; this is consistent with the data on bubble-cell interactions shown by van Wamel et al. [2004] where a cell membrane excursion is higher during the compression phase of the oscillation of a nearby microbubble. The amplitude of the normal stress at the wall is up to a factor of 5 higher than the insonation pressure, which might be explained by the resonant nature of microbubbles.

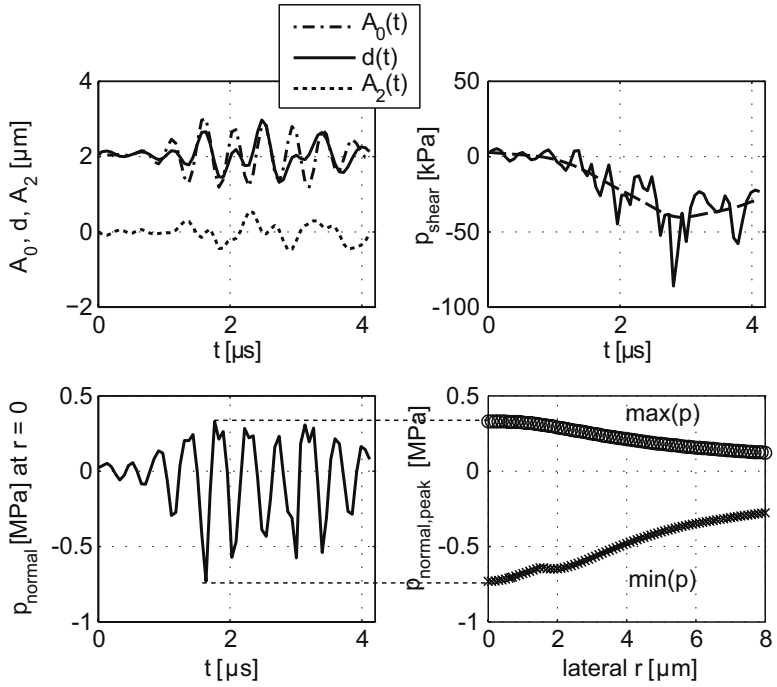

Figure 7.11: Example of calculated normal and shear stresses caused by the ultrasound driven microbubble in contact with the wall. The initial radius of the bubble was 2.1 µm, the insonation pressure was 180 kPa.

A second result is that the shear forces are larger than reported in literature for non-destructively oscillating contrast agent microbubbles. The order of magnitude, 25 – 350 kPa, is higher than the values as calculated by e.g. Forbes et al. [2008] that mention a shear stress of 17 kPa. A possible explanation for the difference could be that the current numerical model incorporates bubble translation and an acoustic boundary layer, which are neglected in the calculations by Forbes et al. [2008]. As can be shown, by artificially setting the radial excursion to zero and allowing only for translation and an A_2 oscillation, the peak shear stress generated by the bubble in Fig. 7.11 is around 30 kPa, compared to a higher peak shear stress of 90 kPa for the full numerical analysis. Such contribution is neglected in a model that does not incorporate a translation of the center of gravity, or surface modes, of the microbubble.

A third result is that, for any given radius, the normal and shear stresses initially show a linear relation with the insonation pressure, but the stresses show a higher increase for larger insonation pressures. In other words, a slight increase in insonation pressure can have a large increase of normal and shear stresses.

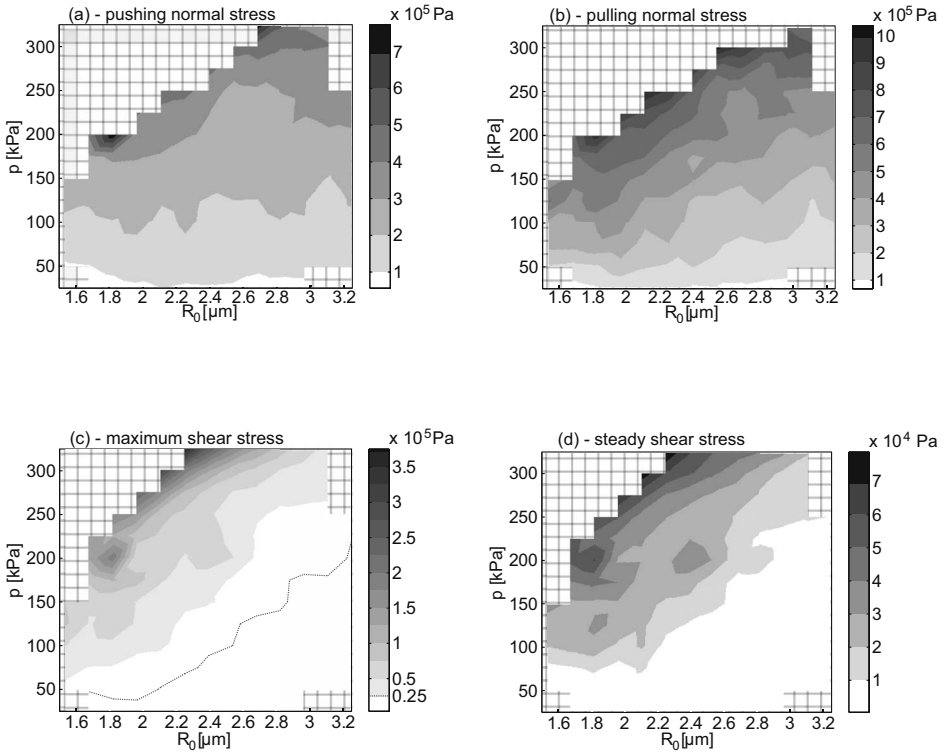

Figure 7.12: Generalized results of stresses acting on the wall, from the entire dataset: (a) peak-positive normal stress (pushing); (b) peak-negative normal stress (pulling); (c) Maximum shear stress; (d) steady shear stress during the final part of the insonation.

More results with the numerical analysis will be given in a future paper.

7.4.3 Influence of shape deformation on classical top view microscope recordings

The value of A_0 can be calculated from both the top view and side view images, as long as the A_2-amplitudes are relatively low. This finding may have various implications:

1. As an implication for the imaging point-of-view, we hypothesize that a conventional top view experimental setup is able to accurately capture the bubble volumetric behavior as long as the relative radial excursion (ΔR / R_0) is small.

2. From a bubble-behavior point-of-view, the current results suggest that many previous experiments with bubbles in a tube were carried out at acoustic pressures that induce nonspherical shape oscillations, see e.g. Marmottant et al. [2005]; Morgan et al. [2000]; Chomas et al. [2001, 2002]. However, the high correlation between spherical-bubble models and those *in vitro* experiments might indicate that small and medium nonspherical shape oscillations of coated bubbles do not significantly influence the radial motion.

3. In general, the far-field acoustic emission of a small source such as the resonant microbubble is predicted mainly by the volumetric oscillation [Longuet-Higgins, 1989]. The volumetric oscillation is equivalent to $\frac{4}{3}\,\pi\,A_0^3$, which can be accurately estimated from top view microscope recordings as long as the relative radial excursion is low.

7.4.4 Applications for subharmonic imaging

The data might serve the verification of models that predict the echo of targeted bubbles versus freely floating bubbles [Lindner, 2001; Christiansen and Lindner, 2005]. One important aspect of targeted bubbles is the appearance of a period-doubling oscillation of the microbubble, which can increase microbubble detection since tissue does not show subharmonic response (see e.g. [Eller and Flynn, 1969; Goertz et al., 2007]). This study shows that a regime can be defined in which the nonspherical and translational oscillations show a one-half subharmonic response. Chomas et al. [2002] have defined two different categories where the subharmonic response can be highest: when the transmit frequency equals the microbubble resonance frequency (TR) and when the transmit is at twice the resonance (T2R). The latter is generally assumed to produce the recorded subharmonic response from microbubbles [Chomas et al., 2002; Kimmel et al., 2007; Goertz et al., 2007]. Following the rationale in Chomas et al. [2002] we hypothesize that we recorded TR behavior, not T2R. The TR period-doubling response is a nonspherical shape oscillation that has potentially lower scattering strength than a T2R response. The acoustic scatter-

ing of these nonspherical shape oscillations, either by direct scattering or through a coupling to the A_0 mode, has yet to be investigated.

Bibliography

Bekeredjian, R., P. A. Grayburn, and R. V. Shohet, "Use of ultrasound contrast agents for gene or drug delivery in cardiovascular medicine," *J Am Coll Cardiol*, 45(3): pp. 329–335, 2005.

Benjamin, T. B. and A. T. Ellis, "The collapse of cavitation bubbles and the pressures thereby produced against solid boundaries," *Phil Trans R Soc Lond A*, 260(1110): pp. 221–240, 1966.

Benjamin, T. B. and A. T. Ellis, "Self-propulsion of asymmetrically vibrating bubbles," *J Fluid Mech*, 212: pp. 65–80, 1990.

Blake, J. R., B. B. Taib, and G. Doherty, "Transient cavities near boundaries. Part 1. Rigid boundary," *J Fluid Mech*, 170: pp. 479–497, 1986.

Caskey, C. F., D. E. Kruse, P. A. Dayton, and K. W. Ferrara, "On the oscillations of microbubbles in tubes with diameters as small as 12 microns," in proc. IEEE ultrasonics symposium, pp. 854–857, IEEE, Rotterdam, The Netherlands, 2005.

Caskey, C. F., S. M. Stieger, S. Qin, P. A. Dayton, and K. W. Ferrara, "Direct observations of ultrasound microbubble contrast agent interaction with the microvessel wall," *J Acoust Soc Am*, 122(2): pp. 1191–1200, 2007.

Chin, C. T., C. T. Lancée, J. M. G. Borsboom, F. Mastik, M. E. Frijlink, N. de Jong, M. Versluis, and D. Lohse, "Brandaris 128: A 25 million frames per second digital camera with 128 highly sensitive frames," *Rev Sci Instr*, 74(12): pp. 5026–5034, 2003.

Chomas, J. E., P. A. Dayton, J. S. Allen, K. E. Morgan, and K. W. Ferrara, "Mechanisms of contrast agent destruction," *IEEE Trans Ultrason Ferroelectr Freq Control*, 48(1): pp. 232–248, 2001.

Chomas, J. E., P. A. Dayton, D. J. May, and K. W. Ferrara, "Nondestructive subharmonic imaging," *IEEE Trans Ultrason Ferroelectr Freq Control*, 49(7): pp. 883–892, 2002.

Chomas, J. E., P. A. Dayton, K. E. Morgan, J. S. Allen, and K. W. Ferrara, "Optimization of microbubble destruction," in proc. IEEE Ultrasonics symposium, IEEE, 1999.

Christiansen, J. P. and J. R. Lindner, "Molecular and cellular imaging with targeted contrast ultrasound," *Proc IEEE*, 93(4): pp. 809–818, 2005.

Doikinov, A. A., "Translational motion of a bubble undergoing shape oscillations," *J Fluid Mech*, 501: pp. 1–24, 2004.

Doinikov, A. A., "Translational motion of two interacting bubbles in a strong acoustic field," *Phys Rev E*, 64(2): p. ref. 026301, 2001.

Dollet, B., S. M. Van der Meer, V. Garbin, N. de Jong, D. Lohse, and M. Versluis, "Nonspherical oscillations of ultrasound contrast agent microbubbles," *Ultrasound Med Biol*, 34(9): pp. 1465–1473, 2008.

Eller, A. I. and H. G. Flynn, "Generation of subharmonics of order one-half by bubbles in a sound field," *J Acoust Soc Am*, 46(3 (part2)): pp. 772–727, 1969.

Feng, Z. C. and G. L. Leal, "Translational instability of a bubble undergoing shape oscillations," *J Fluid Mech*, 7: pp. 1325–1336, 1995.

Forbes, M. M., R. L. Steinberg, and W. D. O'Brien Jr., "Examination of inertial cavitation of optison in producing sonoporation of chinese hamster ovary cells," *Ultrasound Med Biol*, 34(12): pp. 2009–2018, 2008.

Garbin, V., B. Dollet, M. Overvelde, D. Cojoc, E. Di Fabrizio, L. van Wijngaarden, A. Prosperetti, N. de Jong, D. Lohse, and M. Versluis, "History force on coated microbubbles propelled by ultrasound," *Phys Fluids*, 21: p. ref. 092003, 2009.

Goertz, D. E., M. E. Frijlink, D. Tempel, V. Bhagwandas, A. Gisolf, R. Krams, N. de Jong, and A. F. W. van der Steen, "Subharmonic contrast intravascular ultrasound for vasa vasorum imaging," *Ultrasound Med Biol*, 33(12): pp. 1859–1872, 2007.

Ingard, U., "On the reflection of a spherical sound wave from an infinite plane," *J Acoust Soc Am*, 23(3): pp. 329–335, 1951.

Kimmel, E., B. Krasovitski, A. Hoogi, D. Razansky, and D. Adam, "Subharmonic response of encapsulated microbubbles: Conditions for existence and amplification," *Ultrasound Med Biol*, 33(11): pp. 1767–1776, 2007.

Kinoshita, M. and K. Hynynen, "Key factors that affect sonoporation efficiency in *in vitro* settings: The importance of standing waves in sonoporation," *Biochem Biophys Res Commun*, 359: pp. 860–865, 2007.

Klaseboer, E. and B. C. Khoo, "An oscillating bubble near an elastic material," *J Appl Phys*, 96(10): pp. 5808–5818, 2004.

Krasovitski, B. and E. Kimmel, "Shear stress induced by a gas bubble pulsating in an ultrasonic field near a wall," *IEEE Trans Ultrason Ferroelectr Freq Control*, 51(8): pp. 973–979, 2004.

Lindner, J. R., "Targeted ultrasound contrast agents: Diagnostic and therapeutic potential (inv.)," in proc. IEEE Ultras Symp, vol. 1, pp. 1695–1703, 2001.

Longuet-Higgins, M. S., "Monopole emission of sound by asymmetric bubble oscillations. Part 1. Normal modes," *J Fluid Mech*, 201: pp. 525–542, 1989.

Marmottant, P., S. M. van der Meer, M. Emmer, M. Versluis, N. de Jong, S. Hilgenfeldt, and D. Lohse, "A model for large amplitude oscillations of coated bubbles accounting for buckling and rupture," *J Acoust Soc Am*, 118(6): pp. 3499–3505, 2005.

Marmottant, P., M. Versluis, N. de Jong, S. Hilgenfeldt, and D. Lohse, "High-speed imaging of an ultrasound-driven bubble in contact with a wall: "*Narcissus*" effect and resolved acoustic streaming," *Exp Fluids*, 41: pp. 147–153, 2006.

Morgan, K. E., J. S. Allen, P. A. Dayton, J. E. Chomas, A. L. Klibanov, and K. W. Ferrara, "Experimental and theoretical evaluation of microbubble behavior: Effect of transmitted phase and bubble size," *IEEE Trans Ultrason Ferroelectr Freq Control*, 47(6): pp. 1494–1509, 2000.

Nyborg, W. L. and D. L. Miller, "Biophysical implications of bubble dynamics," *App Sci Res*, 38: pp. 17–24, 1982.

Ohl, C.-D., M. Arora, R. Ikink, N. de Jong, M. Versluis, M. Delius, and D. Lohse, "Sonoporation from jetting cavitation bubbles," *Biophys J*, 91(11): pp. 4285–4295, 2006.

Patil, A. V. and J. A. Hossack, "A 3D FEA model for quantifying non-linear bubble dynamics," in proc. 14th Eur Symp Ultras Contrast Imaging, p. 67, Rotterdam, 2009.

Prentice, P., A. Cuschieri, K. Dholakia, M. Prausnitz, and P. Campbell, "Membrane disruption by optically controlled microbubble cavitation," *Nat Phys*, 1(2): pp. 107–110, 2005.

Prosperetti, A., "Nonlinear oscillations of gas bubbles in liquids: transient solutions and the connection between subharmonic signal and cavitation," *J Acoust Soc Am*, 57(4): pp. 810–821, 1975.

Qin, S., C. F. Caskey, and K. W. Ferrara, "Ultrasound contrast microbubbles in imaging and therapy: physical principles and engineering," *Physics Med Biol*, 54: pp. R27–R57, 2009.

Schlichting, H., Boundary Layer Theory, McGraw-Hill, New York, 2nd edn., 1962.

Sun, Y., D. E. Kruse, P. A. Dayton, and K. W. Ferrara, "High-frequency dynamics of ultrasound contrast agents," *IEEE Trans Ultrason Ferroelectr Freq Control*, 52(11): pp. 1981–1991, 2005.

Thomas, D. H., M. Emmer, H. J. Vos, N. de Jong, and V. Sboros, "Optical observations of microbubble oscillation in small tubes," in proc. IEEE Ultras Symp, Rome, Italy, 2009.

van der Geld, C. W. M. and J. G. M. Kuerten, "Axisymmetric dynamics of a bubble near a plane wall," *J Fluid Mech*, 640: pp. 267–305, 2009.

van der Meer, S. M., B. Dollet, M. M. Voormolen, C. T. Chin, A. Bouakaz, N. de Jong, M. Versluis, and D. Lohse, "Microbubble spectroscopy of ultrasound contrast agents," *J Acoust Soc Am*, 121(1): pp. 648–656, 2007.

van Wamel, A., A. Bouakaz, M. Versluis, and N. de Jong, "Micromanipulation of endothelial cells: ultrasound-microbubble-cell interaction," *Ultrasound Med Biol*, 30(9): pp. 1255–1258, 2004.

van Wamel, A., K. Kooiman, M. Harteveld, M. Emmer, F. J. ten Cate, M. Versluis, and N. de Jong, "Vibrating microbubbles poking individual cells: Drug transfer into cells via sonoporation," *J Control Release*, 112(1): pp. 149–155, 2006.

Vos, H. J., B. Dollet, J. G. Bosch, M. Versluis, and N. de Jong, "Nonspherical vibrations of microbubbles in contact with a wall - a pilot study at low mechanical index," *Ultrasound Med Biol*, 34(4): pp. 685–688, 2008.

Vos, H. J., D. E. Goertz, and N. de Jong, "Self-demodulation technique for microbubble excitation," *submitted to IEEE Trans Ultrason Ferroelectr Freq Control*, 2009.

Wu, J. and W. L. Nyborg, "Ultrasound, cavitation bubbles and their interaction with cells," *Adv Drug Delivery Rev*, 60(10): pp. 1103–1116, 2008.

Zhao, S., K. W. Ferrara, and P. A. Dayton, "Asymmetric oscillation of adherent targeted ultrasound contrast agents," *Appl Phys Lett*, 87: p. ref. 134103, 2005.

Chapter 8

The oscillation of microbubbles at body *versus* room temperature

Abstract - **The dynamic behavior of Ultrasound Contrast Agents (UCAs) is normally studied at room temperature ($\sim$ 21°C) although clinical usage of the agents is at $\sim$ 37°C. This paper reports an *in vitro* investigation of the influence of such temperature difference on the behavior of commercial agents SonoVue (Bracco) and Definity (Lantheus Medical Imaging). Microbubbles were held in a transparent tube that was submersed in a water reservoir at room temperature or body temperature. The insonation pulses had a frequency of 1.7 MHz and increasing pressure amplitude from 10 kPa to 80 kPa. Radial excursions were optically resolved using the ultrafast framing Brandaris-128 camera. SonoVue microbubbles that were resonant (diameter $\sim$ 4 μm) showed higher radial excursion at the higher temperature than at the lower temperature, up to a factor of 2. This factor was at most 1.5 for Definity. Both agents showed about 2-fold decrease of acoustic onset level when heated to body temperature. Definity showed higher acoustically-induced deflation when heated to body temperature, while the stability of SonoVue was not affected by the higher temperature.**

Partly based on a proceedings paper for the 2008 IEEE Ultrasonics Symposium, Beijing, China, pp. 982–984, by H. J. Vos, M. Emmer, and N. de Jong. The authors kindly acknowledge Dr. A. L. Klibanov (University of Virginia) for discussing the coating materials of SonoVue and Definity. The authors also thank Dr. M. Versluis and M. L. J. Overvelde (University of Twente) for discussing the research method and interpretation of the results.

8.1 Introduction

The dynamic behavior of Ultrasound Contrast Agents (UCAs) is normally studied at room temperature ($\sim$ 21°C) [Dayton et al., 1999; Gorce et al., 2000; Morgan et al., 2000; de Jong et al., 2002; Goertz et al., 2007; Kimmel et al., 2007; van der Meer et al., 2007; Needles et al., 2008; Stride, 2008]. However in a clinical setting the environment is at body temperature ($\sim$ 37°C). Commercial UCAs SonoVue (Bracco Int., Amsterdam, the Netherlands) and Definity (Lantheus Medical Imaging, North Billerica, MA, USA) consist of micron-ranging bubbles that have a coating consisting of a mixture of phospholipids, stabilizers (PEG stearate), and traces of other molecules. Such coating stabilizes the microbubbles against dissolution and coalescence. The phase transition temperature of commonly used phospholipids monolayers is between 42 – 55°C [Pu et al., 2006], but mixtures could have different transition temperatures. Furthermore, phospholipids coatings have been shown to support coexistence of a condensed phase and expanded phase in the molecule organization [Borden et al., 2006]. A temperature increase from room temperature to body temperature might lead to different organization of the molecules.

A phospholipids coating has been shown to influence the acoustic response of microbubbles through the specific strain-stress relation and viscosity of the coating [Dayton et al., 1999; Marmottant et al., 2005; van der Meer et al., 2007; Sijl et al., 2008; Stride, 2008; Tsiglifis and Pelekasis, 2008]. The difference in organization of the molecules might change either the strain-stress relation or the viscosity, and consequently the acoustic response. It is therefore hypothesized in this study that a difference in temperature can change the response of microbubbles, and that this difference is indicative of changes in the coating. Indeed a population-based study showed strong fluctuations of echogenicity of SonoVue with changing temperature [Guiot et al., 2006]. When slowly heating the population from 37 to 43°C, maximum scattering energy was observed at 40°C. Results on the population behavior of phospholipids coated microbubbles at body temperature compared to room temperature is reported by Mulvana et al. [2009], who explain the different behavior at the two temperatures by a change in size distribution. However, no study has yet been reported that addresses possibly different behavior on single phospholipids coated microbubbles, i.e., in which the size distribution of the population has no influence. This paper studies the relation between single microbubble behavior and the two temperatures.

Microbubble behavior has many features. Besides linear oscillations and the well-known higher harmonic distortion [de Jong et al., 2002], recent literature shows that phospholipids coated microbubbles can show strong nonlinear behavior such as thresholding and compression-only [Marmottant et al., 2005; de Jong et al., 2007; Emmer et al., 2007]. Thresholding is an effect where the acoustic pressure must exceed a certain level before the bubble shows oscillation [Emmer et al., 2007]. Nu-

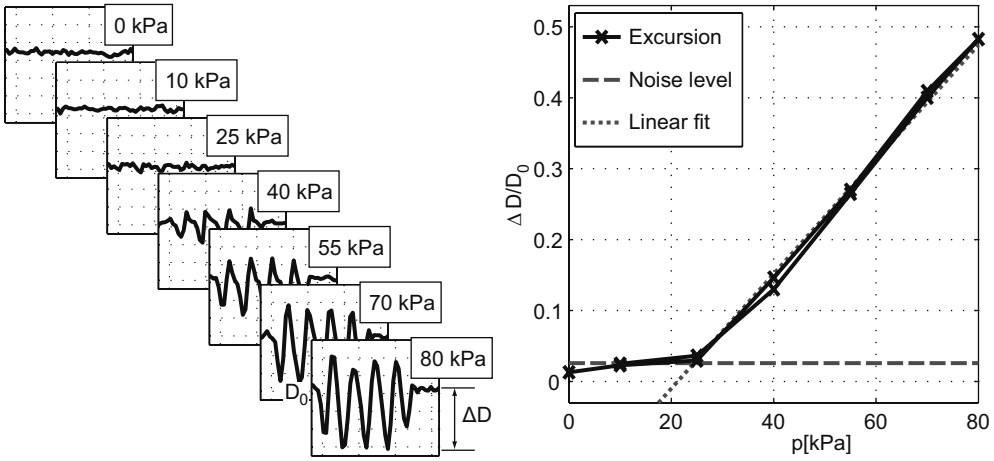

Figure 8.1: Example of data processing to obtain the threshold level of oscillations. This case shows the data of a Definity bubble of 2.9 μm diameter at T_{room}.

merical models implementing a visco-elastic coating cannot predict this effect, and it is hypothesized in literature that a specific strain-stress relation of the shell material such as described by Marmottant et al. [2005] or Borden et al. [2004] is better suited. This implies that the thresholding effect can support detecting differences in shell material properties.

Compression-only behavior is an effect in which the compression half-cycle of the bubble oscillation has higher amplitude than the expansion half-cycle. De Jong et al. [2007] have arbitrarily set a threshold at an expansion-to-compression ratio (E/C) of 0.5; i.e., if the compression is two times larger than the expansion then the bubble shows compression-only behavior (note that a unit value of E/C denotes a symmetric oscillation). This effect is regularly observed for bubbles coated with phospholipids or a polymer (see e.g. [Bouakaz et al., 2005; Marmottant et al., 2005; Kooiman et al., 2009]). It was further quantified by Emmer et al. [2007] who showed that bubbles smaller than 4 μm diameter were susceptible for compression-only when excited with 1.7 MHz pulses, and they experimentally showed that the asymmetry decreased for increasing pressure. Marmottant et al. [2005] also studied this effect and again attributed it to a strain-stress relation specific for phospholipids-coating.

Although the coating reduces diffusivity [Borden and Longo, 2002], coated microbubbles deflate over time and this deflation can be accelerated by acoustic excitation [Chomas et al., 2001; Borden et al., 2005; Guidi et al., 2009]. Chomas et al. [2001]; Borden et al. [2005]; Guidi et al. [2009] all showed that there is a strong size-dependency involved in this process: resonant bubble are most recep-

tive to acoustically-induced deflation while relatively small and large bubbles are not. Hence, repeatedly-pulsed excitation of bubbles of initially different sizes ultimately results in a compressed range of smaller sizes. Borden et al. [2005] showed that this ultimate size range depended on the mixture of phospholipids and stabilizers in the coating. Guidi et al. [2009] suggested an influence of the excitation parameters. This paper further studies the effect of ultrasound-induced deflation by investigating its dependency on temperature; it thus aims to contribute to the discussion of the poorly understood phenomenon of acoustically-induced deflation.

8.2 Experimental setup and methods

8.2.1 Experimental setup

Experiments were performed with Definity and SonoVue. Samples were prepared according to the guidelines of the manufacturers, diluted in Isotone II (Beckman Coulter, Fullerton, CA, USA), and fed into a capillary tube suspended in a pre-heated water reservoir. The setup did not allow for studying one single bubble at the two temperatures, since rapidly changing the water temperature would have also changed gas saturation levels of the water reservoir containing the bubbles. A difference in gas concentration inside and outside the bubbles might also influence the dynamic and dissolution behavior, which was not of interest in this study. Therefore, bubbles taken from a UCA vial were first recorded at room temperature ('T_{room}', $\sim$ 21°C), flushing the capillary after each recording to bring fresh bubbles in the optical view. Next, the water reservoir was heated to $\sim$ 37°C and left for 3 - 5 hours to restore gas equilibrium with the surroundings. Finally, fresh bubbles from the same vial were recorded at the higher temperature ('T_{body}').

Microbubble dynamics were resolved using a microscope and the ultrafast framing speed Brandaris-128 camera. Details on the general setup and the camera can be found in e.g. van der Meer et al. [2007]; Emmer et al. [2007]; Chin et al. [2003]. The resolution in the images was 0.09 μm per pixel. The framing rate was about 13 million frames per second, and insonation pulses contained 4 or 5 cycles of 1.7 MHz frequency, generated by an arbitrary waveform generator (AWG 8026, Tabor Electronics Ltd., Tel Hanan, Israel), a linear power amplifier (A-500, ENI, Rochester, NY, USA), and a single element focused transducer (V397-SU-3", Panametrics-NDT, Waltham, MA, USA). The acoustic pressure was sequentially changed from 0 to 80 kPa to investigate the linear and nonlinear responses, see Fig. 8.1.

8.2.2 Data analysis

In each recording the diameter as a function of time is obtained from the subsequent frames by a minimum-cost algorithm [Emmer et al., 2007; van der Meer et al., 2007]. This response is further digitally processed depending on the analysis

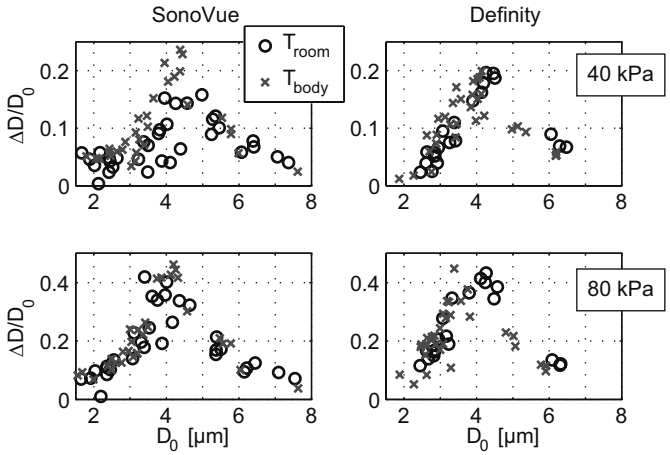

Figure 8.2: Radial excursion of SonoVue (left panels) and Definity (right panels) as a function of equilibrium diameter and insonation pressure (top panels 40 kPa, bottom panels 80 kPa). Insonation frequency 1.7 MHz. Circles and crosses denote data recorded at room temperature and body temperature, respectively.

purpose:

- the fundamental-frequency response, leading to Figs. 8.1b – 8.4, was obtained after band-pass filtering around 1.7 MHz. The maximum peak-zero amplitude of the linear oscillation ΔD is estimated by using a Hilbert transform of this filtered diameter-time curve;
- the radius before (D_0) and after (D_e) insonation (Fig. 8.6) is obtained from the first and last 5 frames, after low-pass filtering (cutoff 0.75 MHz) of the diameter-time curves.
- the expansion to compression ratio E/C (Fig. 8.5) is calculated by $(D_{\max} - D_0)/(D_0 - D_{\min})$ from the raw data.

The acoustic onset level, i.e. the threshold, is deduced from the increasing-pressure recordings as illustrated in Fig. 8.1; details on this method can be found in Emmer et al. [2007]. This example shows the oscillation amplitude as a function of insonation pressure for a Definity bubble at T_{room} having a diameter of 2.9 μm. The noise level depicted in the figure is estimated by the peak-peak relative excursion in the first movie in which no insonation was present (see Fig. 8.1a). Next, a linear least-squared-errors fit is applied to the first 3 data points that exceed the noise level. Finally, the point of intersection of the fitted line with the horizontal axis is denoted as the threshold level, 20 kPa in the example. Negative values of the threshold level are set to zero.

8.3 Results

8.3.1 Radial excursion

A total of 66 SonoVue and 52 Definity microbubbles were recorded at either T_{room} or T_{body}. The microbubbles were about equally distributed over the two temperature groups. Fig. 8.2 shows the relative excursion of the bubbles at 1.7 MHz as a function of initial diameter, for 40 kPa and 80 kPa insonation pressure.

As a first result, the graphs show that bubbles have highest radial excursion when having a diameter around 4 μm for both temperature values and both agents. This diameter is therefore considered as the resonant diameter for 1.7 MHz frequency, compatible with values recently obtained at similar experimental conditions [Dollet et al., 2008]. The data are inconclusive about a possible difference in the resonant diameter between the temperature groups, or between the contrast agents. One reason for this inconclusiveness is that the variation in radial response between bubbles within one group is large, giving difficulty to define a 'peak' in the graphs. Another reason is that a possible difference of resonant size is not large, presumed from the data. We therefore estimate that the interval of resonant diameters ranges from 3.5 to 4.5 μm for all groups. If the text states 'resonant size', then it denotes all bubbles having a size falling within this interval.

As a second result, SonoVue bubbles show larger radial excursion when heated to body temperature than at room temperature; for instance, warmed bubbles with a resonant diameter show about 2-fold larger excursion in the top-left panel. Definity shows highest increase ($\sim$ 1.5 fold) around 3 μm. In general, the oscillation amplitude of Definity is in between that of cold and warm SonoVue. No temperature influence can be observed for bubbles smaller than 3 μm and larger than 5 μm.

8.3.2 Thresholding

Fig. 8.3 shows the threshold levels for all bubbles as a function of initial diameter. SonoVue bubbles having diameter around 4 μm show significant temperature influence; bubbles at T_{body} have on average 2.5-fold lower threshold levels than bubbles at T_{room}. Definity bubbles show 2-fold threshold decrease for bubbles in the same range. General differences between SonoVue and Definity are visible only for smallest diameter ($\sim 2\,\mu m$), at which Definity microbubbles have on average a threshold level of 30 kPa, and SonoVue microbubbles a level of 10 kPa. Microbubbles larger than 6 μm (SonoVue) and 5 μm (Definity) do not show any threshold.

8.3.3 Combined results

For bubbles in the resonant diameter range of 3.5 μm to 4.5 μm the relative excursion $\Delta D/D_0$ was calculated and binned for each driving pressure, see Fig. 8.4. Each bin contained a number of bubbles between 5 and 13. Standard errors within

the bins are shown by vertical bars. SonoVue at T_{body} has about 0.1 higher relative excursion, compared to that at room temperature, for all driving pressures; such difference for Definity is not observed in this diameter range.

8.3.4 Expansion to compression ratios

Fig. 8.5 shows the E/C ratios of SonoVue and Definity at the two temperatures. The graphs show that the ratios are different for SonoVue and Definity. Many SonoVue microbubbles smaller than 3 μm diameter and larger than 7 μm show compression-only behavior while few Definity microbubbles with similar diameters show this effect. Note that we assume a threshold of $E/C < 0.5$ for 'compression-only behavior' [de Jong et al., 2007]. Also, an E/C ratio that is much different from unity denotes an asymmetric oscillation which inherently means a nonlinear response. SonoVue shows a significantly higher E/C ratio around 4 μm at 80 kPa insonation amplitude than at 40 kPa, independent of temperature. Body temperature results in slightly lower E/C ratio at 80 kPa, 4 μm, i.e., the nonlinearity of the bubble is slightly higher at higher temperature, but equal elsewhere. In contrast to SonoVue, the E/C ratio of Definity is independent of the temperature and insonation pressure.

8.3.5 Deflation

Fig. 8.6 shows the decrease of diameter after a single pulse of 80 kPa. Note that the data is somewhat noisy; the error is estimated from the zero-pressure recording to be around 0.1 μm. Nonetheless it is seen that a single pulse can reduce the diameter with over 0.3 μm, which is a 10% diameter decrease. Warm Definity shows much higher size reduction compared to cold Definity, which is most marked for sizes between 3 and 4 μm. Cold Definity of smaller size appears to not decrease in size at all, consistent with the results presented in Ch. 3.

In general SonoVue does not show large differences at the two temperatures, only warm SonoVue bubbles smaller than 2 μm seem more susceptible to deflation than bubbles of 3 μm. Comparing the two agents, when looking around resonance, cold SonoVue shows a higher deflation than cold Definity.

It can be meaningful to plot deflation *versus* radial excursion in a graph since comparison of Figs. 8.2 and 8.6 suggests, for both effects, a correlation with microbubble size. The variables at the axes of such compound graph should be selected with care. Deflation could be expressed as a reduction of diameter, but also as a reduction of surface area, or volume. Since deflation involves shedding of interfacial material, and diffusion generally is linearly dependend on surface area, it seems meaningful to plot the deflation as areal size reduction, $\Delta area$. Furthermore it can be expected that the shedding of the coating material depends either on strain, or on the rate of the strain. The latter is conveniently captured by the dilatation rate,

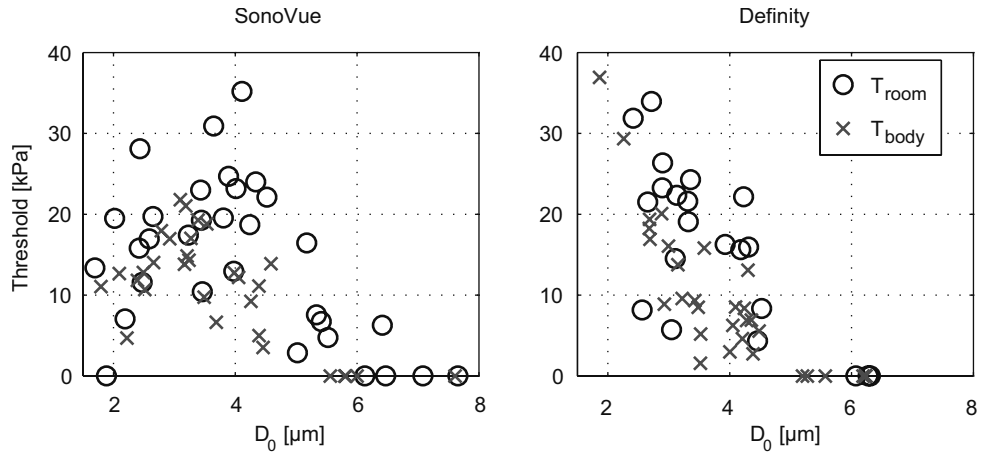

Figure 8.3: Threshold level versus diameter for SonoVue and Definity.

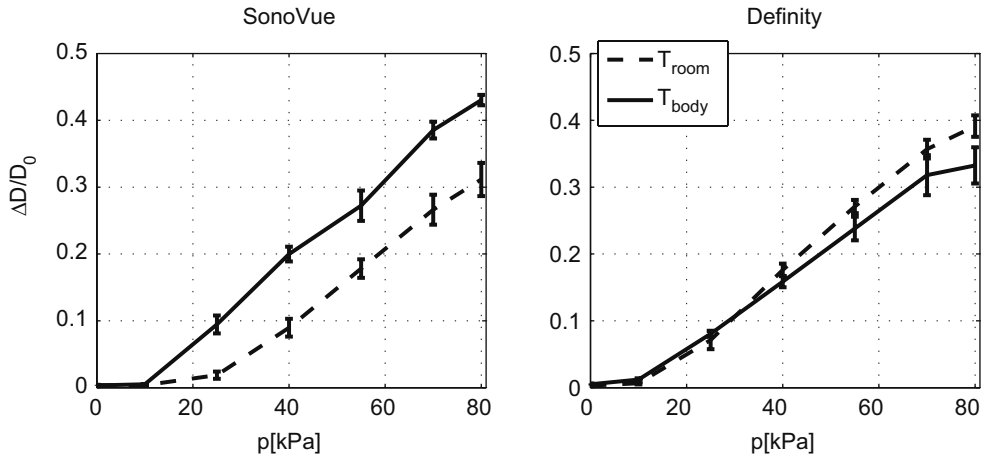

Figure 8.4: Relative radial excursion of resonant (3.5–4.5 µm) SonoVue (N=8) and Definity (N=5 and 13) bubbles when insonified with 1.7 MHz pulses at 10 kPa to 80 kPa. Standard errors are shown by vertical bars.

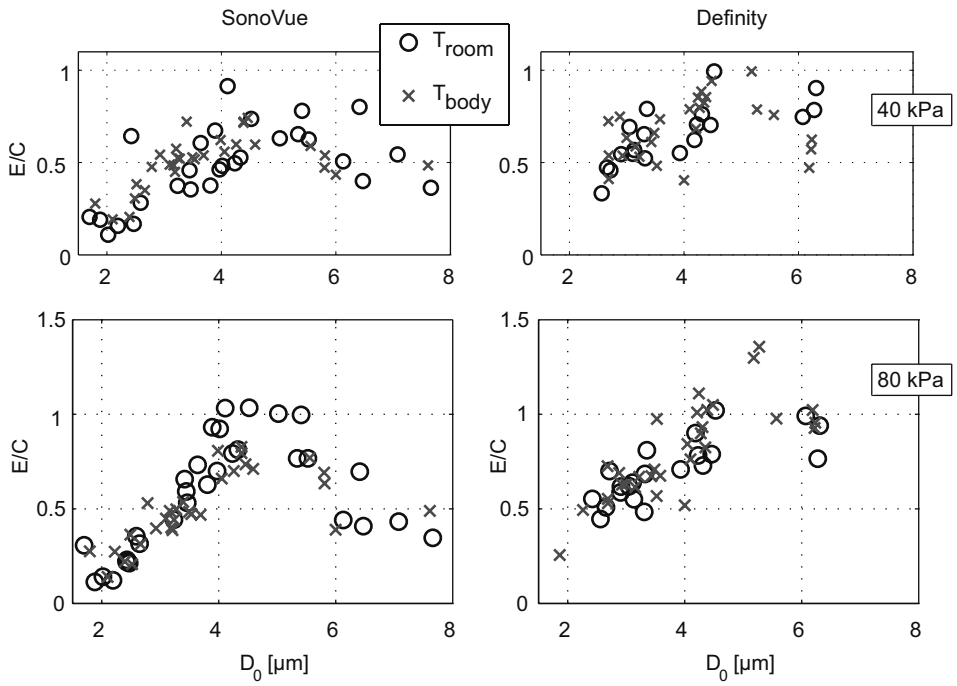

Figure 8.5: Expansion-to-compression ratios of bubbles insonified at 40 kPa (top) and 80 kPa (bottom).

$\dot{R}/R$, which is therefore selected for the horizontal axis in the correlation graph. The value is the maximum dilatation rate during the bubble oscillation, and is obtained from data-processing of each recorded R(t) curve.

Fig. 8.7 shows the relation between peak dilatation rate and reduction of surface area for warm Definity, when insonified with 70 kPa and 80 kPa pulses. A linear trend is observed that can be approximated by a line with a rough slope of 8 $\mu m^2/10^6$ s^{-1}. Such linear trend was clearest for warm Definity; SonoVue and cold Definity also showed higher areal reduction for higher dilatation rate (not shown), but a linear trend was not observed.

8.4 Summary, discussion and conclusion

In general, the oscillation of SonoVue shows higher dependency on temperature compared to Definity, see Table 8.1 that summarizes the influence of the higher temperature on the linear and nonlinear effects. Resonant ($\sim$ 4 μm diameter) SonoVue bubbles show up to 2-fold increase of radial amplitude at body temperature at 40 kPa driving pressure, and 2.5-fold decrease of the threshold level. These differences

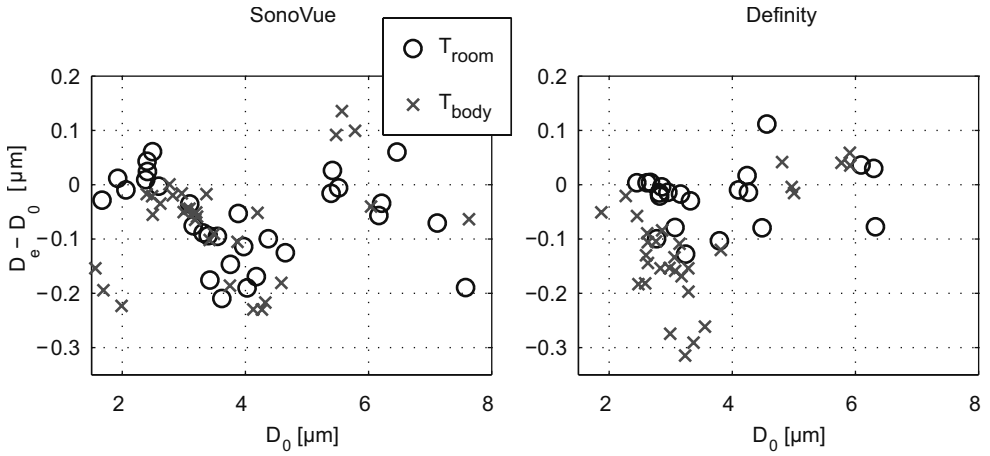

Figure 8.6: Size reduction after a single pulse when excited by a 80 kPa pulse.

are much less for nonresonant diameters, and for Definity (Table 8.1). The fact that the amplitude increase is not equal for the two agents suggests that temperature really influences the microbubble behavior, i.e., it suggests that it cannot be explained only by decreased viscosity of the water or other differences in the experimental setup (the viscosity of water at 37°C is 20% lower than that at 21°C).

8.4.1 Possible explanations

To date no model has been reported that addresses the observed influence of temperature on the linear and nonlinear behavior of coated microbubbles. The next paragraphs discuss the current observations in view of literature that describes the influence of phospholipids coatings on the response of microbubbles.

Marmottant et al. [2005] and Borden et al. [2004] suggest that a phospholipids coating obeys a nonlinear strain-stress relation. Marmottant et al. [2005] simplify

Table 8.1: Result of increasing temperature on various characterization effects.

	SonoVue		Definity	
Effect	resonant	nonresonant	resonant	nonresonant
Amplitude	2× higher	none	1.5 × higher	none
Threshold	2.5 × lower	1.5 × lower	2× lower	none
E/C	slight decrease	none	none	none
Destruction	none	none	higher	higher

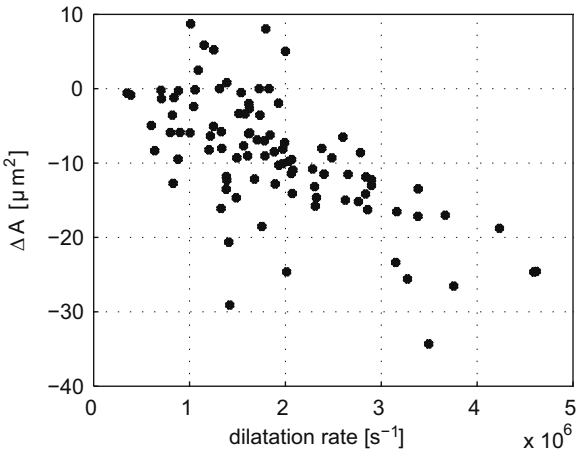

Figure 8.7: Reduction of area (ΔA) versus peak dilatation rate of warm Definity when excited by 70 and 80 kPa pulses.

the relation by a three-state model, in which the states are: buckled, elastic, and ruptured. See Fig. 8.8 for a schematic representation of the states. More details of the model will be discussed in Ch. 9. It is assumed in Ch. 9 that the bubble initially is at the cross-over point between buckled and elastic state. In Marmottant et al. [2005] the three-state model was incorporated in a Rayleigh-Plesset type equation to describe the microbubble response to ultrasound. At low driving amplitude, the model predicts strong nonlinear effects if the shell is alternatively in different states and it predicts only linear effects if the shell stays in a single state. Multi-state oscillations can predict asymmetric oscillations and thresholding.

When looking at the smallest and largest diameters in Fig. 8.5 (E/C *vs.* diameter) SonoVue oscillations show stronger asymmetry than Definity, but the E/C ratio of both did not significantly change with temperature. This suggests that the general behavior of the strain-stress relation of the coating does not significantly change with temperature. This finding is further consolidated by the absence of significant differences in the resonant diameter. A difference in strain-stress relation as predicted by Borden et al. [2004, Fig. 5A] would contradict the observed phenomenon.

Another suggestion on the coating behavior based on the similar levels of the E/C ratio can be made. When the bubbles are injected into the warmed setup, they are fastly heated from room temperature to about 37°C. Gas expansion from T_{room} to T_{body} would increase the volume with 5% and the radius with about 1.5% . This could change the initial state of the microbubble. For instance, at room temperature the bubble resting state could be at the 'buckling radius' [Marmottant et al., 2005], corresponding to $A_{buckling}$ in Fig. 8.8. Heating to body temperature would then lead

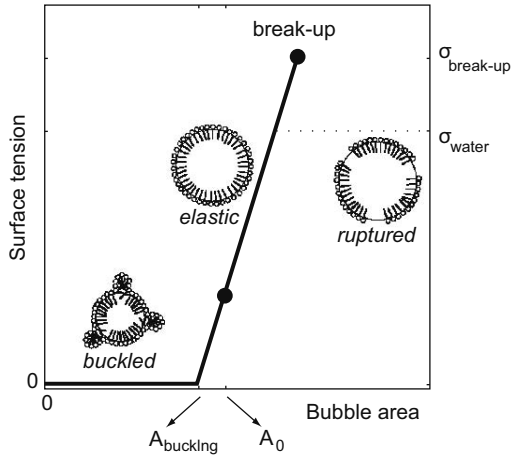

Figure 8.8: Simplification of possible surface tension behavior of a phospholipids microbubble; © 2005 American Society of America, Marmottant et al. [2005].

to a resting state in the elastic regime, such as denoted by A_0. This would lead to a different oscillatory behavior that would mainly be noticed by a difference in E/C ratio; the absence of such difference might suggest that the initial state is not affected by temperature. On the other hand, this absence could also be explained by possible deflation of the bubbles in the time between injection and recording; no definite conclusions can be drawn from the current observations.

In the previous paragraphs it is suggested that neither the strain-stress relation nor the initial state of the coating is influenced by temperature. However, it is clearly seen that the amplitude of oscillation around resonance shows large influence of temperature. From this observation it can be suggested that mainly the viscosity of the coating is lower at the higher temperature. Lower viscosity leads to higher oscillations, which could also explain the lower threshold effect of the bubbles at body temperature.

Leighton [1994] showed that bubble oscillations are dominated by intertia when insonified above resonance (large radii). The inertia of the bubble-surrounding mass is not significantly influenced by temperature. This implies that large-radii bubble behavior should not be influenced by the coating, and hence not by temperature, which is consistent with the observations in the graphs.

Within parentheses, the qualitative arguments in this section should be further assessed by comparing the current observations with predictions of numerical models for phospholipids coatings such as proposed by e.g. Marmottant et al. [2005]; Doinikov and Dayton [2007]; Stride [2008]; Tsiglifis and Pelekasis [2008]. A drawback of such comparison is that those models currently do not provide parameter

values for either SonoVue or Definity. Moreover, the limited number of bubbles in the current dataset and the inherent variations in microbubble response of equal-sized microbubbles might challenge the comparison.

8.4.2 Deflation

With respect to the deflation phenomenon, Definity is less stable at body temperature than at room temperature. In fact, preliminary experiments with Definity at temperatures larger than 37°C showed that also static deflation (i.e., in absence of ultrasound) becomes significant at such temperatures, and bubbles of several micrometers would dissolve in seconds. Such behavior would suggest that the phospholipids (or other materials in the coating) are more easily dissolved in water at temperatures above 37°C. Indeed, the Definity coating mainly contains dipalmitoyl phosphatidylcholine (DPPC) which has a melting point of about 42°C, which is not too far away from 37°C, and lipid mixtures always have shifted melting points. Melting implies drastically increased lateral diffusion rate; molecules in the membrane are not as firmly attached to each other, which could also promote dissolution. However, Definity is stable for at least some minutes *in vivo*, which implies that the coating does not necessarily dissolve at body temperature. The main component of SonoVue is distearoyl phosphatidylcholine (DSPC) which melts at 55°C, which could explain why SonoVue deflation is less affected by a temperature approaching 37°C.

8.4.3 Conclusions

From the data some general conclusions can be drawn. First, the oscillation amplitude of SonoVue and Definity are on the same order of magnitude. Second, the diameter of maximum response at 1.7 MHz is not significantly different, neither for the two agents, nor for the two temperatures. Third, both agents show thresholding and compression-only, at room and body temperature. Fourth, the acoustically-induced deflation is of same order of magnitude for both agents. These observations may lead to the conclusion that SonoVue and Definity microbubbles show similar behavior with minor differences. However, they react differently to temperature.

In conclusion, when studying the behavior of contrast agents, temperature is a significant parameter for bubble oscillation. The effect of thresholding seems higher for lower temperatures; therefore, when studying such effect from a fundamental standpoint, room temperature experiments seem more appropriate. When studying the potential use of nonlinear shell effects in medical imaging, the bubbles should be warmed to body temperature.

Bibliography

Borden, M. A., D. E. Kruse, C. F. Caskey, S. Zhao, P. A. Dayton, and K. W. Ferrara, "Influence of lipid shell physicochemical properties on ultrasound-induced microbubble destruction," *IEEE Trans Ultrason Ferroelectr Freq Control*, 52(11): pp. 1992–2002, 2005.

Borden, M. A. and M. L. Longo, "Dissolution behavior of lipid monolayer-coated, air-filled microbubbles: Effect of lipid hydrophobic chain length," *Langmuir*, 18(24): pp. 9225–9233, 2002.

Borden, M. A., G. V. Martinez, J. Ricker, N. Tsvetkova, M. Longo, R. J. Gillies, P. A. Dayton, and K. W. Ferrara, "Lateral phase separation in lipid-coated microbubbles," *Langmuir*, 22: pp. 4291–4297, 2006.

Borden, M. A., G. Pu, G. J. Runner, and M. L. Longo, "Surface phase behavior and microstructure of lipid/PEG-emulsifier monolayer-coated microbubbles," *Colloids Surfaces B-Biointerfaces*, 35: pp. 209–223, 2004.

Bouakaz, A., M. Versluis, and N. de Jong, "High-speed optical observations of contrast agent destruction," *Ultrasound Med Biol*, 31(3): pp. 391–399, 2005.

Chin, C. T., C. T. Lancée, J. M. G. Borsboom, F. Mastik, M. E. Frijlink, N. de Jong, M. Versluis, and D. Lohse, "Brandaris 128: A 25 million frames per second digital camera with 128 highly sensitive frames," *Rev Sci Instr*, 74(12): pp. 5026–5034, 2003.

Chomas, J. E., P. A. Dayton, J. S. Allen, K. E. Morgan, and K. W. Ferrara, "Mechanisms of contrast agent destruction," *IEEE Trans Ultrason Ferroelectr Freq Control*, 48(1): pp. 232–248, 2001.

Dayton, P. A., K. E. Morgan, A. L. Klibanov, G. H. Brandenburger, and K. W. Ferrara, "Optical and acoustical observations of the effects of ultrasound on contrast agents," *IEEE Trans Ultrason Ferroelectr Freq Control*, 46(1): pp. 220–232, 1999.

de Jong, N., A. Bouakaz, and P. Frinking, "Basic acoustic properties of microbubbles," *Echocardiography*, 19(3): pp. 229–240, 2002.

de Jong, N., M. Emmer, C. T. Chin, A. Bouakaz, F. Mastik, D. Lohse, and M. Versluis, ""Compression-only" behavior of phospholipid-coated contrast bubbles," *Ultrasound Med Biol*, 33(4): pp. 653–656, 2007.

Doinikov, A. A. and P. A. Dayton, "Maxwell rheological model for lipid-shelled ultrasound microbubble contrast agents," *J Acoust Soc Am*, 121(6): pp. 3331–3340, 2007.

Dollet, B., S. M. Van der Meer, V. Garbin, N. de Jong, D. Lohse, and M. Versluis, "Nonspherical oscillations of ultrasound contrast agent microbubbles," *Ultrasound Med Biol*, 34(9): pp. 1465–1473, 2008.

Emmer, M., A. van Wamel, D. E. Goertz, and N. de Jong, "The onset of microbubble vibration," *Ultrasound Med Biol*, 33(6): pp. 941–949, 2007.

Goertz, D. E., N. de Jong, and A. F. W. van der Steen, "Attenuation and size distribution measurements of Definity and manipulated Definity populations," *Ultrasound Med Biol*, 33(9): pp. 1376–1388, 2007.

Gorce, J.-M., M. Arditi, and M. Schneider, "Influence of bubble size distribution on the echogenicity of ultrasound contrast agents - A study of SonoVue," *Invest Radiol*, 35(11): pp. 661–671, 2000.

Guidi, F., H. J. Vos, R. Mori, N. de Jong, and P. Tortoli, "Microbubble characterization through acoustically-induced deflation," *Accepted in IEEE Trans Ultrason Ferroelectr Freq Control*, 2009.

Guiot, C., G. Pastore, M. Napoleone, P. Gabriele, M. Trotta, and R. Cavalli, "Thermal response of contrast agent microbubbles: Preliminary results from physico-chemical and US-imaging characterization," *Ultrasonics*, 44(Supplement 1): pp. e127–e130, 2006.

Kimmel, E., B. Krasovitski, A. Hoogi, D. Razansky, and D. Adam, "Subharmonic response of encapsulated microbubbles: Conditions for existence and amplification," *Ultrasound Med Biol*, 33(11): pp. 1767–1776, 2007.

Kooiman, K., M. R. Böhmer, M. Emmer, H. J. Vos, C. Chlon, W. T. Shi, C. S. Hall, S. H. P. M. de Winter, K. Schroën, M.Versluis, N. de Jong, and A. van Wamel, "Oil-filled polymer microcapsules for ultrasound-mediated delivery of lipophilic drugs," *J Control Release*, 133: pp. 109–118, 2009.

Leighton, T. G., The Acoustic Bubble, Academic Press, London, UK, 1994.

Marmottant, P., S. M. van der Meer, M. Emmer, M. Versluis, N. de Jong, S. Hilgenfeldt, and D. Lohse, "A model for large amplitude oscillations of coated bubbles accounting for buckling and rupture," *J Acoust Soc Am*, 118(6): pp. 3499–3505, 2005.

Morgan, K. E., J. S. Allen, P. A. Dayton, J. E. Chomas, A. L. Klibanov, and K. W. Ferrara, "Experimental and theoretical evaluation of microbubble behavior: Effect of transmitted phase and bubble size," *IEEE Trans Ultrason Ferroelectr Freq Control*, 47(6): pp. 1494–1509, 2000.

Mulvana, H., E. Stride, and R. J. Eckersley, "Temperature dependent behaviour of ultrasound contrast agents," in proc. IEEE Int Ultras Symp, pp. ref. P1–A–07, Rome, Italy, 2009.

Needles, A., D. E. Goertz, R. Karshafian, E. Chérin, A. S. Brown, P. N. Burns, and F. S. Foster, "High-frequency subharmonic pulsed-wave Doppler and color flow imaging of microbubble contrast agents," *Ultrasound Med Biol*, 34(7): pp. 1139–1151, 2008.

Pu, G., M. A. Borden, and M. L. Longo, "Collapse and shedding transitions in binary lipid monolayers coating microbubbles," *Langmuir*, 22: pp. 2993–2999, 2006.

Sijl, J., E. Gaud, P. J. Frinking, M. Arditi, N. de Jong, D. Lohse, and M. Versluis, "Acoustic characterization of single ultrasound contrast agent microbubbles," *J Acoust Soc Am*, 124(6): pp. 4091–4097, 2008.

Stride, E., "The influence of surface adsorption on microbubble dynamics," *Phil Trans R Soc A*, 366(1873): pp. 2103–2115, 2008.

Tsiglifis, K. and N. A. Pelekasis, "Nonlinear radial oscillations of encapsulated microbubbles subject to ultrasound: The effect of membrane constitutive law," *J Acoust Soc Am*, 123(6): pp. 4059–4070, 2008.

van der Meer, S. M., B. Dollet, M. M. Voormolen, C. T. Chin, A. Bouakaz, N. de Jong, M. Versluis, and D. Lohse, "Microbubble spectroscopy of ultrasound contrast agents," *J Acoust Soc Am*, 121(1): pp. 648–656, 2007.

Chapter 9

Radial modulation of single microbubbles

Abstract - **Radial modulation imaging is a new promising technique to improve contrast-enhanced ultrasound images. The method is based on dual-frequency insonation of contrast agent microbubbles. A low frequency (LF) pulse is used to modulate the responses of the microbubbles to a high frequency (HF) imaging pulse. Inverting the LF pulse induces amplitude and phase differences in the HF response of contrast agent microbubbles, which can be detected using Doppler techniques. Although the technique has been successfully implemented, no consensus persists on parameter choice and resulting effects. In a separate study, "compression-only" behavior of coated microbubbles was observed. Compression-only behavior could be beneficial for radial modulation imaging. This was investigated using high-speed camera recordings and simulations. We recorded the vibrations of 78 single microbubbles in a dual-frequency ultrasound field. The results showed that the LF pulse induced significant compression-only behavior, which for microbubble sizes below and at HF resonance resulted in high radial amplitude modulation. It however also appeared that for radial modulation imaging, microbubble size is more important than resonance and compression-only effects.**

Appeared in the IEEE Transactions on Ultrasonics, Ferroelectrics, and Frequency Control, by M. Emmer, H. J. Vos, M. Versluis, and N. de Jong; Vol. 56, Issue 11, pp. 2370-2379, 2009. This work is part of the research program of the 'Stichting voor Fundamenteel Onderzoek der Materie (FOM)', which is financially supported by the 'Nederlandse Organisatie voor Wetenschappelijk Onderzoek (NWO)'.

9.1 Introduction

Ultrasound imaging is widely used in clinical radiology and cardiology applications. The intravenous injection of coated gas microbubbles as a contrast agent significantly enhances the acoustic backscattering from blood and thus the ability to detect blood flow in soft tissue. The microbubbles are effective scatterers owing to the large compressibility difference between the surrounding fluid and the coated gas. Under the influence of an ultrasound field, the microbubbles may vibrate linearly or nonlinearly. Nonlinear vibrations result in a backscattered signal containing higher harmonics of the incident frequency. Current contrast agent detection techniques exploit these harmonic signals, e.g. harmonic imaging [Schrope and Newhouse, 1993], pulse inversion [Hope Simpson et al., 1999], power modulation [Brock-Fisher et al., 1996], and combinations of these methods. However, tissue also generates harmonics due to nonlinear propagation [Duck, 2002], with the result that the detection of contrast microbubble harmonics competes with the detection of tissue harmonics.

New strategies are investigated to further improve the detection of contrast agents. An example of such a strategy is radial modulation imaging, which is based on dual-frequency insonation. In 1984, Newhouse and Mohana Shankar [1984] already measured bubble sizes using double-frequency insonation. Due to the resonance behavior of the microbubbles, the echo will contain sidebands at HF $\pm$ LF as well as higher order terms, unique for each microbubble size [Newhouse and Mohana Shankar, 1984]. This interaction of frequencies is also known in adjacent fields of science, see e.g. Akhatov and Khismatullin [1999]. Since 1984, many studies have proposed to use dual-frequency insonation to enhance the detection of microbubble scattering, e.g. Wyczalkowski and Szeri [2003] combined 1 and 3 MHz in such a way to maximize the acoustic radiation of a bubble at 2 MHz. Roy et al. [1990] applied 10 μs-long combined LF and HF bursts to detect transient cavitation. Deng et al. [2000] were the first to suggest the use of a short HF pulse combined with a long LF pulse. They placed the HF pulse on a LF minimum or maximum to probe various aspects of LF effects. Introduced as a dual-frequency strategy to study microbubble behavior, this strategy expanded when it was introduced as an imaging technique, called radial modulation imaging [Hansen et al., 2005; Shariff et al., 2006b,a].

In the radial modulation imaging technique a combination of two pulses is transmitted. A low frequency (LF) pulse acts as a modulator signal and a high frequency (HF) pulse is used for imaging. This combination of pulses is transmitted repeatedly with alternating positive and negative modulator signals. The contrast microbubbles can be extracted from tissue using techniques analogous to pulsed-wave Doppler techniques [Chérin et al., 2008; Måsøy et al., 2008]. An advantage of the method mentioned is that the contrast agent detection frequency is decoupled from the resonance frequency of the microbubbles, allowing detection at clinically-

high frequencies for a high-resolution detection of the contrast agent [Shariff et al., 2006b; Chérin et al., 2008; Måsøy et al., 2008].

Radial modulation imaging is based on detecting decorrelation of the HF imaging signals induced by the LF modulation. This modulation may affect the amplitude and/or phase of the HF response, which depends on the choice of LF and HF with respect to the resonant frequency of the microbubbles. Literature delivers different messages. Whereas the first papers on the radial modulation imaging technique [Deng et al., 2000; Hansen et al., 2005; Shariff et al., 2006b,a] suggest that LF should be chosen near the resonant frequency of the microbubbles, a more recent paper by Bouakaz et al. [2007] proposed to adjust HF to the resonant frequency of the microbubbles. Bouakaz et al. based their conclusions mainly on experimental results. In other recent studies [Chérin et al., 2008; Angelsen and Hansen, 2007] numerical simulations indicated that best results are obtained when the HF approaches the microbubble resonant frequency from above [Angelsen and Hansen, 2007] or that the LF should be below the resonant frequency of the microbubbles in the population [Chérin et al., 2008].

Current knowledge on the effect of radial modulation is based on "traditional" theory that describes the motion of contrast bubbles using fixed properties for the bubble's coating. These models are not able to predict highly nonlinear behavior for phospholipid-coated bubbles such as "compression-only behavior," which was observed using a high-speed camera system [de Jong et al., 2007]. This highly nonlinear behavior was observed for 40% of the investigated phospholipid-coated bubbles at acoustic pressures between 50 – 200 kPa [de Jong et al., 2007]. Bubbles showing this behavior hardly expanded, but their compression amplitude dominated their expansion amplitude by at least a factor two. The recent model for large amplitude oscillations developed by Marmottant et al. [2005] is able to predict compression-only behavior. Because of the high nonlinearity of this behavior, we expect that compression-only behavior could influence the radial modulation of microbubbles.

In this study, we use high-speed recordings to investigate the behavior of single phospholipid coated microbubbles in a dual-frequency ultrasound field. We investigate the influence of typical phospholipid-coated bubble behavior such as compression-only behavior on the radial modulation of the bubbles. For this purpose, we compare the experimentally obtained results with simulated dual-frequency behavior, whereby "traditional" theory is compared to the model by Marmottant et al. [2005]. We did not fit simulated results to experimental observations, but investigated which model is suitable to predict phospholipid-coated bubble behavior in a dual-frequency ultrasound field. Low intensity ultrasound bursts were applied at frequencies useful for precordial examinations. Gained knowledge is useful for the fundamental understanding of coated bubble behavior as well as the implementation of the radial modulation imaging technique.

9.2 Material and methods

9.2.1 Simulations

We calculate the responses of three types of bubbles in a dual-frequency field, which are 1) free gas bubbles, 2) bubbles coated with a visco-elastic encapsulation, and 3) bubbles coated with an encapsulation that can be in a visco-elastic state, but also in a buckled or ruptured state.

1) To model free gas microbubbles, we follow Marmottant et al. [2005] and applied a popular variant of the Rayleigh-Plesset equation as described by Brenner et al. [2002]. This (modified) Rayleigh-Plesset equation is combined with a polytropic ideal gas law and boundary condition, which gives:

$$\rho_l \left(R\ddot{R} + \frac{3}{2}\dot{R}^2 \right) = \left(P_0 + \frac{2\sigma_w}{R_0} \right) \left(\frac{R}{R_0} \right)^{-3\kappa} \left(1 - \frac{3\kappa}{c}\dot{R} \right) - \frac{2\sigma_w}{R} - \frac{4\mu\dot{R}}{R} - P_0 - P_{ac}(t) \tag{9.1}$$

where R , $\dot{R}$ and $\ddot{R}$ represent the radius, velocity and acceleration of the microbubble wall, R_0 is the resting radius of the microbubble, ρ_l = 10^3 kg/m^3 is the density of water, σ is the surface tension, κ is the polytropic exponent, $c = 1.5 \cdot 10^3$ m/s is the speed of sound in water, μ = 10^{-3} Pa·s is the dynamic viscosity of water, and $P_{ac}(t)$ is the driving acoustic pressure. The influence of thermal damping is expected to be small [Stride and Saffari, 2004; van der Meer et al., 2007]. We therefore ignore thermal damping for the sake of simplicity. The gas core consists of SF_6 and is assumed to be adiabatic, resulting in κ = 1.095 [Marmottant et al., 2005]. The surface tension is constant, $\sigma_w = 7.2 \cdot 10^{-2}$ N/m.

2) Secondly, we simulate the behavior from microbubbles with a visco-elastic coating. We follow the approach by Van der Meer et al. [2007] and use an elasticity modulus (χ) and a viscosity parameter (μ_s) to describe the coating. This model is an example of a "traditional" approach to predict coated bubble behavior whereby the properties of the coating remain constant during the oscillatory cycle of the bubble. The following equation for the radial motion of coated bubbles results:

$$\rho_l \left(R\ddot{R} + \frac{3}{2}\dot{R}^2 \right) = \left(P_0 + \frac{2\sigma_w}{R_0} \right) \left(\frac{R}{R_0} \right)^{-3\kappa} \left(1 - \frac{3\kappa}{c}\dot{R} \right) - \frac{2\sigma_w}{R} - 4\chi \left(\frac{1}{R_0} - \frac{1}{R} \right) - \frac{4\mu\dot{R}}{R} - \frac{4\mu_s(R_0)\dot{R}}{R^2} - P_0 - P_{ac}(t) \tag{9.2}$$

In the paper by van der Meer et al. [2007], it is concluded that the value of μ_s depends on the initial microbubble radius. We determine $\mu_s(R_0)$ by fitting a relationship for this parameter using the data shown in Fig. 8 of the paper by Van der Meer et al. and incorporate $\mu_s(R_0)$ in Eq. 9.2. The relationship is:

$$\mu_s(R_0) = 10^{-9.0+0.37R_0} \text{ kg/s} \tag{9.3}$$

with R_0 in units of μm.

3) Thirdly, the full model by Marmottant et al. [2005] is applied to describe the behavior of phospholipid-coated bubbles in a more realistic way. A coating that is modeled as a visco-elastic solid can be infinitely stretched and compressed without changing the coating's properties. Recently, Marmottant et al. [2005] have shown that this may be unrealistic for coatings composed of phospholipids. A phospholipid coating consists of a monolayer of phospholipid molecules. Acting as a surfactant, this layer of phospholipids decreases the surface tension between gas core and surrounding liquid depending on the concentration of phospholipid molecules. During the oscillatory cycle of the bubble the concentration of phospholipids changes and so does the influence of the coating on the surface tension of the bubble. When the bubble expands, the distance between the phospholipid molecules increases and the bubble will start to behave more and more as a free gas bubble. When the bubble is compressed, at some point, the coating will start to buckle and fold. At this point it is relatively easier to compress the surface than to expand it. In the latter case, the molecules need to be separated from each other. This buckling behavior of the coating may explain the optically observed compression-only behavior of phospholipid-coated bubbles [Marmottant et al., 2005; de Jong et al., 2007].

Marmottant et al. [2005] modeled this typical behavior for phospholipid-coated bubbles by defining an effective surface tension, which can be in three regimes depending on the microbubble radius (see Fig. 8.8),

$$\sigma(R) = \begin{cases} 0 & R \leq R_{buckling} \\ \chi\left(\frac{R^2}{R_{buckling}^2} - 1\right) & R_{buckling} < R < R_{break-up} \\ \sigma_w & R \geq R_{break-up} \end{cases} \tag{9.4}$$

For radii below $R_{buckling}$, the coating of the microbubble buckles and the surface tension vanishes. To assure compression-only behavior, $R_{buckling}$ was taken equal to R_0. For radii between $R_{buckling}$ and $R_{break-up}$, the coating behaves as a visco-elastic material with the same properties as modeled in Eq. 9.2. In this regime, $-\frac{2\sigma(R)}{R}$ reduces to $-\frac{2\sigma_w}{R} - 4\chi\left(\frac{1}{R_0} - \frac{1}{R}\right)$, which results in an equation of motion identical to Eq. 9.2 (see also Marmottant et al. [2005]). For the elasticity modulus $\chi = 1.0$ N/m was taken. When $R \geq R_{break-up}$, the coating ruptures and the surface tension becomes equal to that of the gas-liquid interface of a free gas microbubble σ_w. The effective surface tension is included in the following equation of motion [Marmottant et al., 2005]:

$$\rho_l\left(R\ddot{R} + \frac{3}{2}\dot{R}^2\right) = \left(P_0 + \frac{2\sigma(R_0)}{R_0}\right)\left(\frac{R}{R_0}\right)^{-3\kappa}\left(1 - \frac{3\kappa}{c}\dot{R}\right) - \frac{2\sigma(R)}{R} - \frac{4\mu\dot{R}}{R} - \frac{4\mu_s(R_0)\dot{R}}{R^2} - P_0 - P_{ac}(t) \tag{9.5}$$

To discriminate between the bubbles with a fully elastic coating and the bubbles with a coating that can be in a buckled, elastic or ruptured state, we call the first group of coated bubbles "*elastic type*" and the second group of bubbles "*buckling type*".

Simulations were carried out for microbubble sizes from 0.5 to 6.0 μm in diameter. The input was the acoustic pressure signal applied in the high-speed recordings. This signal was measured using a hydrophone and consisted of a LF pulse and a HF pulse. The LF pulse was a gated four-cycle-sine wave burst at 0.5 MHz center frequency and had a peak negative pressure of 30 kPa. The HF pulse was a gated 33-cycle-sine wave burst at 3.75 MHz centre frequency and had a peak negative pressure of 80 kPa. We calculated the radius of each microbubble as a function of time, $R(t)$, in response to a single HF pulse and in response to a combination of the LF and HF pulses. The predicted scattered wave from the simulated microbubbles was calculated by [Hilgenfeldt et al., 1998],

$$P_s = \rho_l \frac{R}{r}\left(2\dot{R}^2 + R\ddot{R}\right) \tag{9.6}$$

where r is the distance from the microbubble, which was taken equal to the focal distance of the transducers (r = 75 mm) that were used in the experiments. Amplitude values of the radial and acoustic responses were determined using the envelope of these responses, which was calculated by applying IQ-demodulation.

9.2.2 Experiments

High-speed optical recordings were performed using the setup shown in Fig. 9.1. A Perspex water tank filled with air-saturated water contained two single element transducers. The first transducer was used for the LF pulses and had a center frequency of 0.5 MHz, a focal length of 75 mm, and an aperture diameter of 38 mm (V389, Panametrics-NDT, Olympus NDT, Waltham, MA, USA). The other transducer had a center frequency of 3.5 MHz, a focal length of 75 mm, and an aperture diameter of 25 mm (V380, Olympus NDT). Both transducers were focused at the same region-of-interest in a cellulose Cuprophan © capillary tube (inner diameter 160 μm and outer diameter 200 μm, Akzo Nobel Faser AG, Wuppertal, Germany). The transducers were controlled by a two-channel waveform generator (AWG 8026, Tabor Electronics Ltd., Tel Hanan, Israel) and two power amplifiers (LF: 150A100B, AR, Souderton, PA, USA and HF: A-500, ENI, Rochester, NY, USA). The objective of a BX-FM microscope (Olympus Nederland BV, Zoeterwoude, The Netherlands) was positioned above the capillary tube and projected the microbubbles with 240× magnification (LUMPlan 60× water immersion objective and 2×2 magnifiers) onto a customly-built high-speed camera system, the Brandaris-128 [Chin et al., 2003]. This system is capable of digitally acquiring 128 frames with a maximum frame rate of 25 million frames per second. The illumination source was a xenon flash lamp

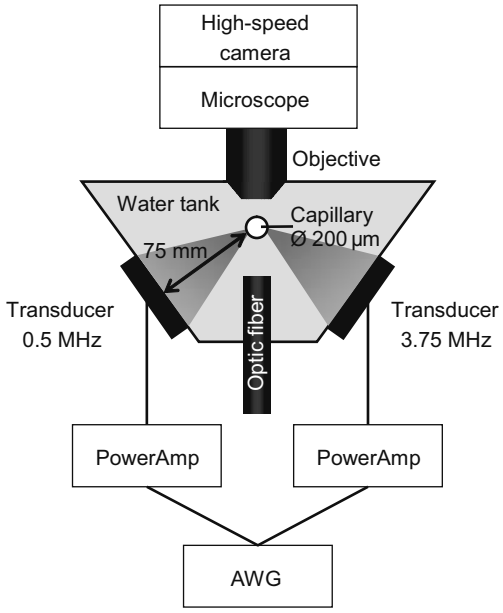

Figure 9.1: Schematical experimental setup for the optical recording of single microbubbles.

(MVS-7010, Perkin-Elmer Optoelectronics, Salem, MA, USA) connected to an optic fiber (Olympus) mounted below the capillary tube and microscope objective.

SonoVue microbubbles were prepared as prescribed by the manufacturer (Bracco SpA, Milan, Italy) and diluted such that after injection in the capillary tube, one to four microbubbles were present in the image frame of $31 \times 42\,\mu m$. The microbubbles were recorded in six sequences of 128 image frames at a frame rate of 12 million frames per second. The time between the sequences was 80 ms. In the first sequence, no ultrasound was applied to determine the resting size of the microbubbles. In the second and fifth sequence, the microbubbles were insonified with a gated four-cycle-sine wave burst at 0.5 MHz center frequency and a peak negative pressure of 30 kPa. In the third and sixth sequence, the microbubbles were insonified with a gated 33-cycle-sine wave burst at 3.75 MHz centre frequency and a peak negative pressure of 80 kPa. Both transducers insonified the microbubbles in the fourth sequence. In a separate experiment, a calibrated 0.2-mm PVDF hydrophone (Precision Acoustics Ltd., Dorchester, UK) was used to verify the acoustic pressures.

From the optical recordings we obtained the microbubble diameter as a function of time, $D(t)$, by measuring the diameter in each image frame with a semi-automatic procedure using a minimal cost algorithm [van der Meer et al., 2007]. In a further analysis the radiated sound pressures are calculated from these optically-obtained diametric responses. However, strong influences of the limited sampling rate and

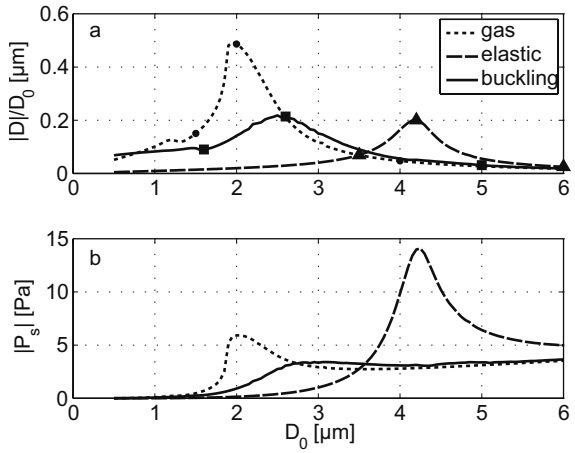

Figure 9.2: (a) Simulated radial responses (amplitude divided by resting diameter), (b) Amplitude of scattered sound pressure as function of resting diameter using a single transmit frequency of 3.75 MHz. Dots (gas), triangles (elastic) and squares (buckling) indicate the selected microbubble sizes for the dual-frequency responses shown in Figs. 9.3–9.5.

of stochastic errors in the microbubble diameter measurements [Emmer et al., 2007] affected especially $\ddot{R}$ in Eq. 9.6. Therefore we have chosen to implement a simplified approach compared to the simulated results, as described next.

Suppose that the bubble responds as a harmonic oscillator. Then its radial response can be expressed by $R(t) = R_0 + A\sin(\omega t)$ whereby A is the amplitude of the radial motion, $A < R_0$ and ω is $2\pi \cdot 3.75 \cdot 10^6$ rad/s. From this expression we derive the second derivative with respect to time, which results in $\ddot{R}(t) = -A\omega^2 \sin(\omega t)$. For low amplitudes, the velocity contribution of the microbubble wall in Eq. 9.6 is small compared to the contribution of the acceleration and was therefore neglected, which results in the following simplified form of Eq. 9.6: $P_s = \rho_l \frac{R^2 \ddot{R}}{r}$. In this equation we insert $\ddot{R}$ and $R^2 = (R_0 + A\sin(\omega t))^2 \approx {R_0}^2$ to arrive at:

$$P_s = -\frac{\rho_l \omega^2 R_0^2 A \sin(\omega t)}{r} \tag{9.7}$$

For bubbles sizes below 5 µm diameter, Eq. 9.7 gives similar results compared to Eq. 9.6.

9.3 Results

9.3.1 Simulations

We simulated the responses of the free gas, *elastic type* and *buckling type* microbubbles in an ultrasound field. First, the responses are mutually compared when

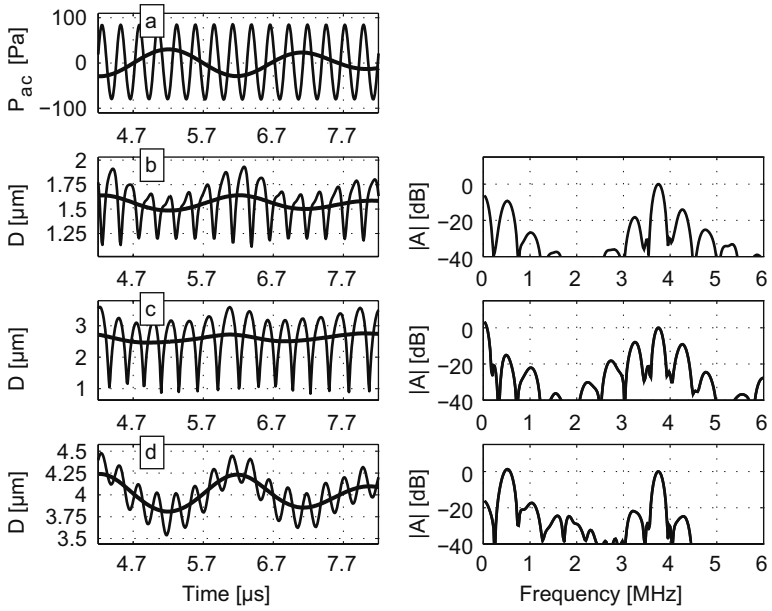

Figure 9.3: Simulated dual-frequency radial responses of *free gas* microbubbles with different resting sizes (thin lines in left column b-d) and corresponding power spectra (right column b-d). To show the effect of modulation by the LF pulse on the bubble size, the bold lines in left column b-d show the low-pass filtered responses (cut-off frequency 1.5 MHz). a) acoustic pressure field, 0.5 MHz pulse (bold line) and 3.75 MHz pulse (thin line). b) D_0: 1.5 µm, c) D_0: 2.0 µm, d) D_0: 4.0 µm

the microbubbles have been insonified with only 3.75 MHz (HF) (Fig. 9.2). The *elastic type* microbubbles gave highest radial excursions for a microbubble size of 4.2 µm diameter (Fig. 9.2a). This maximum indicates the resonant size at a transmit frequency of 3.75 MHz. The resonant size of the *elastic type* microbubbles was greater than that of the free gas microbubbles (2.0 µm) and the resonant size of the *buckling type* microbubbles was found in between these sizes, (2.6 µm).

Using Eq. 9.6 the sound pressures that these microbubbles scattered were calculated (Fig. 9.2b). Microbubble sizes below the resonant size are in the Rayleigh regime of microbubble scattering. Well above resonance, scattering is dominated by the microbubble's physical cross-section and the backscattered sound intensity increases with the radius. Scattered sound pressures were elevated at resonance. Compared to the other microbubble types, the resonance peak of the *buckling type* microbubbles was leveled off and its maximum value was at a size greater than the size of the radial maximum, the maximum was found at 3.0 µm diameter.

Subsequently, the microbubble responses were simulated in a dual-frequency ultrasound field (0.5 and 3.75 MHz). For each type of microbubble, a size below res-

onance, at, and above resonance was selected. These sizes are indicated in Fig. 9.2a. The left column of Fig. 9.3 shows the resulting $D(t)$-data of the free gas microbubbles and in the right column corresponding power spectra are given. To study the modulating effect of the LF pulse, we show the $D(t)$ responses during one period of the LF pulse (Fig. 9.3). First we consider the radial response in Fig. 9.3b. In addition to the dual-frequency response (thin line), we also present the low-pass filtered response (cut-off frequency 1.5 MHz), which shows the effect of the modulating LF pulse on the bubble size (bold line). Comparing the radial responses with the acoustic pressure field shown in Fig. 9.3a, we observe that in the positive phase of the LF pulse the bubble is compressed. In this compression phase of the LF pulse, the peak-peak value of the HF response decreased. In the expansion phase of the LF pulse, the peak-peak value of the HF response increased. This radial modulation effect is expected based on the influence of the resonant size on the bubble's response. In the LF expansion phase the bubble size is driven towards the HF resonant size (HF response increases) and in the LF compression phase the bubble size is driven away from the HF resonant size (HF response decreases). In Fig. 9.3d, we observed similar effects for a bubble insonified above resonance. Then a decrease in size by the LF pulse resulted in an increased HF response and vice versa.

In Fig. 9.4, we observe similar effects for the *elastic type* microbubbles. Also for these bubbles a modulation of the size by the LF pulse towards the HF resonant size resulted in an increased HF response. The effects are however less dramatic compared to the free gas bubbles, because of the high damping of the response by the additional coating.

The LF pulse had a modulating effect on the free gas and *elastic type* microbubbles that one would expect based on theory of a harmonic oscillator. The *buckling type* microbubbles presented in Fig. 9.5 however showed opposite behavior. Fig. 9.5b shows the *buckling type* bubble with a resting size of 1.6 μm diameter that was insonified below HF resonance. In this case, a negative phase of the LF pulse did not result in expansion of the bubble. The LF response (bold line) shows that the bubble size is modulated between 1.4 and 1.6 μm. In the negative phase of the LF pulse, we did not observe an increased HF response. On the contrary, highest peak-peak values of the HF responses occurred in the positive phase of the LF pulse when the microbubble was compressed. Thus for the *buckling type* microbubbles the LF pulse appears to have a limited and opposite modulating effect compared to the free gas and *elastic type* microbubbles. Only in the compression phase we observed an increased HF response. Above HF resonance, the HF response seems more equally distributed among expansion and compression phase of the LF pulse (Fig. 9.5d). In response to the LF pulse all *buckling type* bubbles responded with larger compression amplitudes compared to the expansion amplitudes. This is what has been termed previously "compression-only behavior" [de Jong et al., 2007].

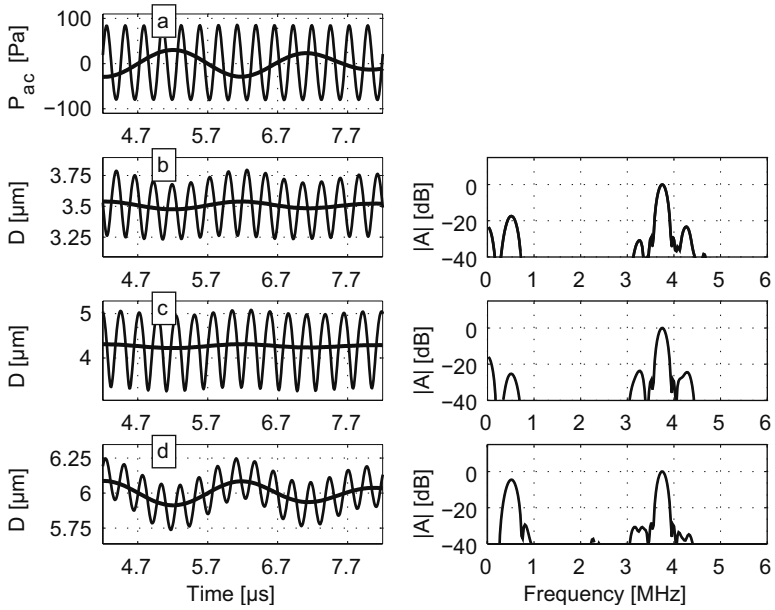

Figure 9.4: Simulated dual-frequency radial responses of *elastic type* microbubbles with different resting sizes (thin lines in left column b-d) and corresponding power spectra (right column b-d). To show the effect of modulation by the LF pulse on the bubble size, the bold lines in left column b-d show the low-pass filtered responses (cut-off frequency 1.5 MHz). a) acoustic pressure field, 0.5 MHz pulse (bold line) and 3.75 MHz pulse (thin line). b) D_0: 3.5 µm, c) D_0: 4.2 µm, d) D_0: 6.0 µm.

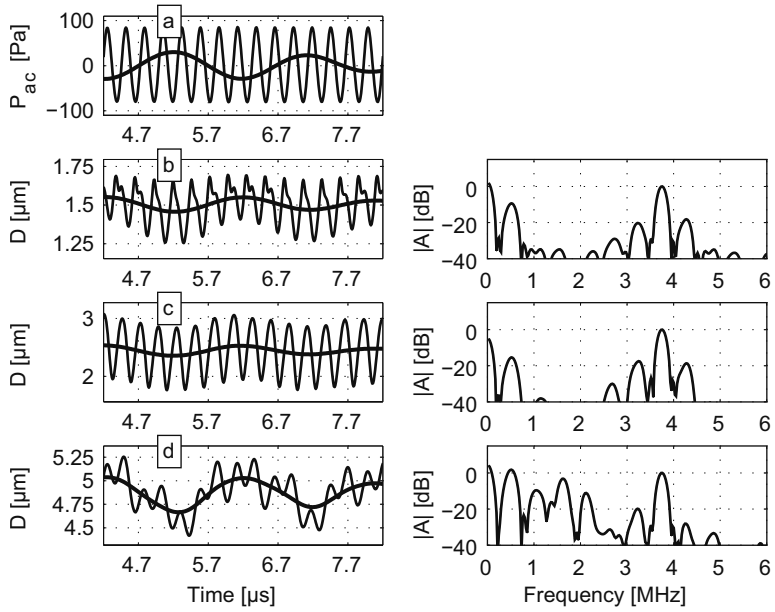

Figure 9.5: Simulated dual-frequency radial responses of *buckling type* microbubbles with different resting sizes (thin lines in left column b-d) and corresponding power spectra (right column b-d). To show the effect of modulation by the LF pulse on the bubble size, the bold lines in left column b-d show the low-pass filtered responses (cut-off frequency 1.5 MHz). a) acoustic pressure field, 0.5 MHz pulse (bold line) and 3.75 MHz pulse (thin line). b) D_0: 1.6 µm, c) D_0: 2.6 µm, d) D_0: 5.0 µm.

The corresponding power spectra in Figs. 9.3–9.5 have been normalized with respect to the response to the insonation frequency of 3.75 MHz. For all types of microbubbles, the free gas, *elastic type* and *buckling type* microbubbles, significant side bands at 3.25 and 4.25 MHz, and to a lesser extent also at 2.75 and 4.75 MHz were observed. These side bands resulted from nonlinear mixing of the LF and HF responses.

9.3.2 Experiments

The vibration of single phospholipids coated microbubbles was recorded using a high-speed camera system. Fig. 9.6 shows a scatter plot of the radial excursions and derived scattered sound pressures of 78 microbubbles insonated with a single transmit frequency of 3.75 MHz. It is observed that the responses of similarly sized bubbles could highly vary. The results of the simulated *buckling type* microbubbles have been included for a comparison with the optical data. In the optical data presented in Fig. 9.6a we observe highest excursion amplitudes for bubble sizes between 2.0 and 3.0 µm diameter. This agrees with the resonant size of the simulated

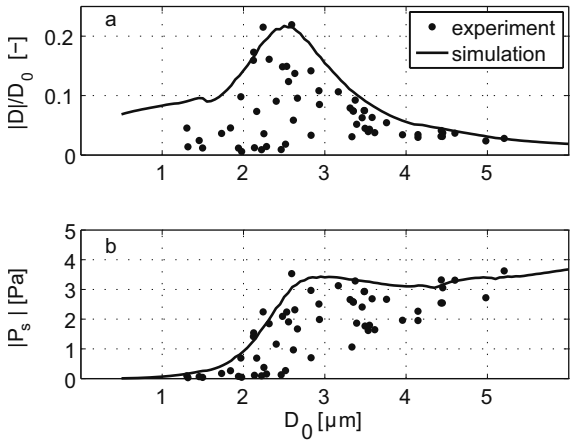

Figure 9.6: (a) Experimental normalized radial responses (amplitude divided by resting diameter); (b) Amplitude of scattered sound pressure at 75 mm as a function of resting diameter. Simulated results for buckling type microbubbles are included.

buckling type microbubbles, which was 2.6 μm diameter.

From the optical radial responses the scattered sound pressures were calculated using Eq. 9.7. The scattered sound pressures of the *buckling type* microbubbles were calculated using Eq. 9.6. The experimentally obtained scattered sound pressures were lower than the simulated pressures, but the general trends are similar. We observed for both the experimental and simulated data a leveled off maximum at a bubble size of 3.0 μm diameter. So the influence of resonance on the maximum scattered sound pressure is limited. Moreover, highest scattered sound pressures occurred for bubble sizes around 3.0 μm diameter, which is greater than the radial maximum at 2.6 μm diameter.

Fig. 9.7 shows the typical $D(t)$ responses and corresponding power spectra of four bubbles. All bubbles showed a response at the insonation frequency of 3.75 MHz. The smallest bubbles of 1.7 and 2.2 μm diameter responded in addition to the transmit, fundamental frequency at the second harmonic. This second harmonic appeared at 4.6 MHz instead of at 7.5 MHz due to aliasing and folding of the second harmonic around the Nyquist frequency. The sampling rate was 12.2 Mfps, which gives a Nyquist frequency of 6.1 MHz. The two largest microbubbles with sizes of 3.6 and 5.0 μm diameter generated a subharmonic response at 1.9 MHz.

Fig. 9.8 shows the results of these microbubbles in a dual-frequency ultrasound field. First, we take a look into the response to the 0.5 MHz pulse. All microbubbles responded with a larger compression amplitude compared to the expansion amplitude. The two smallest microbubbles (1.7 and 2.2 μm diameter) did not show

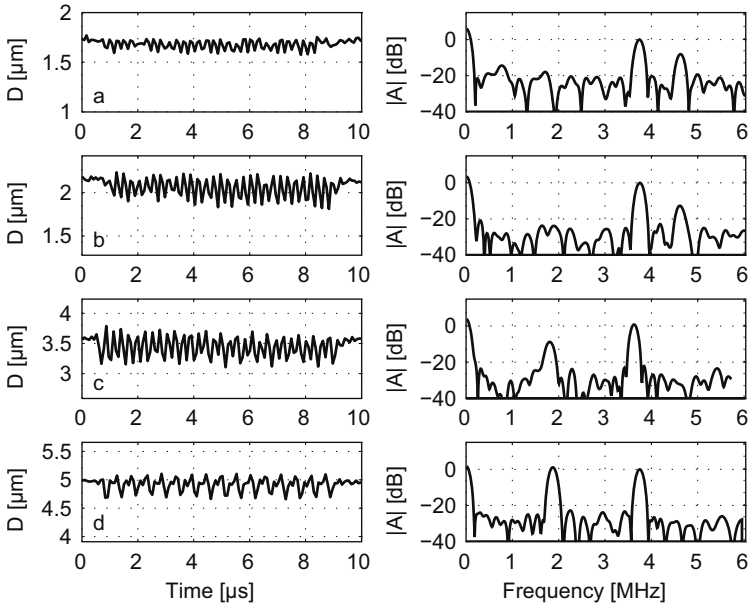

Figure 9.7: Phospholipids coated microbubble responses at a single transmit frequency of 3.75 MHz, diameter-time curves (left column) and corresponding power spectra (right column) for microbubbles with different resting sizes: a) D_0: 1.7 µm, b) D_0: 2.2 µm, c) D_0: 3.6 µm, and d) D_0: 5.0 µm.

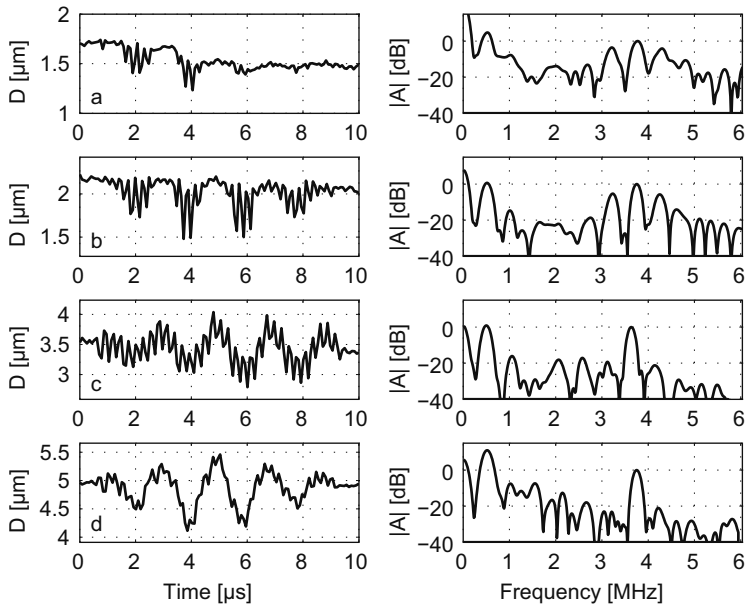

Figure 9.8: Phospholipid-coated microbubble responses in a dual-frequency ultrasound field (0.5 and 3.75 MHz), diameter-time curves (left column) and corresponding power spectra (right column) for microbubbles with different resting sizes: a) D_0: 1.7 µm, b) D_0: 2.2 µm, c) D_0: 3.6 µm, and d) D_0: 5.0 µm.

any expansion at all (Fig. 9.8a and b), but also the two larger microbubbles (3.6 and 5.0 µm diameter) were more compressed than expanded (Fig. 9.8c and d), e.g. for the 5.0 µm diameter microbubble the compression phase had an amplitude of 0.9 µm and the expansion phase 0.5 µm (Fig. 9.8d).

The HF response (Fig. 9.8 was highly modulated for the smallest microbubbles (1.7 and 2.2 µm diameter) and was fully located in the compression phase of the LF response. Corresponding power spectra show high sidebands at $3.75 \pm n \cdot 0.5$ MHz ($n \leq 2$), indicating high nonlinear mixing between the 0.5 and 3.75 MHz responses. To a lesser extent, sidebands were observed for the 3.5 and 5.0 µm microbubbles.

In addition, two other observations were done. When the smallest microbubble of 1.7 µm diameter was insonated, this bubble shrunk in size. It stopped shrinking after two cycles of the LF pulse when its size was 87% of its initial diameter. Shrunken microbubbles were excluded from further study (21 microbubbles from a total of 78 microbubbles). The second observation concerned the subharmonic response of the 5.0 µm microbubble. Comparing Fig. 9.7d with Fig. 9.8d, it was observed that in the dual-frequency field, the subharmonic response had decreased 17 dB. The physical explanation for these observations is currently under investiga-

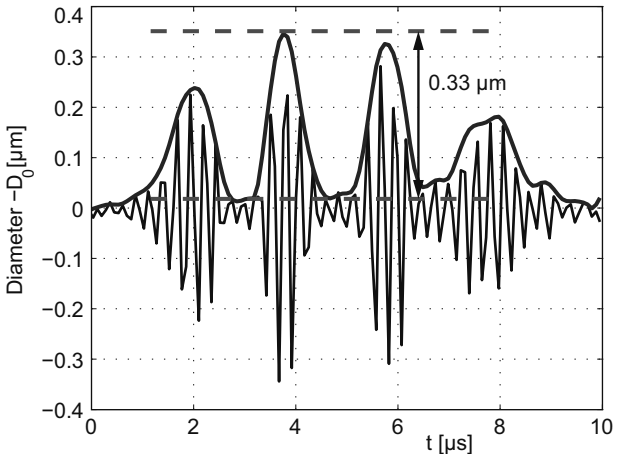

Figure 9.9: Illustration of procedure to determine amplitude modulation. The high-pass filtered radial response of the 2.2 µm diameter from Fig. 9.8b is shown.

tion.

Fig. 9.9 shows the procedure to determine the modulation amplitude of the 3.75 MHz response by the 0.5 MHz pulse. As an example, the $D(t)$ curve of the microbubble with a size of 2.2 µm diameter from Figs. 9.7 and 9.8 was taken. The $D(t)$ curve was high-pass filtered to obtain the 3.75 MHz response only (cut-off frequency 2.25 MHz). Subsequently, the envelope was calculated using IQ-demodulation. The modulation amplitude was determined using a subtraction of the maximum by the minimum value of the envelope, for this example resulting in a modulation amplitude of 0.33 µm.

In Fig. 9.10 the modulation amplitude as a function of resting diameter are depicted for the whole population of recorded microbubbles. Microbubbles with sizes between 1.0 and 3.0 µm diameter were most affected by the LF pulse and showed highest modulation amplitude values. The modulation amplitude decreased with size for microbubbles larger than 3.0 µm diameter. Microbubbles with a size of 5.0 µm hardly showed any modulation effects. Fig. 9.10 includes simulated modulation amplitudes for the buckling type microbubbles. We observe a peak modulation amplitude for resting diameters around 2.2 µm, which is comparable with the experimental results, however, whereas the experimental results showed modulation amplitudes up to 0.34 µm, the simulated results did not exceed 0.11 µm.

For the detection of bubbles with the radial modulation imaging technique, the scattered sound pressures that the bubbles generate are more relevant than their radial motion. We therefore calculated the scattered sound pressures from the radial responses using Eq. 9.7 for both the simulated and experimental results and deter-

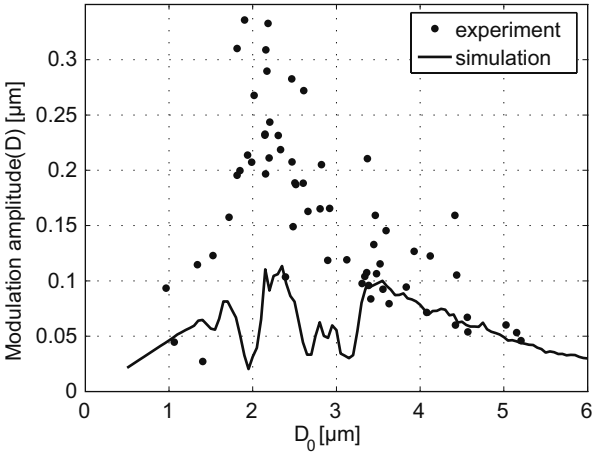

Figure 9.10: Modulation amplitude of diameter as a function of microbubble resting diameter.

mined the modulation amplitude of these scattered sound pressures by following the same procedure as for the radial modulation shown in Fig. 9.9. The resulting modulation amplitudes are shown in Fig. 9.11. The modulation of the scattered sound pressures was different from the radial modulation shown in Fig. 9.10. Whereas the amplitudes of the radial responses were modulated most for sizes between 1.0 and 3.0 μm diameter, highest scattered sound pressure modulation was found for sizes greater than 3.0 μm diameter. Fig. 9.11 also shows the simulated results for the *buckling type* bubbles. A direct comparison between simulations and experiments is difficult because of the wide distribution of the experimental results. The Marmottant model seems to underpredict the effect of modulation for bubble sizes below resonance (2–3 μm diameter) as also appeared in Fig. 9.10. However, the simulation and experimental results both show that highest modulation of the scattered ultrasound can be expected for bubble sizes larger than 2–3 μm diameter.

9.4 Discussion and Conclusion

We studied the behavior of single phospholipids coated microbubbles in a dual-frequency ultrasound field using high-speed recordings and simulations. The two frequencies transmitted were 0.5 and 3.75 MHz. This study showed radial modulation of the bubbles by the 0.5 MHz pulse, which altered the response to the 3.75 MHz pulse compared to single 3.75 MHz frequency insonation (Figs. 9.7 and 9.8).

Compression-only behavior appeared to have a large influence on the radial modulation of phospholipid-coated bubbles. All microbubbles, independent of their size, showed a preference for compression compared to expansion in response to the

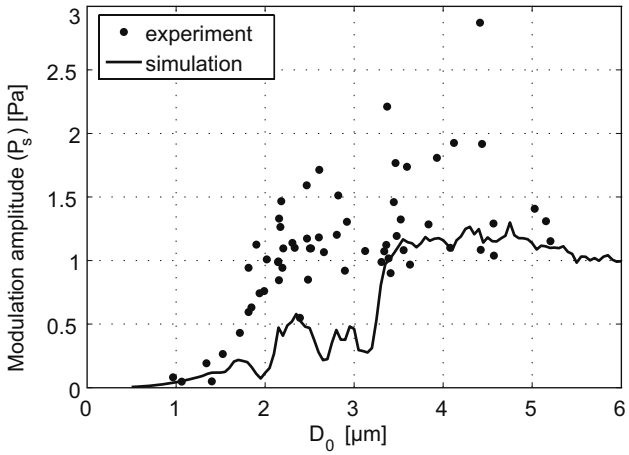

Figure 9.11: Modulation amplitude of scattered sound pressure at 75 mm as a function of microbubble resting diameter.

LF pulse. The LF pulse induced strongest compression-only behavior and strongest modulation of the HF response in the group with smallest bubble sizes (D_0: 1–3 μm), see Fig. 9.10. Microbubbles with sizes just below the HF resonant size showed highest modulation amplitudes up to 0.34 μm. Moderate compression-only behavior and moderate amplitude modulation of the HF response were observed for microbubbles with sizes between 3 and 5 μm diameter. Microbubbles of 5 μm diameter showed least compression-only behavior and smallest modulation of the HF response by the LF pulse.

Both the experimental results and the simulations show the influence of compression only behavior on the radial modulation of contrast bubbles. Traditional theory (free gas and *elastic type* bubbles) does not predict compression-only behavior. The radial modulation predicted by these models is resonance dominated. The LF pulse modulated the bubble size towards and away from the HF resonant size. Upon modulation towards the HF resonant size the HF response increased and upon modulation away from the HF resonant size the HF response decreased, as can be inferred from the radial responses depicted in Figs. 9.3 and 9.4. In the experiments with the high-speed camera and simulations with the Marmottant model we observed opposite modulation behavior, see Figs. 9.5 and 9.8. The HF response increased when the bubble was compressed and decreased or was even absent when the bubble expanded. It is believed that the compression-only behavior, which originates from buckling of the phospholipids coating, induced this radial modulation effect.

Figs. 9.6, 9.10, and 9.11 show that the simulated responses of the *buckling type*

bubbles agree with the experimentally obtained results qualitatively, but not quantitatively. Besides that the experimental results show that individual responses of similarly sized-bubbles can highly vary, better agreement between simulations and experiments may be obtained. This may be achieved by improving the definition of the relationship between the effective surface tension and bubble radius. At present the transitions between the buckling, elastic and ruptured coating regimes are rather *ad hoc* (see Eq. 9.4). To improve this relationship the physical mechanisms of buckling behavior are currently being investigated.

Bouakaz et al. [2007] also presented an optical recording of radial modulation of a phospholipid-coated bubble. This bubble has a size of 4 μm diameter and did not show compression-only behavior. This may be explained by the influence of the coating with respect to the resonant size of the bubble. Below resonance it is expected that the coating influences bubble behavior whereas above resonance inertial effects will dominate. According to our measurements the bubble in the example shown by Bouakaz et al. [2007] was insonified above resonance (Fig. 9.6). In addition, this microbubble was insonified using higher acoustic pressures (120 and 180 kPa). Following the paper by Marmottant et al. [2005], a large oscillation amplitude leads to rupture of the coating with the result that the bubble's behavior will resemble that of a free microbubble.

The second goal of the paper was to investigate the consequences of the observed radial modulation of phospholipid-coated bubbles for the radial modulation imaging technique. We calculated from the radial responses the scattered sound pressures and determined their modulation. The resulting modulation amplitudes provide a basis for the decorrelation between the bubble signals obtained in the radial modulation imaging technique. In this imaging technique, signals are acquired for a certain combination of HF and LF pulses whereby the sign of the LF pulse changes for subsequent signals. In a basic signal processing procedure, obtained signals from both dual frequency combinations are high pass filtered and subtracted. Resulting detection signals have amplitudes that equal the modulation amplitudes presented in Fig. 9.11. In tissue the LF pulse presumably produces less modulation of the HF responses, although a nonlinear interaction of the LF and HF pulse during propagation should be corrected for [Måsøy et al., 2008]. The detection signals are expected to result in an image with a high contrast between tissue and bubbles.

Fig. 9.11 shows that simulations as well as experiments resulted in highest modulation amplitudes and thus highest detection signals for microbubble sizes greater than the HF resonant size of 3 μm diameter. The strong radial amplitude modulation such as observed for microbubble sizes between 1 and 3 μm diameter in Fig. 9.10 did not result in a high detection signal. This is explained by the influence of microbubble size on the scattered sound pressure. A large nonresonant microbubble

can give a larger echo than a smaller microbubble at its resonant frequency as was also mentioned by Newhouse and Mohana Shankar [1984]. A low modulation of a high scattered sound pressure may overweigh a high modulation of a low scattered sound pressure. For example the radial modulation amplitude of the microbubble with a size of 2.2 μm diameter was 15% of its resting size and for the 5.0 μm diameter microbubble, this was only 1% of its resting size. Modulation amplitudes of the scattered sound pressures were however 3.1 Pa for the 2.2 μm diameter microbubble and 8.2 Pa for the 5.0 μm diameter microbubble. It is therefore concluded that to obtain a high detection signal, microbubble size is more effective than the influence of resonance, but also more effective than the influence of compression-only behavior.

Fig. 9.11 indicates that there is an optimum in the relationship between detection signal and bubble size given a set of transmit frequencies. This optimum is found for bubble sizes just above the HF resonant size, which was also found by Angelsen and Hansen [2007]. Moreover, best results for the radial modulation imaging technique are obtained when the bubbles respond linearly to the LF pulse [Bouakaz et al., 2007]. Chérin et al. [2008] explain that harmonic responses to the LF pulse need to be avoided. When the HF pulse is used for imaging and positioned as a short pulse in a longer LF signal, like in the methods suggested by Chérin et al. [2008]; Måsøy et al. [2008]; Shariff et al. [2006b], the image resolution depends on HF provided that the LF signals can be filtered out. The resolution degrades when higher harmonic responses induced by the LF pulse are part of the detection signal. The size of larger bubbles is closer to the LF resonant size, so it is more likely compared to smaller bubbles that these larger bubbles respond nonlinearly to the LF pulse. On the other hand smaller bubbles with sizes just below the resonant size showed relatively more compression-only behavior compared to larger bubbles. In addition to resonant behavior, it is likely that compression-only behavior also results in higher harmonic scattering. Therefore also these microbubbles may generate LF harmonics and in this way decrease image quality. Mixing between LF harmonics and HF responses was not observed in our results. However, possible complications should be investigated.

In this study only the effect of amplitude modulation in a dual-frequency ultrasound field was shown. In addition, we expect phase modulation. To investigate this, we extracted phase information from the experimentally obtained $D(t)$-curves. However, the optical data appeared to be too noisy for a direct derivation of phase. Although not shown in this study, we expect based on the experimental and simulated results that the phase modulation of bubble responses is based on the same mechanisms compared to the amplitude modulation. Thus bubble size is expected to have a similar influence on the phase modulation of the HF response compared to the amplitude modulation of the bubble radius and scattered pressure.

Bibliography

Akhatov, I. S. and D. B. Khismatullin, "Long-wave-short-wave interaction in bubbly liquids," *J Appl Maths Mechs*, 63(6): pp. 917–926, 1999.

Angelsen, B. A. J. and R. Hansen, "SURF imaging - a new method for ultrasound contrast agent imaging," in proc. IEEE Ultras Symp, pp. 531–541, 2007.

Bouakaz, A., M. Versluis, J. Borsboom, and N. de Jong, "Radial modulation of microbubbles for ultrasound contrast imaging," *IEEE Trans Ultrason Ferroelectr Freq Control*, 54(11): pp. 2283–2290, 2007.

Brenner, M. P., S. Hilgenfeldt, and D. Lohse, "Single-bubble sonoluminescence," *Rev Mod Phys*, 74: pp. 425–484, 2002.

Brock-Fisher, G. A., M. D. Poland, and P. G. Rafter, Means for increasing sensitivity in non-linear ultrasound imaging systems, US patent no 5577505, 1996.

Chérin, E., J. Brown, S. E. Måsøy, H. Shariff, R. Karshafian, R. Williams, P. N. Burns, and F. S. Foster, "Radial modulation imaging of microbubble contrast agents at high frequency," *Ultrasound Med Biol*, 34(6): pp. 949–62, 2008.

Chin, C. T., C. Lancée, J. Borsboom, F. Mastik, M. Frijlink, N. de Jong, M. Versluis, and D. Lohse, "Brandaris 128: a 25 million frames per second digital camera with 128 highly sensitive frames," *Rev Sci Instru*, 74(12): pp. 5026–5034, 2003.

de Jong, N., M. Emmer, C. T. Chin, A. Bouakaz, F. Mastik, D. Lohse, and M. Versluis, ""Compression-only" behavior of phospholipid-coated contrast bubbles," *Ultrasound Med Biol*, 33(4): pp. 653–656, 2007.

Deng, C. X., F. L. Lizzi, A. Kalisz, A. Rosado, R. H. Silverman, and D. J. Coleman, "Study of ultrasonic contrast agents using a dual-frequency band technique," *Ultrasound Med Biol*, 26(5): pp. 819–831, 2000.

Duck, F. A., "Nonlinear acoustics in diagnostic ultrasound," *Ultrasound Med Biol*, 28(1): pp. 1–18, 2002.

Emmer, M., A. van Wamel, D. E. Goertz, and N. de Jong, "The onset of microbubble vibration," *Ultrasound Med Biol*, 33(6): pp. 941–949, 2007.

Hansen, R., B. A. J. Angelsen, P. N. Burns, A. Bouakaz, J. Borsboom, M. Versluis, and N. de Jong, "Radial modulation imaging," in proc. The tenth European symposium on ultrasound contrast imaging, Rotterdam, pp. 90–91b, 2005.

Hilgenfeldt, S., D. Lohse, and M. Zomack, "Response of bubbles to diagnostic ultrasound: a unifying theoretical approach," *Eur Phys J B, Condensed Matter Phys*, 4(2): pp. 247–255, 1998.

Hope Simpson, D., C. T. Chin, and P. N. Burns, "Pulse inversion Doppler: A new method for detecting nonlinear echoes from microbubble contrast agents," *IEEE Trans Ultrason Ferroelectr Freq Control*, 46(2): pp. 372–382, 1999.

Måsøy, S.-E., P. Standal, P. Näsholm, T. F. Johansen, B. A. J. Angelsen, and R. Hansen, "SURF imaging: In vivo demonstration of an ultrasound contrast agent detection technique," *IEEE Trans Ultrason Ferroelectr Freq Control*, 55(5): pp. 1112–1121, 2008.

Marmottant, P., S. M. van der Meer, M. Emmer, M. Versluis, N. de Jong, S. Hilgenfeldt, and D. Lohse, "A model for large amplitude oscillations of coated bubbles accounting for buckling and rupture," *J Acoust Soc Am*, 118(6): pp. 3499–3505, 2005.

Newhouse, V. L. and P. Mohana Shankar, "Bubble size measurements using the nonlinear mixing of two frequencies," *J Acoust Soc Am*, 75(5): pp. 1473–1477, 1984.

Roy, R. A., S. I. Madanshetty, and R. E. Apfel, "An acoustic backscattering technique for the detection of transient cavitation produced by microsecond pulses of ultrasound," *J Acoust Soc Am*, 87(6): pp. 2451–8, 1990.

Schrope, B. A. and V. L. Newhouse, "Second harmonic ultrasonic blood perfusion measurement," *Ultrasound Med Biol*, 19(7): pp. 567–79, 1993.

Shariff, H., P. Bevan, R. Karshafian, M. Karakolis, M. Banerjee, and P. N. Burns, "Radial modulation imaging: a dual frequency ultrasound imaging technique for microbubble contrast," in proc. 11th Eur Symp Ultras Contrast Imaging, pp. 64–66, 2006a.

Shariff, H., P. Bevan, R. Karshafian, R. Williams, and P. N. Burns, "Radial modulation imaging: Raising the frequency for contrast imaging," in proc. IEEE Ultras Symp, pp. 104–107, 2006b.

Stride, E. and N. Saffari, "Theoretical and experimental investigation of the behaviour of ultrasound contrast agent particles in whole blood," *Ultrasound Med Biol*, 30(11): pp. 1495–1509, 2004.

van der Meer, S. M., B. Dollet, M. M. Voormolen, C. T. Chin, A. Bouakaz, N. de Jong, M. Versluis, and D. Lohse, "Microbubble spectroscopy of ultrasound contrast agents," *J Acoust Soc Am*, 121(1): pp. 648–656, 2007.

Wyczalkowski, M. and A. J. Szeri, "Optimization of acoustic scattering from dual-frequency driven microbubbles at the difference frequency," *J Acoust Soc Am*, 113(6): pp. 3073–9, 2003.

Chapter 10

Self-demodulation of high-frequency ultrasound

Abstract - **High-frequency (>10 MHz) ultrasound is used in e.g. small animal imaging or intravascular applications. Currently available ultrasound contrast agents (UCAs) have a suboptimal response for high frequencies. This study therefore investigates the nonlinear propagation effects in a high-frequency ultrasound field (25 MHz) and its use for standard UCA and diagnostic frequencies (1–3 MHz). Nonlinear mixing of two high-frequency carrier waves produces a low-frequency wave, known as the self-demodulation or parametric array effect. Hydrophone experiments show that the self-demodulated field of a focused 25 MHz transducer (850 kPa source pressure) has an amplitude of 45 kPa at 1.5 MHz in water. Such pressure level is sufficient for UCA excitation. Experimental values are confirmed by numerical simulations using the KZK equation on a spatially convergent grid.**

Conditionally accepted for publication in the Journal of the Acoustical Society of America, 2009. By H. J. Vos, D. E. Goertz, and N. de Jong. The authors whish to thank dr. V. F. Humphrey (University of Southampton, UK) and dr. J. Huijssen (Delft University of Technology, the Netherlands) for the very helpful discussions on the self-demodulation technique.

10.1 Introduction

Over the past 20 years, high-frequency diagnostic ultrasound ($>$ 10 MHz) has found wide interest in areas such as Intravascular Ultrasound (IVUS) [Frijlink et al., 2006], small animal imaging [Goertz et al., 2007b], and ocular diagnostics [Foster et al., 2000; Kruse et al., 1998]. The improved spatial resolution at higher frequencies allows for imaging smaller anatomic or pathologic structures, such as atherosclerotic plaques. The implementation of flow imaging at higher frequencies has improved both sensitivity and resolution to permit microvascular imaging [Kruse et al., 1998; Goertz et al., 2000]. There remain however limitations in sensitivity due to issues of noise and tissue motion, such as for example in the context of vasa vasorum imaging in coronary arteries. This has led to investigating the use of ultrasound contrast agents (UCAs) [Goertz et al., 2005] that enhance echo signals from the cardiovascular system, thus increasing the contrast to the surrounding tissue. The majority of ultrasound contrast imaging techniques are most efficient if the imaging frequency of the diagnostic system is approximately equal to the resonance frequency of the bubbles [Minnaert, 1933; de Jong et al., 2002]. Commercial UCAs have therefore been developed to be primarily resonant within a limited frequency range, which is usually lower than the frequencies used in the afore-mentioned applications. For example, while contrast-enhanced IVUS and small imaging systems employ imaging frequencies of 15–50 MHz, the major resonance frequency of most conventional UCA bubbles is generally around 1–5 MHz [Gorce et al., 2000; Shi and Forsberg, 2000; Sarkar et al., 2005]. The exception to this is Definity (Lantheus Medical Imaging, North Billerica, MA), which exhibits a dual frequency resonant peak, with a substantial subpopulation of bubbles resonant at higher ultrasound frequencies [Goertz et al., 2007a]. As a result, nonlinear (second and subharmonic) imaging approaches at higher frequencies have been shown to be feasible with Definity, either in native or population modified form, or with experimental bubble formulations that have been fabricated to be comprised primarily of bubbles below approximately 2 μm in diameter [Goertz et al., 2006]. Despite the potential of second and subharmonic imaging of small bubble populations, it has yet to be established that these approaches are optimal for higher frequencies, which motivates the investigation of other approaches.

Often it is suggested in the literature that the detection of UCAs can be improved by using two-frequency approaches such as radial modulation [Deng et al., 2000; Bouakaz et al., 2007; Chérin et al., 2008], and nonlinear mixing [Cathignol et al., 1990; Wu et al., 2005; Chen et al., 2006; Yeh et al., 2008]. Due to a nonlinear response of bubbles, the two frequencies would produce sum-and-difference components which can be detected. For example, two studies exploited the beat frequency f_b of two carrier waves f_1 and f_2 , where $f_b \ll f_1$ and f_2 [Chen et al., 2006; Wu et al., 2007; Yeh et al., 2008]. The beat frequency was scattered by a population of bubbles,

and detected by a separate low-frequency transducer. Wu et al. [2005] earlier used a similar technique, where the low-frequency was generated as a cross-product of all frequency contents of a short pulse. Using this method, Wu et al. reported a contrast-to-tissue ratio of $\pm$ 15 dB (concentration was not reported) that the authors addressed fully to the nonlinear properties of bubbles.

However, in the rationale for such dual-frequency UCA bubble detection techniques it is neglected that sufficiently high pressure levels (on the order of 200 kPa and more), such as those used in the experiments, could introduce significant distortion of the pulse due to nonlinear propagation in the medium. More generally, clinical ultrasound imaging is regularly applied at pressure levels that introduce nonlinear distortion of the imaging pulse, not only leading to higher harmonics of the fundamental frequency [Humphrey, 2000; Duck, 2002], but also to low-frequency contents due to the so-called self-demodulation effect [Berktay, 1965; Averkiou et al., 1993]. Self-demodulation is an effect in which a low-frequency pressure wave develops in a nonlinear medium as a function of the envelope of a high-frequency pulse. The low-frequency wave propagates as if it was generated by a planar low-frequency source, and has directivity about equal to the high-frequency carrier wave. Hence, the term 'parametric array' has often been used in the past to describe such wave generation, particularly in marine applications [Berktay, 1965; Ostrovsky et al., 2005]. Furthermore, self-demodulation has been experimentally shown to be able to excite uncoated gas bubbles [Pace et al., 1997]. The self-demodulation of short pulses was experimentally confirmed using carrier frequencies of 3.5 MHz [Averkiou et al., 1993] and 10 MHz [Rénier et al., 2007].

In an accompanying study, of which preliminary results are reported by Vos et al. [2006], the current writers have found that a short ($\sim$ 2 cycles) ultrasound pulse with a carrier frequency of 10 MHz can excite bubbles having a resonance frequency of about 1 MHz, by repeating the pulse at a PRF of 1 MHz. It was suggested that the self-demodulation effect is the most significant mechanism to convert energy from the 10 MHz carrier wave into the lower bubble resonance frequency. However, no previous reports were found to address this effect in relevant settings for UCAs and high-frequency diagnostic ultrasound. This manuscript therefore characterizes the self-demodulation effect using both numerical simulations and acoustical experiments, at frequencies and pressure levels suitable for high-frequency contrast-enhanced ultrasound imaging.

10.2 Methods

10.2.1 Nonlinear ultrasound propagation

Transition pressure level for shock waves

The propagation of ultrasound can be described in three different regimes [Duck, 2002; Hamilton and Blackstock ed., 1998; Leighton, 2007]. The first is the acoustical limit, which applies for very small amplitudes of the acoustic wave. The propagation is linear in such case. The second is a weakly nonlinear regime, in which waves can interact with other waves and itself; nonlinear distortion gives rise to second and higher harmonics of the fundamental pulse frequency, and also to lower frequencies due to the self-demodulation effect of noncontinuous waves. The third approximation is the shock-front regime, in which nonlinear response of the medium has deformed an initially sinusoidal wave into saw-tooth-like waves including a spatial discontinuity of the pressure. Such spatial discontinuity leads to high nonlinear dissipation of the acoustic energy [Bacon, 1984; Naze Tjøtta et al., 1990; Rudenko, 1995; Hamilton and Blackstock ed., 1998].

The current study addresses both the weakly nonlinear and the shockwave regime. The transition pressure level between the two regimes can be estimated by considering the ultrasound field and medium properties. Bacon [1984] theoretically derived the pressure in the focal region of a focused transducer for which the shockfront is fully developed. Eq. 6 in Bacon [1984] is rewritten to

$$p_f = \frac{\sigma_d \rho c^3 \sqrt{G^2 - 1}}{\omega \beta \, d \ln\left(G + \sqrt{G^2 - 1}\right)}. \tag{10.1}$$

Here, p_f is the peak rarefaction pressure in the focus, σ_d is a dimensionless parameter related to the amount of distortion of the pulse [Duck and Perkins, 1988; Duck, 2002]; the shockfront is fully developed for $\sigma_d = \pi/2$ [Bacon, 1984]. Symbol ρ denotes the density of the medium (998 kg/m^3 for water), c the speed of sound (1482 m/s), ω the driving frequency (rad/s), β the nonlinear parameter (3.5 [Duck, 2002]), and d the geometrical curvature of the surface, approximately equal to the focal distance if $G \gg 1$. The acoustical gain G describes the focusing strength of a transducer, defined by the ratio of the pressure level in the focus to the pressure level at the transducer surface, neglecting attenuation. The gain can be calculated by $G = \omega a^2/2cd$, with a the aperture radius of the transducer.

Eq. 10.1 assumes a Gaussian axial beam profile, and neglects attenuation. Nevertheless it will serve as an estimator for the transition pressure from weakly nonlinear distortion to the full shock theory throughout this paper.

Weakly-nonlinear approximation of self-demodulation

As was derived by Berktay [1965] based on Westervelt's equation, the self-demodulation wave can be described as a function of the pulse envelope $E(t)$ only, i.e., independent of the carrier wave frequency and phase, as long as the time-scale of the envelope is much larger than the inverse of the carrier frequency. Then, the self-demodulation pressure wave $p_{sd}(t)$ can be approximated by [Berktay, 1965]

$$p_{sd}(t) \propto \frac{d^2}{dt^2}|E(t)|^2 \tag{10.2}$$

The current study exploits a transmitted ultrasound field $p_t(t)$ composed of a carrier wave having sine-wave envelope,

$$p_t(t) = A \sin\left(\frac{\omega_{sd}}{2}t\right) \cdot \sin(\omega_c t) \tag{10.3}$$

which, when employing Eq. 10.2, becomes

$$p_{sd}(t) \propto A^2\omega_{sd}^2 \sin(\omega_{sd}t) \tag{10.4}$$

with A the wave amplitude, ω the angular frequency, 'sd' denoting self-demodulation and 'c' the carrier wave ($\omega_{sd} \ll \omega_c$). Since $E(t)$ is a sine-wave envelope in Eq. 10.3, $|E|^2$ has a frequency two times the frequency of $E(t)$. Furthermore, the second time derivative has a magnitude that depends linearly on $\omega_{sd}^2 A^2$. Hence the amplitude of the low-frequency component $p_{sd}(t)$ in Eq. 10.3 relates quadratically to the envelope frequency.

The transmitted pulse $p_t(t)$ in Eq. 10.3 is described likely by:

$$p_t(t) = \frac{A}{2}\sin(\omega_1 t) + \frac{A}{2}\sin(\omega_2 t) \tag{10.5}$$

with $\omega_1 = \omega_c - \frac{\omega_{sd}}{2}$ and $\omega_1 = \omega_c + \frac{\omega_{sd}}{2}$. Hence, the frequency spectrum of $p_t(t)$ shows two separated peaks centred around the carrier frequency ω_c, with a difference frequency equal to ω_{sd}, the self-demodulation frequency.

A more thorough analysis of such bi-frequency source signal is found in the Fenlon solution [Fenlon, 1972; Hamilton and Blackstock ed., 1998] which also addresses the nonlinear interaction between secondary frequency components, i.e., from all sum-and-difference combinations of $m \cdot \omega_1 + n \cdot \omega_2$, m and n integers. However Eq. 10.2 provides an easy concept with the limitation that the approximation is only valid for low-level source pressures, when secondary effects such as multiple harmonics of the difference frequency are negligible. At the pressure levels reported in the current study, the secondary effects including shockfronts will be shown to be significant, motivating the use of a numerical simulation model.

Numerical ultrasound propagation model

Simulation models of nonlinear propagation of ultrasound have found wide interest in the past [Duck, 2002; Rudenko, 1995; Lee and Hamilton, 1995; Hart and Hamilton, 1988; Humphrey, 1992; Blackstock, 1964; Tavakkoli et al., 1998]. One common approach for calculating the ultrasound field is the implementation of a parabolic wave-equation as developed by Khokhlov, Zabolotskaya, and Kuznetsov (KZK) [Hamilton and Blackstock ed., 1998]. The KZK-equation incorporates diffraction, absorption, and nonlinear propagation. As described by e.g. Lee and Hamilton [1995], the equations can be solved in the time-space-domain using a finite difference algorithm. Such approach has been shown to be able to predict the self-demodulation of a short pulse [Averkiou et al., 1993; Lee and Hamilton, 1995; Averkiou and Hamilton, 1997; Callé et al., 2002], and shockfronts [Humphrey, 2000; Rudenko, 1995].

In the experiments described in this paper, a strongly focused transducer was used, having an acoustical gain of 19. While the implementation of Lee and Hamilton is strictly limited to gains lower than 10, Hart and Hamilton [1988] have proposed a simulation grid that is suitable for strongly focused transducers. In Hart and Hamilton [1988], the KZK-equation is solved in frequency domain, while the current authors have chosen to adapt the time-domain numerical algorithm of Lee and Hamilton to work on the converging grid proposed by Hart and Hamilton. Details of the implementation are found in the Appendix. In the simulations the attenuation in water was taken 25 10^{-3} Np/m/MHz^2 [Duck, 1990], i.e., a sound diffusivity of water of 4 10^{-6} m^2/s [Lee and Hamilton, 1995], and a converging-grid parameter δ of 7 [Hart and Hamilton, 1988]. The grid resolution close to the transducer surface in the lateral direction was 16 μm (relative resolution of 0.005 of the aperture radius) and the axial stepsize was 38 μm. In focus these were 14 μm and 29 μm, respectively, showing the convergence of the grid.

10.2.2 Experimental setup

In order to verify the numerical results, an experimental setup was used to measure the actual ultrasound field of a 25 MHz single element transducer (V324-1" focus, Olympus NDT, Waltham, MA). This transducer has an effective diameter of 6.3 mm and 27 mm focal distance, giving an acoustical gain of 19, at 25 MHz. With reference to Fig. 10.1, an arbitrary waveform generator (AWG520, Tektronix, Beaverton, OR) was connected through a –4dB precision attenuator (VAT-4+, Mini-Circuits, Brooklyn, NY) to a linear power amplifier (1000W, 10 MHz – 86 MHz, LPI-10, ENI, Rochester, NY). The output of the power amplifier was band-pass filtered using a custom high-power 8 – 28 MHz 5$^{\text{th}}$ order Butterworth filter to reduce any residual low-frequency content, and fed to the transducer. The transducer is characterized to generate a surface pressure of $\sim$ 1.7 MPa peak-peak when driven by a 234 V peak-

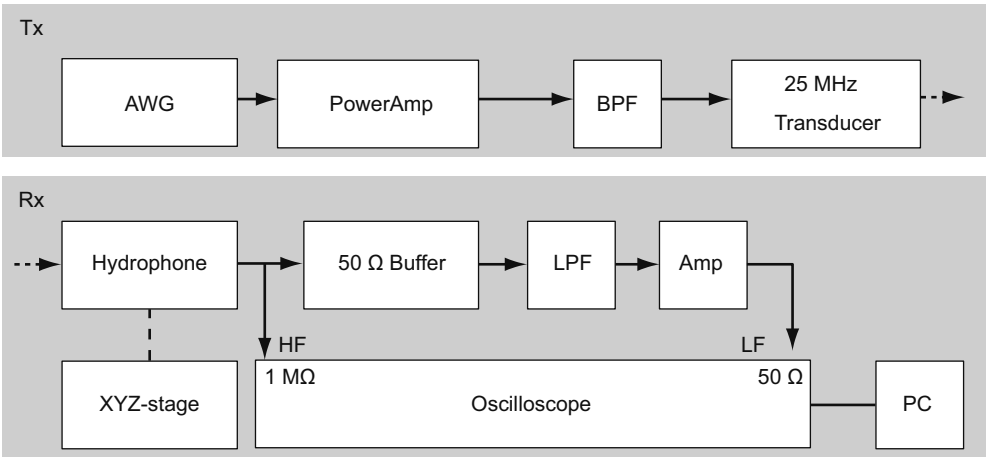

Figure 10.1: Block diagram of the experimental setup. AWG is the arbitrary waveform generator. BPF is band-pass filter (8 – 28 MHz). LPF is low-pass filter (10.7 MHz).

peak signal at 25 MHz. The acoustic pressure was measured by a calibrated needle hydrophone (0.075 mm diameter PVDF, Precision Acoustics Ltd., Dorchester, Dorset, UK) immersed in a large water tank. The tank contained tap-water left overnight to obtain room-temperature gas saturated water. The hydrophone was mounted on a computer-controlled precision XYZ stage. Although significant low-frequency content was present in the electric signal at the output of the high-power amplifier due to nonlinear amplification, this was strongly reduced by the band-pass filter at the output (reduction $>$ 40 dB at 1.5 and 3 MHz) and by the reduced efficiency of the transducer at 1.5 and 3 MHz (additional reduction of $>$ 20 dB).

The expected low-frequency pressure levels are in the order of –30 dB to –50 dB below the high-frequency levels, and the receiving electronic circuit had to be extremely linear in order to avoid any nonlinear mixing. Therefore, the signal was split into a low-frequency (LF) and a high-frequency (HF) track. Again with reference to Fig. 10.1, the hydrophone signal was fed to a first channel of a 1 gigasamples-per-second digital oscilloscope (Tektronix TDS3014B), set to 1 MΩ impedance and 256-averaging mode (HF track). The hydrophone signal was in parallel fed to a custom-built 50 Ω buffer amplifier (buf 602-opamp on a TI DEM-BUF-SO-1A demonstration fixture, Texas Instruments, Dallas, TX), a low-pass filter (Mini-circuits 10.7 MHz), and amplified with a 36 dB low-noise amplifier (MiTEQ AU-1189, Hauppauge, NY) (LF track). This signal was averaged on a second channel of the oscilloscope.

The signal levels were carefully checked to be within the linearity-limits of the internal hydrophone amplifier, buffer amplifier, and low-noise amplifier. Also the amplification and attenuation of the components have been carefully characterized

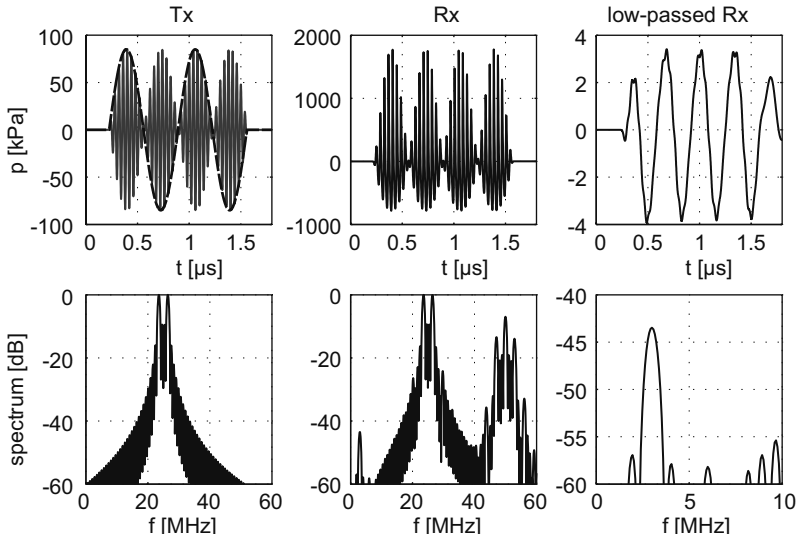

Figure 10.2: Simulation result of transmitting an ultrasound pulse constructed by the summation of a 23.5 MHz and 26.5 MHz wave, with 85 kPa amplitude (upper left), its frequency contents (lower left), and the resulting pulse (middle) and low-pass filtered pulse (right) in focus. The conversion of energy to lower frequency is caused by the self-demodulation mechanism.

over the full range of frequencies employed (1 – 50 MHz). Final SNR values were at least 17 dB at the low-frequency range (1 – 10 MHz) and 52 dB at the high-frequency range (20 – 60 MHz).

10.3 Results

10.3.1 General principle

In the numerical simulation a pulse is constructed by summation of sinusoidal signals of 23.5 MHz (f_1) and 26.5 MHz (f_2) (see Fig. 10.2 – left panel). The amplitude of the source pressure is set to 85 kPa which results in focal pressures in the weakly-nonlinear regime. The bottom panel shows the normalized frequency spectrum of the transmitted pulse obtained by the Fourier transform. The propagated pulse (Fig. 10.2 – top middle) shows a rarefaction pressure level (0.7 MPa) smaller than the compression pressure level (1.6 MPa), demonstrating the distortion of the originally symmetric pulse. The spectrum in the bottom-middle panel contains the fundamental frequencies f_1 and f_2, their second harmonic frequencies, $2f_1$ and $2f_2$, and the sum-and-difference components 50 MHz and 3.0 MHz.

The pulse in focus is low-pass filtered (sixth-order Butterworth, –6 dB cut-off point at 6 MHz) and shown in Fig. 10.2, top right panel. The amplitude of the low-frequency content is about 3 kPa. The corresponding spectral densities at the

low-frequency are shown in the bottom panel. Note that the filtering operation is linear, and the low-frequency content is a 'physical' wave that can autonomously interact with a bubble, even if the high-frequency carrier wave is attenuated in the focus.

Similarly, Fig. 10.3 shows the spectra of focal pulses with respective envelopes of zero MHz (i.e., no modulation), 1.5 MHz, and 3 MHz. The increase of difference frequency $f_1 - f_2$ leads to higher level of the self-demodulation frequency, as expected from application of Eq. 10.4. The time-domain pulses showed amplitude of 1.1 kPa of the 1.5 MHz-envelope pulse, and 5.7 kPa for the 3 MHz-envelope pulse. Such increase by a factor of 5 with double envelope frequency is roughly predicted by Eq. 10.4. With respect to the tone burst, a self-demodulation signal will appear depending on the second derivative of the envelope squared (see Eq. 10.2), but the level of this signal is outside of the displayed dynamic range.

When setting the source pressure amplitude to 850 kPa (Fig. 10.4), the threshold of 1.7 MPa of focal pressure predicted by Eq. 10.1 is exceeded. The pulse in focus has formed a full shock front, with a peak-negative value of 1.7 MPa and peak-positive value up to 7 MPa. The spectra in Fig. 10.4 show many more sum-and-difference components, originating from interactions of both primary and secondary waves. The pulse contains high second and higher harmonic contents of the low-frequency wave; for example, with the 3 MHz envelope frequency, low-frequency waves with a frequency of 6 and 9 MHz are visible. Furthermore, the high-frequency contents show many side-bands with interspacing frequencies equal to the envelope frequency. Also, cross-products between f_1, f_2 and f_{sd} show up, at e.g. 20.5 MHz and 29.5 MHz for a 3 MHz envelope. Low-pass filtered waves had time-domain amplitudes of 45 kPa and 130 kPa for the 1.5 and 3.0 MHz envelopes respectively, indicating a pressure increase of roughly a factor of 3 while the envelope frequency doubles. In comparison to the weakly-nonlinear example, this shows that the formation of the shockfront reduces the squared dependency of the self-demodulation amplitude on the envelope frequency.

10.3.2 Transmit pressure dependency

Fig. 10.5 shows the influence of the source pressure amplitude on the frequency content of the pulse at focus. For amplitudes lower than approximately 200 kPa, corresponding to a fullshock threshold of 1.7 MPa pressure in focus (Eq. 10.1; dash-dotted lines in Fig. 10.5), the high-frequency f_c component has a linear relationship with source amplitude, whereas the low-frequency amplitude f_{sd} depends quadratically on the transmit pressure, as expected in the weakly-nonlinear regime. The second harmonic of the low-frequency content (2 f_{sd}) depends approximately cubically on the source level. This is unexpected since the bi-frequency solution of Fenlon predicts a power-of-four dependency [Fenlon, 1972]. The difference will be

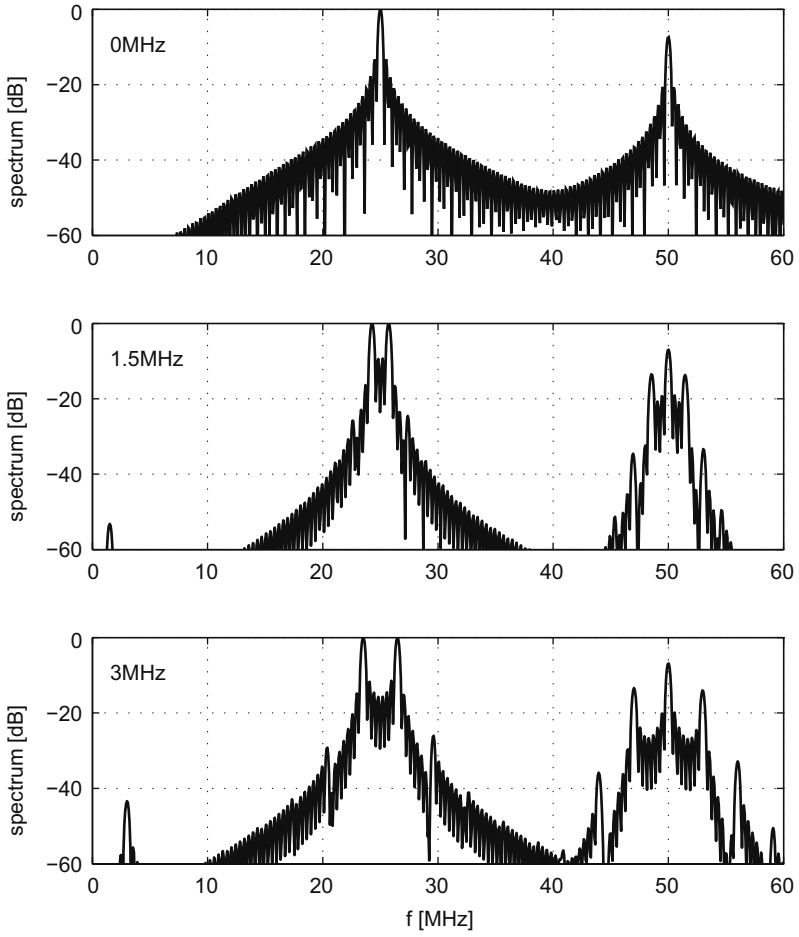

Figure 10.3: Fourier spectra of weak-nonlinearly propagated pulses having center frequency of 25 MHz, source pressure amplitude of 85 kPa. The envelope frequencies are 0 MHz, 1.5 MHz, and 3 MHz.

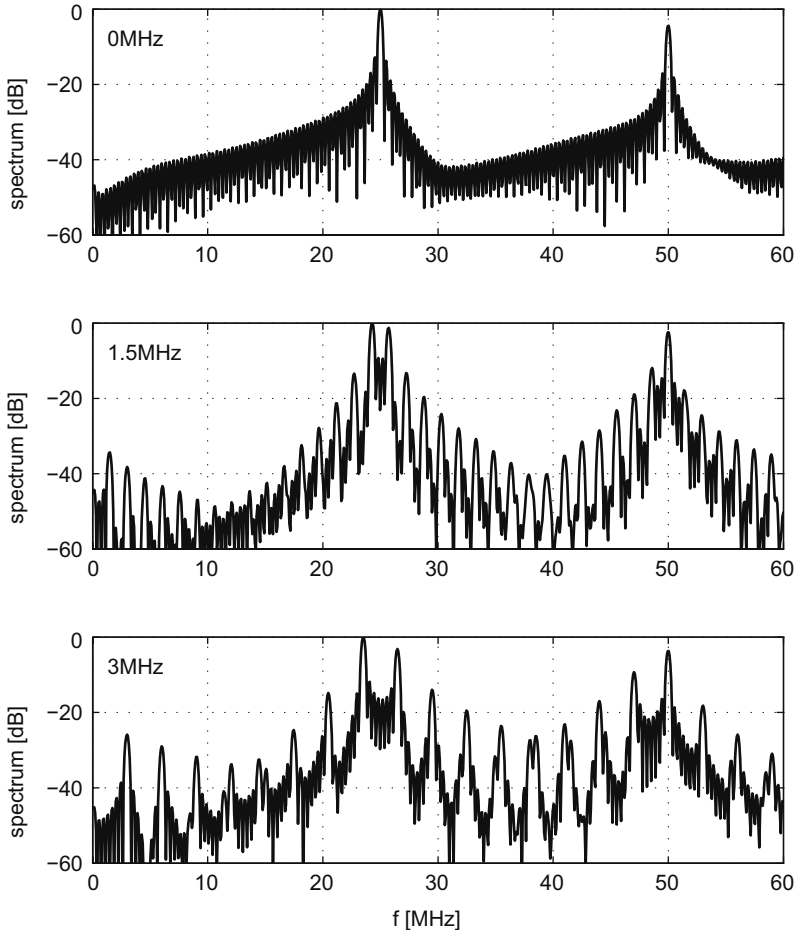

Figure 10.4: Fourier spectra of strongly nonlinearly propagated pulses, having a source pressure amplitude of 850 kPa. The envelope frequencies and other parameters values are equal as those leading to Fig. 10.3.

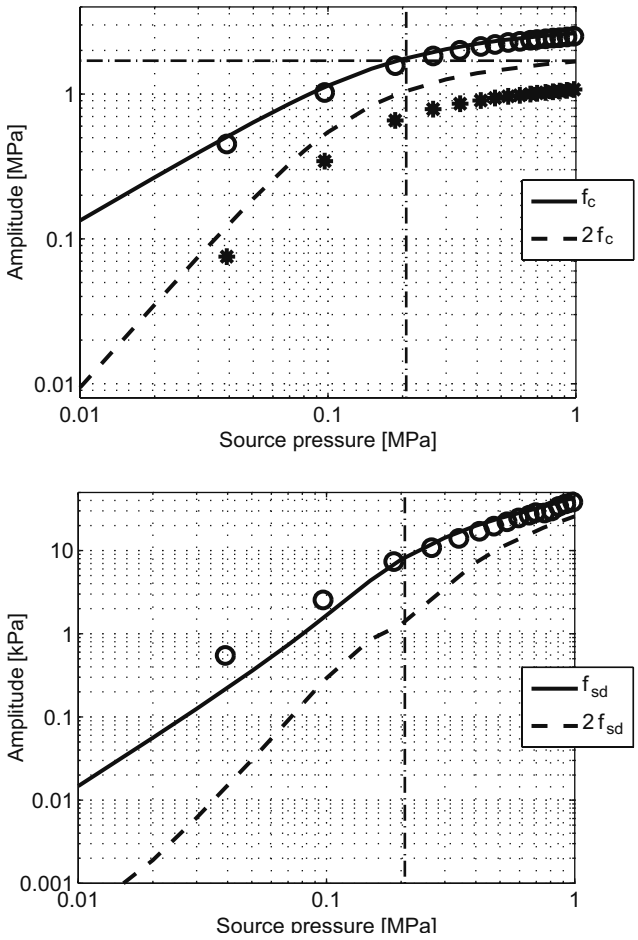

Figure 10.5: (a) High-frequency and (b) low-frequency pressure levels in the focus as a function of the source pressure. Circles denote experimental values. Carrier frequency f_c was 25 MHz, self-demodulation frequency f_{sd} was 1.5 MHz. The vertical line marks the fullshock pressure threshold of 1.7 MPa as predicted by Eq. 10.1 for this transducer.

further addressed in the Discussion section.

Above 200 kPa source pressure, the fundamental f_c component in the focus starts to deviate from a linear dependency, showing a flattening towards the acoustic saturation limit [Blackstock, 1964; Hamilton and Blackstock ed., 1998]. This is consistent with the expectation of nonlinear increase of dissipation associated with the presence of a shock front [Hamilton and Blackstock ed., 1998]. Furthermore, the low-frequency (f_{sd}) amplitude starts to deviate from squared dependency to an almost linear relation, which is different from propagation in the weakly-nonlinear regime.

Note that although the theoretical acoustical gain of this transducer at 25 MHz is 19, the actual ratio between source pressure and focal pressure for low amplitudes is only 12.5 (see Fig. 10.5a, e.g., source pressure: 10 kPa, focal pressure: 125 kPa). The difference of 52% (3.6 dB) can be fully attributed to the attenuation in water, which is about 2.2 10^{-3} dB/cm/MHz^2 [Duck, 1990]; at 25 MHz and a focal distance of 27 mm, the ultrasound is expected to be attenuated by 3.7 dB.

Experimentally obtained values are shown by dots in Fig. 10.5. The measured values of f_c and f_{sd} agree within 10% of the numerical predictions. The second harmonic amplitude at 2 f_c is about 40% (3 dB) lower than the predicted amplitudes throughout the full range.

10.3.3 Beam profiles

Fig. 10.6 shows the predicted axial beam profile of the transducer in the full shock regime. The envelope frequency is set to generate 1.5 MHz self-demodulation waves and the pressure at the transducer surface is 850 kPa amplitude, similar to the experimental value. Pulses obtained along the beam axis are digitally band-pass filtered at the carrier wave frequency (–6 dB cut-off points at 20 MHz and 30 MHz, Butterworth 4$^{\text{th}}$ order), at the second harmonic frequency (40 – 60 MHz), at the self-demodulation frequency (0.75 – 2.25 MHz) and at twice the self-demodulation frequency (2.25 – 3.75 MHz). The plotted amplitudes are obtained in the time-domain after Hilbert transforming the filtered pulses.

At the carrier frequency f_c and its second harmonic the highest amplitudes appear at 27 mm which is the focal region. The self-demodulation wave begins to plateau at 15 mm distance from the transducer, reaching a peak amplitude of –35 dB before decreasing after 25 mm. The amplitude of the 3 MHz wave, twice the self-demodulation frequency, is up to –40 dB in focus. Since 0 dB corresponds to 2.5 MPa in this figure, the amplitudes of the waves at 1.5 MHz and 3 MHz are 45 and 25 kPa, respectively.

Figure 10.6 also shows the experimentally obtained amplitudes. The hydrophone was positioned along the beam axis at incremental distances from the transducer of 1 mm to 75 mm, in steps of 1 mm. The amplitude levels are obtained from the

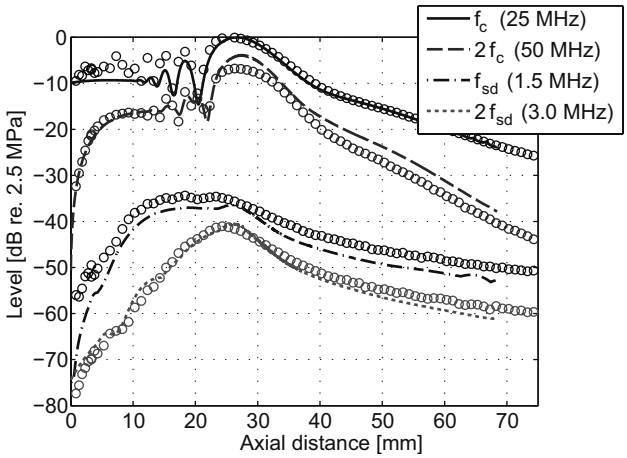

Figure 10.6: Simulated (lines) and experimental (circles) axial beam profile at the fundamental frequency (25 MHz), second harmonic (50 MHz), self-demodulation frequency (1.5 MHz) and double self-demodulation frequency (3 MHz) as a function of distance from the transducer. Source amplitude 850 kPa.

recorded pulses with the same filter characteristics as in the simulation, and compensated for the hydrophone sensitivity. At 1 mm from the transducer, the amplitude of the self-demodulation pulse is over 50 dB smaller than the fundamental level, but achieves a maximum of –35 dB in the region before the focus. The normalization value was equal to that of the simulation. Note that the level at the second harmonic frequency matches the predicted values except for the focal region, where a difference of 3 dB is observed (cf. Fig. 10.5).

The lateral beam profile in the focal region (27 mm from the transducer) is plotted in Fig. 10.7. The –6 dB width of the fundamental frequency beam is 0.4 mm, while the self-demodulation beam measures approximately 3 mm. The highfrequency second harmonic beam at 50 MHz has about 0.3 mm width, and the low-frequency second harmonic beam at 3 MHz has 1.4 mm width.

The experimental lateral beam shown in Fig. 10.7 is very similar in shape and amplitude to the predicted beam. The fundamental-frequency side lobes show a slightly different spatial frequency, which could be attributed to a slight error in the estimation of the transducer geometry used for the simulation. Furthermore, the second harmonic levels are well predicted except for within the focal region, and for $z \geq 0.7$ mm.

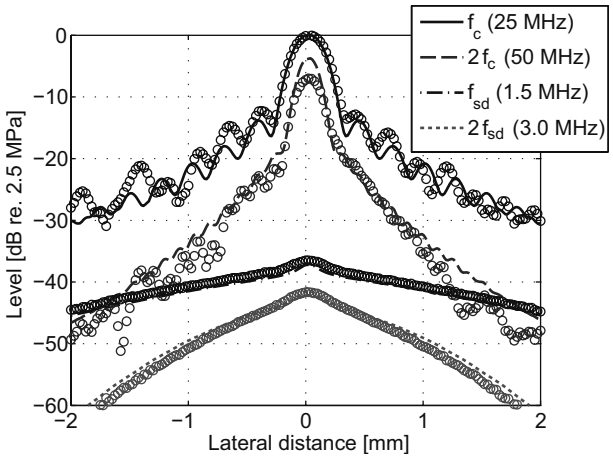

Figure 10.7: Simulated (lines) and experimental (circles) lateral beam profile in focus (27 mm from transducer).

10.3.4 Influence of focusing and medium

Based on the simulation model, some additional comments can be made regarding the application of the self-demodulation technique.

First, focusing generally increases the pressure levels and therefore the self-demodulation pressure. For example, when modeling a focal distance of 13.5 mm (acoustic gain of 40) instead of 27 mm, with source pressure of 850 kPa, the self-demodulation pressure increases from 45 kPa to 170 kPa. The change in focal distance also increases the primary wave amplitude in focus, and for comparison, reducing the source pressure in the latter configuration to 425 kPa gives a 92 kPa self-demodulation wave. Note that in such comparison the self-demodulation wave depends almost linearly on the source pressure, and not quadratic as expected from Eq. 10.4, since nonlinear shock wave dissipation is significant. As another example, taking a flat surface (i.e., unfocused) instead of curved one, the self-demodulation level is 4 kPa. Compared to the focused geometry the conversion is much lower. This can be attributed to the lower acoustical gain and high attenuation in water at 25 MHz giving lower fundamental-frequency pressure levels.

Second, the application of the self-demodulation technique *in vivo* implies a different propagation medium. Tissue generally has a higher nonlinearity value than water, but also higher attenuation. For example, liver tissue has a nonlinearity β of 4.4, compared to 3.5 of water [Duck, 1990]. The attenuation is about 20 dB/cm at 25 MHz, while water has attenuation of about 1.4 dB/cm at 25 MHz [Duck, 1990]. Combining tissue values with the focused transducer model gives a maximum self-demodulation pressure level of 6 kPa (peak rarefaction amplitude of 1.1 MPa of the

Table 10.1: Preliminary simulation results with two transducers models, in water and tissue. Carrier frequency is 25 MHz, envelope frequency is 1.5 MHz.

Aperture diameter	Focal distance	Acoustical gain	Source pressure	Amplitude of self-demodulation wave	
				Water	Tissue
mm	mm	-	MPa	kPa	kPa
6	12.7	36	0.5	100	4
			5	800	250
0.9	flat	2	1.5	7	3
			5	60	30

25 MHz primary field), which is low for contrast excitation applications [van der Meer et al., 2007]. In clinical applications it would be better to use strongly focused transducers. For example, a 25 MHz-probe of the commercially available high-frequency scanner Vevo-770 (RMV 707B, VisualSonics, Toronto, Canada) has a diameter of 6 mm and focal length of 12.7 mm (gain 36). The acoustic pressure close to the transducer was 0.5 MPa, measured with the hydrophone setup. Inserting such model in the simulation with liver tissue, the self-demodulation pressure is 4 kPa. By artificially increasing the source pressure to 5 MPa, which might be achieved in future using more efficient transducers [Brown et al., 2007], a self-demodulation value of 250 kPa can be obtained, see Table 10.1. The peak rarefaction pressure value of the 25 MHz wave is 4.5 MPa. Note that the high attenuation has resisted the formation of shockwaves, giving an almost squared relation of the self-demodulation with source pressure in tissue; this relation could help evaluating the applicability of high-frequency systems for self-demodulation techniques.

Third, the combination of the self-demodulation technique with intravascular ultrasound (IVUS) transducers might be beneficial for contrast agent excitation. Such catheter based transducers are limited in size to about 0.9 mm diameter, and the source pressure can reach higher values, currently up to at least 1.5 MPa. For this application, the simulated self-demodulation pressures will not exceed 3 kPa in tissue. However, the propagation in tissue is in the weakly-nonlinear regime. We estimate it would be necessary to increase IVUS source pressures by a factor of three in order to generate a self-demodulation signal sufficiently strong to excite contrast agents.

10.4 Discussion and conclusions

10.4.1 General principle

Figures 10.2 – 10.5 show the general results of the self-demodulation technique. The full shock threshold level is well predicted by Eq. 10.1, even in the case of strong attenuation at such high carrier frequencies (Fig. 10.5). A focal pressure far below this threshold shows self-demodulation tendency described by Berktay [Berktay, 1965], cf. Eq. 10.2, but a pressure close to the threshold resulted in significant spectral content at many distinct frequencies. In particular, the second and higher harmonic frequency of the low-frequency wave are clearly visible in Fig. 10.4. The origin of these signals is the interaction of primary and/or secondary frequency components. For example, a 3 MHz wave could originate from the interaction of for example 22.75 MHz ($f_1 - f_{sd}$) and 25.75 MHz (f_2), or secondary frequencies only, for example 48.5 MHz (2 f_1) and 51.5 MHz (2 f_2). One way to look at the higher difference frequency is based on Berktay's approximation, Eq. 10.2. Because the envelope shown in Fig. 10.2 (middle panel) is not a sine-wave anymore, but rather a sum of sine-waves having multiple-integer frequencies of the fundamental, Eq. 10.2 will also predict multiple-integers of the self-demodulation frequency.

An alternative approach to estimating the other harmonic components is to employ the Fenlon solution [Fenlon, 1972; Hamilton and Blackstock ed., 1998]. Analysis with the Fenlon solution shows that the amplitude of the second difference frequency should increase with the source pressure to the fourth-power, rather than the cubic dependency predicted by the KZK simulations. Fenlon's solution assumes neither attenuation nor diffraction, and has analytical solutions, which all could potentially explain a difference with the numerical KZK results. Therefore, to locate the origin of the difference, we performed additional numerical simulations. First, to isolate the effects of attenuation, the diffraction step was removed from the numerical simulation while keeping the other simulation parameters equal. This basically yields a numerical implementation of the plane-wave Burgers equation in time domain [Hamilton and Blackstock ed., 1998]. In these simulations, the amplitude of the second difference frequency showed a fourth-power dependency on the source pressure, independent of the attenuation values employed. From this it was concluded that any deviation from the fourth-power dependency is not caused by attenuation or numerical implementation alone. We then performed converging-grid KZK simulations for the strongly focused case using a range of attenuation values, while keeping all other simulation parameters equal to those reported in the Methods section. It was found that when attenuation was sufficiently low (e.g., 2.5 10^{-3} Np/m/MHz^2, 10% of the attenuation in water), the results for the second difference frequency showed a fourth-power dependency, consistent with the predictions of Fenlon's equation. From these results it is concluded that diffraction alone does not produce deviations from the fourth-power relationship, but rather it may be a suf-

ficiently high attenuation level in combination with a strongly focused source that is responsible for the cubic dependency of the amplitude of the second difference frequency. Nonetheless, a numerical artifact could not be ruled out fully.

Another striking feature is seen in the lateral beam profiles at 1.5 MHz and 3 MHz (Fig. 10.7). The –6dB beam width of the low-frequency wave is 3 mm, which equals 3 λ (wavelength $\lambda \approx 1$ mm at 1.5 MHz). The 3 MHz wave has –6 dB beam of 1.4 mm, again equal to about 3 λ ($\lambda \approx 0.5$ mm at 3 MHz). The absolute beam width decreases with the harmonic number as earlier reported [Naze Tjøtta et al., 1990] and the equality of the relative beam widths implies equal sources of the secondary waves, as long as the phenomenon is diffraction limited. Also, note that the carrier beam width in focus is only 0.4 mm, much smaller than that of the self-demodulation wave, but the fundamental freqeuncy field is much wider in the pre-focal region, where the self-demodulation wave is building up.

The –6 dB beam width of 3 mm (Fig. 10.7) could be somewhat disappointing for imaging applications since the parametric approach has been used in the past to generate narrow low-frequency beams with relatively small transducers. However, conventionally producing such beam width at 27 mm distance from a 6.3 mm transducer is impossible at 1.5 MHz (from KZK simulation: 6 mm beam width at 27 mm distance) [Berktay, 1965]. Also, the second harmonic beam width of such transducer transmitting a 0.75 MHz ultrasound field still produces larger beam width (4 mm). Therefore, the self-demodulation technique provides narrowest beam. Apart from the lateral beam width, the axial focal region is smaller and more pronounced than with conventional 1.5 MHz ultrasound field generation.

When comparing the simulation results of the beam profiles to the experimental ones, Figs. 10.6 and 10.7, in general very similar levels occur for all four frequency components (except for the focal region – see below). This finding has two major implications. First, it implies that the simulations using the KZK equation predicts correct attenuation and diffraction for the given transducer model. Second, it also correctly predicts the nonlinear distortion of the pulse. These are not trivial results since the parabolic assumption in the wave propagation is challenged by the geometries employed in this study. However, Naze Tjøtta et al. [1991] derived that the parabolic approximation is valid as long as the ratio of focal distance d and aperture radius a is larger than 3.5, which is the case in the current study ($d/a \sim 8$).

The 2 f_c level in focus is predicted by the model to be –4 dB compared to fundamental level, while the measured value is at –7 dB; this difference is also seen in Fig. 10.5. A –4 dB second harmonic level is perhaps surprising since nonlinear propagation theory predicts an absolute maximum of –6 dB [Duck, 2002]. The current writers can only hypothesize that the error originates from an underestimation of the shockwave dissipation, since the shockwave is most prominent in the focal region.

10.4.2 Implications

The role of attenuation is two-fold in the self-demodulation process. In general terms the self-demodulation process merits a highly absorptive medium to isolate the low-frequency components from the high-frequency primary waves. However attenuation also reduces the pressure level which in turn could affect the nonlinear conversion. Focusing of the beam produces a 40-fold increase of the self-demodulation amplitude in water, as shown with the additional simulations, because of the higher gain but also because of less attenuation since the distance to the focal region is reduced. Note that Naze Tjøtta et al. [1991] earlier stated that focusing has only limited effect on the self-demodulation amplitude, but their finding was based on zero-absorption calculations.

The self-demodulation technique allows for engineering pulses e.g. without any transient head or tail, cf. Fig. 10.2, or for generating very wide-band low-frequency signals [Berktay, 1965; Pace et al., 1997]. This can be advantageous over conventional linear generation of pulses in an experimental setup with a possibly limited bandwidth. To produce low-frequency wide-band signals, a high-frequency carrier wave with Gaussian envelope suffices [Berktay, 1965; Pace et al., 1997]. In fact, by carefully applying Berktay's approximation on a Gaussian-enveloped pulse, it can be shown that the center frequency of the self-demodulated wave is equal to the -3 dB absolute bandwidth of the transmission pulse [Berktay, 1965]. This rule of thumb could help in analysing the frequency spectrum of a nonlinearly propagating acoustic pulse.

Furthermore, the technique provides acoustic amplitudes suitable for contrast microbubble excitation. This has two major implications. First, the effect can for example be used in spectroscopy measurements as shown by the current authors [Vos et al., 2006, 2009]. The high pressure amplitudes of the primary field in water could give rise to microbubble destruction that should be avoided. An acoustic filter [Humphrey, 1992; Vos et al., 2009] or absorptive medium such as tissue could reduce the level of the primary waves. A pressure value of 1.1 MPa in tissue at 25 MHz, as reported in the Result section, is close to the microbubble destruction level at 20 MHz [Needles et al., 2008] but below that of 30 MHz [Goertz et al., 2006]. However the approach is most suitable for imaging larger bubbles (i.e., resonant at the low frequencies) and these will be far less susceptible to being destroyed by high frequency ultrasound than smaller bubbles that are closer to resonance. Microbubble destruction is further considered in an accompanying paper [Vos et al., 2009].

Second, the finding might be important for the work by e.g. Wu et al. [2005] and Chen et al. [2006] who use a semi-dual frequency technique to increase the detection signals of contrast bubbles. In the rationale all low-frequency content in the echoes are suggested to be generated by nonlinear behavior of microbubbles. The current study however shows that nonlinear propagation cannot be *a priori* neglected. In contrast detection applications where the main low-frequency generation

mechanism is nonlinear propagation, the low-frequency content will also be present in tissue-scattered signals, and the agents merely increase contrast by linear scattering. Hydrophone experiments or numerical propagation simulations showing the exact frequency content of the acoustic excitation pulse could elucidate the relative significance of nonlinear propagation compared to nonlinear scattering of bubbles.

10.4.3 Concluding remarks

This paper presents numerical and experimental results of the self-demodulation effect, using ultrasound conditions that are relevant for high-frequency medical imaging. The mechanism provides sufficient acoustic pressure in water, 45 kPa, to excite an ultrasound contrast agent (UCA) microbubble [van der Meer et al., 2007; Emmer et al., 2007]. Although the self-demodulation technique has been previously used to investigate uncoated gas bubbles in water, see e.g. Pace et al. [1997], no reports have been found to address the possibility of its use in combination with UCAs.

The poor efficiency of the self-demodulation mechanism is a disadvantage. In the reported experiments, the source pressure is 850 kPa giving 45 kPa low-frequency amplitude. Tissue attenuation decreases the self-demodulation pressure dramatically (Table 10.1), which can be overcome by focusing and/or increased transmit amplitudes. Another solution is a reduction of carrier frequency to e.g. the range 10 MHz – 20 MHz. Such range is currently used for small animal imaging and carotid artery scanning and might therefore be easily implemented in current clinical systems.

APPENDIX. KZK on a converging/diverging grid

Hart and Hamilton have described a numerical implementation of the KZK-equation for strongly focused spherical transducers accounting for absorption, diffraction, and nonlinear propagation [Hart and Hamilton, 1988]. The spatial numerical grid converges from the transducer to the focal region and diverges afterwards, thus having highest resolution in the focal region where high spatial variations in the pressure are expected. The equations developed by Hart and Hamilton [1988] solve the KZK in the frequency domain, while the current writers have opted for an implementation in the time domain, analogous to the derivation by Lee and Hamilton [1995]. Such an implementation in the time-domain is computationally more effective when acoustic shock fronts are expected compared to the frequency-domain solution [Lee and Hamilton, 1995]. However, the numerical calculation scheme in Lee and Hamilton [1995] has to be adapted to suit the converging/diverging grid.

The reader is referred to the PhD dissertation of Lee [1993] for a full description of the numerical implementation, and Hart and Hamilton [1988] and Naze Tjøtta

et al. [1991] for the theory on the converging/diverging grid. The KZK equation in reduced units for the converging/diverging grid reads [Hart and Hamilton, 1988]

$$\left((\sigma \pm \delta)^2 \, \frac{\partial^2}{\partial \bar{\tau} \, \partial \sigma} - \frac{1}{4G} \bar{\nabla}_{\perp}^2 - (\sigma \pm \delta)^2 \, A \, \frac{\partial^3}{\partial \bar{\tau}^3}\right) \bar{P} = (\sigma \pm \delta) \, \frac{B}{2} \, \frac{\partial^2 \bar{P}^2}{\partial \bar{\tau}^2} \tag{10.6}$$

with σ ($\geq$ –1) the axial distance to the transducer, δ ($>$ 1) the parameter that governs the convergence of the grid, $\bar{\tau}$ the retarded time ($\geq$ 0), G the acoustic gain, and $\bar{\nabla}_{\perp}^2$ the two-dimensional Laplace operator with respect to $\bar{u}$ ($\geq$ 0) which is the lateral distance to the beam axis. The parameters A and B characterize the absorption and source amplitude, respectively [Hart and Hamilton, 1988]. The pressure signal is denoted by $\bar{P}$. The value of σ equals -1 at the transducer surface, and 0 in the geometrical focus of the transducer. The '-' sign in front of δ is chosen if σ is negative and '+' elsewhere [Hart and Hamilton, 1988].

Compared to the time-domain code description in Lee [1993], diffraction and nonlinear propagation have to be adapted for the current grid; attenuation is unchanged. In Lee [1993], Eqs. 3.30 – 3.32 and Eqs. 3.40 – 3.42 express the numerical implementation of the diffraction term. These are unchanged. However, the value of R defined in Eqs. 3.33 and 3.43 becomes

$$R = \frac{\Delta \bar{\tau} (\Delta \sigma)_k}{(\sigma_{k+1} \pm \delta)^2 (\Delta \bar{u})^2} \tag{10.7}$$

with k the index associated to finite steps of σ.

Calculation of the nonlinear propagation term is less straightforward, due to the change of sign before δ at σ = 0. Eq. 3.56 in Lee [1993] is replaced by

$$\frac{\partial \bar{P}}{\partial \sigma} = \frac{N \bar{P}}{(\sigma \pm \delta)} \, \frac{\partial \bar{P}}{\partial \bar{\tau}} \tag{10.8}$$

with N the parameter of nonlinearity. Equation 10.8 is solved using a stretched coordinate ζ [Lee, 1993],

$$\frac{d\varsigma}{d\sigma} \, \frac{\partial \bar{P}}{\partial \varsigma} = \frac{N \bar{P}}{(\sigma \pm \delta)} \, \frac{\partial \bar{P}}{\partial \bar{\tau}}. \tag{10.9}$$

With a definition of

$$\frac{d\varsigma}{d\sigma} = \frac{1}{(\sigma \pm \delta)} \tag{10.10}$$

Eq. 10.9 is reduced to

$$\frac{\partial \bar{P}}{\partial \varsigma} = N \bar{P} \, \frac{\partial \bar{P}}{\partial \bar{\tau}} \tag{10.11}$$

and Eq. 10.10 is rewritten to

$$\varsigma = \int_{-1}^{\sigma} \frac{d\sigma'}{(\sigma' \pm \delta)} \tag{10.12}$$

where the integration limits are dictated by the boundary condition: ζ=0 when σ=-1, and the '-' sign should be chosen when σ', the integration variable, is negative.

Tedious but straightforward evaluation of 10.12 for all $\sigma < 0$ and $\sigma \geq 0$ results in

$$\varsigma = \int_{-1}^{\sigma} \frac{d\sigma'}{(\sigma' \pm \delta)} = \ln\left(\frac{|\sigma| + \delta}{\delta + 1}\right) \tag{10.13}$$

Following Lee, an exact implicit solution of Eq. 10.11 is of the format

$$\bar{P}\left(\sigma, \bar{\tau}\right) = F\left(\bar{\tau} + N\bar{P}\varsigma\right) \tag{10.14}$$

and at the subsequent spatial step, combining Eqs. 10.14 and 10.13,

$$\bar{P}\left(\sigma + \Delta\sigma, \bar{\tau}\right) = F\left(\bar{\tau} + N\bar{P}\ln\left[\frac{|\sigma| + \Delta\sigma + \delta}{\delta + 1}\right]\right) \tag{10.15}$$

Rewriting the argument of the natural logarithm in Eq. 10.15 and combining with Eq. 10.14 yields the forward stepping algorithm

$$\bar{P}\left(\sigma + \Delta\sigma, \bar{\tau}\right) = \bar{P}\left(\sigma, \bar{\tau} + N\bar{P}\ln\left[1 + \frac{\Delta\sigma}{|\sigma| + \delta}\right]\right) \tag{10.16}$$

The numerical implementation of the nonlinear differential equation is thus (compare with Eq. 3.71 in Lee [1993]),

$$P_{i,j}^{k+1} = \frac{P_{i,j}^{k}}{1 - N\left[\left(P_{i+1,j}^{k} - P_{i,j}^{k}\right)/\Delta\bar{\tau}\right]\ln\left[\frac{1+(\Delta\sigma)_k}{(|\sigma_k|+\delta)}\right]} \tag{10.17}$$

for $P_{i,j}^{k} \geq 0$.

For $P_{i,j}^{k} < 0$ the pressure difference takes the form of $\left(P_{i,j}^{k} - P_{i-1,j}^{k}\right)$, analogous to Lee's implementation.

Bibliography

Averkiou, M. A. and M. F. Hamilton, "Nonlinear distortion of short pulses radiated by plane and focused circular pistons," *J Acoust Soc Am*, 102(5): pp. 2539–2548, 1997.

Averkiou, M. A., Y. S. Lee, and M. F. Hamilton, "Self-demodulation of amplitude-modulated and frequency-modulated pulses in a thermoviscous fluid," *J Acoust Soc Am*, 94(5): pp. 2876–2883, 1993.

Bacon, D. R., "Finite amplitude distortion of the pulsed fields used in diagnostic ultrasound," *Ultrasound Med Biol*, 10(2): pp. 189–195, 1984.

Berktay, H. O., "Possible exploitation of non-linear acoustics in underwater transmitting applications," *J Sound Vib*, 2(4): pp. 435–461, 1965.

Blackstock, D. T., "Thermoviscous attenuation of plane, periodic, finite-amplitude sound waves," *J Acoust Soc Am*, 36(3): pp. 534–542, 1964.

Bouakaz, A., M. Versluis, J. Borsboom, and N. de Jong, "Radial modulation of microbubbles for ultrasound contrast imaging," *IEEE Trans Ultrason Ferroelectr Freq Control*, 54(11): pp. 2283–2290, 2007.

Brown, J. A., F. S. Foster, A. Needles, E. Chérin, and G. R. Lockwood, "Fabrication and performance of a 40-MHz linear array based on a 1-3 composite with geometric elevation focusing," *IEEE Trans Ultrason Ferroelectr Freq Control*, 54(9): pp. 1888–1894, 2007.

Callé, S., J. P. Remenieras, O. Bou Matar, and F. Patat, "Presence of nonlinear interference effects as a source of low frequency excitation force in vibro-acoustography," *Ultrasonics*, 40: pp. 873–878, 2002.

Cathignol, D., J. Y. Chapelon, V. L. Newhouse, and P. Mohana Shankar, "Bubble sizing with high spatial resolution." *IEEE Trans Ultrason Ferroelectr Freq Control*, 37(1): pp. 30–37, 1990.

Chen, S., R. Kinnick, J. F. Greenleaf, and M. Fatemi, "Difference frequency and its harmonic emitted by microbubbles under dual frequency excitation," *Ultrasonics*, 44: pp. e123–e126, 2006.

Chérin, E., J. Brown, S.-E. Måsøy, H. H. Shariff, R. Karshafian, R. Williams, P. N. Burns, and F. S. Foster, "Radial modulation imaging of microbubble contrast agents at high frequency," *Ultrasound Med Biol*, 34(6): pp. 949–962, 2008.

de Jong, N., A. Bouakaz, and P. Frinking, "Basic acoustic properties of microbubbles," *Echocardiography*, 19(3): pp. 229–240, 2002.

Deng, C. X., F. L. Lizzi, A. Kalisz, A. Rosado, R. H. Silverman, and D. J. Coleman, "Study of ultrasonic contrast agents using a dual-frequency band technique," *Ultrasound Med Biol*, 26(5): pp. 819–831, 2000.

Duck, F. A., Physical properties of tissue, Academic press Ltd., 1990.

Duck, F. A., "Nonlinear acoustics in diagnostic ultrasound," *Ultrasound Med Biol*, 28(1): pp. 1–18, 2002.

Duck, F. A. and M. A. Perkins, "Amplitude-dependent losses in ultrasound exposure measurement," *IEEE Trans Ultrason Ferroelectr Freq Control*, 35(2): pp. 232–241, 1988.

Emmer, M., A. van Wamel, D. E. Goertz, and N. de Jong, "The onset of microbubble vibration," *Ultrasound Med Biol*, 33(6): pp. 941–949, 2007.

Fenlon, F. H., "An extension of the bessel-fubini series for a multiple frequency CW acoustic source of finite amplitude," *J Acoust Soc Am*, 51(1 (part 2)): pp. 284–289, 1972.

Foster, F. S., C. J. Pavlin, K. A. Harasiewicz, D. A. Christopher, and D. H. Turnbull, "Advances in ultrasound biomicroscopy," *Ultrasound Med Biol*, 26(1): pp. 1–27, 2000.

Frijlink, M. E., D. E. Goertz, H. J. Vos, E. Tesselaar, G. Blacquière, A. Gisolf, R. Krams, and A. F. W. van der Steen, "Harmonic intravascular ultrasound imaging with a dual-frequency catheter," *Ultrasound Med Biol*, 32(11): pp. 1649–1654, 2006.

Goertz, D. E., D. A. Christopher, J. L. Yu, R. S. Kerbel, P. N. Burns, and F. S. Foster, "High-frequency color flow imaging of the microcirculation," *Ultrasound Med Biol*, 26(1): pp. 63–71,

2000.

Goertz, D. E., N. de Jong, and A. F. W. van der Steen, "Attenuation and size distribution measurements of Definity and manipulated Definity populations," *Ultrasound Med Biol*, 33(9): pp. 1376–1388, 2007a.

Goertz, D. E., M. E. Frijlink, N. de Jong, and A. F. W. van der Steen, "High frequency nonlinear scattering from a micrometer to submicrometer sized lipid encapsulated contrast agent," *Ultrasound Med Biol*, 32(4): pp. 569–577, 2006.

Goertz, D. E., M. E. Frijlink, D. Tempel, V. Bhagwandas, A. Gisolf, R. Krams, N. de Jong, and A. F. W. van der Steen, "Subharmonic contrast intravascular ultrasound for vasa vasorum imaging," *Ultrasound Med Biol*, 33(12): pp. 1859–1872, 2007b.

Goertz, D. E., A. Needles, P. N. Burns, and F. S. Foster, "High-frequency, nonlinear flow imaging of microbubble contrast agents," *IEEE Trans Ultrason Ferroelectr Freq Control*, 52(3): pp. 495–502, 2005.

Gorce, J.-M., M. Arditi, and M. Schneider, "Influence of bubble size distribution on the echogenicity of ultrasound contrast agents - A study of SonoVue," *Invest Radiol*, 35(11): pp. 661–671, 2000.

Hamilton, M. F. and D. T. Blackstock ed., Nonlinear acoustics, Academic Press, 1998.

Hart, T. S. and M. F. Hamilton, "Nonlinear effects in focused sound beams," *J Acoust Soc Am*, 84(4): pp. 1488–1496, 1988.

Humphrey, V. F., "Non-linear acoustics as a laboratory tool," in proc. Instit Acoust, vol. 14, No. 3, pp. 99–113, 1992.

Humphrey, V. F., "Nonlinear propagation in ultrasonic fields: measurements, modelling and harmonic imaging," *Ultrasonics*, 38: pp. 267–272, 2000.

Kruse, D. E., R. H. Silverman, R. J. Fornaris, D. J. Coleman, and K. W. Ferrara, "A swept-scanning mode for estimation of blood velocity in the microvasculature," *IEEE Trans Ultrason Ferroelectr Freq Control*, 45(6): pp. 1437–1440, 1998.

Lee, Y. S., Numerical solution of the KZK equation for pulsed finite amplitude sound beams in thermoviscous fluids, Ph.D. thesis, Texas, 1993.

Lee, Y. S. and M. F. Hamilton, "Time-domain modeling of pulsed finite-amplitude sound beams," *J Acoust Soc Am*, 97(2): pp. 906–917, 1995.

Leighton, T. G., "Review - what is ultrasound?" *Progress Biophys Mol Biol*, 93(1): pp. 3–83, 2007.

Minnaert, M., "On musical air-bubbles and the sounds of running water," *Philosoph Mag*, 16: pp. 235–248, 1933.

Naze Tjøtta, J., S. Tjøtta, and E. H. Vefring, "Propagation and interaction of two collinear finite amplitude sound beams," *J Acoust Soc Am*, 88(6): pp. 2859–2870, 1990.

Naze Tjøtta, J., S. Tjøtta, and E. H. Vefring, "Effects of focusing on the nonlinear interaction between two collinear finite amplitude sound beams," *J Acoust Soc Am*, 89(3): pp. 1017–1027, 1991.

Needles, A., D. E. Goertz, R. Karshafian, E. Chérin, A. S. Brown, P. N. Burns, and F. S. Foster, "High-frequency subharmonic pulsed-wave Doppler and color flow imaging of microbubble contrast agents," *Ultrasound Med Biol*, 34(7): pp. 1139–1151, 2008.

Ostrovsky, L. A., S. N. Gurbatov, and J. N. Didenkulov, "Nonlinear acoustics in Nizhni Novgorod," *Acoust Phys*, 51(2): pp. 114–127, 2005.

Pace, N. G., A. Cowley, and A. M. Campbell, "Short pulse acoustic excitation of microbubbles," *J Acoust Soc Am*, 102(3): pp. 1474–1479, 1997.

Rénier, M., C. Barrière, and D. Royer, "Optical measurements of the self-demodulated displacement and its interpretation in terms of radiation pressure," *J Acoust Soc Am*, 121(6): pp. 3341–3348, 2007.

Rudenko, O. V., "Nonlinear sawtooth-shaped waves," *Phys Uspekhi*, 38(9): pp. 965–990, 1995.

Sarkar, K., W. T. Shi, D. Chatterjee, and F. Forsberg, "Characterization of ultrasound contrast microbubbles using in vitro experiments and viscous and viscoelastic interface models for encapsulation," *J Acoust Soc Am*, 118(1): pp. 539–550, 2005.

Shi, W. T. and F. Forsberg, "Ultrasonic characterization of the nonlinear properties of contrast microbubbles," *Ultrasound Med Biol*, 26(1): pp. 93–104, 2000.

Tavakkoli, J., D. Cathignol, R. Souchon, and O. A. Sapozhnikov, "Modeling of pulsed finite-amplitude focused sound beams in time domain," *J Acoust Soc Am*, 104(4): pp. 2061–2072, 1998.

van der Meer, S. M., B. Dollet, M. M. Voormolen, C. T. Chin, A. Bouakaz, N. de Jong, M. Versluis, and D. Lohse, "Microbubble spectroscopy of ultrasound contrast agents," *J Acoust Soc Am*, 121(1): pp. 648–656, 2007.

Vos, H. J., D. E. Goertz, and N. de Jong, "Pulse repetition rate excitation of contrast agents," in proc. IEEE Ultras Symp, pp. 216–219, Vancouver, BC, 2006.

Vos, H. J., D. E. Goertz, and N. de Jong, "Self-demodulation technique for microbubble excitation," *conditionally accepted in the IEEE Trans Ultrason Ferroelectr Freq Control*, 2009.

Wu, C.-Y., W.-H. Chao, Y.-H. Chou, and Y. Watanabe, "Analyses of characteristics of semi-intermodulated imaging based on multi-bifrequency approximation," *Jpn J Appl Phys*, 46(7B): pp. 4841–4846, 2007.

Wu, C.-Y., J. Tsao, and Y.-H. Chou, "An ultrasonic microbubble semi-intermodulated imaging technique," *Ultrasound Med Biol*, 31(9): pp. 1199–1210, 2005.

Yeh, C.-K., S.-Y. Su, C.-C. Shen, and M.-L. Li, "Dual high-frequency difference excitation for contrast detection," *IEEE Trans Ultrason Ferroelectr Freq Control*, 55(10): pp. 2164–2176, 2008.

Chapter 11

Self-demodulation technique for microbubble excitation

Abstract - **This study investigates the use of a self-demodulation signal as a means of microbubble excitation. The self-demodulation signal is generated by a nonlinearly propagating ultrasound pulse, whereby it is defined in large part by the envelope characteristics of a high-frequency carrier wave. Carrier waves of 10 and 25 MHz are used to generate low-frequency waves between 0.5 and 3.5 MHz at amplitudes in the range of 25 to 80 kPa in water. We demonstrate with high speed camera observations that it is possible to induce microbubble oscillations with the low frequency signal arising from the self-demodulation propagation process. As an application we determined the resonance frequency of Definity contrast agent microbubbles with radius ranging from 1.5 to 5 μm by sweeping the self-demodulation frequency in the range 0.5 to 3.5 MHz.**

Conditionally accepted for publication in the IEEE Transactions of Ultrasonics, Ferroelectrics, and Frequency Control, by H. J. Vos, D. E. Goertz, and N. de Jong. The authors gratefully acknowledge Prof. V. F. Humphrey (University of Southampton, UK) for suggesting the use of an acoustical filter to discriminate between possible sources of nonlinearity.

11.1 Introduction

In medical diagnostic echography, ultrasound contrast agents (UCAs) are released into the blood circulation to enhance echo signals from the cardiovascular system that would otherwise be masked by surrounding tissue [Feinstein, 2004]. Typically, the agents consist of small gas bubbles (0.5 – 5 μm radius) stabilized by an albumin, phospholipids or polymer coating to reduce dissolution and prevent coalescence. The combination of gas, coating and surrounding liquid constitute a damped oscillator having a resonance frequency that strongly depends on the bubble radius [Minnaert, 1933; de Jong et al., 2002]. At the resonance frequency, bubbles have higher scattering strength than that predicted by their compressibility alone, although the resonant effect is reduced by the increased damping introduced by the viscosity of the coating material [Gorce et al., 2000; van der Meer et al., 2007; Sijl et al., 2008; Guidi et al., 2009]. In a clinical setting the scattering of bubbles has to compete with the scattering of surrounding tissue, and simple detection of the fundamental-frequency echo and conversion to ultrasound images usually does not provide the necessary contrast to deduce the vascular structure of e.g. vasa vasorum and suspected cancer lesions [McGahan and Goldberg, 2008]. This is particularly true when only small quantities of bubbles are present within the sample volume.

Newer detection strategies have therefore been introduced that strive to enhance the signals from bubbles and suppress those from tissue. Such strategies are usually based on the nonlinear response of contrast bubbles to ultrasound. Amongst other examples, phospholipids-coated microbubbles are shown to generate higher harmonics of the insonation frequency [de Jong et al., 2002], subharmonics [Needles et al., 2008], and are shown to respond nonlinearly to the insonation pressure level [Emmer et al., 2007]. Also, they are able to act as nonlinear mixers producing frequency cross-products in dual-frequency insonation [Newhouse and Mohana Shankar, 1984; Chen et al., 2006; Wu and Tsao, 2003].

When looking into the details of all these studies, an important finding is that in regular clinical diagnostic ultrasound, even at relatively low pressures, nonlinear propagation in tissue cannot be neglected. As a first example, both second harmonic detection techniques [McGahan and Goldberg, 2008] and radial modulation [Måsøy et al., 2008] suffer from propagation distortion which increases the background tissue noise. This drawback is partly overcome by reducing the transmission amplitude, at the expense of limited penetration depth. Another example is the semi-intermodulation technique as proposed by Wu et al. [2005], similar to the difference-frequency technique as proposed by Chen et al. [2006]. Nonlinear response of the microbubble to a multi-frequency pulse is received at a frequency much lower than the transmission frequency (it was explicitly stated that this was no subharmonic effect). In their rationale it is stated that tissue cannot produce such signal, which is wrong, since nonlinear propagation could result in a residual low-

frequency content due to the so-called self-demodulation or parametric-array effect [Berktay, 1965; Averkiou and Hamilton, 1997; Vos et al., 2009]. This effect could possibly corrupt the results obtained with the semi-intermodulation or similar techniques.

In this paper, we hypothesize that the self-demodulation propagation effect itself can be exploited for the purposes of ultrasound contrast microbubble excitation. A low-pressure, low-frequency wave is generated as a function of the envelope of a high-intensity, high-frequency ultrasound pulse. This nonlinear effect has been proposed for e.g. depth-probing SONAR applications in the form of a parametric array [Berktay, 1965], since it can generate low-frequency collimated ultrasound beams using relatively small high-frequency transducers. The beam of such small transducers would otherwise suffer from diffraction limits. Increasing the frequency has the general benefit of a higher spatial resolution, usually at the cost of penetration depth through increased attenuation; however, the generated low-frequency wave does not suffer from this high attenuation. Conversion of energy can be poor [Berktay, 1965], nonetheless the current authors have shown in a previous paper that the effect can generate a pressure wave of 30 – 45 kPa at 1.5 MHz using a 25 MHz carrier frequency [Vos et al., 2009]. Such pressure levels should be sufficient to excite microbubbles, as shown preliminary in a conference paper [Vos et al., 2006]. This paper further investigates the relative effect of self-demodulation on contrast microbubbles, compared to their own nonlinear response, in clinically relevant acoustic conditions. The excitation technique is further employed in a spectroscopy method to obtain resonance data from microbubbles *in vitro*.

11.2 Methods and materials

11.2.1 Self-demodulation principle

Fig. 11.1 illustrates the main aspects of self-demodulation (see also Humphrey [1992]; Averkiou and Hamilton [1997]; Pace et al. [1997]; Vos et al. [2009]). The upper graphs depict a carrier wave with sinusoidal envelope traveling through water. According to the theory by Berktay [1965], in a weakly-nonlinear propagation regime [Vos et al., 2009], a low-frequency wave will develop depending on the envelope only:

$$p_{sd}(t) \propto \frac{d^2}{dt^2} E(t)^2 \tag{11.1}$$

with $E(t)$ the envelope function and $p_{sd}(t)$ the self-demodulation pressure wave. Referring to Fig. 11.1, the square of the envelope function is shown in the middle panel, and the self-demodulation wave according to Eq. 11.1 is shown in the right upper graph. All curves are normalized for clarity. From a signal analysis point of view, the frequency content of the self-demodulation wave can be attributed to the difference frequency of the two carrier waves; the resulting beat frequency is

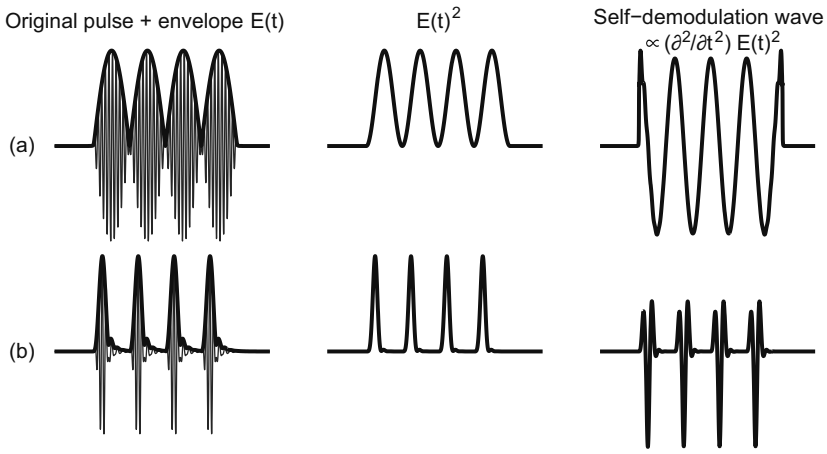

Figure 11.1: Examples of self-demodulation principle following Eq. 11.1 [Berktay, 1965]. (a) A sine-wave envelope (left hand side) results in a sine-wave at double frequency when squared (center), which produces a self-demodulation sine-wave when the second time derivative is taken according to Eq. 11.1 (right). (b) Repetition of a 2-cycle tone burst produces a complex self-demodulation wave, with frequency content at the repetition frequency but also at other frequencies.

converted into a 'real' wave because of nonlinear response of the medium.

The lower graphs in Fig. 11.1 show the self-demodulation wave as a function of short ($\sim$ 2 cycle) pulses, repeated at high pulse repetition frequency (PRF). Since each self-demodulation wave will contain many different frequencies (the original pulse has an arbitrary envelope), the repetition of the pulse will create a complex pattern in the time and frequency domain. Nonetheless, repetition of the pulse will increase the frequency content at the PRF [1], which is useful for microbubble excitation.

11.2.2 Nonlinear propagation *versus* nonlinear bubble response

Microbubbles themselves can also produce nonlinear mixing signals at, for example, the difference frequency of two carrier waves [Khismatullin and Nadim, 2002; Wu et al., 2005; Chen et al., 2006]. Thus if a microbubble shows a difference-frequency response to a wave such as depicted in Fig. 11.1a the relative importance

[1] The frequency content can be reasoned using Fourier analysis. In the time domain, the repetition of single pulses is equivalent to the convolution of single pulses with a series of Dirac pulses. Such convolution appears in frequency domain as the multiplication of the single pulse frequency content with, again, a series of Dirac pulses. Hence the frequency content of the single pulse is amplified only at the PRF and integer multiples of the PRF. Note that this means that if the single pulse does not contain significant low-frequency energy, finite repetition of the single pulse will not introduce such content either.

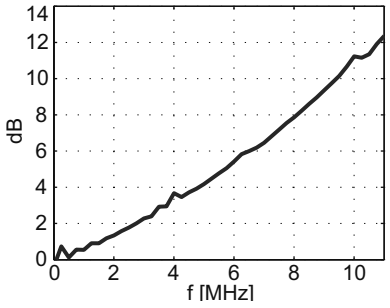

Figure 11.2: Attenuation of the 2-mm silicone sheet, acting as a low-pass acoustic filter.

of the nonlinear microbubble effect compared to the nonlinear propagation effect is not known *a priori*. However, from a contrast agent detection point of view, knowing the origin of the nonlinear signals is very important since nonlinear bubble response can potentially increase the detection signals, while nonlinear tissue response will degrade the detection potential. Therefore the current study also aims to elucidate the origin of observed microbubble difference-frequency response.

In very general terms, nonlinear signals depend squarely on the excitation amplitude. For the case of microbubbles, perturbation analysis of a model of an uncoated gas bubble [Wu and Tsao, 2003; Chen et al., 2006] indeed showed that the amplitude of the bubble nonlinear mixing signal depends squarely on the excitation amplitude. Analysis of Eq. 11.1, however, shows that also the amplitude of the self-demodulation wave relates to the squared excitation amplitude (for the lower range of excitation pressures - see Vos et al. [2009]). Consequently, changing the excitation pressure in the experiments to observe the microbubble response will not discriminate between the two different sources of nonlinearity.

We have therefore chosen to implement an acoustic filter in our setup [Humphrey, 1992]. The filter consists of a 2-mm thickness sheet of silicone having a strongly frequency-dependent attenuation (Fig. 11.2). Putting such filter in the acoustic field close to the microbubble will reduce the high-frequency wave amplitude, but will hardly change the low-frequency content as generated by the nonlinear propagation. Then, it is reasoned that if the microbubble oscillation does not depend on the presence of the filter, the most significant source of the low-frequency content must be nonlinear propagation in water, not the nonlinear mixing property of microbubbles. This method is further deployed in the Results section.

The use of an acoustic low-pass filter also has the general benefit of lower acoustically-induced deflation [Borden et al., 2005; Guidi et al., 2009] as induced by the high-pressure carrier waves. This significantly increased the lifetime of the microbubbles during the experiments, especially when a single bubble was excited with many pulses as described in the experiments.

11.2.3 Acoustic setup

Acoustic pulses were generated having either 10 MHz or 25 MHz carrier frequency. The 10-MHz pulse was generated by a 3-inch focused transducer (Panametrics V311, Olympus NDT, Waltham, MA), connected to a 1 – 35 MHz linear power amplifier (A-500RF, ENI, Rochester, NY). Self-demodulation frequencies were in the range of 0.5 – 1.5 MHz. Peak rarefaction pressures were up to 1.3 MPa in focus at 10 MHz. Pressure levels were measured with a calibrated hydrophone (needle-type PVDF 0.2 mm, Precision Acoustics, Dorchester, Dorset, UK). Hydrophone signals were recorded by a digital oscilloscope (TDS3014B, Tektronix, Beaverton, OR) and transferred to a PC for further processing.

A 25 MHz focused transducer (V324-1", Olympus NDT, Waltham, MA) having an acoustical gain of 19 was used for the higher frequencies. An arbitrary waveform generator (AWG520, Tektronix) was connected to a 10 – 80 MHz linear power amplifier (2100L 1000W, ENI, Rochester, NY). The output of the power amplifier was band-pass filtered using a high-power 8 – 28 MHz 5^{th} order Butterworth filter to avoid any residual low-frequency contents, and fed to the transducer. Ultrasound levels were measured using a needle-type 75 μm diameter PVDF hydrophone (Precision Acoustics).

11.2.4 Optic setup and microbubbles

Experiments were performed using Definity microbubbles (Lantheus Medical Imaging, North Billerica, MA), which contain a gaseous C_3F_8 core stabilized by a phospholipids coating. With reference to Fig. 11.3, a highly diluted population of bubbles was injected into a capillary fibre (Cuprophan, Akzo Nobel, Faser AG, Germany) with an outer diameter of 200 μm. The fibre was submerged in tap water having a temperature of 34°C, which was kept constant using a heat exchanger connected to a heating bath. This temperature was chosen to approach the body temperature, but still being below 37°C as such temperature resulted in high bubble deflation rates during the experiment (see also Chapter 8). The fibre is optically and acoustically transparent, and was positioned in the optical focus of a microscope (Olympus BX-FM, Tokyo, Japan). The microscope was connected to the Brandaris-128 camera system [Chin et al., 2003], which captures 128 frames at speeds up to 25 million frames per second (Mfps). The resolution in the frames is 0.18 μm per pixel.

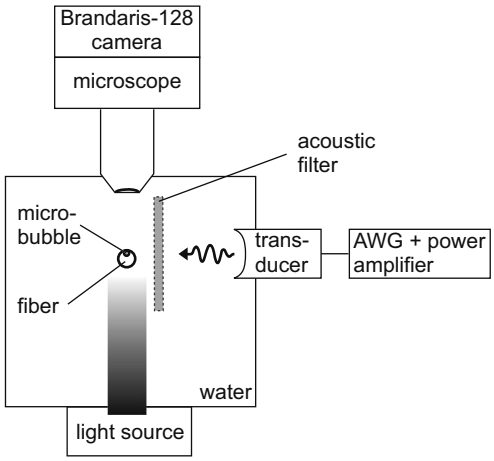

Figure 11.3: Schematic drawing of the setup to optically record the microbubble oscillation. The acoustic filter is a 2 mm thick sheet of silicone. AWG = Arbitrary waveform generator.

11.2.5 Microbubble model

The radial motion of encapsulated bubbles was calculated by solving a modified version of the Herring equation [Vokurka, 1986; Leighton, 1994] with additional terms to model the coating of phospholipids. Various models have been presented for a thin shell, in which the shell thickness d_s is much smaller than the initial radius R_0 [Hoff et al., 2000; Dayton et al., 2002; de Jong et al., 2002; Marmottant et al., 2005; Sarkar et al., 2005]. We have chosen to incorporate a shell expressing viscoelastic behavior. The model is valid only for small radial excursions [Marmottant et al., 2005], which corresponds to our experimental conditions. The radial excursion $R(t)$ as a function of the driving pressure $p_a(t)$ can be predicted by solving [Marmottant et al., 2005; Sarkar et al., 2005]:

$$\rho\left(R\ddot{R}+\tfrac{3}{2}\dot{R}^2\right)=\left(p_0+\tfrac{2\sigma_0}{R_0}\right)\left(\tfrac{R_0}{R}\right)^{3k}\left(1-\tfrac{3k}{c}\dot{R}\right)-\tfrac{2\sigma}{R}-\tfrac{4\mu\dot{R}}{R} \\ -\tfrac{4\kappa_s\dot{R}}{R^2}-(p_0+p_a)\,. \tag{11.2}$$

See Table 11.1 for a description of the used symbols and their values. The value of the polytrophic exponent k is approximated to unity for microbubbles containing a polyatomic gas such as C_3F_8 [Marmottant et al., 2005].

The surface tension σ of a phospholipids-coated bubble is modelled by [Gorce et al., 2000; Morgan et al., 2000; Marmottant et al., 2005; van der Meer et al., 2007]:

$$\sigma=\sigma_0+2\chi\left(\frac{R}{R_0}-1\right) \tag{11.3}$$

In our simulations, shell parameters were initially set to χ = 0.6 N/m and κ_s =

Table 11.1: List of symbols

Symbol	Description	Value / Unit
ρ	liquid density	998 kg/m^3
R	Radius *	m
p_0	Ambient pressure	101 kPa
σ	Surface tension *	N/m
k	polytrophic exponent	1.0
c	Speed of sound	1505 m/s **
μ	liquid viscosity	$0.8{\cdot}10^{-3}$ Pa·s **
κ_s	shell viscosity parameter	$1.5{\cdot}10^{-8}$ kg/s
χ	Shell elastic compression modulus	0.6 N/m
p_a	Driving acoustic pressure	Pa

* A subscript '$_0$' with these symbols denote the initial state of this value, i.e., at t=0.
** values at 34 °C, from CRC [2001] and Duck [1990].

$1.5 \cdot 10^8$ kg/s. These values are within range of the values for phospholipids coatings found in literature for 1 – 10 MHz, although only Kimmel et al. [2007] report specific combinations of values for Definity microbubbles obtained through attenuation experiments at room temperature. The initial surface tension σ_0 is taken as $\sigma_{\text{free}}/2$, with σ_{free} the surface tension of a free water-gas surface (0.072 N/m). We reason that a finite surface tension remains in the equilibrium state of a coated bubble: a non-zero surface tension produces a Laplace pressure inside the bubble, that in turn poses a partial pressure difference inside and outside the bubble. This partial pressure difference causes gas diffusion and hence bubble shrinkage; observed dissolution times are in the range of minutes to hours [Borden and Longo, 2002].

11.3 Results

11.3.1 Acoustic field

Fig. 11.4 shows a hydrophone measurement of the ultrasound pulse in the focus of the 10 MHz transducer. The carrier frequency was 10 MHz, with an envelope giving 1 MHz self-demodulation wave. The pulse spectrum in the lower left panel shows significant content at a frequency of 1 MHz, having about 40 kPa amplitude, due to nonlinear propagation. It also shows a 2 MHz signal which is 5 dB lower than that at 1 MHz. As shown in the right panels of Fig. 11.4, an acoustic filter placed in front (3 mm distance) of the hydrophone reduces the self-demodulation wave by only 2 dB. The high-frequency content is reduced by about 11 dB, and its second harmonic (20 MHz) by more than 20 dB. This is well predicted by the attenuation of the sheet as depicted in Fig. 11.2. Due to a lower speed of sound in the material,

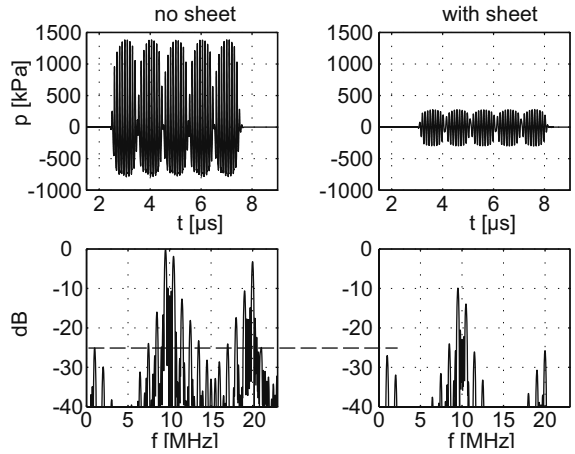

Figure 11.4: Hydrophone-recorded signals of the ultrasound field and corresponding spectrum in the acoustic focus. Left panel shows a 10-MHz carrier, 1-MHz envelope signal. Right panel shows the signal with an acoustic filter (silicone sheet) placed close to the hydrophone surface. The horizontal line denotes the $\sim$ 2 dB lower self-demodulation content due to the filter.

the pulse arrived 0.6 µs later when the sheet was in the propagation path (top-right panel).

11.3.2 Microbubble response

To demonstrate the principle of bubble vibration caused by the selfdemodulation field we first excited a bubble of 4.0 µm radius with pulses like those depicted in Fig. 11.4. The response of the bubble was captured with the high speed camera running at 19.6 million frames per second (Mfps). With reference to Fig. 11.5 (left panel), the microbubble showed an excursion of 0.35 µm (0.7 µm peak-peak) together with the high-frequency oscillation. Shortly after, the same bubble was irradiated, this time with the sheet placed in the acoustic field at 5 mm distance from the bubble. The high-frequency oscillation of the bubble at around 10 MHz is reduced significantly (Fig. 11.5 right panel), while a 1-MHz oscillation of 0.3 µm amplitude remained. The bubble has reduced in size of about 9%, which is not expected to significantly change its general behavior [van der Meer et al., 2007]. The spectral density functions in the bottom panels show that the high frequency component (>9 MHz) was reduced by at least 8 dB by the acoustic low-pass filter.

As a reference the experimentally observed microbubble responses are compared to numerical simulations. The recorded pressure signals (cf. Fig. 11.4) served as input ($p_a(t)$ in Eq. 11.2). In the left graphs of Fig. 11.6 a 4.0 µm microbubble is seen to oscillate with amplitude of about 0.55 µm, which is a factor of 1.6 times

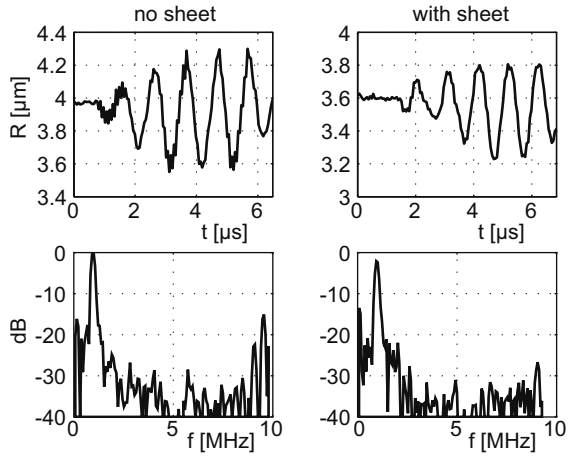

Figure 11.5: Optically recorded response curves of a 4.0 µm radius Definity microbubble. Left-upper panel shows the radial excursion of the bubble when irradiated with the self-demodulation sequence. Right-upper panel shows the same bubble irradiated with the same sequence, but with the acoustic filter positioned between the bubble and the transducer. The lower panels show the spectral density functions of the vibration. The Nyquist frequencies were 9.8 and 9.3 MHz (19.6 Mfps and 18.5 Mfps, respectively).

higher than the experimentally observed excursion. The placement of the acoustic filter in the acoustic beam (centre panel) reduces the low-frequency oscillation by about 2 dB, while the 10 MHz-content was reduced by 10 dB, which is fully accounted for by the reduction of the high-frequency content in the driving pulse. Subsequently the hydrophone signal was digitally high-pass filtered to reduce the self-demodulation pressure wave at input. As a result, the microbubble oscillation at 1 MHz decreased by about 25 dB. This example shows that also in simulation the microbubble responds linearly to the driving pulse, which contained the low-frequency because of nonlinear propagation; the nonlinear mixing property of the microbubble is a minor effect in this simulation.

11.3.3 Resonant microbubble effects

As an example of application for the self-demodulation technique, microbubbles are excited by different self-demodulation sequences, thus investigating the influence of the envelope, and the resonant response of microbubbles to the sequences.

In a first example a short pulse was transmitted composed of a 10-MHz excitation signal of 2 periods ($\sim$ 0.2 µs duration), at a peak rarefaction pressure of 1.3 MPa in focus. The electric signal was high-pass filtered at the output of the power amplifier to avoid transmitting any residual low-frequency signal. The self-demodulation

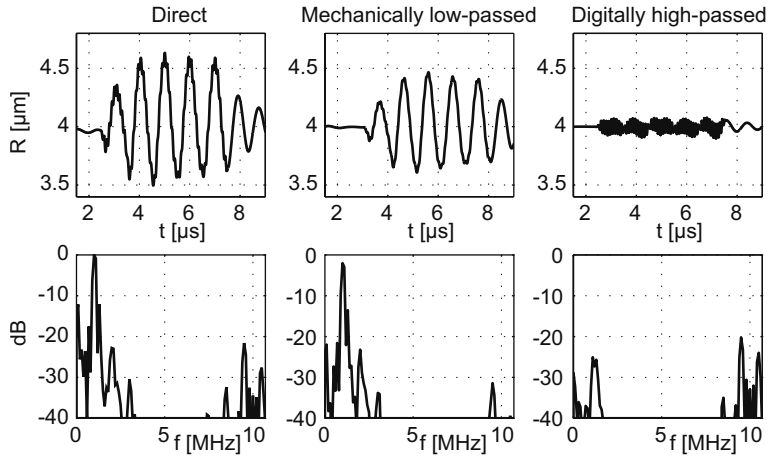

Figure 11.6: Simulation-predicted bubble responses for three different input pressure signals. The pressure signals in the left and centre panel were measured with the hydrophone (see Fig. 11.4). The right-panel result was obtained after digital high-pass filtering of the direct hydrophone signal.

wave in focus had amplitude on the order of 80 kPa with center frequency of 3 MHz. A microbubble of 3.1 µm radius showed significant response to such excitation pulse, see Fig. 11.7a. The pulse is acting on the bubble between 1.2 µs and 1.5 µs, which is denoted by the star in the graph. The bubble shows significant ring-down for 4 µs, having a decay time over at least three cycles. Note that the frequency of the ring-down oscillation ($\sim$ 1.4 MHz here) denotes the damped unforced resonance frequency of the microbubble.

In a second example the short pulse was repeated five times at a repetition frequency of 0.9 MHz, 1.05 MHz and 1.2 MHz. The response of same bubble is plotted in Figs. 11.7b-d. In Fig. 11.7c, the timing is such that each pulse enhances the radial excursion of the bubble already achieved after the previous ones. Thus, the forced resonance frequency of this microbubble is $\sim$ 1.05 MHz. The radial oscillation finally has 0.4 µm amplitude, with larger expansion than compression. In Figs. 11.6b and d, the pulse timing does not lead to an increase of the radial excursion.

As a second method to measure the resonance frequency, microbubbles were irradiated by 25 MHz carrier-frequency pulses having a sine-wave envelope such as depicted in Fig. 11.1a. The self-demodulation frequency f_{sd} ranged from 1.7 MHz to 2.8 MHz. Transducer source pressure was in the order of 0.5 MPa – 1 MPa, which leads to highly nonlinear distortion of the ultrasound pulse in the focus of the transducer for this transducer [Vos et al., 2009], and Eq. 11.1 is not valid anymore. In such regime the self-demodulation pressure level tends to depend approximately linear on the source pressure, instead of quadratic [Vos et al., 2009]. Thus, the source pres-

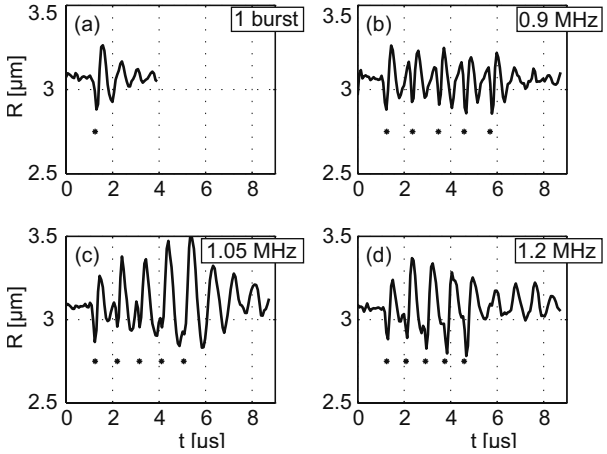

Figure 11.7: Recorded response-time curves of a 3.1 μm radius Definity microbubble. Stars denote the time of arrival of the short (0.2 μs) pulses with centre frequency of 10 MHz, 1.3 MPa peak-negative pressure. The camera was recording at a frame rate of 14.8 Mfps.

sure amplitude was changed by a factor f_{sd}^{-1} to keep the self-demodulation pressure levels roughly equal, $\sim$ 40 kPa. Such value provides significant radial response of the microbubble to the excitation pulse.

Fig. 11.8 shows the spectra of the radial responses of a 2.0 μm radius microbubble. Since the camera operated at 14.1 Mfps (Nyquist frequency of 7 MHz) only the low-frequency oscillation could be recorded. A segmented mode [Chin et al., 2003] allowed recording 12 movies of 64 frames each, thus increasing the spectral density in the spectroscopy approach. Simplifying the spectroscopy methods previously described by van der Meer et al. [2007], the resonance frequency of this bubble was estimated by the frequency at which the highest radial excursion was achieved. Inherently this is the damped forced resonance frequency [Leighton, 1994; Khismatullin and Nadim, 2002]. In the current example the maximum response is found at a driving frequency of 2.2 MHz. The excursion at that frequency was 0.35 μm peak-peak.

11.3.4 Spectroscopy

We investigated the resonance frequency for a range of microbubble sizes using both the 10 MHz and the 25 MHz setup, see Fig. 11.9. In the 10-MHz experiments microbubbles were insonified by 5 successive sequences of 5 short pulses each, while changing the pulse repetition frequency. The sequences had a PRF varying between 0.6 and 1.5 MHz. The acoustic filter was placed in the ultrasound field to reduce microbubble deflation. In the 25-MHz experiments the envelope was a sine-wave,

similar as the approach depicted in Figs. 11.1a and 11.8, while the self-demodulation frequency ranged between 1.3 and 3 MHz.

In the 10-MHz experiments, only 6 out of 19 recordings enabled estimating the resonance frequency. The other 13 bubbles showed a maximum response at either the lowest or the highest bounding frequency and were thus discarded. This was a direct result of the use of only 5 sequences to probe the microbubble response. In the 25-MHz experiments 10 different self-demodulation frequencies were used and no recordings had to be discarded.

For all recordings with the 10-MHz carrier frequency a single short pulse was employed to also study the unforced damped resonance frequency of the microbubble (*cf.* Fig. 11.6a). The ring-down frequency after such short pulse was estimated for 16 out of 19 bubbles, whereas the remaining 3 recordings had too low excursion. The unforced resonance frequency (circles in Fig. 11.9) was generally 10% to 30% higher than the forced resonance frequency (squares and stars) for any given radius. Such value is indicative of significant damping [Khismatullin and Nadim, 2002].

As a reference the numerically calculated resonance frequencies as a function of radius are also plotted in Fig. 11.9, for shell values $\chi = 0.6$ N/m and $\chi = 0.24$ N/m, $\kappa_s = 1.5 \cdot 10^{-8}$ kg/s, and no shell (i.e., $\chi = 0$, $\kappa_s = 0$, $\sigma = \sigma_0 = 0.072$ N/m). The elasticity value of 0.24 N/m is obtained by a root-mean-square minimizing fit through the damped forced resonance-frequency data-points in Fig. 11.9. The resonance frequency in the numerical simulation model is found by maximizing the radial response while varying the excitation frequency. The pressure amplitude was set to 40 kPa.

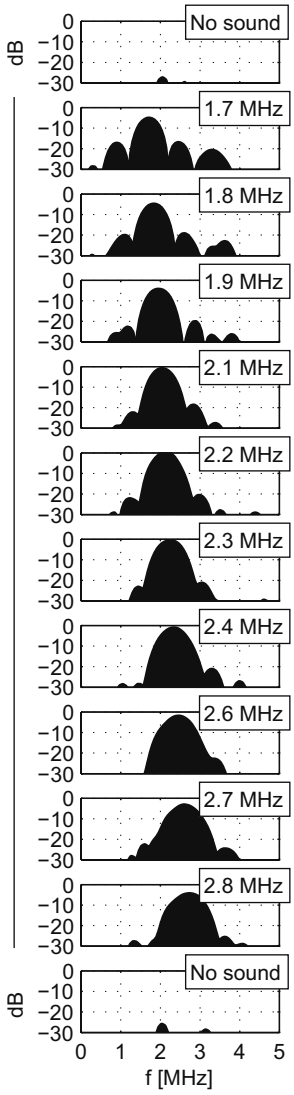

Figure 11.8: Optically recorded spectral density functions of a 2.0 μm radius bubble irradiated with self-demodulation frequencies of 1.7 – 2.8 MHz. The carrier frequency was 25 MHz in these experiments, the camera operated at 14.1 Mfps.

11.4 Discussion

11.4.1 Self-demodulation as an excitation technique

Although self-demodulation of nonlinearly propagating ultrasound pulses has been used before by Pace

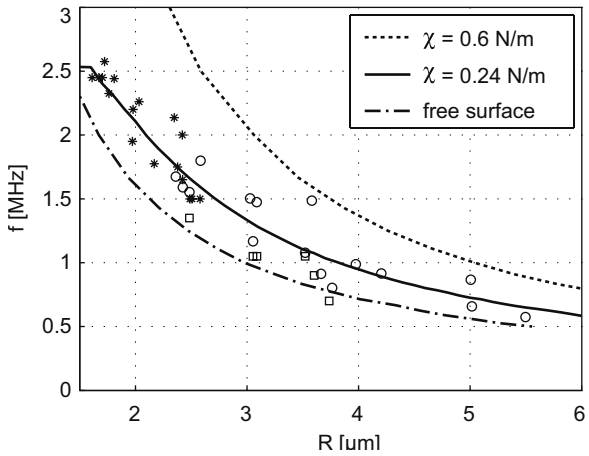

Figure 11.9: Measured resonance frequencies of Definity microbubbles as measured with the self-demodulation excitation technique. Squares are obtained by a pulse repetition approach with the 10 MHz carrier frequency equipment, circles are obtained by single pulse ring-down. Stars are obtained by using the 25 MHz carrier frequency equipment. Prediction curves are obtained using Eq. 11.2, at the displayed elasticity (viscosity parameter $\kappa_s = 1.5 \cdot 10^{-8}$ kg/s). A 'free surface' means no shell, i.e. χ = 0, κ_s = 0, and σ = 0.072 N/m.

et al. [1997] to investigate larger uncoated gas bubbles, we currently show that the self-demodulation technique can excite also ultrasound contrast agent microbubbles. Using clinically relevant frequencies and pressures, microbubbles showed significant radial oscillation at the self-demodulation frequencies, thus potentially acting as a secondary ultrasound source at that frequency. By using both a sine-wave envelope and the fast repetition of short pulses it is shown that the exact envelope of the carrier wave is not important for the excitation method. This finding is relevant for transmit equipment having plain pulsed electronics such as medical intravascular ultrasound (IVUS) systems. Nonetheless the narrow-beam characteristics of the self-demodulation wave [Berktay, 1965; Humphrey, 1992; Vos et al., 2009] are only exploited if low-frequency contents are avoided in the transmission signal.

When a 10-MHz carrier pulse of 0.8 MPa peak-rarefaction excited the microbubbles, bubbles with a radius roughly smaller than 2 μm deflated. We believe that acoustically driven diffusion was the main cause for the deflation [Guidi et al., 2009; Borden et al., 2005]. An acoustic low-pass filter reduced the deflation effects of the high-pressure carrier wave significantly, without major changes to the self-demodulation amplitude. The alternative solution, using 25 MHz carrier frequency pulses, also proved to reduce the bubble dissolution significantly. However, it showed too low efficacy at low self-demodulation frequencies (< 1.5 MHz), and the expectedly needed transmit voltage (> 300 V_{pp}) to produce sufficient self-

demodulation pressure exceeded the maximum amplifier output voltage. Therefore the 10-MHz carrier wave was used, with an acoustic filter, for self-demodulation frequencies below 1.5 MHz.

A high source pressure can lead to high nonlinear distortion of the ultrasound wave that introduces harmonic frequencies of the envelope frequency [Vos et al., 2009]. For example, a low-frequency wave designed to have 1 MHz frequency also contained 2 MHz frequency contents at 5 dB lower level (see Fig. 11.4). These might complicate the analysis of bubble response at for example the second harmonic frequency. It might also bias the spectroscopy method. However, by pre-selecting the frequency range in the spectroscopy method for a given microbubble size the chance for a possible error was minimized. Retrospective confirmation is given by the fact that the ring-down frequency of the unforced damped oscillation is on the same order as the resonance frequency, as shown in Fig. 11.9.

11.4.2 Microbubble behavior

The potential contribution of nonlinear microbubble response to the high- frequency carrier wave was investigated through the use of an acoustic low-pass filter. The observed oscillation maintained its amplitude despite a 10-dB reduction of the carrier signal by the filter (Figs. 11.5 and 11.6). The reduction of only 2 dB, which is roughly the low-frequency attenuation of the filter, shows that the bubble responds linearly to the excitation pulse in the current setting. This hypothesis is further consolidated by the 25-dB lower response to the high-pass filtered signal in Fig. 11.6.

The spectroscopy data suggest that Definity microbubbles have a lower resonance frequency, and consequently lower shell elasticity, than predicted before. Goertz et al. [2007] obtained a value of $\chi \approx 0.8$ N/m for both a decanted and a mechanically filtered Definity population, analyzed at a frequency range of 12 – 27 MHz (note that, by comparing definitions, $\chi = S_p/2$). Van der Meer et al. [2007] found an elasticity value of $\chi = 0.54$ N/m for an other type of phospholipids-coated microbubbles (SonoVue). The fitted elasticity value ($\chi = 0.24$ N/m) in the current study is lower by more than a factor of two compared to these values. The current study is performed in water at 34°C and it has been suggested before that an increase of temperature could lower the elasticity parameter of phospholipids [Borden et al., 2004; Vos et al., 2008]. As a final note, the comparison of experimental data with the free-surface model strongly suggests that the shell elasticity is significantly larger than zero.

Recent literature suggests that the currently used simulation model does not apply for phospholipids-coated microbubbles, since either the shell elasticity presumably depends largely on the instantaneous microbubble size, or the viscosity value presumably depends on the instant shear rate [Marmottant et al., 2005; Doinikov and Dayton, 2007; Stride, 2008; Tsiglifis and Pelekasis, 2008]. Such nonlinearity

could lead to a situation where the compression phase of the oscillation is more pronounced than the expansion phase (sometimes termed 'compression-only' [Marmottant et al., 2005; de Jong et al., 2007] but better termed 'enhanced-compression'). During such asymmetric oscillation the average radius decreases, scattering a pressure wave with frequency content similar to that produced by the propagation self-demodulation effect. The currently used model is not able to predict such enhanced compression at low excitation pressure. Nonetheless, we motivate our choice of the current model by the fact that the nonlinear shell model has neither been verified for Definity agent, nor for any phospholipids-coated bubbles at the elevated temperature. Finally, the carrier frequency is much higher than the expected resonance frequency, which is a regime where the nonlinear shell model has neither been verified. However, the difference in excursion between the observed and predicted responses might be explained by the exact numerical implementation of the shell behavior. Another hypothesis is that the actual shell viscosity is higher than assumed in the bubble model ($\kappa_s = 1.5 \cdot 10^{-8}$ kg/s); Van der Meer et al. [2007] suggested $\kappa_s \sim 3 \cdot 10^{-8}$ kg/s for a phospholipids-coated bubble with radius of 4.0 μm.

A small note regarding the recording of the microbubble high-frequency oscillation should be made. A framing rate of 19.6 Mfps, used in one of the reported experiments, leads to a Nyquist frequency of 9.8 MHz, and consequently the excitation pulse with main frequency components between 0 MHz (i.e., the initial radius of the bubble) and 10.5 MHz could not be entirely captured, and the high frequency components appear in an aliased fashion. However, the framing exposure function of the camera [Chin et al., 2003] results in a temporal averaging effect that could lead to an estimated signal reduction of 4 dB close to the Nyquist frequency. For this effect was not compensated in the figures since the reduction value has not been experimentally verified, and a 4-dB error would not change the results significantly.

11.4.3 Applications

The self-demodulation effect could combine high-frequency ultrasound equipment with lower-frequency resonant microbubbles. For example, while contrast-enhanced intravascular ultrasound (IVUS) employs imaging frequencies of 15 – 50 MHz, the major resonance frequency of conventional UCA bubbles is generally around 1 – 8 MHz [Gorce et al., 2000; Shi et al., 2002; Sarkar et al., 2005]. Another clinical example is the characterization of hazardous arterial gaseous emboli (see Evans [2003] for a review), which have sizes of roughly 10 – 200 μm. The resonance frequencies of these bubbles range from roughly 25 kHz to 500 kHz, while detection equipment applies 2 MHz, or higher in the case of carotid-artery scanning; such frequency mismatch leads to reduced ability to correctly size the emboli.

A trivial contrast detection scheme would be to record the low-frequency echo of the region of interest [Wu et al., 2005]. However, this needs an additional low-

frequency receiving system. Furthermore, as shown in this study, nonlinear propagation plays a major role in the used settings and tissue scattering will also contain the low-frequency signals. Hence, any increase of contrast in a medical application might be mainly caused by increased linear scattering by bubbles, which is proven not to be very efficient [Forsberg et al., 2000; McGahan and Goldberg, 2008]. Therefore direct detection of the low-frequency contents using low-frequency equipment might not prove optimal for contrast-enhancing applications.

An improved contrast detection technique might be a radial manipulation approach [Måsøy et al., 2008]. This technique exploits the high compressibility of UCA microbubbles, leading to decorrelation of bubble echoes when manipulated with a low-frequency wave. The decrease in correlation could be detected by regular Doppler techniques [Hope Simpson et al., 2001; Chérin et al., 2008; Måsøy et al., 2008]. A preliminary study using an IVUS transducer to transmit both the low-frequency manipulation pulse and high-frequency detection pulses showed that the low-frequency diffraction of the unfocused element resulted in low radial modulation, and subsequently in low detection signals [Goertz et al., 2006]. The current excitation method however overcomes this problem since the low-frequency beam inherits its characteristics from the high-frequency beam.

Bibliography

Averkiou, M. A. and M. F. Hamilton, "Nonlinear distortion of short pulses radiated by plane and focused circular pistons," *J Acoust Soc Am*, 102(5): pp. 2539–2548, 1997.

Berktay, H. O., "Possible exploitation of non-linear acoustics in underwater transmitting applications," *J Sound Vib*, 2(4): pp. 435–461, 1965.

Borden, M. A., D. E. Kruse, C. F. Caskey, S. Zhao, P. A. Dayton, and K. W. Ferrara, "Influence of lipid shell physicochemical properties on ultrasound-induced microbubble destruction," *IEEE Trans Ultrason Ferroelectr Freq Control*, 52(11): pp. 1992–2002, 2005.

Borden, M. A. and M. L. Longo, "Dissolution behavior of lipid monolayer-coated, air-filled microbubbles: Effect of lipid hydrophobic chain length," *Langmuir*, 18(24): pp. 9225–9233, 2002.

Borden, M. A., G. Pu, G. J. Runner, and M. L. Longo, "Surface phase behavior and microstructure of lipid/PEG-emulsifier monolayer-coated microbubbles," *Colloids Surfaces B-Biointerfaces*, 35: pp. 209–223, 2004.

Chen, S., R. Kinnick, J. F. Greenleaf, and M. Fatemi, "Difference frequency and its harmonic emitted by microbubbles under dual frequency excitation," *Ultrasonics*, 44: pp. e123–e126, 2006.

Chérin, E., J. Brown, S.-E. Måsøy, H. H. Shariff, R. Karshafian, R. Williams, P. N. Burns, and F. S. Foster, "Radial modulation imaging of microbubble contrast agents at high frequency," *Ultrasound Med Biol*, 34(6): pp. 949–962, 2008.

Chin, C. T., C. T. Lancée, J. M. G. Borsboom, F. Mastik, M. E. Frijlink, N. de Jong, M. Versluis, and D. Lohse, "Brandaris 128: A 25 million frames per second digital camera with 128 highly sensitive frames," *Rev Sci Instr*, 74(12): pp. 5026–5034, 2003.

CRC, Handbook of Chemistry and Physics (82th edition), CRC, Boca Raton, FL, 2001.

Dayton, P. A., J. S. Allen, and K. W. Ferrara, "The magnitude of radiation force on ultrasound contrast agents," *J Acoust Soc Am*, 112(5): pp. 2183–2192, 2002.

de Jong, N., A. Bouakaz, and P. Frinking, "Basic acoustic properties of microbubbles," *Echocardiography*, 19(3): pp. 229–240, 2002.

de Jong, N., M. Emmer, C. T. Chin, A. Bouakaz, F. Mastik, D. Lohse, and M. Versluis, ""Compression-only" behavior of phospholipid-coated contrast bubbles," *Ultrasound Med Biol*, 33(4): pp. 653–656, 2007.

Doinikov, A. A. and P. A. Dayton, "Maxwell rheological model for lipid-shelled ultrasound microbubble contrast agents," *J Acoust Soc Am*, 121(6): pp. 3331–3340, 2007.

Duck, F. A., Physical properties of tissue, Academic press Ltd., 1990.

Emmer, M., A. van Wamel, D. E. Goertz, and N. de Jong, "The onset of microbubble vibration," *Ultrasound Med Biol*, 33(6): pp. 941–949, 2007.

Evans, D. H., "Ultrasonic detection of cerebral emboli," in proc. IEEE Ultras Symp, pp. 316–326, 2003.

Feinstein, S. B., "The powerful microbubble: from bench to bedside, from intravascular indicator to therapeutic delivery system, and beyond," *Am J Physiol Heart Circ Physiol*, 287(2): pp. H450–457, 2004.

Forsberg, F., J. B. Liu, H. J. Chiou, N. M. Rawool, L. Parker, and B. B. Goldberg, "Comparison of fundamental and wideband harmonic contrast imaging of liver tumors," *Ultrasonics*, 38(1-8): pp. 110–113, 2000.

Goertz, D., M. E. Frijlink, H. J. Vos, N. de Jong, and A. F. W. van der Steen, "Dual frequency microbubble imaging for high frequency ultrasound systems," in proc. IEEE Ultras Symp, Vancouver, Canada, 2006.

Goertz, D. E., N. de Jong, and A. F. W. van der Steen, "Attenuation and size distribution measurements of Definity and manipulated Definity populations," *Ultrasound Med Biol*, 33(9): pp. 1376–1388, 2007.

Gorce, J.-M., M. Arditi, and M. Schneider, "Influence of bubble size distribution on the echogenicity of ultrasound contrast agents - A study of SonoVue," *Invest Radiol*, 35(11): pp. 661–671, 2000.

Guidi, F., H. J. Vos, R. Mori, N. de Jong, and P. Tortoli, "Microbubble characterization through acoustically-induced deflation," *Accepted in IEEE Trans Ultrason Ferroelectr Freq Control*, 2009.

Hoff, L., P. C. Sontum, and J. M. Hovem, "Oscillations of polymeric microbubbles: Effect of the encapsulating shell," *J Acoust Soc Am*, 107(4): pp. 2272–2280, 2000.

Hope Simpson, D., P. N. Burns, and M. A. Averkiou, "Techniques for perfusion imaging with microbubble contrast agents," *IEEE Trans Ultrason Ferroelectr Freq Control*, 48(6): pp. 1483–1494, 2001.

Humphrey, V. F., "Non-linear acoustics as a laboratory tool," in proc. Proc Instit Acoust, vol. 14, No. 3, pp. 99–113, 1992.

Khismatullin, D. B. and A. Nadim, "Radial oscillations of encapsulated microbubbles in viscoelastic liquids," *Phys Fluids*, 14(10): pp. 3524–3557, 2002.

Kimmel, E., B. Krasovitski, A. Hoogi, D. Razansky, and D. Adam, "Subharmonic response of encapsulated microbubbles: Conditions for existence and amplification," *Ultrasound Med Biol*, 33(11): pp. 1767–1776, 2007.

Leighton, T. G., The Acoustic Bubble, Academic Press, London, UK, 1994.

Måsøy, S.-E., O. Standal, P. Näsholm, T. F. Johansen, B. Angelsen, and R. Hansen, "Surf imaging: *In vivo* demonstration of an ultrasound contrast agent detection technique," *IEEE Trans Ultrason Ferroelectr Freq Control*, 55(5): pp. 1112–1121, 2008.

Marmottant, P., S. M. van der Meer, M. Emmer, M. Versluis, N. de Jong, S. Hilgenfeldt, and D. Lohse, "A model for large amplitude oscillations of coated bubbles accounting for buckling and rupture," *J Acoust Soc Am*, 118(6): pp. 3499–3505, 2005.

McGahan, J. P. and B. B. Goldberg, Diagnostic Ultrasound, Informa Health Care, 2008.

Minnaert, M., "On musical air-bubbles and the sounds of running water," *Philosoph Mag*, 16: pp. 235–248, 1933.

Morgan, K. E., J. S. Allen, P. A. Dayton, J. E. Chomas, A. L. Klibanov, and K. W. Ferrara, "Experimental and theoretical evaluation of microbubble behavior: Effect of transmitted phase and bubble size," *IEEE Trans Ultrason Ferroelectr Freq Control*, 47(6): pp. 1494–1509, 2000.

Needles, A., D. E. Goertz, R. Karshafian, E. Chérin, A. S. Brown, P. N. Burns, and F. S. Foster, "High-frequency subharmonic pulsed-wave Doppler and color flow imaging of microbubble contrast agents," *Ultrasound Med Biol*, 34(7): pp. 1139–1151, 2008.

Newhouse, V. L. and P. Mohana Shankar, "Bubble size measurements using the nonlinear mixing of two frequencies," *J Acoust Soc Am*, 75(5): pp. 1473–1477, 1984.

Pace, N. G., A. Cowley, and A. M. Campbell, "Short pulse acoustic excitation of microbubbles," *J Acoust Soc Am*, 102(3): pp. 1474–1479, 1997.

Sarkar, K., W. T. Shi, D. Chatterjee, and F. Forsberg, "Characterization of ultrasound contrast microbubbles using in vitro experiments and viscous and viscoelastic interface models for encapsulation," *J Acoust Soc Am*, 118(1): pp. 539–550, 2005.

Shi, W. T., L. Hoff, and F. Forsberg, "Subharmonic performance of contrast microbubbles: an experimental and numerical investigation," in proc. IEEE Ultras Symp, pp. 1957–1960, Munich, Germany, 2002.

Sijl, J., E. Gaud, P. J. A. Frinking, M. Arditi, N. de Jong, D. Lohse, and M. Versluis, "Acoustic characterization of single ultrasound contrast agent microbubbles," *J Acoust Soc Am*, 124(6): pp. 4091–4097, 2008.

Stride, E., "The influence of surface adsorption on microbubble dynamics," *Phil Trans R Soc A*, 366(1873): pp. 2103–2115, 2008.

Tsiglifis, K. and N. A. Pelekasis, "Nonlinear radial oscillations of encapsulated microbubbles subject to ultrasound: The effect of membrane constitutive law," *J Acoust Soc Am*, 123(6): pp. 4059–4070, 2008.

van der Meer, S. M., B. Dollet, M. M. Voormolen, C. T. Chin, A. Bouakaz, N. de Jong, M. Versluis, and D. Lohse, "Microbubble spectroscopy of ultrasound contrast agents," *J Acoust Soc Am*, 121(1): pp. 648–656, 2007.

Vokurka, K., "Comparison of Rayleigh's, Herring's, and Gilmore's models of gas bubbles," *Acustica*, 59(3): pp. 214–219, 1986.

Vos, H. J., M. Emmer, and N. de Jong, "Oscillation of single microbubbles at room versus body temperature," in proc. IEEE Ultras Symp, pp. 982–984, Beijing, China, 2008.

Vos, H. J., D. E. Goertz, and N. de Jong, "Pulse repetition rate excitation of contrast agents," in proc. IEEE Ultras Symp, pp. 216–219, Vancouver, BC, 2006.

Vos, H. J., D. E. Goertz, and N. de Jong, "Self-demodulation for high-frequency diagnostic ultrasound," *conditionally accepted in J Acoust Soc Am*, 2009.

Wu, C.-Y. and J. Tsao, "The ultrasonic weak short-pulse responses of microbubbles based on a two-frequency approximation," *J Acoust Soc Am*, 114(5): pp. 2662–2671, 2003.

Wu, C.-Y., J. Tsao, and Y.-H. Chou, "An ultrasonic microbubble semi-intermodulated imaging technique," *Ultrasound Med Biol*, 31(9): pp. 1199–1210, 2005.

Chapter 12

Ultrasound contrast agent detection technique using high-frequency manipulation pulses

Abstract - **Most of current ultrasound contrast agent detection techniques suffer from nonlinear propagation in tissue. This chapter proposes a new dual pulse technique that is based on low-frequency imaging pulses, alternately accompanied by a high-frequency manipulation pulse. The high-frequency pulse procudes a change in the response of microbubbles to the low-frequency imaging pulse, but the pulse does presumably not manipulate the response of tissue, even in conditions where mild nonlinear propagation is expected. This difference in response of microbubbles and tissue can be used to improve contrast. The manipulation of contrast microbubbles with high-frequency pulses has been observed optically by the current authors, but no study has yet been reported to address or apply this effect.**

Experimental data are acquired in the study described in Chapter 9, 'Radial modulation of single microbubbles'.

12.1 Introduction

In medical diagnostic echography, ultrasound contrast agents (UCAs) are released into the blood circulation to enhance echo signals from the cardiovascular system that would otherwise be shadowed by surrounding tissue [Feinstein, 2006]. Typically, the agents consist of small gas bubbles (0.5 – 5 μm diameter) stabilized by an albumin, phospholipids or polymer coating to reduce dissolution. The high compressibility of the gas compared to the surrounding medium results in large scattering of the ultrasound wave by the microbubbles; volumetric vibrations are induced by the imaging ultrasound. In a clinical setting, the signals produced by the scattering of bubbles have to compete with the signals produced by the scattering of tissue. The ratio between the two signals is called the contrast-to-tissue ratio (CTR). A large number of the CTR is preferable for contrast-enhanced ultrasound. It is widely accepted that, especially when a small amount of agent is to be detected, simple recording of the fundamental-frequency echo does not provide a large CTR.

Newer detection strategies have therefore been introduced that strive to optimize the signals from bubbles and reduce the signals produced by tissue. Such strategies are generally based on the nonlinear response of bubbles to ultrasound. Phospholipids coated microbubbles can show *enhanced-compression* oscillations, during which the radial oscillation shows more compression than expansion. This effect is presumably caused by highly nonlinear coating properties [Marmottant et al., 2005; de Jong et al., 2007]. The effect is sometimes called *compression-only*, although this might be a misleading term since some expansion can generally still be observed. Phospholipids coated bubbles have further been shown to generate higher harmonics of the insonation frequency [de Jong et al., 2002; Bouakaz et al., 2002], subharmonics [Eller and Flynn, 1969; Chomas et al., 2002; Shi et al., 2002; Goertz et al., 2007; Needles et al., 2008], ultralow harmonics [Wu et al., 2005], and they have been shown to respond nonlinearly to the insonation pressure level [Emmer et al., 2007]. Also, they are able to act as nonlinear mixers in dual-frequency insonation producing frequency cross-products [Ostrovsky et al., 1998; Shi and Forsberg, 2000; Deng et al., 2000; Chen et al., 2006; Yeh et al., 2008] which can be used for imaging. Furthermore, transient aspects related to bubble resonant behavior have been extensively studied in the context of contrast detection methods [Morgan et al., 2000; Borsboom, 2004; Shi et al., 2006; Mleczko et al., 2007; Mahue et al., 2009]. When looking into the details of all of these studies, a major finding is that the acoustic response originating from nonlinear and/or transient responses is very often smaller than the fundamental bubble response; noise in the receiving section of the ultrasound equipment could mask the bubble responses. Therefore bubble detection methods should enhance the signals from bubbles, or at least not suppress the signals, in order to have sufficient signal-to-noise ratio (SNR). Both a CTR and SNR of 45 dB is the final goal, since general ultrasound equipment has no higher dynamic

range in video processing than 45 dB.

Even at relatively low pressures in regular diagnostic ultrasound, nonlinear propogation of tissue cannot be neglected *a priori* [Duck, 2002; Vos et al., 2009a,b]. Examples of the influence of nonlinear tissue propagation on various detection techniques are given below:

- Pulse inversion is a technique in which a second transmitted pulse is the sign-inverted replica of the first pulse [Hope Simpson et al., 2001]. After summation of the echoes of the two pulses, any response at the second harmonic frequency (mainly from bubbles) is doubled in amplitude, while any response at the fundamental frequency (mainly from tissue) is suppressed [Hope Simpson et al., 2001]. A drawback of pulse inversion is distortion of the ultrasound pulse caused by nonlinear propagation of the finite-amplitude pressure wave. The distortion also produces second harmonic frequency content, and thus limits the contrast enhancement. This drawback is partly worked around by reducing the transmission amplitude, at the cost of limited penetration depth.

- Superharmonic imaging is based on the reception of contrast signals in a frequency band much higher than the transmit frequency, so called superharmonic imaging [Bouakaz et al., 2002; Gessner et al., 2009]. The signals from nonlinear propagation in tissue are very low in that frequency band, while bubbles produce relatively high signals.

- Radial modulation is a technique in which microbubbles are manipulated with a low-frequency wave to provide decorrelation of high-frequency imaging pulses [Bouakaz et al., 2007; Chérin et al., 2008; Måsøy et al., 2008; Emmer et al., 2009] - see also Ch. 9. Unexpectedly, tissue also generates strong decorrelation. An explanation for this is given in Måsøy et al. [2008]: the imaging pulses are 'surfing' on the compression or rarefaction half-cycle of the manipulation wave. The local speed of sound in the compression half-cycle is higher than the speed of sound in the rarefaction half-cycle, leading to time-of-flight-dependent decorrelation of the imaging pulses. Hence, special care should be taken to compensate for this nonlinear effect that severely reduces tissue suppression.

- The semi-intermodulation technique as proposed by Wu et al. [2005] is a technique in which a bubble-echo at a frequency much lower than the transmission frequency is received. In the rationale it was stated that tissue cannot produce such low-frequency signal, which is not correct; Vos et al. [2009a] (see also Ch. 10 (Self-demodulation)) showed that tissue can also produce a low-frequency signal that depends on the envelope of the pulse, through nonlinear propagation. The nonlinear propagation signals could mask the bubble signals.

From these examples it is derived that, for optimal contrast, not only linear tissue signals have to be suppressed but also nonlinear tissue signals. A generic suppression method is the subtraction of the echoes of two pulses that are equal; nonlinear propagation is presumably equally present in the two echoes, and subtraction will cancel out both linear and nonlinear tissue signals, as long as the tissue is not moving. Then, the imaging signal has to compete only with noise. However, bubbles should be manipulated during one of the two pulses to create a contrast signal; the manipulation should not corrupt the tissue signal cancellation.

This chapter describes a dual pulse detection scheme based on high-frequency manipulation of nonlinearly oscillating microbubbles. It will be shown using a numerical nonlinear propagation model that nonlinear propagation in tissue will probably result in low-amplitude signals only.

12.2 Methods

12.3 Data acquisition

In the experiments reported in Ch. 9 (Radial modulation) microbubbles were insonified with ultrasound pulses of one of three different compositions: (1) a single 0.5 MHz tone burst of 2.5 cycles, 30 kPa (LF pulse); (2) a single 3.75 MHz tone burst of 36 cycles, 80 kPa (HF pulse); (3) a simultaneous summation ('combination pulse') of pulse 1 and 2. The main conclusion from that study was that the response to the HF pulse was modulated by the LF pulse. However, not reported in Ch. 9 and the accompanying paper [Emmer et al., 2009], is that also the opposite was observed: the response to the LF pulse was changed by the HF pulse. This change of LF response is described in more detail in this chapter. For details of the setup and the data analysis the reader is referred to Ch. 9 or Emmer et al. [2009].

12.3.1 Contrast detection method using high-frequency manipulation pulses

The proposed method is based on a dual pulse transmission sequence. The first pulse is a tone burst at low frequency, of few cycles. After reception of the echoes from the first pulse, a second pulse is transmitted. The second pulse contains a high-frequency tone burst in addition to the low-frequency tone burst. The high-frequency tone burst manipulates the response of microbubbles to the low-frequency tone burst, while it presumably not manipulates the response of tissue to the low-frequency tone burst. The data-processing consists of subtraction of the two received echoes in time domain. Two echoes from tissue are presumably equal, and subtraction of the echoes cancels tissue signals. Two echoes from microbubbles are different, and subtraction therefore gives a non-zero contrast signal. This contrast signal can be further processed to form an image with.

Since the method has not yet been tested *in vitro*, a preliminary estimate of ef-

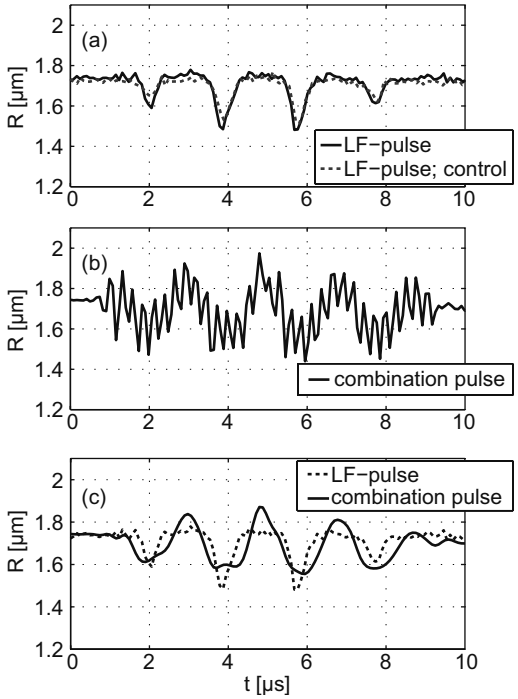

Figure 12.1: (a) Recorded responses of a 1.7 µm microbubble to a 0.5 MHz, 30 kPa pulse (LF pulse). The 'control' is the response of the same bubble to a similar LF pulse, while in the mean time it was excited once with the combination pulse. The response is repeatable. (b) Recorded response to a combination of the LF pulse with a 3.75 MHz, 80 kPa pulse (combination pulse). (c) Same data as in (a) and (b), but filtered to remove the high-frequency oscillation.

ficacy is reported in this Chapter. The change of echo response of microbubbles at the low frequency by the HF pulse is quantified based on optical microbubbles recordings. Possible change of tissue response is calculated with a nonlinear ultrasound propagation simulation model, extended with estimates of tissue ultrasound scattering. Since the data show that HF microbubble manipulation had effects on the low-frequency response (0.5 MHz) but also on the second harmonic frequency (1 MHz), detection signals are band-pass filtered at these two frequencies.

12.4 Results

12.4.1 Microbubble signals

Fig. 12.1 shows an example of the response of a microbubble with radius 1.7 μm insonified by a 0.5 MHz, 30 kPa pulse (LF pulse), and by a combination of the low-frequency pulse with a 3.75 MHz, 80 kPa pulse ('combination pulse' in Fig. 12.1b). The 'control' is the response of the same bubble to the LF pulse after the combination pulse ($\sim$ 80 ms later), showing that the response is repeatable. Figs. 12.1a and 12.1b show the raw data of the radial excursion, and Fig. 12.1c shows the radial excursion after digital low-pass filtering to remove the high-frequency oscillation.

The radius-time trace in Fig. 12.1c shows a much smaller expansion than compression. A quantitative measure of the asymmetry in radial excursion is obtained by calculating the ratio of the relative expansion to the relative compression following de Jong et al. [2007]. The expansion is defined as the difference between the maximum radius and initial radius ($\mathrm{E} = R_{\max} - R_0$), and compression likewise ($\mathrm{C} = -(R_{\min} - R_0)$). The expansion to compression ratio (ECR) of this response is 0.17; Note that unity ECR value is expected for a linearly responding microbubble. In response to the combination pulse (Fig. 12.1c), the radial excursion is seen to be more symmetric around the initial radius. The ECR of this trace is 0.69.

The enhanced-compression effect is accompanied by high-amplitude second harmonic content in the oscillation. Fig. 12.2 shows the Fourier spectra of the microbubble oscillations of Fig. 12.1. The spectra show largest difference (8 dB) at the second harmonic frequency (1 MHz) of the transmission frequency, but also a 4-dB difference at the transmission frequency of 0.5 MHz.

By using the theory and methods of Ch. 4 (optical-acoustic conversion), the radial responses of the microbubble are converted into a derived pressure trace. The pressure is calculated for a distance of 75 mm, which is relevant for e.g. liver imaging. Tissue attenuation during back-propagation of the echo is not accounted for in the calculations, but assuming an attenuation value of 0.8 dB/cm/MHz [liver; Duck, 1990], a respective attenuation of 3 dB and 6 dB of the fundamental and second harmonic frequency wave can be expected.

Fig. 12.3 shows the predicted pressure traces of the example microbubble when

insonified with the LF pulse or the combination pulse. The HF frequency contents (3.75 MHz and higher) are suppressed by low-pass filtering. The two pressure traces differ significantly. When subtracting the two pressure pulses, a bubble detection signal results that is depicted in Fig. 12.4a. The right panel of this figure shows the Fourier spectrum. Again it is observed that the largest difference between the microbubble responses is present at the second harmonic of the low frequency pulse, i.e., at 1 MHz. The amplitude of the 1 MHz detection signal is about 0.1 Pa, and that of the 0.5 MHz signal is about 0.02 Pa.

12.4.2 ECR of all bubbles in the dataset

As seen in Fig. 12.1b, a convenient parameter characterizing the high-frequency manipulation of LF radial responses of microbubbles is the expansion to compression ratio (ECR). Fig. 12.5 shows the ECR of the response of the 58 microbubble in the dataset. The radii were ranging from 0.6 to 2.6 μm. Diamonds denote the ECR of the response to LF pulse excitation and dots denote the response to combination pulse excitation. The average ECR for all microbubbles is 0.16 and 0.33, respectively. For radii smaller than 1.4 μm and larger than 2.4 μm the differences in ECR are not large, but the ECR for microbubbles within the range 1.4 to 2.4 μm show large differences. Within this range only, the average ECR is 0.12 and 0.43 (N = 27) for the LF pulse and combination pulse excitation, respectively.

This analysis shows that the largest HF manipulation of the radial LF response is obtained for bubbles with radii ranging from 1.4 to 2.4 μm. However, since the echo of the microbubbles is strongly related to the initial size of the microbubbles (see Chs. 4 and 9), the manipulation of the LF *echo* should also be studied, besides the LF *radial* response. The HF manipulation of the LF echo is studied in the next subsection.

12.4.3 Detection signals of all bubbles in the dataset

The echo-analysis as described above is repeated for the 58 microbubbles in the dataset. The numerical difference in echo amplitude of the response to the LF pulse and combination pulse is plotted in Fig. 12.6. For convenience the echo response is band-pass filtered around 0.5 MHz and 1 MHz. Fig. 12.6 shows the amplitude of the detection signals as a function of the initial microbubble size. The signal-to-noise ratio of the optical recordings was about 20 dB in the 0.5 MHz and 1 MHz frequency bands. The graph shows a different trend than Fig. 12.5. In Fig. 12.5, the radial manipulation was found highest for mid-range microbubble sizes. In Fig. 12.6 the echo manipulation is highest for microbubbles of largest sizes. The latter trend can be explained by the cubic relation between the initial radius and echo amplitude for a given relative excursion amplitude (see Eq. 4.5), analogous to the analysis in Ch. 9: Small differences in the high-amplitude echo of large bubbles give a high

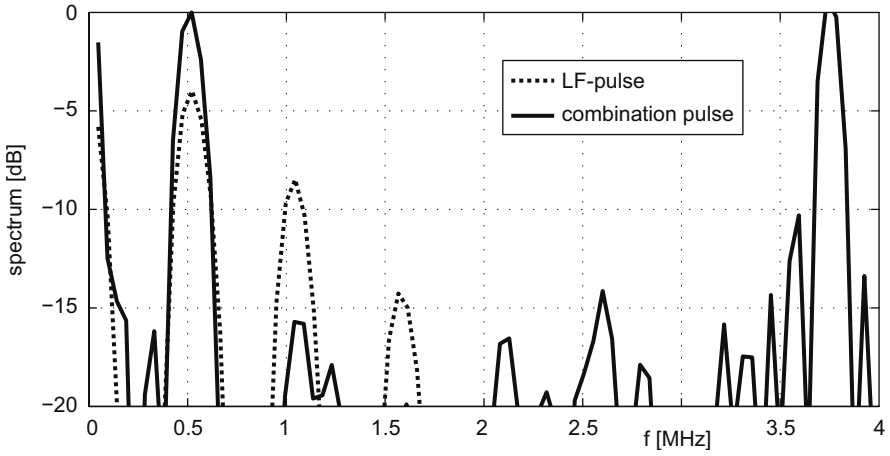

Figure 12.2: Fourier spectra of the radius-time traces of Fig. 12.1.

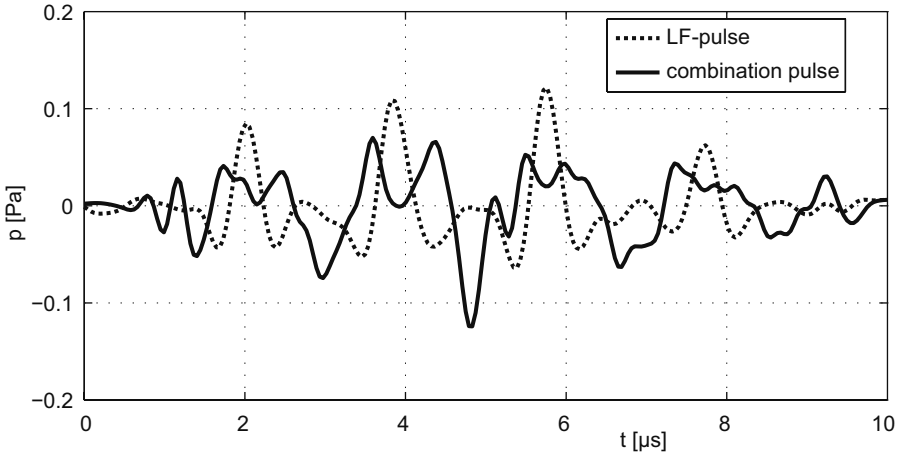

Figure 12.3: Numerically predicted pressure traces, derived from the radius-time traces in Fig. 12.1 at 75 mm from the microbubble. The pressure-time traces were low-pass filtered to remove the 3.75 MHz contents.

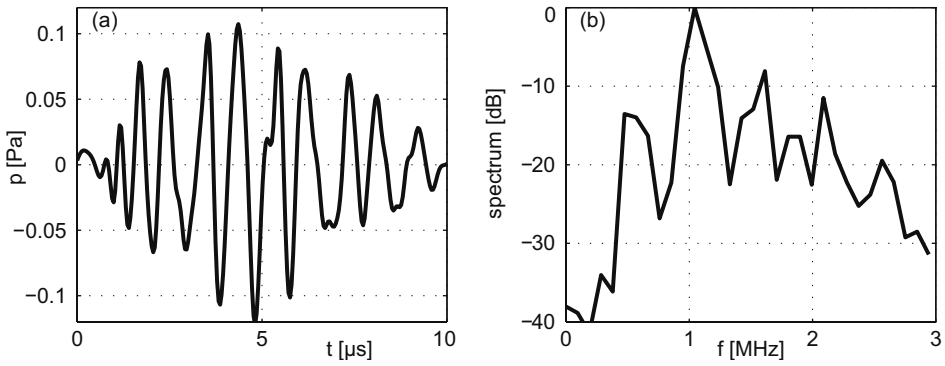

Figure 12.4: Numerically predicted bubble detection signal, by subtraction of the two pressure-time traces shown in Fig. 12.3.

detection signal. Large differences in the low-amplitude echo of small bubbles give a low detection signal.

12.4.4 Spurious tissue signals

The spurious signals of tissue are calculated in two steps. First, a nonlinear ultrasound propagation method is used to model the forward propagation of the two pulses. Second, the scattering of the wave and backward propagation are modeled by a multiplication of the forward traveling pulse with a constant factor that mimickes the scattering strength of tissue and back-propagation attenuation. The resulting 'tissue' signal is compared to the 'contrast' signal calculated above.

Nonlinear propagation in tissue is modeled using the KZK equation as described by Lee and Hamilton [1995] - see also the appendix of Ch. 10 (Selfdemodulation). In the calculations the parameter values of water are taken, equal to those reported in Ch. 10. The reason for taking water values instead of tissue values is that water is believed to produce higher nonlinear distortion than tissue, and thus water would give a 'worse case' than tissue.

Two simulation runs were employed. First, the propagation of an LF pulse of 0.5 MHz was calculated. The source pressure was such that the peak rarefaction pressure in focus ($\sim$ 75 mm from the transducer) was 30 kPa. Second, the propagation was calculated of a pulse constructed by summation of the LF pulse and a 3.75 MHz pulse with the same envelope as the LF pulse; the peak rarefaction pressure in focus at 3.75 MHz was 80 kPa. Next, both signals in focus were reduced by 60 dB, thus mimicking the scattering strength of tissue and backpropagation from

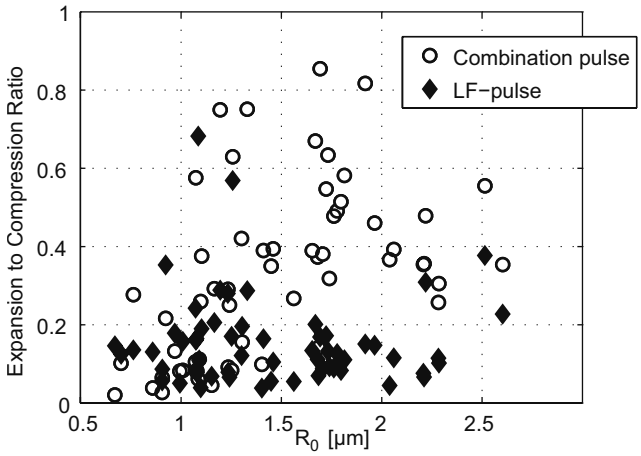

Figure 12.5: Expansion to Compression Ratio of all microbubbles in the dataset.

the imaging region towards the receiving transducer. The two resulting signals were subtracted, which actually produces the 'raw' spurious tissue signal. Finally, the tissue signal is band-pass filtered around 0.5 MHz and 1 MHz, respectively, before plotting. Such data-processing yields a 'tissue'-signal that counteracts the contrast detection efficacy. The results of the calculations are shown in Fig. 12.7.

The 'tissue'-signal after subtraction is non-zero. This is perhaps a little surprising since generally it is assumed that nonlinear propagation generates sum-and-difference frequencies; a signal with frequency contents of 0.5 MHz and 1 MHz cannot be described by a sum-and-difference combination of 3.75 MHz and 0.5 MHz. The reason for the non-zero 'tissue-signal' is nonlinear propagation of the high-frequency pulse that produces low-frequency contents, as described in Ch. 10. In the transducer focal region the amplitude difference between the LF pulse with and without the additional HF pulse is very small. The difference is $\sim$ 150 Pa at 0.5 MHz, while the pulse itself has an amplitude of about 30 kPa. Yet, it produces a 'tissue'-signal amplitude of 0.15 Pa at 0.5 MHz and 0.02 Pa at 1 MHz. Although the results rely heavily on the assumed scattering strength of tissue, they show that 'tissue'-signals cannot be excluded *a priori*, unfortunately.

12.5 Discussion

Figs. 12.6 and 12.7 show the main preliminary results of the proposed method. Subtraction of the two bubble echoes results in a bubble detection signal of up to 0.6 Pa with maximum frequency content at 1 MHz, which is the second harmonic frequency of the imaging pulse. Such detection signal will be just above the noise

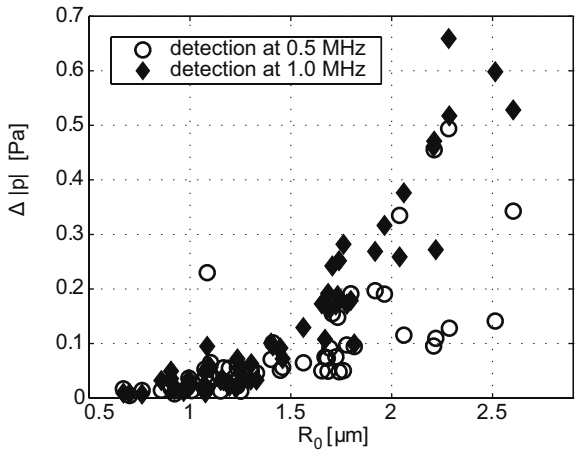

Figure 12.6: Amplitude level of microbubble detection signals at 0.5 MHz and 1.0 MHz.

level of a custom low-noise system (see Chapter 3 (Deflation-assisted characterization) - presumably commercial research scanners will have similar SNR). Tissue is expected to produce a lower signal level, 0.02 Pa at 1 MHz, which is probably below the noise level. From this data the expected CTR is up to 30 dB, or 24 dB if attenuation of the contrast signals by tissue is taken into account. This preliminary result would suggest that the high-frequency manipulation technique results in low but significant contrast signals, while tissue signals are suppressed to below the noise level. This should however be tested with a dual-frequency experimental setup, such as described by Bouakaz et al. [2004] or Måsøy et al. [2008]. It is anticipated that Doppler-based techniques can improve the SNR significantly.

An advantage of the method is that neither the low-frequency pulse nor the high-frequency pulse have specific demands for their envelope. Even relatively basic transmission systems using unipolar excitation circuitry would be able to implement the technique, as long as the frequency bands of the LF section and the HF section of the equipment are sufficiently separated.

Another advantage is that the method is presumably sensitive for contrast signals only in the overlapping region between the low-frequency and the high-frequency beam. Generally a high-frequency beam has smaller lateral dimensions than a low-frequency beam. Furthermore, the grating lobes in the ultrasound fields at the two different frequencies generally do not overlap, and thus they are suppressed. The overall axial resolution might be determined by both the lower frequency of the imaging pulse and the duration of the detection signal which is dominated by the high-frequency pulse length. Ultimately, by choosing an optimal high-frequency pulse length the full bandwidth of the low-frequency receive system may

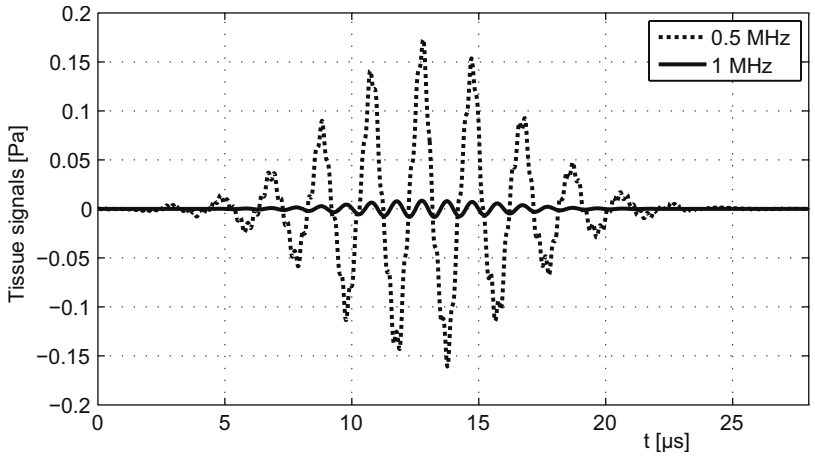

Figure 12.7: Simulated expected signal from tissue that can be attributed to a nonlinear interaction of the high-frequency manipulation pulse with the low-frequency imaging pulse. A tissue scattering & backpropagation attenuation coefficient of –60 dB is assumed.

be used.

Further study is needed for finding the optimal combination of frequencies and pressure amplitudes with respect to contrast detectibility, imaging resolution, tissue signal attenuation, and destruction rate of the contrast material.

Bibliography

Borsboom, J. M. G., Advanced detection strategies for ultrasound contrast detection, Ph.D. thesis, Erasmus University Rotterdam, 2004.

Bouakaz, A., S. Frigstad, F. J. ten Cate, and N. de Jong, "Super harmonic imaging: A new imaging technique for improved contrast detection," *Ultrasound Med Biol*, 28(1): pp. 59–68, 2002.

Bouakaz, A., F. J. ten Cate, and N. de Jong, "A new ultrasonic transducer for improved contrast nonlinear imaging," *Physics Med Biol*, 49(16): pp. 3515–3525, 2004.

Bouakaz, A., M. Versluis, J. M. G. Borsboom, and N. de Jong, "Radial modulation of microbubbles for ultrasound contrast imaging," *IEEE Trans Ultrason Ferroelectr Freq Control*, 54(11): pp. 2283–2290, 2007.

Chen, S., R. Kinnick, J. F. Greenleaf, and M. Fatemi, "Difference frequency and its harmonic emitted by microbubbles under dual frequency excitation," *Ultrasonics*, 44: pp. e123–e126, 2006.

Chérin, E., J. Brown, S.-E. Måsøy, H. H. Shariff, R. Karshafian, R. Williams, P. N. Burns, and F. S. Foster, "Radial modulation imaging of microbubble contrast agents at high frequency," *Ultrasound Med Biol*, 34(6): pp. 949–962, 2008.

Chomas, J. E., P. A. Dayton, D. J. May, and K. W. Ferrara, "Nondestructive subharmonic imaging," *IEEE Trans Ultrason Ferroelectr Freq Control*, 49(7): pp. 883–892, 2002.

de Jong, N., A. Bouakaz, and P. Frinking, "Basic acoustic properties of microbubbles," *Echocardiography*, 19(3): pp. 229–240, 2002.

de Jong, N., M. Emmer, C. T. Chin, A. Bouakaz, F. Mastik, D. Lohse, and M. Versluis, ""Compression-only" behavior of phospholipid-coated contrast bubbles," *Ultrasound Med Biol*, 33(4): pp. 653–656, 2007.

Deng, C. X., F. L. Lizzi, A. Kalisz, A. Rosado, R. H. Silverman, and D. J. Coleman, "Study of ultrasonic contrast agents using a dual-frequency band technique," *Ultrasound Med Biol*, 26(5): pp. 819–831, 2000.

Duck, F. A., Physical properties of tissue, Academic press Ltd., 1990.

Duck, F. A., "Nonlinear acoustics in diagnostic ultrasound," *Ultrasound Med Biol*, 28(1): pp. 1–18, 2002.

Eller, A. I. and H. G. Flynn, "Generation of subharmonics of order one-half by bubbles in a sound field," *J Acoust Soc Am*, 46(3 (part2)): pp. 772–727, 1969.

Emmer, M., A. van Wamel, D. E. Goertz, and N. de Jong, "The onset of microbubble vibration," *Ultrasound Med Biol*, 33(6): pp. 941–949, 2007.

Emmer, M., H. J. Vos, and N. de Jong, "Radial modulation of single microbubbles," *IEEE Trans Ultrason Ferroelectr Freq Control*, 56(11): pp. 2370–2379, 2009.

Feinstein, S. B., "Contrast ultrasound imaging of the carotid artery vasa vasorum and atherosclerotic plaque neovascularization," *J Am Coll Cardiol*, 48(2): pp. 236–243, 2006.

Gessner, R., M. Lee, M. Lukacs, F. S. Foster, and P. A. Dayton, "High-resolution in-vivo ultraharmonic contrast imaging using a dual-frequency transducer," in proc. IEEE Int Ultras Symp, Rome, Italy, 2009.

Goertz, D. E., M. E. Frijlink, D. Tempel, V. Bhagwandas, A. Gisolf, R. Krams, N. de Jong, and A. F. W. van der Steen, "Subharmonic contrast intravascular ultrasound for vasa vasorum imaging," *Ultrasound Med Biol*, 33(12): pp. 1859–1872, 2007.

Hope Simpson, D., P. N. Burns, and M. A. Averkiou, "Techniques for perfusion imaging with microbubble contrast agents," *IEEE Trans Ultrason Ferroelectr Freq Control*, 48(6): pp. 1483–1494, 2001.

Lee, Y. S. and M. F. Hamilton, "Time-domain modeling of pulsed finite-amplitude sound beams," *J Acoust Soc Am*, 97(2): pp. 906–917, 1995.

Måsøy, S.-E., O. Standal, P. Näsholm, T. F. Johansen, B. Angelsen, and R. Hansen, "SURF imaging: *In vivo* demonstration of an ultrasound contrast agent detection technique," *IEEE Trans Ultrason Ferroelectr Freq Control*, 55(5): pp. 1112–1121, 2008.

Mahue, V., J. M. Mari, R. Eckersley, and M.-X. Tang, "Comparison of pulse subtraction Doppler and pulse inversion Doppler," in proc. IEEE Ultrasonics Symposium, pp. ref. P1–A–02, Rome, Italy, 2009.

Marmottant, P., S. M. van der Meer, M. Emmer, M. Versluis, N. de Jong, S. Hilgenfeldt, and D. Lohse, "A model for large amplitude oscillations of coated bubbles accounting for buckling and rupture," *J Acoust Soc Am*, 118(6): pp. 3499–3505, 2005.

Mleczko, M., W. G. Wilkening, and G. Schmitz, "Optimal pulse sequences for the suppression of memoryless tissue harmonics," in proc. IEEE Ultras Symp, pp. 542–545, New York, NY, USA, 2007.

Morgan, K. E., J. S. Allen, P. A. Dayton, J. E. Chomas, A. L. Klibanov, and K. W. Ferrara, "Experimental and theoretical evaluation of microbubble behavior: Effect of transmitted

phase and bubble size," *IEEE Trans Ultrason Ferroelectr Freq Control*, 47(6): pp. 1494–1509, 2000.

Needles, A., D. E. Goertz, R. Karshafian, E. Chérin, A. S. Brown, P. N. Burns, and F. S. Foster, "High-frequency subharmonic pulsed-wave Doppler and color flow imaging of microbubble contrast agents," *Ultrasound Med Biol*, 34(7): pp. 1139–1151, 2008.

Ostrovsky, L. A., A. M. Sutin, I. A. Soustova, A. I. Matveyev, and A. I. Potapov, "Nonlinear, low-frequency sound generation in a bubble layer: Theory and laboratory experiment," *J Acoust Soc Am*, 104(2): pp. 722–726, 1998.

Shi, W. T. and F. Forsberg, "Ultrasonic characterization of the nonlinear properties of contrast microbubbles," *Ultrasound Med Biol*, 26(1): pp. 93–104, 2000.

Shi, W. T., C. S. Hall, and P. G. Rafter, "Contrast resonance imaging with embedded ultrasound imaging pulses," in proc. IEEE Ultras Symp, pp. 212–215, Vancouver, 2006.

Shi, W. T., L. Hoff, and F. Forsberg, "Subharmonic performance of contrast microbubbles: an experimental and numerical investigation," in proc. IEEE Ultras Symp, pp. 1957–1960, Munich, Germany, 2002.

Vos, H. J., D. E. Goertz, and N. de Jong, "Self-demodulation for high-frequency diagnostic ultrasound," *conditionally accepted in J Acoust Soc Am*, 2009a.

Vos, H. J., D. E. Goertz, and N. de Jong, "Self-demodulation technique for microbubble excitation," *submitted to IEEE Trans Ultrason Ferroelectr Freq Control*, 2009b.

Wu, C.-Y., J. Tsao, and Y.-H. Chou, "An ultrasonic microbubble semi-intermodulated imaging technique," *Ultrasound Med Biol*, 31(9): pp. 1199–1210, 2005.

Yeh, C.-K., S.-Y. Su, C.-C. Shen, and M.-L. Li, "Dual high-frequency difference excitation for contrast detection," *IEEE Trans Ultrason Ferroelectr Freq Control*, 55(10): pp. 2164–2176, 2008.

Chapter 13

Discussion and Conclusions

Abstract - **This thesis describes various aspects of the behavior of ultrasound-excited phospholipids coated microbubbles. High-speed observations with the Brandaris-128 camera, acoustic recordings, and numerical simulations of single microbubbles allowed detailing this behavior. Experiments with a population of different-sized microbubbles would not have allowed such detailing. The setups used calibrated equipment to allow absolute measurement of the pressure and radial excursions. This chapter discusses the microbubble behavior, and connects this behavior to contrast detection techniques. Hints towards future directions of research are provided.**

13.1 Microbubble behavior

The various studies in this thesis have addressed the behavior of isolated phospholipids coated microbubbles. A thesis-wide observation is that microbubble behavior can be classified in three regimes of the relative radial excursion during the oscillation. See Table 13.1 for an overview of these regimes. Although the boundaries between the regimes are obtained from a rough estimate and might in detail depend on e.g. initial size, excitation frequency and temperature, the results can feed first expectations and can serve the discussion of microbubble behavior. To give an example, a microbubble excited at a resonance frequency of 2 MHz has a radial excursion of 25% when the driving pressure amplitude is 40 kPa (MI 0.03), and 40% when the driving amplitude is 80 kPa. Off-resonance excitation gives lower excursion (see Chapter 8). The nonlinear response, and the influence of the coating, are mainly estimated from Chapters 8 (temperature influence) and 9 (radial modulation) and from literature [Morgan et al., 2000]. Chapters 6 (sideview setup) and 7 (orthogonal microscope) addressed the nonspherical deformations of microbubbles when oscillating in contact with a wall. The deflation behavior is obtained from Chapter 3 (deflation-assisted characterization) and Chapter 8.

13.1.1 Nonlinearity

The table states that the influence of the coating is large at small radial excursions (as also described in the PhD thesis of Emmer [2009]). This is a remarkable effect since a phospholipids coating consists of a monolayer of molecules of only some nanometer thickness that affects the oscillation of micron-sized bubbles. In the small-excursion regime the exact shell dynamics are as important as fluid dynamics and gas compressibility, and since a phospholipids coating has a nonlinear strain-stress relationship [Marmottant et al., 2005; Borden et al., 2006], bubbles show a nonlinear response in this regime. The nonlinearity can lead to various effects, such as 'compression-only' producing high-amplitude harmonic frequencies, and strong nonlinear mixing of two excitation pulses.

The nonlinearity at low radial excursion has an important experimental impli-

Table 13.1: Microbubble behavior classified by the relative radial excursion amplitude.

Regime (rel. exc. amplitude)	Nonlinear response	Shape	Deflation effect	Influence coating
$< 25\%$	large	spherical	small	large
25% - 50%	medium	nonspherical	medium	small
$> 50\%$	large	nonspherical	large	negligible

cation: when studying nonlinear coating effects, the oscillation amplitude should be low. This was done on purpose in Chapters 8 (temperature influence), 9 (radial modulation) and 12 (high-frequency manipulation) since those studies specifically address the effects of the coating. It is also insightful to assess the oscillation regime in the deflation-assisted characterization experiments of Chapter 3. In that study the radial excursion of the microbubbles was not observed directly. However, a retrospective estimate of the radial excursion is possible by combining the results with the numerical integration technique of Chapter 4 (optical-acoustic conversion). By doing so, a relative radial excursion of 8% is estimated for a microbubble radius of 2 μm when excited by 60 kPa, 2 MHz pulses [1]. The oscillation thus is in the small-excursion regime and the microbubble echo shown in Fig. 3.3b indeed shows some harmonic distortion. Optical verification using the Brandaris-128 camera such as described in Chapter 5 shows that this first estimate is only off by a factor of roughly 2.

Within parentheses, Emmer [2009] has already noted that at extremely low radial excursion (practically, a relative excursion in the order of 1%) a phospholipids coated bubble might respond linearly to the driving ultrasound pulse, since the coating is in the elastic state as defined by Marmottant et al. [2005]. Such low excursion is however difficult to detect with the current experimental setups. Morover, the clinical relevance of such small excursion is low, and therefore not included in the analysis above.

13.1.2 Nonspherical shape oscillations

The occurence of nonspherical shape oscillations perpendicular to the wall at low-amplitude driving pressure was a little unexpected since we believed that the coating would dampen these shape oscillations, or that they would otherwise be visible in the top view. Chapters 6 (side view setup) and 7 (orthogonal microscope) prove the opposite. These chapters even show that period-doubling oscillations seen in top view could be erroneously interpreted as volumetric subharmonic oscillations. Nonetheless, retrospective analysis can now show that nonspherical oscillations have presumably played no big role in the optical-acoustic verification experiments of Chapter 4, neither have they during the deflation experiments of Chapter 3, since the radial excursion was low in both studies.

Nonspherical shape oscillations, having a period-doubling nature, might produce subharmonic echoes that are favorable for contrast agent detection. The recordings presented in this thesis do not provide definite proof. However, Longuet-Higgins [1989] theoretically shows that the echo level scattered by shape oscillation decays with r^{-2}, instead of the r^{-1} decay of a volumetric-oscillation echo. Thus,

[1] see Fig. 3.5, and combination of Eqs. 3.1 and 9.7: amplitude $A = \sqrt{\mathrm{SCS}_{\mathrm{norm}}} \cdot P_a / \left(\rho\omega^2 R_0\right) = \sqrt{-3\mathrm{dB}} \cdot 62\,10^3 / (10^3 \cdot (2\pi\,2\,10^6)^2 \cdot 2\,10^{-6}) = 0.165\,\mu\mathrm{m}$

the subharmonic signal produced by period-doubling shape oscillations would not be detected at larger distance. On the other hand, the nonspherical shape oscillations might couple to a volumetric oscillation through nonlinear interactions, which would result in an extra contribution at the fundamental frequency. This nonlinear coupling was found to be small for uncoated bubbles [Longuet-Higgins, 1989]. However, a surface coating showing nonlinear strain-stress relations and/or inhomogeneous configuration, like phospholipids monolayers [Borden et al., 2006], might enhance the nonlinear coupling between shape oscillations and volumetric oscillations. Such effect could be studied with combined optical and acoustic recordings of single microbubbles in free space that show nonspherical shape oscillations.

13.1.3 Damping effects

Strong damping of the microbubble oscillation has been observed. The total damping will have contributions from viscosity of the liquid and coating, heat diffusion, sound radiation, and possibly others. The estimation of the damping by liquid viscosity is complicated because of the contact with the capillary wall. Hence, distinction between the contribution of the liquid viscosity and coating viscosity cannot be made from the current study. Moreover, direct (i.e., without the indirect way of model-based estimates) quantification of the damping due to the coating would require recordings of uncoated bubbles, which are unstable and thus challenge the experimental method. When comparing the measurement results to models only a qualitative estimate can be made of the bubble damping due to the coating. From the observed high damping of microbubble oscillations, a large influence can be expected from the coating (Chapters 3, 8 and 11). In fact, the theoretical resonance curve depicted in Fig. 11.9 (resonance frequency *versus* microbubble size) shows a different trend for smallest sizes compared to larger sizes; this behavior is indicative of a second-order mass-spring system in which damping dominates resonance effects [Khismatullin and Nadim, 2002]. Another example can be found in Fig. 3.7c where the normalized scattering cross section of bubbles vs. the radius does not show a resonance peak anymore, although the echo-phase curves suggest that the studied bubbles have a natural frequency equal to the excitation frequency. These results suggest that coated microbubbles in those experimental conditions are strongly damped, thus inhibiting the advantageous resonance effects that are usually advertised as 'beneficial for contrast imaging' [Feinstein, 2004].

Special consideration should be given to the restriction 'in the present experimental condition' in the previous paragraph, of which the main aspect is the fact that the bubbles are examined inside a microcapillary. This has two implications:

1. the bubble is in close contact with a wall, which situation could induce additional viscous damping [Garbin et al., 2007; Dollet, 2009; van der Meer et al., 2007]. Van der Meer et al. [2007] model the additional damping due to a wall

by a doubling of the viscosity of water. However, the damping can be expected to be frequency and size dependent [Ohl et al., 2006]. Moreover, since not only the damping but also the resonant characteristics of the microbubble are changed by the wall, a simple approximation might not be valid in all cases.

2. The acoustic wave amplitude inside the capillary tube could be different from the undisturbed wave outside of the tube; the difference can be significant in the higher-frequency range used in this thesis (>5 MHz) [Qin et al., 2008]. Since the pressure values that are reported in experimental studies are obtained by a hydrophone that is located outside the tube, this could also be a source of error.

Therefore, unfortunately, the current results cannot be duplicated to freely-floating microbubbles without further considerations of the points mentioned above.

13.1.4 Deflation

The thin phospholipids coating provides a very flexible layer. Yet, diffusion of gas from the microbubble core into the bulk is still successfully slowed down by the coating, leading to survival times of bubbles in the order of minutes to hours in an experimental setup. This allowed examining microbubbles without the complication of sudden dissolution. However, insonation sometimes leads to accelerated dissolution; this ultrasound-induced deflation was especially significant for higher radial excursion (Table 13.1). Therefore the driving pressure amplitude and pulse repetition numbers were kept relatively low in the experiments when this effect was not wanted.

A deflation of 10% of the radius was assumed not to significantly change the microbubble behavior. A retrospective validation of this assumption can be based on the results of Chapter 3 (deflation-assisted characterization), where a decrease of bubble size of 10% could change the amplitude by at most 50% (6 dB – see Fig. 3.5). This decrease is within range of the fluctuations in echo amplitude expected for a certain size. On the other hand, in the extreme case, the reduction of radial amplitude of 50% might bring the bubble oscillations in another regime. The 10% criterium might therefore be better set to a lower value in future studies, although it is acknowledged that a lower value means that more experimental results have to be discarded because of too large deflation.

13.1.5 Microbubble differences within one agent, and between agents

Microbubbles of the same size behave differently. Examples are seen throughout this thesis (in particular Figs. 3.5, 8.2, 9.6, 11.9, and 12.5). This remarkable feature shows the large influence of the coating, despite its thinness. The exact mechanism

for the fluctuations is not known, but a hypothesis can be given based on the work by Borden et al. [2006]. In that paper it is shown that phospholipids monolayers can organize like islands of condensed phase material in a sea of expanded phase. The organization has chaotic nature, and consequently the number and size of the islands is not known *a priori* at a given surface [Borden et al., 2006]. Yet, each configuration can yield its own unique strain-stress relation, and a unique initial surface tension, that influences the response of the microbubble. To further study this hypothesis an experimental setup could be devised in which the expanded phase is labeled with fluorescent dye, and in which a relation is investigated between the number and size of island and the radial excursion.

With respect to the differences between the various agents used in the experiments, several observations can be done. Chapter 8 (temperature influence) concludes that SonoVue and Definity microbubbles show similar levels of the fundamental acoustic response. For the *in vivo* application of the different agents, this finding implies that large differences in fundamental signal between the agents could not be explained by the difference in bubble response, but should be explained either by differences in agent concentration, or by differences in the size distribution function. Large differences in nonlinear response, however, might also be explained by the bubble response specific for the different agents. For example, SonoVue appears to show larger compression-only behavior than Definity, which could result in higher second harmonic levels from a SonoVue population, if the size distribution and microbubble concentration are equal.

BR14 and Definity show subharmonic oscillations (see Chapters 4 and 5) at an excitation level where regular models do not predict any subharmonic (see also Frinking [2009]). However, such low-amplitude subharmonic response was not seen with the small-animal agent Targeson (Chapter 7 - orthogonal microscope), which has similar phospholipids coating as Definity and SonoVue. The reasons for these differences are currently not known and may be studied in more detail in future.

13.2 Clinical relevance

13.2.1 Tissue attenuation of the scattered echo

Single microbubbles can be relatively easily detected and studied in an experimental setup with the right equipment, however *in vivo* detection is frustated by tissue scattering and attenuation. A calculation example might demonstrate this statement.

Using the experimenal setup described in Chapter 3 (deflation-assisted characterization) it was found that a resonant bubble, insonified at 2 MHz, 125 kPa amplitude (M.I. of roughly 0.1), scatters the wave with an amplitude of 10 Pa at 2.5

Table 13.2: Expected fundamental (f_0) and second harmonic ($2f_0$) echo amplitudes in units of Pa from a resonant microbubble located in water and at varying depth in tissue. The insonation wave has an amplitude of 125 kPa amplitude and a frequency of 2 MHz (M.I. 0.1).

	water	tissue		
	2.5 cm	2.5 cm	5 cm	10 cm
f_0	10 Pa	6.3	2	0.4
$2f_0$	1.5	0.6	0.1	0.01

cm distance. The second harmonic echo amplitude is 1.5 Pa in these conditions [2]. Using these levels as a reference, echo amplitudes can be roughly estimated when the wave is propagating in tissue, see Table 13.2. It is assumed that tissue attenuates ultrasound by 0.8 dB/cm/MHz (liver, [Duck, 1990]), and that the scattered waves are spherically diverging, giving an extra $1/r$ decay of the amplitude.

The table shows that the second harmonic amplitude at 5 cm is 0.1 Pa, which rapidly decreases further at increasing imaging depth. Such level is at the noise level of the experimental setup described in Chapter 3, which presumably has similar or better noise performance than commercial scanners. Hence, even when a detection scheme would be able to perfectly cancel tissue signals, the second harmonic signal of single microbubbles is weak compared to noise.

Echoes from a subharmonic frequency oscillation experience the opposite effect: tissue attenuation is lower than that of the fundamental-frequency oscillation. Unfortunately, because of the ω^2 dependency of the echo on the radial excursion (Chapter 4), the scattering strength of subharmonics is lower by a factor of four. It depends on the exact numbers whether the low tissue attenuation outweighs the lower scattering strength.

13.2.2 Selection of detection signals

Reflecting further on the aspects of tissue attenuation, nonlinear conversion, and scattering strength, it is yet unclear which frequency components should be used for the optimal detection scheme. Second harmonic detection signals are presumably significantly lower than fundamental-frequency signals because of both the inherent nonlinear conversion loss, and the higher attenuation in tissue at the higher frequency. Moreover, tissue also generates second harmonic signals that disturb the contrast detection signals. Subharmonic frequencies generated by the bubble have less tissue attenuation, and are not masked by tissue signals; however, the amplitude of subharmonic scattering from bubbles is inherently lower, and generated by

[2] Values presented by R. Mori and H. J. Vos at the 13th European Symposium on Ultrasound Contrast Imaging, Rotterdam, the Netherlands, January 2009

only small part of the full population. Fundamental-frequency detection schemes potentially have the highest signal-to-noise ratio (and hence highest imaging depth) but tissue suppression is most difficult.

Positive examples of a detection technique that optimize both SNR and tissue suppression are power modulation, which is widely used in clinical equipment, and the super harmonic imaging technique [Bouakaz et al., 2002]. Furthermore, dual-pulse detection schemes that work with fundamental-frequency imaging pulses such as radial modulation also potentially provide good SNR, but worse tissue suppression. A fundamental-frequency imaging method with high frequency manipulation pulses (Chapter 12) might perform well because of both high echo levels and good tissue signal suppression.

13.2.3 Blood viscosity

Blood has higher viscosity than water, which would result in lower response from microbubbles, and possibly lower detection signals, than found in studies in water. This drawback might be counteracted by the fact that lower radial excursions increase the importance of nonlinear coating dynamics (see Table 13.1). More study is needed to see which effect is stronger.

13.2.4 Bubble deflation

The inherent bubble deflation and destruction might frustrate echo-related quantitative perfusion measurements. In such measurement the scattering strength is assumed to relate only to the concentration of the agent, while also deflation changes the scattering strength. In fact, deflation reduces the fundamental-frequency scattering, but could potentially increase the second-harmonic scattering through the increased occurrence of "compression-only" behavior of smaller bubbles (see Chapter 5). This might lead to the unfortunate situation where the imaging method (fundamental or harmonic mode) biases the outcome of the clinical exam.

The fact that insonified microbubbles deflate to a certain compressed size range (Chapter 3 - deflation-assisted characterization) could be used to condition the contrast agent in order to produce a population with a more narrow size range than the original agent has in the vial. The properties of this conditioned agent would be better known and the detection scheme could be better tuned to these properties.

13.2.5 Self-demodulation excitation

The self-demodulation technique for microbubble excitation (Chapter 11) has both advantages and disadvantages compared to conventional transmission in a clinical environment. A simple detection of the low-frequency signals might not improve the contrast-to-tissue ratio since tissue scattering also contains the low-

frequency signals (Chapter 10 - self-demodulation of ultrasound). However, since microbubbles show strongly nonlinear responses, they might produce even larger detection signals than tissue. For example, compression-only can be an outstanding effect to produce a self-demodulation signal, since the period-averaged radius decreases during the excitation; this will produce a low-frequency pressure wave just like nonlinear propagation does. This self-demodulation effect of microbubbles would confirm the findings by Wu et al. [2007] and Chen et al. [2006], who indeed found a self-demodulation type signal originating from microbubbles. Nevertheless their experiments should be revised for possible occurrence of water-induced nonlinear propagation leading to similar low-frequency signals. The self-demodulation method potentially produces smaller effective beamwidth than conventional imaging, which is advantageous for imaging.

13.3 Hints towards the future

Research never stops. This section will therefore summarize possible near-future and far-future studies that take advantage of the current findings.

13.3.1 Detection techniques

Contrast detection schemes should enhance contrast signals and suppress tissue signals, and should provide sufficient signal-to-noise ratio (SNR). Subharmonic detection techniques potentially have very good tissue suppression, but implementation of this technique in commercial equipment has not been done yet. A reason for this could be the wide-band specifications of the equipment. However, since recent equipment more often enables second-harmonic imaging that requires the same bandwidth as subharmonic imaging, it can be expected that subharmonic imaging will be investigated more in near future.

Emerging experimental topics such as chirp imaging, second harmonic suppression technique and $f_0 + 3f_0$ excitation have shown *in vitro* that they could increase contrast to tissue ratio. However, since experimental conditions usually are milder than clinical conditions, their efficiency has yet to be proven. Very wide-band or dual-band detection schemes such as radial modulation, superharmonics, and the high-frequency manipulation technique proposed in this thesis (Chapter 12) might not be commercially realizable in near-future because of the absence of clinical scanners that comply with the frequency specifications.

13.3.2 From lab to clinic

The experiments in this thesis have been performed in a cellulose tube, containing few bubbles and clean water. Such well-defined environment is very useful for studying the behavior of microbubbles, but the step to clinical UCA detection

applications is large. Testing the various detection techniques in a tissue-mimicking phantom with different vessel sizes (including smallest capillaries) and tissue scattering, at body temperature, and carrying blood-like liquid, should show the probable efficacy of detection techniques in an early stage.

13.3.3 New agents

Stride et al. [2008] showed that changing the coating of microbubbles can increase the nonlinear responses significantly at low excitation pressures. Not shown in this thesis, but optically and acoustically observed by the current author, is the strong nonlinear response of the polymer coated bubbles investigated in Chapter 2. Similar nonlinear responses were also shown by Bouakaz et al. [2005] and Kooiman et al. [2009] for different polymer coated microbubbles; compression-only is regularly observed. The downside of polymer coating is a high viscosity, and strong inhomogeneity. The combination of these two effects might result in the situation where only small fraction of the insonified bubbles actually oscillate, and that strong threshold behavior is present; the latter is beneficial for contrast detection. Hints that support this hypothesis are given by a study by Kooiman et al. [2009] with an experimental polymer-coated agent.

13.3.4 Theranostics

Next to the diagnostic value of contrast agents, microbubbles will be further tested for use in therapeutic applications, or for use in a combination of these two applications (called theranostics). In the near-future more knowledge is needed on cell-bubble interactions. When does sonoporation occur? When do cells survive? There is a great need for direct observations of microbubble oscillation amplitudes and shapes to link to cell membrane deformation, such as done in the preliminary studies by van Wamel et al. [2004, 2006].

Moreover, microparticles as drug and gene delivery vehicles are to be optimized, for which the final goal should be delivering-on-demand, i.e., a deposition of 100% on the right spot only, at the right time. This delivering-on-demand would seriously reduce unwanted side effects of drug administration, and would provide a new chapter in the history of microbubble applications.

Bibliography

Borden, M. A., G. V. Martinez, J. Ricker, N. Tsvetkova, M. Longo, R. J. Gillies, P. A. Dayton, and K. W. Ferrara, "Lateral phase separation in lipid-coated microbubbles," *Langmuir*, 22: pp. 4291–4297, 2006.

Bouakaz, A., S. Frigstad, F. J. ten Cate, and N. de Jong, "Super harmonic imaging: A new imaging technique for improved contrast detection," *Ultrasound Med Biol*, 28(1): pp. 59–68, 2002.

Bouakaz, A., M. Versluis, and N. de Jong, "High-speed optical observations of contrast agent destruction," *Ultrasound Med Biol*, 31(3): pp. 391–399, 2005.

Chen, S., R. Kinnick, J. F. Greenleaf, and M. Fatemi, "Difference frequency and its harmonic emitted by microbubbles under dual frequency excitation," *Ultrasonics*, 44: pp. e123–e126, 2006.

Dollet, B., "Notes on the numerical simulations of the analytical solutions of surface modes close to a wall," *personal notes*, 2009.

Duck, F. A., Physical properties of tissue, Academic press Ltd., 1990.

Emmer, M., The onset of bubble vibration, Ph.D. thesis, ErasmusMC, Rotterdam, the Netherlands, 2009.

Feinstein, S. B., "The powerful microbubble: From bench to bedside, from intravascular indicator to therapeutic delivery system, and beyond," *Am J Physiol Heart Circ Physiol*, 287(2): pp. H450–457, 2004.

Frinking, P., "Subharmonic behaviour," in proc. 13th Eur Symp Ultras Contrast Agents, Rotterdam, the Netherlands, 2009.

Garbin, V., D. Cojoc, E. Ferrari, E. Di Fabrizio, M. L. J. Overvelde, S. M. van der Meer, N. de Jong, D. Lohse, and M. Versluis, "Changes in microbubble dynamics near a boundary revealed by combined optical micromanipulation and high-speed imaging," *Appl Phys Lett*, 90: p. ref. 114103, 2007.

Khismatullin, D. B. and A. Nadim, "Radial oscillations of encapsulated microbubbles in viscoelastic liquids," *Phys Fluids*, 14(10): pp. 3524–3557, 2002.

Kooiman, K., M. R. Böhmer, M. Emmer, H. J. Vos, C. Chlon, W. T. Shi, C. S. Hall, S. H. P. M. de Winter, K. Schroën, M.Versluis, N. de Jong, and A. van Wamel, "Oil-filled polymer microcapsules for ultrasound-mediated delivery of lipophilic drugs," *J Control Release*, 133: pp. 109–118, 2009.

Longuet-Higgins, M. S., "Monopole emission of sound by asymmetric bubble oscillations. Part 1. Normal modes," *J Fluid Mech*, 201: pp. 525–542, 1989.

Marmottant, P., S. M. van der Meer, M. Emmer, M. Versluis, N. de Jong, S. Hilgenfeldt, and D. Lohse, "A model for large amplitude oscillations of coated bubbles accounting for buckling and rupture," *J Acoust Soc Am*, 118(6): pp. 3499–3505, 2005.

Morgan, K. E., J. S. Allen, P. A. Dayton, J. E. Chomas, A. L. Klibanov, and K. W. Ferrara, "Experimental and theoretical evaluation of microbubble behavior: Effect of transmitted phase and bubble size," *IEEE Trans Ultrason Ferroelectr Freq Control*, 47(6): pp. 1494–1509, 2000.

Ohl, C.-D., M. Arora, R. Ikink, N. de Jong, M. Versluis, M. Delius, and D. Lohse, "Sonoporation from jetting cavitation bubbles," *Biophys J*, 91(11): pp. 4285–4295, 2006.

Qin, S., D. E. Kruse, and K. W. Ferrara, "Transmitted ultrasound pressure variation in micro blood vessel phantoms," *Ultrasound Med Biol*, 34(6): pp. 1014–1020, 2008.

Stride, E., K. Pancholi, M. Edirisinghe, and S. Samarasinghe, "Increasing the nonlinear character of microbubble oscillations at low acoustic pressures," *J R Soc Interface*, 5: pp. 807–811, 2008.

van der Meer, S. M., B. Dollet, M. M. Voormolen, C. T. Chin, A. Bouakaz, N. de Jong, M. Versluis, and D. Lohse, "Microbubble spectroscopy of ultrasound contrast agents," *J Acoust Soc Am*, 121(1): pp. 648–656, 2007.

van Wamel, A., A. Bouakaz, M. Versluis, and N. de Jong, "Micromanipulation of endothelial cells: ultrasound-microbubble-cell interaction," *Ultrasound Med Biol*, 30(9): pp. 1255–1258, 2004.

van Wamel, A., K. Kooiman, M. Harteveld, M. Emmer, F. J. ten Cate, M. Versluis, and N. de Jong, "Vibrating microbubbles poking individual cells: Drug transfer into cells via sonoporation," *J Control Release*, 112(1): pp. 149–155, 2006.

Wu, C.-Y., W.-H. Chao, Y.-H. Chou, and Y. Watanabe, "Analysis of characteristics of semi-intermodulated imaging based on multi-bifrequency approximation," *Jpn J Appl Phys*, 46(7B): pp. 4841–4846, 2007.

Summary

The imaging of smaller vessels and organ perfusion has high clinical value for diagnosis of cardiovascular diseases and cancer. However, imaging of smaller vessels and the capillary bed with clinical ultrasound is difficult because blood has lower scattering strength than tissue. Ultrasound contrast agents (UCAs) can potentially increase the scattering from blood. The agents consist of gas bubbles with sizes of some micrometer that are stabilized by a thin coating of e.g. polymers, albumin, or phospholipids molecules, and are injected intravenously. These bubbles are excited by the ultrasound field into a volumetric oscillation, and thus act as a secundary scattering scattering source. Imaging of contrast microbubbles is the topic of this thesis.

In recent years many acoustic detection schemes have been proposed to enhance contrast signals and suppress tissue signals. Linear fundamental-frequency scattering of microbubbles does not provide sufficient contrast, but microbubbles can also respond nonlinearly, which is beneficial for their detection. The proposed schemes have however great difficulty to detect very low concentration or even single microbubbles when surrounded by tissue. The main reason provided in literature is that tissue propagation also produces nonlinear signals that mask nonlinear signals from microbubbles. It could therefore be worthwile to search for nonlinear behavior of bubbles that does not have to compete with nonlinear tissue signals.

Given this background this thesis investigates single contrast agent microbubbles with optical, acoustical, and numerical techniques to study the influence of the microbubble structure and size on the linear and nonlinear responses. It particularly addresses phospholipids-coated agents since only this type of agent is currently approved for clinical use in the Netherlands and most other countries in the world. In the various studies the microbubbles are excited with frequencies and pressures that are in the range of those used diagnostically: frequencies of 0.5 to 25 MHz, and acoustic pressure amplitudes from 10 kPa to roughly 1 MPa. A large part of the studies has been carried out with a unique ultrafast framing camera, the brandaris-128 [3]. This camera contains a fast rotating mirror that sweeps a microscopic image over 128 consecutive cameras. This allows recording a microbubble response with rates up to 25 million frames per second. The movies provide a detailed description of the radial oscillations and shape.

Next to the standard diagnostic applications of ultrasound contrast agents, upcoming therapeutic applications are described in **Chapter 1**. First application is a targeting modality, in which the shell contains ligands to adhere to disease-specific

[3] www.brandaris128.nl

molecules on cells. This will lead to an accumulation of the bubbles in a diseased region which can next be detected. A second application is drug- and gene delivery, in which the microbubbles are the carrying vehicle of drug or genes. High-intensity focused ultrasound destroys the bubbles on the right spot and the drug is administred very locally, thus reducing unwanted side effects in the body. A third application is a transient opening of the cell membrane when a vibrating microbubbles is nearby (so called sonoporation). This opening allows drugs from the blood pool to enter the cell with a locally high concentration. These effects are sideways addressed in this thesis.

Chapter 2 describes a standard numerical model to predict the radial response of microbubbles and combines it with a force balance of translational forces. Ultrasound radiation force is caused by the interaction of a passing wave and the volumetric oscillation of the bubble. The behavior of individual bubbles that are freely moving in a water tank is observed, and it is shown that it depends on the bubble physical dimensions as well as on the viscoelastic properties of the encapsulation. An original method is distilled that estimates the viscoelastic properties of bubble encapsulation by fitting the experimental maximum bubble velocities to numerically-predicted ones.

Ultrasound contrast agent microbubbles have the tendency to deflate, which effect is enhanced when they are insonified. **Chapter 3** proposes to combine acoustic and optical methods to investigate the behavior of isolated lipid-shelled microbubbles during deflation. The backscattered pressure amplitude typically decreases with decreasing bubble size, independent of resonant behavior. This is contradicting the general assumption that resonance effects significantly increase the scattering; we explain our result with a high observed damping of the microbubble oscillation. The relative phase shift of the echo during the deflation process has been found to exceed $\pi/2$ which shows that the bubbles are insonified at their resonance frequency. It was also observed that microbubbles have highest deflation rate when they are insonified around their resonance frequency. When insonified well above or well below their resonance frequency they do not deflate at all.

In **Chapter 4** the relation is investigated between the optically observed radial oscillations and the acoustically recorded echo of isolated microbubbles. The echo can be predicted from the recorded radial dynamics through an equation that is based on the conservation of mass and momentum. Vice versa the radial dynamics of a microbubble can be correctly determined from the remotely recorded acoustic response. The combination of optical and acoustical data is further used in **Chapter 5**. The experimental study addresses the relation between size and nonlinear responses of isolated lipid-coated microbubbles. Ultrasound-induced deflation is used to sample the bubble at multiple sizes. Bubbles with size smaller than the resonant size show compression-only and expansion-only behavior (more expansion

than compression during the oscillation cycle) that is accompanied by strong second harmonic scattering. Subharmonic oscillations are observed for bubbles with size larger than resonant.

Radially oscillating microbubbles can deform when in contact with a wall. These nonspherical shapes have a preferential orientation perpendicular to the wall. Conventional microscope setups for microbubble studies have their optical axis perpendicular to the wall ('top view'), consequently they have a limited view of the deformation of the bubble. We have developed a method in **Chapter 6** to image the bubble in a *side view* by integrating a mirror in the microscope setup. When insonified by a 1 MHz, 140 kPa ultrasound pulse, a 9 μm diameter coated bubble appeared spherical in the top view, but showed an alternatively oblate and prolate shape in the side view. Working further on these results, microbubbles nearby a wall can achieve not only strong nonspherical oscillations, but their center of gravity will also show an oscillation. **Chapter 7** quantifies these oscillations at conditions relevant for clinical ultrasound contrast imaging. The experimental setup consists of two microscope objectives placed orthogonally. Images from the two objectives were recombined and relayed to the Brandaris-128 camera, thus allowing for a truly simultaneous imaging of the bubble in two orthogonal optical planes. Analysis of the clips shows nonspherical shapes that are described by the spherical harmonic of the 2^{nd} degree, having oscillation amplitude of the same order as that of the radial oscillations. A model-based estimate reveals a shear stress of 25 kPa up to 350 kPa at the wall because of the vibrating bubble. A normal stress up to 1 MPa is estimated at the wall. Such values might explain sonoporation, although also the observed micro jets could provide an explanation.

The dynamic behavior of UCAs is normally studied at room temperature ($\sim$ 21°C) although clinical usage of the agents is at $\sim$ 37°C. **Chapter 8** investigates the influence of such temperature difference on the dynamic behavior of microbubbles from the commercial agents SonoVue (Bracco) and Definity (Lantheus Medical Imaging). Microbubbles are submersed in water at room temperature or body temperature and insonified. Radial excursion of single microbubbles is resolved using the ultrafast framing camera Brandaris-128. SonoVue microbubbles that are resonant show higher radial excursion at the higher temperature, up to a factor of 2. This factor is at most 1.5 for Definity. Both agents show about 2-fold decrease of acoustic onset level when heated to body temperature. Although significant changes in the shell occur with changing temperature, the nonlinear thresholding and compression-only effects still exist at body temperature.

Working more on contrast agent detectability, a recent imaging modality called radial modulation is investigated. The modality is based on dual-frequency insonation of contrast agent microbubbles; low frequency (LF) pulses are used to modulate the response of the microbubbles to a high frequency (HF) imaging pulse.

Although the technique has been successfully implemented before, no consensus persists on parameter choice, and the dominating microbubble effects. The modality is investigated in **Chapter 9** using optical recordings and simulations of single microbubbles. The results show that the LF pulse induces significant *c*ompression-only behavior, in which the compression half-cycle of the bubble oscillation is more pronounced than the expansion half-cycle. Compression-only-related effects results in high radial amplitude modulation for microbubble sizes below and at HF resonance. This shows the large influence of the coating. It however also appeared that, for imaging, microbubble size is more important than resonance and compression-only effects.

High-frequency (>10 MHz) ultrasound is used in e.g. small animal imaging or intravascular applications. Currently available UCAs have a suboptimal response for high frequencies. **Chapter 10** therefore investigates the nonlinear propagation effects in a high-frequency ultrasound field (25 MHz) and its use for standard UCA and diagnostic frequencies (1-3 MHz). Nonlinear mixing of two high-frequency carrier waves produces a low-frequency wave, known as the self-demodulation or parametric array effect. Hydrophone experiments show that the amplitude of the self-demodulated field would be sufficient for UCA excitation. Experimental values are confirmed by numerical simulations using the KZK equation on a spatially convergent grid. **Chapter 11** shows with high speed camera observations that it is indeed possible to induce microbubble oscillations with the low frequency signal arising from the self-demodulation propagation process. As an application we determine the resonance frequency of Definity contrast agent microbubbles with radius ranging from 1.5 to 5 μm by sweeping the self-demodulation frequency in the range 0.5 to 3.5 MHz.

Most of current ultrasound contrast agent detection techniques suffer from nonlinear propagation in tissue. **Chapter 12** proposes a new dual-pulse technique that is based on a LF imaging pulse, intermittently accompanied by a HF manipulation pulse (as opposed to the radial modulation approach, where the HF pulse is used for imaging). Optical recordings showed that phospholipids coated microbubbles excited by an LF pulse show compression-only behavior. When the LF pulse is accompanied by the HF manipulation pulse the compression-only is significantly reduced, as is the nonlinear higher harmonic frequency content. This difference in microbubble response could be used to produce contrast detection signals.

From an experimental point of view it is concluded that microbubble oscillation is probably strongly affected by the vessel wall and body temperature; experimental setups should take these effects in account.

It is further discussed that there are three oscillation regimes of the microbubble oscillation, and nonlinear behavior due to the coating is most pronounced at low oscillation amplitudes. This implies that clinical contrast detection schemes

should work in this regime. However, it is yet unclear which frequency components should be used for the optimal detection scheme, since a trade-off has to be found between the signal-to-noise ratio and tissue signal suppression. This trade-off might be worked around by the introduction of dual-pulse detection schemes that work at the fundamental frequency. Such might provide the best solution for single microbubble imaging.

Samenvatting

Het afbeelden van kleinere vaten en de orgaanperfusie is van groot klinisch belang voor de diagnose van hart- en vaatziekten en kanker. Ultrageluidafbeeldingstechnieken hebben echter moeite met het weergeven van de kleinere vaten en het vaatbed omdat bloed een lager echosignaal geeft dan weefsel. Ultrageluidcontrastmiddelen kunnen de verstrooiing van bloed vergroten. Deze middelen bestaan uit gasbellen van enkele micrometers groot die gestabiliseerd worden door een dunne schil van bijvoorbeeld polymeren, albumine, of fosfolipide moleculen, en worden intraveneus ingespoten in de bloedbaan. De bellen worden geëxciteerd door het ultrageluidveld waardoor ze in een volumetrische trilling komen, die op haar beurt het geluid verstrooit. Het afbeelden van contrastbellen is onderwerp van dit proefschrift.

De afgelopen jaren zijn verschillende detectiemethoden voorgesteld om de signalen van de bellen te versterken en tegelijkertijd de verstrooiing van weefsel te onderdrukken. De verstrooiing door de bellen van de grondfrequentie levert niet genoeg contrast op. Ze kunnen echter ook niet-lineaire akoestische responsie geven wat voordelig is voor de detectie. Deze methoden hebben grote moeite om zeer kleine concentraties, of zelfs enkele bellen, te kunnen detecteren wanneer ze omringd worden door weefsel. De meeste niet-lineaire detectiemethodes worden namelijk tegengewerkt doordat propagatie van de ultrageluidgolf in weefsel ook niet-lineaire signalen geeft. Het zou daarom lonend kunnen zijn om op zoek te gaan naar niet-lineair gedrag van bellen dat niet hoeft te wedijveren met niet-lineaire signalen van weefsel.

Tegen deze achtergrond beschrijft dit proefschrift een aantal onderzoeken naar vele individuele microbellen met behulp van optische, akoestische en numerieke methodes. Er wordt voornamelijk gekeken naar de invloed van de samenstelling en grootte van de bellen op de lineaire en niet-lineaire responsies. De bellen werden aangestraald met geluidsgolven van verschillende frequenties en drukken, welke behoren tot de reguliere waarden voor klinisch ultrageluid: frequenties van 0.5 tot 25 MHz en akoestische drukken van 10 kPa tot ongeveer 1 MPa. Een groot deel van de studies is uitgevoerd met behulp van een zeer snelle camera, de Brandaris-128 [4]. Dit unieke camerasysteem heeft een roterende spiegel waardoor een microscoopbeeld snel op 128 opeenvolgende camera's wordt geprojecteerd. Hierdoor kan een bel worden opgenomen met een snelheid tot 25 miljoen beelden per seconde en kan de trilling en vorm goed geanalyseerd worden.

Hoofdstuk 1 beschrijft de standaard contrast-toepassingen zoals beschreven in het voorgaande deel, maar beschrijft ook drie opkomende diagnostische en thera-

[4] www.brandaris128.nl

peutische toepassingen van microbellen. De eerste toepassing is de toevoeging van speciale moleculen aan de schil waardoor de bellen blijven haken aan cellen die een bepaald ziektebeeld laten zien. Hierdoor zullen bellen ophopen in de zieke delen van het lichaam alwaar ze zullen worden gedetecteerd. De tweede is het lokaal toedienen van medicijnen of genen, waarbij de microbellen of hun schillen worden gevuld met het medicijn of de genen. Door lokaal aanstralen met ultrageluid worden de bellen stukgemaakt waarna ze het material achterlaten. Een derde toepassing is het tijdelijk openen van de celwand wanneer een trillende bel zich in de buurt bevindt. Medicijnen uit het bloed kunnen hierdoor de cel binnendringen en daar hun werking doen. Deze nieuwe toepassingen worden zijdelings genoemd in dit proefschrift.

Hoofdstuk 2 beschrijft een standaard numeriek model om de belresponsie te bepalen en combineert dit model met een beschouwing van de verschillende krachten die werken om de verplaatsing als gevolg van akoestische stralingsdruk uit te rekenen. De drijvende kracht wordt veroorzaakt door een passerende ultrageluidgolf op een oscillerende bel. Een akoestische meetopstelling maakt het mogelijk om de maximale verplaatsing van bellen experimenteel te bepalen. De parameters in het model zijn vervolgens automatisch aangepast zodat deze de maximale verplaatsing goed voorspelt, waaruit een schatting van de elasticiteit en viscositeit van de schil wordt gevonden.

Als bellen worden aangestraald met ultrageluidgolven dan lopen ze sneller leeg dan anders. Dit effect wordt gebruikt in **hoofdstuk 3** waarin Definity (Lantheus Medical Imaging, North Billerica, MA) contrastbellen met verschillende frequenties worden aangestraald en de echo wordt opgenomen met een gevoelige transducer en ontvangstcircuit. Hierdoor ontstaat een hoge bemonsteringsdichtheid van de echo als functie van de initiële belstraal. De amplitude van de echo neemt af voor afnemende belgrootte. Dit is verwonderlijk omdat er meestal vanuit wordt gegaan dat resonantie-effecten de amplitude van de echo sterk verhogen. De reden voor het verschil is waarschijnlijk dat de schil van de bellen de trilling dempt. Dit resultaat kan ook verklaren waarom bellen niet goed contrasteren als slechts hun lineaire responsie op de grondfrequentie wordt gemeten. Overigens is gebleken dat bellen vooral leeglopen als ze rond hun resonantiefrequentie worden aangestraald; bellen waarvan de resonantiefrequentie ver onder of juist boven de excitatiefrequentie ligt, lopen niet leeg.

In **hoofdstuk 4** wordt de onderlinge relatie onderzocht tussen de radiële belexcursies en de uitgezonden geluidsgolven van geïsoleerde bellen. Een vergelijking gebaseerd op het behoud van massa en impuls blijkt radiële uitwijkingen van tienden van een micrometer te kunnen afleiden uit het akoestische signaal. De combinatie van optische en akoestische data is ook gebruikt in **hoofdstuk 5**. De experimentele studie behandelt de relatie tussen de grootte en niet-lineaire responsie

van microbellen met een fosfolipide schil. Het gecontroleerd laten leeglopen van de bellen is gebruikt om ze te bemonsteren op verschillende grootte. Bellen die kleiner zijn dan de resonantiegrootte laten *compression-only* en *expansion-only* zien (waarbij de expansie van de bel groter is dan de compressie tijdens een trilling), wat gepaard gaat met sterke signalen op de tweede en hogere harmonische frequentie. Subharmonische signalen ontstaan voor bellen die groter zijn dan resonant.

Oscillerende bellen kunnen vervormen als ze in contact zijn met een wand. De niet-sferische vormen hebben een voorkeursrichting die loodrecht op de wand staat, maar doordat gangbare microscoopopstellingen hun optische as ook loodrecht op de wand hebben, kunnen deze de vervorming niet goed afbeelden. **Hoofdstuk 6** beschrijft een methode om met behulp van een spiegeltje de bel van de zijkant te bekijken. **Hoofdstuk 7** breidt deze opstelling uit met een tweede objectief om zowel het bovenaanzicht als het zijaanzicht tegelijk op te nemen met de camera. Het blijkt dat bellen al bij middelmatige drukken vervormen en ze een voorkeur hebben voor een alternerende uitgerekte en samengedrukte vorm. De wand zorgt ook voor een grote translatie van het massamiddelpunt. Verder kunnen microjets ontstaan als bellen met 200 kPa, 2.25 MHz worden aangestraald. Berekeningen zijn uitgevoerd waaruit blijkt dat de afschuifkrachten op de wand in de orde van 25 kPa tot 350 kPa zijn. Verder zijn de normaalkrachten geschat op een maximum van 1 MPa. Dit soort waarden kunnen membraanporatie verklaren, maar ook de waargenomen micro jets zouden sonoporatie kunnen verklaren.

De invloed van temperatuur op het belgedrag is bestudeerd in **hoofdstuk 8**. De commerciële contrastmiddelen SonoVue (Bracco imaging) en Definity zijn bemonsterd in een waterbad van 21°C en 37°C met ultrageluidpulsen. Het blijkt dat de twee beltypes ongeveer hetzelfde reageren op de geluidspulsen, ook al heeft temperatuur een grotere invloed op SonoVue dan op Definity. Voor beide contrastmiddelen lijkt te gelden dat een hogere temperatuur zorgt voor een lagere viscositeit van de schil, maar dat niet-lineair gedrag van de schil niet wezenlijk verandert. Dit is gunstig omdat de meeste studies bij kamertemperatuur worden uitgevoerd en de resultaten dus ook kwalitatief gelden als de bellen op lichaamstemperatuur worden gebracht.

De hieropvolgende hoofdstukken onderzoeken verschillende detectiemethoden in meer detail. De eerste methode is de recent geïntroduceerde *radial modulation imaging* die gebaseerd is op het uitzenden van een dubbele-frequentie puls. Het laag-frequent (LF) gedeelte moduleert de responsie van bellen op het hoog-frequent (HF) gedeelte. Alhoewel de methode succesvol is ingezet is er geen consensus over de beste keuze van parameterwaarden, en ook niet over de achterliggende verschijnselen die resultaat opleveren.

Uit deze studie blijkt dat *compression-only*, waarbij bellen een trilling uitvoeren met een kleinere expansie dan compressie, een grote invloed heeft op het belgedrag van kleinere bellen tijdens de dubbele-frequentie aanstraling. Echter, omdat kleinere

bellen minder verstrooiing geven dan grotere bellen, heeft compression only minder effect op het totale detectiesignaal en doen alle bellen evenveel mee in het voorspelde detectiesignaal.

Hoogfrequent ultrageluid (>10 MHz) wordt veel gebruikt in bijvoorbeeld het afbeelden van kleine dieren en in intravasculaire ultrageluidcatheters. Het nadeel van de huidige contrastmiddelen is echter dat ze geen optimale responsie op die hoge frequenties geven. **Hoofdstuk 10** bestudeert daarom de niet-lineaire propagatie-effecten in een hoog-frequent ultrageluidveld (25 MHz) en het gebruik daarvan voor standaard contrastmiddelen en diagnostische frequenties (1-3 MHz). Het niet-lineair mixen van twee hoog-frequente draaggolven geeft een laag-frequente golf, wat ook bekend staat als zelf-demodulatie of het *parametric array* effect. Zowel een numerieke als een experimentele methode laten zien dat de amplitude van de laag-frequent golf voldoende zou moeten zijn om een bel te exciteren. **Hoofdstuk 11** laat in een experiment zien dat een bel inderdaad gaat trillen als gevolg van het niet-lineair ontstane signaal. De methode is verder gebruikt om de resonantiefrequentie van verwarmde Definity-bellen te schatten.

De meeste huidige detectiemethoden worden tegengewerkt door de niet-lineaire propagatie in weefsel. De techniek beschreven in **hoofdstuk 12** probeert dit te omzeilen door tweemaal dezelfde laag-frequent puls uit te zenden, waarbij om de andere puls een hoog-frequente manipulatiepuls wordt meegezonden. Dit is dus het tegenovergestelde van het eerder genoemde radial modulation imaging. Optische experimenten hebben laten zien dat de hoog-frequent puls de responsie van de bel op de laag-frequent puls manipuleert. De verschillen tussen de twee gereflecteerde signalen vormen het detectiesignaal.

Er wordt geconcludeerd vanuit een experimenteel oogpunt dat de omgeving en de temperatuur van de bel in het lichaam van grote invloed is op de trilling en dat hier rekening mee moet worden gehouden in een experimentele meetopstelling voor contrastmiddelonderzoek.

Uit het voorgaande werk wordt verder geconcludeerd dat bellen kunnen trillen in 3 verschillende regiems. Het meest opvallende regiem is die waarbij de beltrilling een kleine uitwijking heeft en de schil een grote niet-lineaire responsie veroorzaakt. Aangezien deze niet-lineaire responsie voordelig is voor de detectie van bellen, impliceert dit dat detectiemethoden in dit regiem moeten werken. Het is echter nog onduidelijk welke frequentie-componenten gebruikt zouden moeten worden voor de optimale detectie, omdat er een afweging gemaakt moet worden tussen de signaal-ruis verhouding en signaalonderdrukking van weefsel. Deze afweging zou kunnen worden omzeild door gebruik te maken van duo-puls technieken die werken op de fundamentele frequentie. Dit zou uiteindelijk de beste oplossing kunnen zijn voor het afbeelden van enkele bellen.

Dankwoord

Zo'n promotieonderzoek, da's niet niks. Dat lukt ook nooit alleen, en vele mensen hebben direct of indirect geholpen tijdens de afgelopen jaren. Als eerste wil ik daarom mijn promotoren, Prof.dr.ir. Ton van der Steen en Prof.dr.ir. Nico de Jong, hartelijk danken voor al jullie enthousiasme en vertrouwen. Dankzij jullie niet-aflatende inzet zit de afdeling niet alleen fysiek, maar ook wetenschappelijk op een ongekende hoogte. Ton, ik heb de kijkjes achter de schermen van de financiering van wetenschappelijk onderzoek altijd erg verhelderend gevonden. Nico, we hebben heel wat uren gediscussieerd over de experimentele methodes, de resultaten, en de wetenschappelijke output, maar daar bovenop heb jij me ook geleerd om de menselijke kant van het onderzoek en de personen te blijven zien, en dat je best in je pak kan sleutelen aan de Brandaris-128 camera.

I would also like to thank the 'reading' members of the doctorate committee, Prof.dr.ir. Marion de Jong, Dr. Michel Versluis, and Prof.dr. Piero Tortoli, for their willingness to join the doctorate committee, and their effort to review the thesis manuscript. I am also grateful to the other members of the doctore committee, Prof.dr. P. N. Burns, dr. M. A. Averkiou, and dr. F. J. ten Cate, for their willingness to discuss the work during the defense.

De afdeling Biomedical Engineering kent vele gezichten. Hans Bosch en Charles wil ik bedanken voor jullie snelle en doordachte antwoorden op de meest uiteenlopende vragen, en Hans, ik bewonder je enorme organisatietalent. Annemieke wil ik bedanken voor de leuke discussies over cellen en bellen, en ik bewonder jouw richtingsgevoel voor interessante biomedische onderzoeken. I would also like to thank Dave Goertz for teaching me how to do Real Experiments, how to model, and how to ask the right questions. I regret you couldn't be my supervisor but I am truly happy that the cooperation was not stopped by the Atlantic Ocean.

Van de oudere PhD/post doc garde, die er al (bijna) was toen ik begon bij de afdeling, wil ik bedanken (op volgorde van buro): Jerome, Paul, Guillaume, Michiel, Egon, Klazina, Miranda, Marcia, Esther, Marco, Marijn, Martijn, Antoinette, en Radj, voor alle gezelligheid tijdens de lunches, dineetjes, congressen, muziekmiddagen, en indertijd ook natuurlijk de filmavonden... Marcia, als inhoudelijk meest-directe collega hebben we heel wat uren doorgebracht binnen en buiten het lab, en ik heb met plezier met je samengewerkt aan het bestuderen van die belletjes... Ook bewonder ik je autonome wetenschappelijk denken zeer!

De nieuwere PhD/post-doc/geen PhD garde heeft zich wat meer over de twee verdiepingen verspreid, maar niettemin is de band erg sterk: Margreet, Sandra, altijd gezellig om jullie te spreken; Mike, Telli, Mirza, Toshi, it is always a pleasure

to discuss science and non-science with you, en Gijs, David, Krista, jullie hebben een gezellig lab en zeker ook bedankt voor alle lunches samen! Tom, succes met de eerste loodjes... Paul, Marlies, Marcia, Tom, Esther, Egon, hartelijk dank voor het vrijmaken van tijd om een en ander door te lezen van mijn proefschrift.

I would also like to thank 'my' MSc students for their enthusiasm, efforts and of course results obtained in their work: Riccardo Fabbri, Frederic, Katerina, and Jacopo. Whatever you are going to do I am very positive you'll all find a perfect match with your knowledge, spirit, and interests!

Dan zijn er nog vele op de afdeling die zogenaamd ondersteunen, maar dat gelukkig ook in zeer directe zin doen, want samen dragen ze de gehele afdeling. Bovenal wil ik Mieke noemen als centrale spil binnen de afdeling, zonder wie mijn promotie zeker in de soep gelopen zou zijn, maar ook Jan, Robert, Frits, Hans Verdoes, Marianne, computer-Roland, Gerard, Cees, jullie zijn erg fijne collega's om mee te werken en mee te kletsen! Leo, Wim, Geert, Michiel, dankzij jullie inzet en gouden handen zijn die belletjes tenminste een beetje te bedwingen.

Piero, La (;-)) ringrazio per essere il mio babbo a Firenze, porto di salvezza, e per essere tanto paziente quando sono invaso la tua camera colle idee scientifiche stranissime. Francesco, il mio più grande fratello, e sempre una festa parlare e collaborare con te, il tuo entusiasmo e tanto contagioso. Riccardo, grande Ricc, il mio fratello gemello, mi piace tantissimo la nostra collaborazione, e che pensi dalla duo-presentatizione a Rotterdam, ottimo ottimo... Anche gli altri dal MSDLab a Firenze con cui ho collaborato, Fabio, Luca, Paolo, Stefano, Allessandro, Enrico, Riccardo Fabbri, vi ringrazio per lo ottimo anno a Firenze, e per la grande ospitalità con cui avete assorbito l'olandese strano. Tanti grazie per tutto.

Ik heb elke keer weer met plezier de trein naar Twente gepakt om te discussiëren over het gedrag van die bellen, en mijn dank aan de Physics of Fluids-groep is groot voor het delen van het enthousiasme over dat onderwerp. Michel, je fysisch inzicht en kritische vragen hebben me steeds weer met beide benen op de grond gezet, waarvoor veel dank. Als jij naar een tekst hebt gekeken komt hij volledig rood terug, maar na die verbeteringen is die opeens leesbaar geworden. Jeroen, Marlies, Sander, Benjamin, Valeria, Erik, Timo: hartelijk dank voor alle gezellige gesprekken en nuttige meetings, waar dan ook ter wereld, het is echt een plezier om met jullie samen te werken.

Ik wil ook dr. Koos Huijssen bedanken voor jouw heldere blik op niet-lineaire ultrageluidpropagatie. Also I would like to thank Prof.dr. V.F. Humphrey for the brief but extremely useful comments on nonlinear ultrasound propagation, given during the various symposia where we met.

Ik ben vast niet de enige promovendus die de laatste dagen voor de drukkerdeadline 's avonds tot laat doorwerkt, maar dat het maken van het omslagontwerp ook tot in de nachtelijke uren gebeurt, had ik nooit zo bedacht; en dat met een dikke buik.

Margreet, hartelijk dank voor het maken van de prachtige omslag en uitnodiging!

Op de achtergrond maar altijd dichtbij zijn mijn ouders, die ik hartelijk wil bedanken voor hun steun in al de jaren van mijn leven. Jullie hebben me geleerd geduld te hebben, rustig door te werken, en dromen te volgen. Ook bedankt voor het geduld als de stoppen in huis weer eens doorsloegen, vroeger, als ik aan het knutselen was. Dit proefschrift was nooit tot stand gekomen als jullie me niet hadden aangemoedigd en gesteund in mijn keuzes! Harco, Letty, we zijn samen bezig een grote gezellige familie te vormen, en ik geniet altijd als we weer samen zijn.

Annemarie, ik wil jou bedanken voor je liefde, de gezelligheid en ons plezier samen. Door dik en dun kan ik vertrouwen op je compassie en medeleven. Ik wil je ook bedanken voor je geduld zo vlak voor de promotiedeadlines, als ik weer eens achter m'n laptoppie kruip om nog 'even' te werken... We gaan nu een huis kopen met echte bomen in de tuin, en ik kijk er naar uit samen met jou de 100 te halen!

Merlijn, je bent een groot tovenaar die alle harten steelt met een simpele glimlach... daar doen we het allemaal voor.

Curriculum Vitae

Hendrik J. (Rik) Vos was born on January 23, 1978, in Zwartsluis, the Netherlands. He received his pre-university education at the Katholiek Gelders Lyceum in Arnhem. In 1996 he started his Applied Physics BSc/MSc at Delft University of Technology, the Netherlands. He was an active member of the student fraternity Sanctus Virgilius during his studies in Delft. Also, in 1998/1999, he was full time member of the board of the Applied Physics Student Association.

During his BSc years he took an internship at Fokker Space, Leiden (now Dutch Space) on a matrix tactile sensor aimed for use on robotic arms in space. During his MSc he took an internship at IRCAM (Institut de Recherche et Coordination Acoustique/Musique, Paris, France) where he investigated the sound radiation from a violin and performed a 3D reproduction of its sound and the radiation pattern. His MSc research project involved the design and prototyping of a medical 20-40MHz IntraVascular UltraSound (IVUS) transducer. In 2004 he received the MSc degree, with honours, in Applied Physics.

In 2004 he won a grant from the Dutch VSB foundation for a one-year post-Master research at the Universitá di Firenze, Italy. Part of the stay was also funded by the UMEDS EU project partly running at the University of Florence. In that year he worked on models and experimental methods to describe the behavior of microbubbles which are used as medical ultrasound contrast agents.

During his graduate years (2005 – 2010) pursuing a PhD at the Biomedical Department of the Erasmus Medical Center, Rotterdam, the Netherlands, he has developed and improved the tools and equipment to image and model the behavior of single microbubbles. The results are reported in this PhD thesis. During his graduate years he has attended many international scientific conferences, meetings and courses (see attached portfolio). Furthermore, he has contributed regularly to the yearly international IEEE Ultrasonics Symposium in the years 2004 - 2009, and to the yearly European Symposium on Ultrasound Contrast Agents in the years 2005 - 2009. The first two years of his graduate project were financed in the framework of the TAMIRUT project (A new bio-sensor concept for medical diagnosis: targeted micro-bubbles and remote ultrasound transduction - NMP-2004-IST-NMP-2) by the European Union, and he contributed to all half-yearly meetings in that period. Many studies have been reported in international scientific journals (see Publication list).

His current interests include the development of technical equipment in general, and medical devices in particular, approached from a firm physical angle.

Rik Vos is living with his partner Annemarie and their son Merlijn (2008).

List of publications

Papers in preparation / in review / in press (Dec 2009)

H. J. Vos, D. E. Goertz, and N. de Jong, "Self-demodulation technique for microbubble excitation," *IEEE Transactions on Ultrasonics, Ferroelectrics, and Frequency Control*, 2009 - conditionally accepted.

H. J. Vos, D. E. Goertz, and N. de Jong, "Self-demodulation of high-frequency ultrasound," *Journal of the Acoustical Society of America*, 2009 - conditionally accepted.

F. Guidi, **H. J. Vos**, R. Mori, N. de Jong, and P. Tortoli, "Microbubble characterization through acoustically-induced deflation," *IEEE Transactions on Ultrasonics, Ferroelectrics, and Frequency Control*, 2009 - in press.

J. Sijl, **H. J. Vos**, T. Rozendal, N. de Jong, D. Lohse, and M. Versluis, "Combined optical and acoustical characterization of single ultrasound contrast microbubbles," *Journal of the Acoustical Society of America*, 2009 - in preparation.

P. L. M. J. van Neer, **H. J. Vos**, and N. de Jong, "Phase transfer of ultrasound transducers," *IEEE Transactions on Ultrasonics, Ferroelectrics, and Frequency Control*, 2009 - in review.

Patent

H. J. Vos, D. E. Goertz, and N. de Jong, "Pulse repetition rate excitation of contrast material," Erasmus Universitair Medisch Centrum Rotterdam, United Kingdom / the Netherlands, UK 0601380.9, 2006.

Peer-reviewed papers

M. Emmer, **H. J. Vos**, M. Versluis, N. de Jong, "Radial modulation of single microbubbles" *IEEE Transactions on Ultrasonics, Ferroelectrics, and Frequency Control*, vol. 56, nr. 11, pp. 2370-2379, 2009.

P. Tortoli, F. Guidi, R. Mori, and **H. J. Vos**, "The use of microbubbles in Doppler

ultrasound studies," *Medical & Biological Engineering & Computing*, vol. 47, nr. 8, pp. 827-838, 2009.

M. Emmer, **H. J. Vos**, D. E. Goertz, A. van Wamel, M. Versluis, and N. de Jong, "Pressure-dependent attenuation and scattering of phospholipid-coated microbubbles at low acoustic pressures," *Ultrasound in Medicine & Biology*, vol. 35, nr. 1, pp. 102-111, 2009.

K. Kooiman, M. R. Böhmer, M. Emmer, **H. J. Vos**, C. Chlon, W. T. Shi, C. S. Hall, S. H. P. M. de Winter, K. Schroën, M. Versluis, N. de Jong, and A. van Wamel, "Oil-filled polymer microcapsules for ultrasound-mediated delivery of lipophilic drugs," *Journal of Controlled Release*, vol. 133, nr. 2, pp. 109-118, 2009.

H. J. Vos, B. Dollet, J. G. Bosch, M. Versluis, and N. de Jong, "Nonspherical vibrations of microbubbles in contact with a wall: a pilot study at low mechanical index," *Ultrasound in Medicine & Biology*, vol. 34, nr. 4, pp. 685-688, 2008.

F. Guidi, **H. J. Vos**, and P. Tortoli, "Novel display modes for microbubble characterization," *IEEE Transactions on Ultrasonics, Ferroelectrics, and Frequency Control*, vol. 54, nr. 7, cover image, 2007.

H. J. Vos, F. Guidi, E. Boni, and P. Tortoli, "Method for microbubble characterization using primary radiation force," *IEEE Transactions on Ultrasonics, Ferroelectrics, and Frequency Control*, vol. 54, nr. 7, pp. 1333-1345, 2007.

M. Emmer, **H. J. Vos**, D. E. Goertz, A. van Wamel, M. Versluis, and N. de Jong, "Clinical relevance of pressure-dependent scattering at low acoustic pressures," *Ultrasonics*, vol. 47c, nrs. 1-4, pp. 74-77, 2007.

A. F. W. van der Steen, R. A. Baldewsing, F. L. Degertekin, S. Emelianov, M. E. Frijlink, Y. Furukawa, D. E. Goertz, M. Karaman, P. T. Khuri-Yakub, K. Kim, F. Mastik, T. Moriya, Ö. Oralkan, Y. Saijo, J. A. Schaar, P. W. Serruys, S. Sethuraman, A. Tanaka, **H. J. Vos**, R. Witte, and M. O'Donnell, "Ivus beyond the horizon," *EuroIntervention*, vol. 2, nr. 5, pp. 132-142, 2006.

M. E. Frijlink, D. E. Goertz, **H. J. Vos**, E. Tesselaar, G. Blacquière, A. Gisolf, R. Krams, and A. F. W. van der Steen, "Harmonic intravascular ultrasound imaging with a dual-frequency catheter," *Ultrasound in Medicine & Biology*, vol. 32, nr. 11, pp. 1649-1654, 2006.

H. J. Vos, M. E. Frijlink, E. Droog, D. E. Goertz, G. Blacquière, A. Gisolf, N. de Jong, and A. F. W. van der Steen, "Transducer for harmonic intravascular ultrasound

imaging," *IEEE Transactions on Ultrasonics, Ferroelectrics, and Frequency Control*, vol. 52, nr. 12, pp. 2418-2422, 2005.

Conference papers

H. J. Vos, R. Mori, J. Viti, J. Sijl, F. Guidi, P. Tortoli, N. de Jong, "Ultrafast framing optical and acoustical recordings of nonlinearly oscillating microbubbles," in proc. IEEE International Ultrasonics Symposium, Rome, Italy, ref. P2-C-03, 2009

D. Thomas, M. Emmer, **H. J. Vos**, V. Sboros, N. de Jong, "Optical observations of microbubble oscillation in small tubes," in proc. IEEE International Ultrasonics Symposium, Rome, Italy, ref. P-S-11, 2009.

D. Maresca, M. Muller, M. Emmer, **H. J. Vos**, A. F. W. van der Steen, N. de Jong, "Acoustic Size Distribution Analyzer for Microbubbles," in proc. IEEE International Ultrasonics Symposium, Rome, Italy, ref. P2-C-01, 2009.

F. Guidi, R. Mori, **H. J. Vos**, N. de Jong, and P. Tortoli, "Ultrasound induced deflation: A method to study the behavior of single bubbles with varying radius," in proc. IEEE International Ultrasonics Symposium, Beijng, China, pp. 1679-1682, 2008.

M. Overvelde, **H. J. Vos**, N. de Jong, and M. Versluis, "Ultrasound contrast agent microbubble dynamics," in: **Ultrasound contrast agents - Targeting and processing methods for theranostics**, G. Paradossi, P. Pellegretti, and A. Trucco (Eds.), Springer-Verlag Milano, Italy, pp. 79-98, 2009.

F. Guidi, R. Mori, **H. J. Vos**, and P. Tortoli, "Bubble Behaviour Testing (BBT) system for UCA characterization," in: **Ultrasound contrast agents - Targeting and processing methods for theranostics**, G. Paradossi, P. Pellegretti, and A. Trucco (Eds.), Springer-Verlag Milano, Italy, pp. 157-174, 2009.

H. J. Vos, M. Emmer, and N. de Jong, "Oscillation of single microbubbles at room *versus* body temperature," in proc. IEEE International Ultrasonics Symposium, Beijing, China, pp. 982-984, 2008.

K. Kooiman, M. R. Böhmer, M. Emmer, **H. J. Vos**, C. Chlon, W. T. Shi, C. S. Hall, S. H. P. M. de Winter, K. Schroën, M. Versluis, N. de Jong, and A. van Wamel, "Oil-filled polymeric ultrasound contrast agent as local drug delivery system for lipophilic drugs.," in proc. IEEE International Ultrasonics Symposium, Beijing, China, pp. 333-336, 2008.

M. Emmer, **H. J. Vos**, and N. de Jong, "Dual-frequency insonation of single microbubbles," in proc. Acoustics '08 (ASA), Paris, France, pp. 921-925, 2008.

H. J. Vos, M. Versluis, and N. de Jong, "Orthogonal observations of vibrating microbubbles," in proc. IEEE Ultrasonics Symposium, New York, NY, USA, pp. 765-768, 2007.

J. Sijl, **H. J. Vos**, N. de Jong, D. Lohse, and M. Versluis, "Combined optical and acoustical characterization of individual US contrast microbubbles," in proc. 19th International Congress on Acoustics, Madrid, pp. unknown - 6 pages, 2007.

F. Guidi, P. Tortoli, **H. J. Vos**, and N. de Jong, "Simultaneous optical and acoustical observation of microbubbles behavior," in proc. IEEE Ultrasonics Symposium, Vancouver, Canada, pp. 1358-1361, 2006.

H. J. Vos, D. E. Goertz, and N. de Jong, "Pulse repetition rate excitation of contrast agents," in proc. IEEE Ultrasonics Symposium, Vancouver, Canada, pp. 216-219, 2006.

M. E. Frijlink, D. E. Goertz, **H. J. Vos**, E. Droog, G. Blacquière, A. Gisolf, and A. F. W. van der Steen, "Harmonic intravascular ultrasound imaging with a dual-frequency catheter," in proc. IEEE Ultrasonics Symposium, Rotterdam, the Netherlands, pp. 241-244, 2005.

H. J. Vos, F. Guidi, E. Boni, and P. Tortoli, "Acoustical investigation of freely moving single microbubbles," in proc. IEEE Ultrasonics Symposium, Rotterdam, pp. 755-758, 2005.

F. Guidi, **H. J. Vos**, F. Nicchi, E. Boni, and P. Tortoli, "Acoustical imaging of individual microbubbles," in proc. International Acoustical Imaging conference, San Diego, M. P. André (Ed.), pp. 257-265, 2005.

H. J. Vos, M. E. Frijlink, E. Droog, D. E. Goertz, G. Blacquière, A. Gisolf, N. de Jong, and A. F. W. van der Steen, "A 20-40 MHz ultrasound transducer for intravascular harmonic imaging," in proc. IEEE International Ultrasonics, Ferroelectrics, and Frequency Control Joint 50th Anniversary Conference, Montreal, Canada, pp. 1966-1969, 2004.

H. J. Vos, O. Warusfel, N. Misdariis, and D. de Vries, "Analysis and reproduction of the frequency spectrum and directivity of a violin," in proc. NAG bijeenkomst, Utrecht, pp. 6-11, 2003.

Poster (P) and Oral (O) presentations, without paper

R. Mori, **H. J. Vos** (duo-presentation), F. Guidi, N. de Jong, and P. Tortoli, "Microbubble characterization through acousto-optic analysis of deflating bubbles (O)," at 14th European Symposium on Ultrasound Contrast Imaging, Rotterdam, the Netherlands, 2009.

A. van Wamel, V. Garbin, **H. J. Vos**, M. Overvelde, J. Sijl, M. Emmer, D. Lohse, M. Versluis, and N. de Jong, "Targeted versus free circulating ultrasound contrast agents: Towards new molecular imaging strategies (O)," at Molecular Imaging Congress, Nice, France, 2008.

J. Sijl, T. Rozendal, **H. J. Vos**, B. Dollet, N. de Jong, D. Lohse, and M. Versluis, "Acoustical resonance behavior of single ultrasound contrast agent microbubbles (P)," at 13th European Symposium on Ultrasound Contrast Imaging, Rotterdam, the Netherlands, 2008.

K. Kooiman, M. R. Böhmer, M. Emmer, **H. J. Vos**, C. Chlon, M. Foppen-Harteveld, N. de Jong, and A. v. Wamel, "A new drug delivery system for liphophilic drugs using polymeric ultrasound contrast agents (P)," at 13th European Symposium on Ultrasound Contrast Imaging, Rotterdam, the Netherlands, 2008.

H. J. Vos, M. Emmer, and N. de Jong, "radial manipulation of single microbubbles (O)," at 13th European Symposium on Ultrasound Contrast Imaging, Rotterdam, the Netherlands, 2008.

K. Kooiman, M. R. Böhmer, M. Emmer, **H. J. Vos**, C. Chlon, W. T. Shi, C. S. Hall, S. H. P. M. de Winter, K. Schroën, M. Versluis, N. de Jong, and A. van Wamel, "Microcapsules for ultrasound-mediated delivery of lipophilic drugs (O)," at Microbubbles for Ultrasound Imaging and Drug Delivery: New Applications with BURSTing Bubbles, workshop at Philips Research, High tech campus, Eindhoven, 2008.

J. Sijl, T. Rozendal, **H. J. Vos**, B. Dollet, N. de Jong, D. Lohse, and M. Versluis, "Combined optical and acoustical characterization of single ultrasound contrast agent microbubbles (O)," at International Congress of Acoustics, Paris, France, 2008.

M. Emmer, **H. J. Vos**, A. van Wamel, D. E. Goertz, M. Versluis, and N. de Jong, "Vibrating microbubbles at low acoustic pressures (O)," at 12th European Symposium on Ultrasound Contrast Imaging, Rotterdam, the Netherlands, 2007.

J. Sijl, **H. J. Vos**, N. de Jong, D. Lohse, and M. Versluis, "Combined optical and acoustical characterization of coated microbubbles (O)," at 60th Annual Meeting of

the APS Division of Fluid Dynamics, Salt Lake City, Utah, 2007.

N. de Jong, M. Emmer, **H. J. Vos**, and A. van Wamel, "Microbubble behaviour (O)," at Conference of Contrast Agent Imaging, Chicago (Feinstein ed.), 2007.

H. J. Vos, D. E. Goertz, and N. de Jong, "Repetition rate imaging of bubbles (O)," at 11th European Symposium on Ultrasound Contrast Imaging, Rotterdam, the Netherlands, 2006.

F. Guidi, F. Nicchi, **H. J. Vos**, and P. Tortoli, "A novel integrated system for real-time acoustical investigations on microbubbles (P)," at 10th European Symposium on Ultrasound Contrast Imaging, Rotterdam, the Netherlands, 2005.

Academic reports

H. J. Vos, "Single Microbubble Imaging," PhD thesis, Erasmus MC Rotterdam, the Netherlands, 2010.

H. J. Vos, "The modelling, design and prototyping of a 20MHz - 40MHz harmonic intravascular ultrasound transducer," M.Sc. thesis, Delft University of Technology, the Netherlands, 2004.

Supervised academic reports

K. Brisimi, report: ``Acoustic measurements with bubbles based on the self demodulation method´´, 6-month post-M.Sc. project, visiting from the University of Thrace, Greece, 2008.

F. Lemmel, report: ``The Brandaris Camera - implementation of a Region of Interest´´, M.Sc. project, visiting from Delft University of Technology, the Netherlands, 2008.

J. Viti, report: ``Combined optical and acoustical recordings of microbubbles´´, M.Sc. project, visiting from University of Florence, Italy, 2009 (in preparation).

PhD portfolio

Courses	**Year**	**ECTS**
Cardiovascular imaging and diagnostics (Coeur, Erasmus MC)	2006	1.5
Medical imaging: principles of ultrasound and magnetic resonance (European School on Medical Physics, Archamps)	2006	1.5
English Biomedical Writing and Communication (Erasmus MC)	2007	4.0
Classical Methods for Data-analysis (nihes)	2007	5.7
Effectief omgaan met tijd en prioriteit (Erasmus MC)	2007	0.3
Symposia		
IEEE Ultrasonics Symposium (Rotterdam)	2005	1.2
11^{th} European Symposium on Ultrasound Contrast Imaging (Rotterdam)	2006	0.6
IEEE Ultrasonics Symposium (Vancouver)	2006	1.2
12^{th} European Symposium on Ultrasound Contrast Imaging (Rotterdam)	2007	0.6
International Congress of Acoustics (Paris)	2007	1.5
IEEE Ultrasonics Symposium (New York)	2007	1.2
14^{th} New England Doppler meeting (Maastricht)	2007	1.2
13^{th} European Symposium on Ultrasound Contrast Imaging (Rotterdam)	2008	0.6
14^{th} European Symposium on Ultrasound Contrast Imaging (Rotterdam)	2009	0.6
IEEE International Ultrasonics Symposium (Rome)	2009	1.2
Supervising activities		
Supervising post-M.Sc. student visiting from the University of Thrace (6 months)	2008	2
Supervising M.Sc. student visiting from Delft University of Technology (6 months)	2008	2
Supervising M.Sc. student visiting from University of Florence (4 months)	2009	1

...

Teaching activities	Year	ECTS
Lecture 'bubble-wall interactions', TAMIRUT project meeting (Limassol)	2006	0.3
Lecture 'How does the microbubble vibrate close to a wall?', TAMIRUT project meeting (Potsdam-Golm)	2007	0.3
Lecture 'Orthogonal view microscope', University of Twente (Enschede)	2007	0.3